On the physico-chemical properties of softwood hemicellulose and compounds derived from it

Naidjonoka, Polina

2021

On the physico-chemical properties of softwood hemicellulose and compounds derived from it

POLINA NAIDJONOKA | DIVISION OF PHYSICAL CHEMISTRY | LUND UNIVERSITY

On the physico-chemical properties of softwood hemicellulose
and compounds derived from it

On the physico-chemical properties of softwood hemicellulose and compounds derived from it

by Polina Naidjonoka

LUND

UNIVERSITY

DOCTORAL DISSERTATION

by due permission of the Faculty of Science, Lund University, Sweden.
To be defended on Friday, the 15th of January 2021 at 09:00 in Lecture hall A at the Department of Chemistry, Lund University.

Faculty opponent

Assoc. Prof. Monika Österberg
Aalto University, Finland

Title and subtitle

On the physico-chemical properties of softwood hemicellulose and compounds derived from it:

Abstract

   Hemicellulose is the second largest polysaccharide group available in nature after cellulose. Hemicellulose is present in plant cell walls along with cellulose and lignin. It is an abundant and biodegradable material that could potentially replace fossil-based products. The focus of this thesis is the properties and valorization of softwood hemicellulose (galactoglucomannan).

In the first part of the thesis, the nature of the interactions between hemicellulose and cellulose was investigated. The adsorption studies of several types of hemicelluloses to cellulose model surfaces were performed using ellipsometry, QCM-D and neutron reflectometry. The results showed that the binding between hemicellulose and cellulose involves specific interactions facilitated by similarity in the backbone unit conformation. The adsorption showed the molecular weight dependency with the largest adsorbed amount obtained for a hemicellulose with the largest molecular weight at a low concentration regime. The opposite trend was observed at higher concentrations. Neutron reflectometry results demonstrated that lower molecular weight hemicellulose samples with higher flexibility were able to more extensively diffuse into the amorphous parts of the cellulose layer.

In the second part of this work, the properties of various hemicellulose-based colloidal systems were evaluated. Softwood hemicellulose extract provided excellent stabilizing effect to lipid liquid crystalline phase nanoparticles. These nanoparticles showed high colloidal stability over the period of at least 42 days with no major changes in the hydrodynamic diameter and the polydispersity index.

Inclusion of mannans derived from hemicellulose in the structure of thermoresponsive NIPAm-based copolymers shifted the transition temperature to higher values. Mannan side groups were here suggested to create a hydrophilic shell around the hydrophobic particle that provided a stabilizing effect at the elevated temperatures up to 70°C.

Finally, the hemicellulose-based surfactant mixture demonstrated surface active properties with formation of two separate kinds of micelles as evidenced by the two inflection points in the surface tension curve.

Key words

Hemicellulose, galactoglucomannan, cellulose films, alkyl glycosides, thermo-responsive copolymers, glycopolymers, cubic phase nanoparticles, neutron reflectometry, small angle x-ray scattering, adsorption.

Classification system and/or index terms (if any)

I, the undersigned, being the copyright owner of the abstract of the above-mentioned dissertation, hereby grant to all reference sources the permission to publish and disseminate the abstract of the above-mentioned dissertation.

Signature _____   Date _____ 2020-12-04 _____

DOKUMENTDATABLAD enl SIS 61 41 21

On the physico-chemical properties of softwood hemicellulose and compounds derived from it

by Polina Naidjonoka

This doctoral thesis is constructed as a summary of research papers and consists of two parts. An introductory text puts the research work into context and summarizes the main conclusions of the papers. Then, the research publications themselves are reproduced. The research papers may either have been already published or are manuscripts at various stages.

Front cover image by Jelena Dashunina-Naidjonok

Cover illustration back: Topography profile of a cellulose film

Table of Contents

Acknowledgments

And now comes the most difficult part to summarize in a few lines, the whole family of fkem! The biggest thanks goes to Helena Persson, Maria Södergren and Maria Lövgren for helping with all of the things I needed help with. And, of course, my personal hero, Chris Ward, the reason why I feel confident in adjusting all the little screws in the ellipsometer. Thanks for all of the fun times we spent trying to figure out Rudolph :) I will always remember the invention of the donut!

Thanks to the people that made KC my home when I arrived - Maria, Vicky, Luigi, Jasper, Thiago, Maxime, Marta, Axel, João, Johan, Linda, Dora and Junhao.

Maria, you deserve a separate thank you for showing me the ways of science. I am extremely grateful to you for being there for me from welcoming me on my first day to reading my thesis.

Now goes the second generation of the awesome people at KC. I was extremely lucky with the arrival of Alexis, Jen and Marco in my office. Thanks for all of the fun, weird, serious and crazy moments we had. Thanks for bearing me in all of my grumpy moments, and I don't only mean the end of my PhD studies. Thanks to Ben for the eternally warm attitude and for never refusing whenever I needed help, especially at the end of it.

And, of course, thanks to all of the other fkem people for making it a lovely place to return to every day!

My dear family, there are not enough words to express how grateful I am to all of you (Mom, dad and Ksenija). Mom and dad for always believing in me and giving everything you have to make me happy. Ksenija, for being my big role model and mostly for inspiring me to not live in a place as far as China.

My dear aunt Tamara and uncle Pjotr. I would not have been writing this, if it weren't for you. You believed in me when I decided to finish my studies in Sweden and go for a PhD. I will be forever grateful to you for giving me this opportunity and for being curious about the boring science I was involved in.

Sahil, you are the last one I will mention because you have suffered the most. The cooking, the cleaning, the motivational speeches, rationalizing my life choices in the middle of the night. You have done it all and more! Thanks for your patience and the motivating power.

Popular Science Summary

Sugar - a medicine both for our soul and planet

Every kitchen in the world, be it in sunny Philadelphia, fairytale Lapland or fashionable Paris, contains a little jar of sugar hidden at the back of the cupboard. Sugar is the ingredient we cannot imagine our lives without. Pancakes for breakfast? Chocolate bar when you are feeling down? Even if you are not a big fan of sweets, a teaspoon of sugar in a gravy is a game changer. And just how satisfying it is to observe tiny sugar crystals disappearing in a cup of a warm tea. Well, the main reason why it happens is because sugar is a hydrophilic or "water loving" molecule. Our regular sugar, so-called sucrose, is a carbohydrate consisting of two simple sugar units: glucose and fructose. Another very well known carbohydrate made of glucose is cellulose. Cellulose is the main component in paper, cotton kitchen towels or wood that the cupboard is made of. However, if we put a piece of paper in a cup of tea, it does not magically disappear and all we are left with is the ruined tea. So what is it that makes cellulose so different from sugar?

Cellulose is a polysaccharide found in plant cell walls. It contains up to 15,000 connected glucose units as compared to only one glucose in the sucrose molecule. The main function of cellulose in cell walls is to provide mechanical support to the cell, as well as to protect it from deformation. In order to do that, cellulose chains interact strongly with each other to create highly ordered sheets that then form fibrils and bundles of fibrils until a rigid network is built. Breaking apart such a rigid network is extremely difficult, nonetheless, possible with the right tools. In order to produce our little piece of paper, wood is mechanically and chemically processed to separate large fibres, as well as to purify cellulose from other wood components. Cellulose chains, however, are not completely disintegrated to maintain strong and cohesive qualities important in paper products.

As you may have noticed from the title, this thesis is not about cellulose, or not entirely about cellulose. Plant cell walls contain another polysaccharide called hemicellulose and as opposed to cellulose, it is a group of carbohydrates and may contain several types of simple sugar units such as mannose, xylose, glucose, galactose and others. Hemicellulose occurs inside or on the surface of cellulose microfibrils giving the necessary elasticity as well as additional strength to the walls. In some cells, hemicellulose is even stored as an energy source. Hemicelluloses are generally much smaller in size than cellulose which makes it more soluble in water, although some pretreatment is often required.

The amount of hemicellulose present in some types of wood may be as high as 30 %. Moreover, water-soluble portions of hemicellulose end up discarded in the waste streams after wood pulping which makes it an abundant and underutilized material.

Due to its biodegradable nature and diverse structure, hemicellulose presents a potential use in a variety of applications. Significant effort is devoted to creating novel hemicellulose-based components to substitute non-renewable fossil-based ones that negatively impact our planet. To achieve this, every step of the process has to be optimized, starting from the extraction procedure to obtain the highest possible purity and ending with finding the right tools to tailor the structure and properties of hemicellulose. In this thesis, the nature of hemicellulose is studied on a molecular level, specifically in relation to the interactions with cellulose. In addition, several materials produced from hemicellulose are presented that could potentially be used in hygiene products and detergents, packaging, drug delivery and many other applications.

Научно-популярное введение для моих родных

Один из самых распространённых типов углеводов - это целлюлоза. Большое количество целлюлозы находится в древесине и разных видах растений, например, в хлопке. Целлюлоза - это очень длинная молекула (полисахарид), которую составляют, соединенные в цепь, молекулы глюкозы. Свойства такого полисахарида очень сильно отличаются от свойств единой молекулы глюкозы.

Глюкоза также входит в состав обычного и всеми любимого сахара, ведь чай без сахара - это деньги на ветер! Или наоборот, сколько не добавляй сахара в чай, он всё равно растворяется. А вы когда-нибудь задумывались почему сахар растворяется в чае? На самом деле всё очень просто: простые углеводы – гидрофильные или воду любящие молекулы. А, например, масло или воск - это гидрофобные или воду нелюбящие молекулы, поэтому они в воде не растворяются. Почему же тогда кусочек бумаги, главный компонент которого - целлюлоза, в чае не растворяется? Ведь целлюлоза состоит из того же сахара! Как я уже упомянула до этого, целлюлоза – очень длинная молекула и чаще всего состоит из нескольких цепей, которые взаимодействуют друг с другом.

Целлюлоза находится в клеточных стенках растений и её главная задача - предание прочности и твёрдсти клеткам. Цепи целлюлозы крепко взаимодействуют друг с другом и создают волокна, которые, в свою очередь, образуют прочную сетку, способную поддержать рост растений. При производстве бумаги дерево подвергается механической или химической обработке, во время которой структура большей части волокон разрушается. Последующее разъединение волокон на цепи целлюлозы - это не простой процесс. Взаимодействие между цепями целлюлозы настолько крепкое, что волокна целлюлозы имеют своего рода гидрофобный характер и не растворяются при контакте с водой.

Но моя диссертация не про целлюлозу, а про гемицеллюлозу! Гемицеллюлоза - это похожий на целлюлозу полисахарид, но в отличие от целлюлозы, гемицеллюлоза состоит из разных видов простых углеводов, например, маннозы, глюкозы, ксилозы и галактозы. Вместе с целлюлозой, гемицеллюлоза находится в клеточных стенках растений. Гемицеллюлоза намного меньше целлюлозы и в большинстве случаев растворима в воде. При переработке дерева, большая часть гемицеллюлоз выбрасывается вместе с отходными водами.

Гемицеллюлозы - возобновляемый источник, который может заменить ископаемое сырьё в производстве, например, гигиенических продуктов или пластиковой упаковки, а также фармацевтических составов. В этой диссертации было создано и характеризировано несколько видов коллоидальных соединений на основе гемицеллюлозы.

Коллоиды - это частички размером от 1 до 1000 нанометров. Слово это иностранное и не очень понятное, но на самом деле встречается в ежедневной жизни намного чаще, чем кажется. Одна из самых известных коллоидных систем - это молоко, в котором гидрофобные частички жира образуют эмульсию в воде. Они также являются главной причиной белого цвета молока. Коллоиды в молоке препятствуют прохождению лучей света и в результате свет преломляется в разных направлениях. Немного более интересный пример коллоидной системы - это мицеллярная вода. Да, да, та самая жидкость, которую можно найти в ванной комнате каждой современной девушки. Мицеллы состоят из амфифильных молекул, в структуру которых, входят как гидрофобные, так и гидрофильные части. При достаточной концентрации в воде, амфифильные молекулы организуют себя так, чтобы гидрофильная часть защищала гидрофобные части от контакта с молекулами воды. Чаще всего, мицеллы - это круглые частички, которые состоят из гидрофобного ядра и гидрофильной оболочки. Так как в большинстве случаев наша косметика состоит из гидрофобных молекул, мицеллы растворяют частички косметики и стабилизируют их внутри ядра.

Косметические и моющие средства - это только маленькая часть индустрии, где используются коллоиды. К сожалению, большинство этих средств в наше время произведено на основе ископаемых ресурсов, что приводит к стремительному изменению климата. Гемицеллюлоза - это возобновляемый и биоразлагаемый материал, использование которого, может не только замедлить изменение климата, но и улучшить свойства продукции.

List of Publications

This thesis is based on the following publications, referred to by their Roman numerals:

I **On the interaction of softwood hemicellulose with cellulose surfaces in relation to molecular structure and physicochemical properties of hemicellulose**

P. Naidjonoka, M. Arcos Hernandez, G. K. Pálsson, F. Heinrich, H. Stålbrand, T. Nylander
Soft Matter **2020**, 16, 7063-7076

II **Adsorption of hemicellulose to cellulose films and cellulose crystallinity**

P. Naidjonoka, C. Dicko, C. J. Garvey, J. Gilbert, C. J. Kinane, A. Caruana, A. Vorobiev, R. Russell, S. Holt, H. Stålbrand, T. Nylander
Manuscript

III **Bicontinuous cubic liquid crystalline phase nanoparticles stabilized by softwood hemicellulose**

P. Naidjonoka, M. Fornasier, D. Pålsson, G. Rudolph, B. Al-Rudainy, S. Murgia, T. Nylander
Submitted Colloids and Surfaces B **2020**

IV **Thermoresponsive glycopolymers based on N-isopropyl acrylamide and enzymatically synthesized β-mannosyl acrylates**

M. Arcos-Hernandez, **P. Naidjonoka**, S. J. Butler, T. Nylander, H. Stålbrand, P. Jannasch
Under revision Biomacromolecules **2020**

V **β-Mannanase-catalyzed synthesis of alkyl mannooligosides**

J. Morrill, A. Månberger, A. Rosengren, **P. Naidjonoka**, P. von Freiesleben, K. B. R. M. Krogh, K. E. Bergquist, T. Nylander, E. N. Karlsson, P. Aldercreutz, H. Stålbrand
Applied Microbiology and Biotechnology **2018**, 102, 5149-5163

All papers are reproduced with permission from their respective copyright holders.

Publications not included in this thesis:

Facile control of surfactant lamellar phase transition and adsorption behavior
R. A. Gonçalves, **P. Naidjonoka**, T. Nylander, B. Lindman, M. L. Yeng
RSC Advances **2020**, 10, 18025-18034

Author Contributions

I **On the interaction of softwood hemicellulose with cellulose surfaces in relation to molecular structure and physicochemical properties of hemicellulose**

PN performed all the experimental work except for NMR analysis. PN analyzed and interpreted the data with the help from co-authors. PN wrote the manuscript with input from co-authors.

II **Adsorption of hemicellulose to cellulose films and cellulose crystallinity**

PN performed all the experimental work with the help from CD. Data analysis and interpretation was performed by PN and co-authors. PN wrote the manuscript with input from co-authors.

III **Bicontinuous cubic liquid crystalline phase nanoparticles stabilized by softwood hemicellulose**

PN, MF and TN designed the study. DP and PN performed the experimental work. Data analysis and interpretation was performed by PN and co-authors. PN and MF wrote the manuscript with input from co-authors.

IV **Thermoresponsive glycopolymers based on N-isopropyl acrylamide and enzymatically synthesized β-mannosyl acrylates**

PN performed SAXS and DLS. Data analysis and interpretation was performed by PN and co-authors. PN wrote a part in the manuscript related to the physicochemical characterization with input from co-authors.

V **β-Mannanase-catalyzed synthesis of alkyl mannooligosides**

PN performed surface tension measurements. Data analysis and interpretation was performed by PN and co-authors. PN wrote a part in the manuscript related to the surface tension measurements with input from co-authors.

1 Introduction

Due to rapidly emerging consequences of climate change, transition from fossil-based resources is one of the burning issues the modern scientific community is dealing with. A great deal of creative solutions has already been proposed for novel, environmentally-friendly fuels, packaging materials, hygiene products etc. Biopolymers have shown a significant potential, thanks to their versatile and, most importantly, biodegradable nature. For a long time, the attention was focused mainly on cellulose as it is the most abundant biopolymer in nature. However, it is a very complex polysaccharide that brings additional challenges to the table such as limited solubility in common solvents. Moreover, production of cellulose-based materials requires additional deforestation which contributes negatively to the climate change.

Hemicellulose, on the other hand, is in many cases readily soluble in water and is often discarded with process waters from wood pulping. In the last five years alone, 36,100 articles have been published associated with hemicellulose where 16,700 of these articles involved softwood hemicellulose. Not all of these studies are related to the development of potential applications. Significant amount of research has been done on, for instance, optimization of wood pulp membrane filtration to prevent fouling caused by adsorption of hemicelluloses or fundamental questions about the nature of interactions inside plant cell walls. This still indicates growing interest in hemicellulose.

In this thesis, we explore the potential of softwood hemicellulose as a raw material in creation of several types of materials that could either substitute the existing widely used components or provide solution for future obstacles. A special attention is devoted to hemicellulose properties in relation to cellulose as this has been and still remains an open discussion. However, I hope that this thesis holds answers to at least some of the questions.

1.1 Plant cell wall polysaccharides

Plant cell walls provide mechanical strength and resistance to deformation while allowing solute and signal exchange between cells. Growing cells are surrounded by primary walls that have an expandable nature with tensile strength of up to 100 MPa.[1] Ensuing the initial growth period, some cells develop secondary walls which, in addition to mechanical support, serve as polysaccharide storage units.[1,2]

The main components found in plant cell walls are cellulose, hemicellulose and lignin (Figure 1.1). Minor amounts of proteins and pectic substances are also present. Cellulose is a linear polymer that consists of $(1\rightarrow4)$-β-D-glucopyranose units known as glucan chains which aggregate together into crystalline cellulose microfibrils of $\sim$ 3 nm in width.[1] Hemicellulose, on the other hand, is a group of polysaccharides that includes both linear and branched polysaccharides. Hemicelluloses prevent cellulose from aggregating into larger fibrils by adsorbing to the cellulose surface. The chemical composition of hemicellulose varies depending on the plant and cell wall (primary or secondary) type. Hemicelluloses can be divided into xyloglycans or xylans, xyloglucans, β-glucans with mixed linkages and mannans based on the major sugar monomers present in the structure.[3]
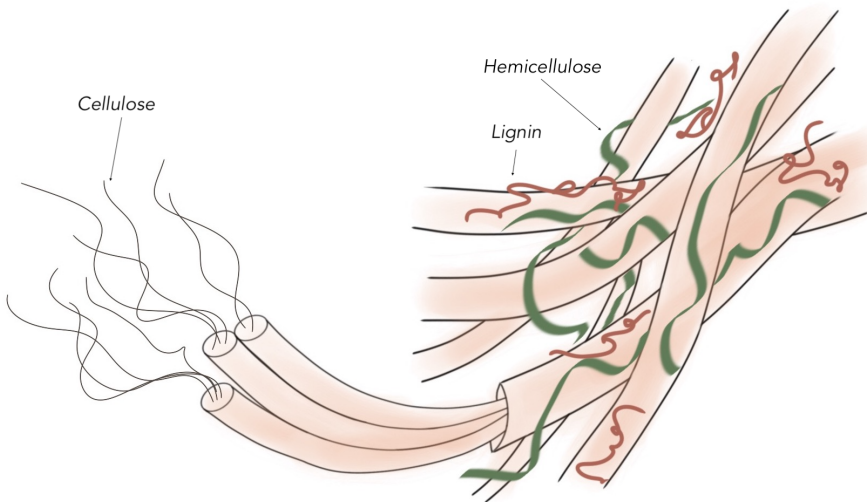
Figure 1.1 Schematic representation of the fibril network inside plant cell walls and the main components involved in it.

Xylans are the main non-cellulosic polysaccharides found in the secondary cell walls of dicotyl plants. In addition, the amount of xylans can reach up to 50 % in grasses

and cereals. Xyloglucans, on the other hand, are found in all higher order plant primary cell walls and as storage polysaccharides in secondary walls of some species. Cellulose-like β-glucans with mixed linkages are only produced in cereal grains with oats and barley being commercially important sources of these hemicelluloses.

The last group of hemicelluloses is mannanoglycans or mannans. Mannans can be further divided into galactomannans and galactoglucomannans (Figure 1.2). Galactomannans with a low number of galactose units (~ 4 %) are present in the seed endosperm of ivory nut (*Phytelephas macrocarpa*) and date (*Phoenix dactylifera*). In addition, green arabica coffee beans also contain a high amount of such mannans. Galactomannans with a higher degree of galactose substitution (30 − 96%) are principal hemicelluloses originating in the endosperm of a variety of leguminous seeds including guar (*Cyanopsis tetragonoloba*) and locust bean or carob (*Caesalpinia spinosa*). Their bulk and interfacial behavior are further described in Chapter 3. Galactoglucomannans, however, are the major hemicellulosic components found in the secondary cell walls of softwoods.[2,3] Since galactoglucomannans are the main focus of this thesis, they are described in detail in the following section.
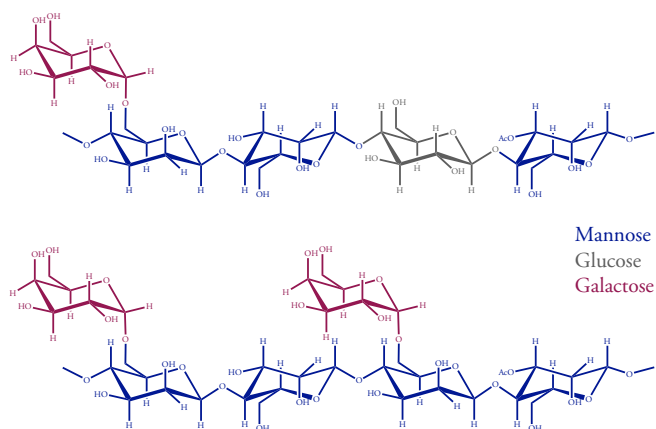
Figure 1.2   General structure of galactoglucomannan (top) and galactomannan (bottom).

Lignin is a group of polyphenolic polymers that are strongly associated, and sometimes even covalently bound with polysaccharides in cell walls. The main constituents in lignin are para-coumaryl alcohol, coniferyl alcohol and sinapyl alcohol(see Figure 1.3). For softwoods, coniferyl alcohol is the most common monomer.[4]

p-Coumaryl alcohol   Coniferyl alcohol   Sinapyl alcohol
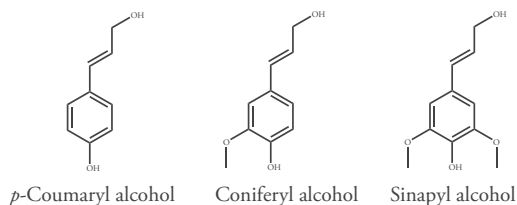
Figure 1.3 The molecular structure of the main constituents in lignin.

1.2   Softwood hemicellulose

The major hemicellulose group found in softwood, such as spruce and pine, is *O*-acetyl-galactoglucomannan (GGM). Dry wood mass contains up to 25 w/w% of GGM. The backbone of GGM consists of β-(1→4)-D-mannopyranose, partially substituted with β-(1→4)-D-glucopyranose, branches on mannose units of α-D-galactopyranose attached through the 1→6 linkages, as well as *O*-acetyl groups attached to the C-2 and C-3 positions.[5,6] The degree of polymerization of GGM is much smaller than that of cellulose with a molecular weight of around 16,000-24,000 Da.[7] Galactose and acetyl side groups contribute to a better solubility of hemicellulose in water. The composition of galactose:glucose:mannose in GGM can vary significantly based on the degree of substitution from 0.1:1:3 up to 1:1:3.[6]

1.3   Hemicellulose applications

The aim of this section is to highlight few studies that involve hemicellulose relevant to the scope of this thesis. I will also introduce several important phenomena and terminology that will be discussed frequently in Chapters 3 and 4.

1.3.1   Hemicellulose-cellulose composites

As previously discussed, hemicellulose interacts with cellulose in plant cell walls. The nature of these interactions is of a great interest in relation to papermaking and pulping since the presence of hemicelluloses dissolved in the process waters causes a variety of adverse effects. These include the growth of fungi and bacteria as well as interactions with papermaking chemicals.[8]
However, hemicellulose has also been shown to improve paper strength.[9] Therefore, multiple studies have been done on the adsorption of hemicelluloses to different types of cellulose surfaces.[10-13] Several attempts have been made to replicate the

4

synergy between hemicellulose and cellulose in plant cell walls by reinforcing cellulose hydrogels with hemicellulose.[14-18] Hemicellulose has been shown to improve elastic and tensile strength, as well as toughness of the artificial cellulose hydrogels confirming the role it has in the cell wall architecture. In addition, the importance of hemicelluloses on the diffusion of several plant-based macromolecules has been highlighted in cellulosic hydrogels.[19] Apart from mechanical strength, hemicellulose-cellulose composite films have been reported to have excellent oxygen barrier performance offering an attractive alternative to conventional packaging materials.[20]

Hemicellulose-based hydrogels have also shown a great potential in several areas such as tissue engineering, drug delivery, etc.[21-24] For instance, xylan-based hydrogels with thermo- and pH- responsive behavior have demonstrated excellent encapsulation and release properties of acetylsalicylic acid in the intestinal and gastric fluids.[25] Hemicellulose hydrogel microspheres, on the other hand, have been tested as nanovehicles for the transport of caffeine and bovine serum albumine.[26]

1.3.2 Alkyl glycosides

Surface active agents (or surfactants) are amphiphilic molecules meaning that the chemical structure contains both hydrophilic and hydrophobic parts. Such molecules are able to lower surface free energy of a system. At a certain concentration, a so-called critical micelle concentration (CMC), surfactants self-assemble into a variety of structures in order to minimise unwanted hydrophilic/hydrophobic interactions between the surfactant and solvent. The type of structures surfactants self-assemble into depends on the molecular shape of the surfactant itself (see Figure 1.4). This can be described by a critical packing parameter (P) defined as[27]

$$P = \frac{V_{\text{tail}}}{a_{\text{head}} \cdot l_{\text{tail}}} \tag{1.1}$$

where V_{tail}, a_{head}, and l_{tail} are the tail volume, the cross-section area of the head group and the length of the tail, respectively.

Micelles are the simplest structures that surfactants form above the CMC. In water, surfactants self-assemble with their hydrophilic head group outwards and the hydrophobic tail inwards, creating a hydrophilic shell that protects oil-like interior. Examples of compounds with surface active properties are lipids, polymers, block copolymer to list a few. All of these molecules can be used to form a vast array of intriguing structures.
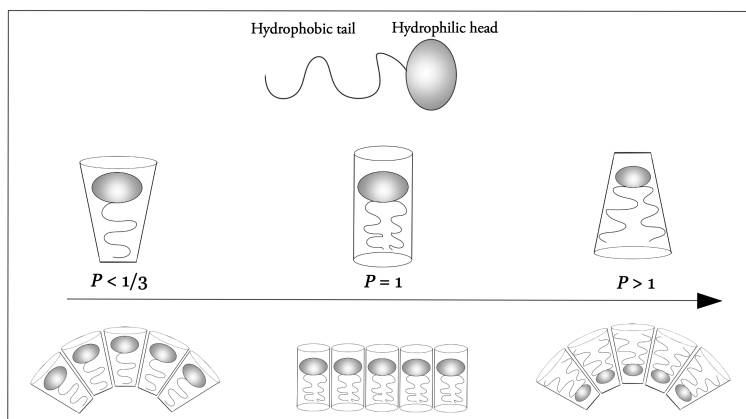
Figure 1.4 Schematic representation of surfactant molecules and self-assembly structures depending on their critical packing parameter (*P*).

Alkyl glycosides are surfactants that have a head group made of at least one sugar unit and an alkyl tail.[28] Due to their biodegradable and nontoxic nature, alkyl glycosides have gained wide popularity and have been commercially used in a variety of formulated products.[28] These surfactants are mainly produced from starch or glucose syrup as a raw material.[29] However, several studies have investigated the synthesis of alkyl glycosides from cereal and wood based hemicelluloses.[29-32] Utilisation of hemicelluloses as a raw material does not require additional deforestation and in some cases even allows production of surfactants containing specific glycosidic bonds that are otherwise highly challenging to synthesise.[32]

1.3.3   Stabilization of lipid-water interface

As stated in the previous subsection, polar lipids are natural surface active molecules. When mixed with water, lipids self-assemble into a range of structures depending on the concentration, pH, temperature and packing parameter. At high enough concentrations, lipids self-assemble into phases with long-range orientations characteristic of solid crystals yet with liquid-like molecular mobility and are, therefore, referred to as lipid liquid crystalline (LLC) phases. Among the most common LLC phases are lamellar, hexagonal, inverse micelles (L_2) and cubic bicontinuous phases (Figure 1.5). Lamellar phase contains planar bilayer sheets separated by water layers whereas hexagonal phase consists of densely packed cylindrical micelles arranged in a hexagonal pattern which can be direct (H_1) or inverse hexagonal (H_2). Cubic bicontinuous phase has a 3-dimensional lattice formed by a curved non-intersecting bilayer folded in a way that creates two continuous yet disconnected water channels.

There are three types of cubic bicontinuous phases - primitive (Im3m), the gyroid (Ia3d) and the double-diamond (Pn3m).
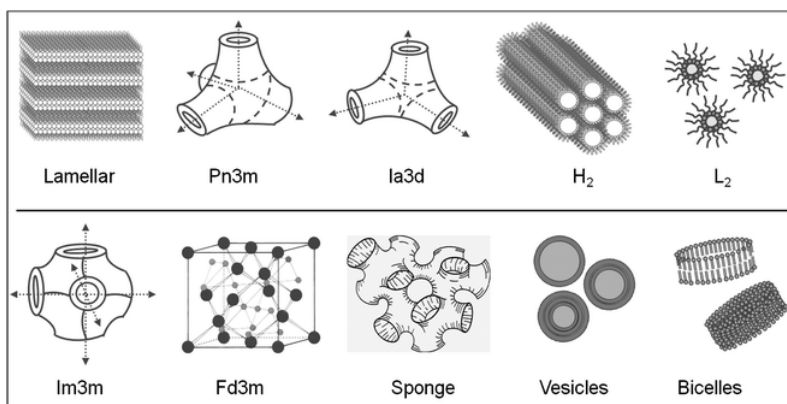
Figure 1.5 Architecture of different lipid liquid crystalline phases. Reproduced from Ref. [33] with permission from the PCCP Owner Societies.

Nanoparticles (NPs) produced from lipid bulk phases have gained a special interest as they can be used for drug encapsulation and delivery purposes. In order to obtain such lipid crystalline nanoparticles (LCNPs), energy input is required. The most common technique, the so-called top-down approach, involves breaking apart the lipid bulk phase in excess water into smaller aggregates that will then create the nanoparticles. The bottom-up approach, on the other hand, is based on diluting a surfactant in an aqueous solution with a stabilizer, after which the mixture is homogenized. The dispersions of lamellar, hexagonal and bicontinuous cubic phases are called vesicles, hexosomes and cubosomes, respectively.

LCNPs often require a stabilizer to achieve a long term colloidal stability. Both electrostatic and steric stabilization can be used to prevent such nanoparticles from aggregating. One of the most commonly used groups of stabilizers for cubosomes and hexosomes is poloxamers (Pluronics) that have hydrophilic (poly(ethylene oxide) and hydrophobic (poly(propylene oxide)) blocks. Poloxamers, however, are known to affect the internal structure of NPs. [34]

The ability of hemicelluloses to stabilize the interface between lipids and water has been highlighted in relation to oil-in-water emulsions. [35,35-38] The improved stability and a more monodispersed particle size of emulsions has been linked to the presence of lignin in the hemicellulose extracts. [35,36,39] The main mechanism behind the stabilization effect is believed to be based on lignin interacting with the

hydrophobic parts of lipid and thereby anchoring associated hemicellulose to the interface. The hemicellulose chains can then impart steric stabilization. Furthermore, lignin hampers lipid oxidation, thus improving stability of the emulsions even more.[39]

Until now, the stabilization of cubic phase nanoparticles has only been achieved with other kinds of polysaccharides such as starch and cellulose.[40-42] However, the structure of these polysaccharides was modified by adding hydrophobic groups.

1.3.4   Glycopolymers

Glycopolymers present an excellent vehicle for targeted drug delivery since carbohydrate moieties can facilitate cell recognition and binding.[43] Due to extensive research on synthetic polymers, it is also possible to synthesise glycopolymers with specific properties such as thermoresponsive behavior. Furthermore, with careful choice of polymer one can easily tune the transition temperature to, for instance, body temperature.[44,45]

Tamarind seed xyloglucans have been used to synthesise tailored bottlebrush-like glycopolymers to enhance binding to nanocrystalline cellulose.[46] In another study, seed hemicellulose from locust bean gum has been used as a raw material for the preparation of conjugates with hydroxyethyl methacrylate (HEMA).[47]

2 | Experimental techniques

In this chapter, the main techniques used in the work behind this thesis will be presented with a general description. Characterization on the surface was performed using several techniques such as Ellipsometry, Quartz Crystal Microbalance with Dissipation, Neutron Reflectometry, Atomic Force Microscopy and Attenuated Total Reflection - Fourier-Transform Infrared spectroscopy. Samples in solution were investigated with the help of different scattering techniques - Dynamic and Static Light Scattering and Small Angle X-Ray Scattering. In order to confirm the morphology in solution, some samples were imaged with Cryogenic Transmission Electron Microscopy. In addition, surfactant properties of hexyl-mannosides were investigated with Tensiometry.

2.1 Surface techniques

2.1.1 Ellipsometry
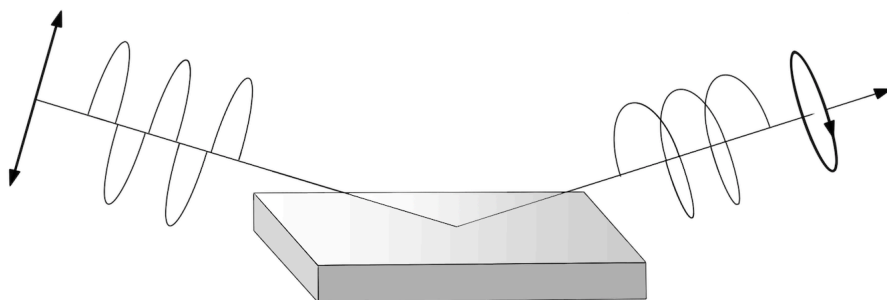
Figure 2.1 A schematic representation of principles behind ellipsometry

Ellipsometry is an optical technique based on a change in a polarization state of a light wave upon reflection from an interface. In a typical setup, a light beam with a known polarization state is incident on an interface between two media. The change in the surface properties, for example, formation of a thin film, will lead to a change in the polarization state of the reflected light.[48,49] The polarization of the reflected light is described by ellipsometric angles, Ψ and Δ, which represent the relative attenuation and relative phase shifts of two orthogonal components of the light wave, parallel, p, and perpendicular, s, to the incidence plane. The ellipsometric angles are related to the reflection coefficients r_p and r_s as shown in the Equation 2.1 where ρ is the complex amplitude reflection ratio[50]

$$\rho = \frac{r_p}{r_s} = \tan(\Psi)\exp(j\Delta).\tag{2.1}$$

The complex amplitude reflection ratio is measured directly by the ellipsometer and the complex refractive index is determined based on the reflection coefficients as follows from Equation 2.2 and Equation 2.3

$$r_s = \frac{E_{rs}}{E_{is}} = \frac{N_1\cos\theta_1 - N_2\cos\theta_2}{N_1\cos\theta_1 + N_2\cos\theta_2}\tag{2.2}$$

$$r_p = \frac{E_{rp}}{E_{ip}} = \frac{N_2\cos\theta_1 - N_1\cos\theta_2}{N_2\cos\theta_1 + N_1\cos\theta_2}\tag{2.3}$$

where E_i and E_r stand for the electric field amplitude of the incident and the reflected light, respectively. N_1 and N_2 are the complex refractive indices of two isotropic media and θ is the incident angle.

A general null ellipsometry set-up consists of

- a light source that emits unpolarized light,

- a linear polarizer that converts unpolarized light to a linearly polarized light,

- a compensator that changes the polarization state of the light wave to produce elliptically polarized light by retarding its orthogonal components by different amounts,

- a surface that reflects the incoming light and thereby changes the state of polarization of the light,

- an analyzer or another linear polarizer,

- a detector that measures the reflected light intensity after the analyzer.[51]

The first type of ellipsometer developed was a null ellipsometer. This is also the ellipsometer used in this work in Paper 1. The main principle behind null ellipsometry is that at a certain analyzer and polarizer positions the intensity of the light is minimized or nulled at the detector due to a perpendicular orientation of two polarizers.[50]

The ellipsometry measurements were carried out on three types of surfaces: hydrophilic silica, hydrophobized silica and spin-coated cellulose surface. Each silica wafer was characterized in air and liquid in order to determine the thickness of a silicon oxide layer.

The obtained data was fitted to the model containing the following layers: SiO_2-cellulose/hemicellulose. The software (Ellipso) was used to calculate the refractive index (n) and the optical thickness of the layer (d), based on the measured Δ and Ψ angles. The adsorbed amount (Γ) was calculated by applying Equation 2.4

$$\Gamma = \frac{d(n - n_0)}{dn/dc} \tag{2.4}$$

where n_0 is the refractive index of the solvent and dn/dc is the refractive index increment. Table 2.1 shows dn/dc values used to calculate adsorbed amount in Chapter 3.

Table 2.1 dn/dc values of the polysaccharides studied in Chapter 3.

Polysaccharide	dn/dc [mL g^{-1}]	Ref
LBG, LBG*, GG	0.135	[52]
GGMs	0.148	[53]
Cellulose	0.131	[54]

2.1.2   Neutron Reflectometry (NR)

Similar to ellipsometry, the reflection from the surface is measured in NR experiments. However, the focus here is on the total intensity of the reflected neutron beam instead of the change in the polarization of light. In specular NR, where the angle of incidence is equal to the angle of reflection, the intensity of the reflected neutron beam is monitored as a function of neutron momentum transfer perpendicular to the reflecting surface, Q_z. The momentum transfer can be calculated from the wavelength (λ) and the angle (θ) of incident neutron beam, given by the Equation 2.5[55]

$$Q_z = \frac{4\pi}{\lambda} \sin \theta \tag{2.5}$$

A neutron beam is directed towards a surface at a grazing incident angle where due to its high penetrating power, it propagates through the solid medium (for example,

silicon crystal) and is reflected at the interface.[56] The obtained specular reflectivity profile gives information on the thickness of the layer, density profile and interface roughness.[55]

The key advantage of using neutron source as a probe is the ability of neutrons to distinguish between different isotopes, for example, ^1H and ^2H, due to distinctly different scattering length densities (SLD). By choosing a solvent with a specific D_2O and H_2O ratio and/or selectively deuterated molecules, it is possible to "hide" some parts of the layer and "highlight" others.

In this work, three isotopic solvent contrasts were used: D_2O, H_2O and contrast matched silicon water (CMSi). NR measurements were performed on a hydrophobized silica (Paper I) and spin-coated d-cellulose surfaces (Paper II). Bare silica surface was characterized in three contrasts at the beginning of each experiment. When the measurement involved cellulose surface, the characterized silica surface was then spin-coated with d-cellulose solution and characterized in three solvents again. The sample was then injected in the cell and left to adsorb to either hydrophobized or cellulose surface for a certain amount of time. After that, the surface was rinsed and characterized in at least two contrasts.

The obtained neutron reflectivity curves were analyzed by fitting with Abeles matrix method for a stratified interface.[57-59]

NR measurements were performed on MAGIK, Platypus and POLREF reflectometers available at Center for Neutron Research (NIST, USA), Australian Nuclear Science and Technology Organisation (ANSTO, Australia) and Rutherford Appleton laboratory (UK), respectively.

2.1.3 Quartz Crystal Microbalance with Dissipation (QCM-D)
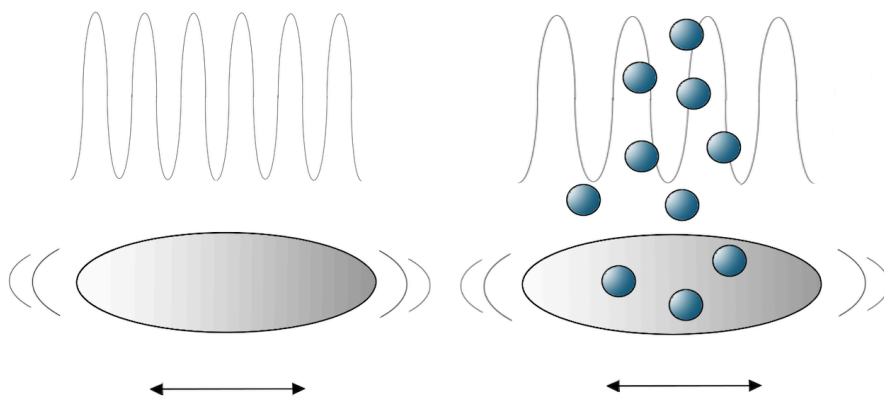
Figure 2.2 A schematic representation of principles behind QCM-D

A QCM-D measurement involves a piezoelectric oscillator which is excited to a near resonance frequency with an alternating voltage driving source. Changes in the mass cause a decrease in the resonant frequency (Δf) of the piezoelectric crystal.[60] If the added mass is relatively small, rigid and evenly distributed on the crystal, the adsorbed amount (Δm) is proportional to the changes in frequency, given by the Sauerbrey relation[61] presented below

$$\Delta m = \frac{C}{n} \Delta f \tag{2.6}$$

where C is a proportionality constant and n is an overtone number.

In addition to the change in frequency, modern QCM instruments are equipped to measure the energy loss when the voltage is switched off. The dissipation energy (ΔD) is strongly affected by the viscoelastic properties of the added layer, therefore is an indication of the layer rigidity. The Sauerbrey equation is only valid if the ΔD is below 10^{-6}. Several approaches have been developed to model viscoelastic films with high ΔD values. The most commonly used model is the Voigt viscoelastic model where the film is described by a complex shear modulus

$$G = G' + iG'' = \mu_f + i2\pi f \eta_f = \mu_f(1 + i2\pi f \tau) \tag{2.7}$$

where μ_f, η_f and τ is the elastic shear modulus, the shear viscosity and the characteristic relaxation time of the film, respectively. The change in the resonant frequency (Δf) and the dissipation (ΔD) can be then derived from the viscoelastic properties of the

film as shown in Equation 2.8 and Equation 2.9

$$\Delta f = \frac{Im(\beta)}{2\pi t_q \rho_q}$$

(2.8)

and

$$\Delta D = -\frac{Re(\beta)}{\pi f t_q \rho_q}$$

(2.9)

where t_q is the thickness and ρ_q is the density of the quartz surface. β depends on the thickness and density of the film and is described in detail elsewhere.[60]

QCM-D experiments were performed using quartz crystals coated with a SiO_2 layer (QSX 303, Q-Sense) with a proportionality constant of -17.7 ng $\cdot$ s $\cdot$ cm^{-2} and 5 MHz resonant frequency. The obtained change in frequency and dissipation were analyzed by fitting the Voigt viscoelastic model[62] to the experimental data using Dfind software (QSence, Biolin Scientific).

2.1.4 Atomic Force Microscopy (AFM)

Atomic Force Microscopy was first introduced in 1986 and has since been widely used as an imaging tool for a range of applications.[63-65] In contrast to other microscopy techniques, AFM is an indirect imaging technique where the image is created based on the probe-sample interactions. The AFM probe consists of a sharp tip attached to a flexible microcantilever that is kept at a distance relative to the sample surface. The AFM probe can be operated in contact or non-contact mode. In contact mode, the bending of the cantilever caused by the forces between the tip and the sample is traced by a laser beam reflected off of the cantilever.[65,66] In non-contact mode, the tip is positioned at a larger distance from the sample where the attractive forces between the tip and the sample are dominant. The tip is moved across the sample while oscillating at a resonant frequency. The attractive interactions with the surface lead to a change in the resonant frequency and hence in the vibrational amplitude. These changes are then converted to the z dimension to produce a topographical profile of the surface.[66] Imaging in air was performed using silicon cantilever with 42 N/m spring constant and 330 kHz resonance frequency, whereas in liquid mode, silicon tip with 3 N/m spring constant and 75 kHz resonance frequency was utilized.

2.1.5   Attenuated total reflectance Fourier transform infrared spectroscopy (ATR-FTIR)

Infrared (IR) spectroscopy is an analytical technique that gives information on molecular structure and interactions in the sample. As opposed to traditional IR, in the FTIR spectrometers the infrared radiation is split into two parts which are reflected from a stationary and a moving mirror. The reflected light is recombined at the beam splitter producing constructive and destructive interferences. Fourier transformation is then used to convert the interference pattern or interferogram to the frequency domain. [67,68]

In ATR-FTIR spectroscopy, a sample is placed in contact with a crystal that has a higher refractive index than the sample such as diamond and zinc selenide. When the IR radiation beam reaches the interface between the sample and the crystal, it is totally reflected due to the difference in refractive indices. This causes a fraction of the beam to extend into the sample as an evanescent wave that has the same frequency as the incoming beam. The sample absorbs part of IR radiation in the evanescent wave and the intensity of the totally reflected beam is thus reduced or attenuated. [68]

ATR-FTIR spectroscopy was used to investigate crystalline properties of the bacterial cellulose films. This was done by elucidating the amount of inaccessible hydroxyl groups in the polymer network of cellulose. Deuterated and non-deuterated cellulose solution was spin-coated on the FTIR diamond crystal in a similar manner as for ellipsometry and NR. Dry cellulose films were first measured under ambient conditions and then subjected to a D_2O vapor environment. Once the exchange has reached steady state, the number of the exchanged -OH groups (r_{OH}) was determined using Equation 2.10 [69-71]

$$r_{OH} = \frac{1.34 \cdot A_{OD}}{1.34 \cdot A_{OD} + A_{OH}} \tag{2.10}$$

where A_{OD} and A_{OH} are the integrated area of the peaks between 2260 - 2700 cm^{-1} and 3050 - 3680 cm^{-1}, respectively.

2.2   Scattering techniques

So far, I have described techniques that either require a surface or sample is characterized in relation to a surface. However, surface affects the structure and morphology of the sample due to different kinds of interactions. This subsection focuses on the

techniques that can be used to characterize the structure and other properties of an object in a solution or a dispersion.

2.2.1 Static Scattering

Scattering techniques follow interactions between an object in solution and a radiation source. When a radiation beam interacts with a particle in its path, the trajectory of the beam will be deflected or in other words the radiation energy is scattered. The intensity of the scattered energy can be used to determine the structure of the particle provided that the scattering is elastic (there is no energy loss in the process) and the intensity comes solely from the primary scattering.[72,73]

The most commonly used radiation sources are light, x-rays and neutrons. Each of the sources interact with different parts of the sample. Visible light and x-ray beam interact with electrons of atoms and the difference in electron density between a sample and a solvent determines the contrast. Neutrons, on the other hand, interact with the nuclei of atoms and are therefore sensitive to different isotopes as mentioned earlier in the Neutron Reflectometry subsection.

The scattered radiation recorded at different scattering angles θ can be described by a scattering vector ($\overrightarrow{q}$). The magnitude of the scattering vector is given by

$$q = |\overrightarrow{q}| = \frac{4\pi}{\lambda_0} \sin(\frac{\theta}{2}) \tag{2.11}$$

where λ_0 is the wavelength of the incoming radiation beam. The intensity of scattering results from number density (N_p), volume of a particle (V_p), contrast or difference in SLD between the sample and the solvent ($\Delta\rho$), form factor ($P(q)$) and structure factor ($S(q)$). Intensity ($I(q)$) is then determined by

$$I(q) = N_p V_p^2 \Delta\rho^2 P(q) S(q) + background. \tag{2.12}$$

Form factor and structure factor give information on intra- and inter-particle interactions, respectively. Scattering measurements are usually performed in a dilute regime in order to avoid inter-particle interactions. Since the scattering intensity in such regime is mainly affected by $P(q)$, the size and shape of a particle can be determined more easily.

The analysis of static scattering data can be done in several ways. Some parameters can be calculated directly form a scattering curve based on scattering theory. One of such parameters is radius of gyration (R_g). R_g is an indication of the size of

a particle and in combination with hydrodynamic radius (R_h) gives information on the shape.

R_g is calculated based on Guinier approximation which is only valid at low q-values where $qR_g < 1$. The scattering intensity in this q region is approximated to be the result of the zero angle scattering (I_0) and R_g as shown in Equation 2.13[72]

$$I(q) = I_0 e^{\frac{-(qR_G)^2}{3}}.$$ (2.13)

Multiple approaches have been developed for the calculation of R_g. Most of them involve plotting one or the other variant of scattering intensity as a function of q^2. Radius of gyration of hemicellulose described in (Paper II) was calculated using Zimm plot approach in which a plot of $I(q)^{-1}$ versus q^2 is constructed.

Scattering profiles of objects with a highly ordered arrangement in their structure like lipid liquid crystalline (LLC) phases contain well-defined peaks, also known as Bragg peaks. These peaks result from constructive interferences and appear if the Bragg condition is fulfilled[74]

$$n\lambda = 2d\sin\left(\frac{\theta}{2}\right)$$ (2.14)

where n is an integer, λ is the wavelength of radiation, d is the distance between crystalline planes and θ is the scattering angle. The ratio between q positions of the Bragg peaks indicates the type of LLC phase. Further depending on the LLC type, a lattice parameter (a) and water channel radius (r_w) can be determined. For a bicontinuous cubic phase these parameters are calculated from[75]

$$a = d\sqrt{h^2 + k^2 + l^2}$$ (2.15)

and

$$r_w = (a - l)\sqrt{\frac{A_0}{-2\pi\chi}}$$ (2.16)

where h, k and l are the Miller indices describing crystalline planes, χ and A_0 are the Euler characteristic and the surface area of the infinite periodic minimal surface (IPMS) geometry.

Another way of evaluating static scattering data is by applying a certain theoretical model. This method, however, requires certain knowledge about the system prior to analysis to find the correct model. Therefore, complementary measurements like dynamic light scattering or microscopy are often required to give an indication

of structure or to confirm the obtained result. Models used for the analysis of Small Angle X-ray scattering data of softwood hemicellulose, hemicellulose stabilised nanoparticles and pNIPAm/mannan co-polymers are described in detail in Chapter 4.

2.2.2 Dynamic Scattering

Dynamic light scattering follows a particle undergoing Brownian motion in a solution. The moving particle will cause scattering intensity fluctuations that in turn can be related to the mobility or diffusion described by the diffusion constant, D, of the particle. The Stokes-Einstein relation can be used to extract a hydrodynamic radius, R_h, from the diffusion coefficient

$$D = \frac{k_B T}{6\pi\eta R_h} \tag{2.17}$$

where k_B is Boltzmann's constant, T is the absolute temperature, η is the viscosity of the solvent.

The diffusion coefficient is determined from an intensity auto-correlated function. The intensity fluctuation is measured over a certain time with a very small time step. The intensity at each time step is then correlated to the initial intensity and plotted as a function of time step or lag time (τ). Normalized intensity auto-correlation function is given by Siegert relation[76]

$$g^{(2)}(q,\tau) = 1 + \beta\left(g^{(1)}(q,\tau)\right)^2 \tag{2.18}$$

where β is an instrumental constant, $g^{(1)}(q,\tau)$ is the normalised time auto-correlation function of the electromagnetic field.

In order to determine diffusion coefficient for a polydisperse sample with spherical particles, *method of cumulants* is often applied.[77] In this method, the field correlation function is given by Laplace transform of relaxation rates ($P(\Gamma)$)

$$g^{(1)}(\tau) \equiv \int_0^\infty P(\Gamma) e^{-\Gamma\tau} d\Gamma \tag{2.19}$$

where the relaxation rate is $\Gamma = -q^2 D$ and $\int P(\Gamma) d\Gamma = 1$. The exponential is linearalized and yields the so-called Z-averaged relaxation rate ($\bar{\Gamma}$)

$$\ln(g^{(1)}) = -\bar{\Gamma}\tau + \frac{1}{2}\left(\frac{\overline{\Gamma^2} - \bar{\Gamma}^2}{\bar{\Gamma}^2}\right)(\bar{\Gamma}\tau)^2 + \dots \tag{2.20}$$

In addition, the polydispersity of spherical particles can be determined from the second term in Equation 2.20.[72]

2.3 Cryogenic Transmission Electron Microscopy (cryo-TEM)

Cryo-TEM is a microscopy technique that allows imaging of a biological sample in a solution state. This is achieved by rapidly freezing the sample on a carbon grid. A small amount of sample is placed on the carbon grid which is then plunged into liquid ethane at -183 °C to avoid introduction of ice crystals. The imaging is performed in frozen state at liquid nitrogen or helium temperatures ($\sim$ -175°C).[78-80]

The frozen sample is placed in the microscope where an electron beam is directed towards the grid. Electromagnetic lenses are used to focus the scattered electrons and magnify the image at the detector.[81]

Cryo-TEM was used to image softwood hemicellulose in Paper I and hemicellulose stabilised cubosomes in Paper III. In addition, the structure of novel glycopolymers was captured at 25°C and 50°C in Paper IV.

2.4 Tensiometry

In order to determine critical micelle concentration (CMC) of hexyl olygosides, surface tension (γ) was measured at different concentrations (see Paper I) with a pendant drop technique. The shape of the drop is captured and related to the surface tension through the Young-Laplace equation which describes the Laplace pressure across a curved interface[82,83]

$$\gamma(\frac{1}{R_1} + \frac{1}{R_2}) = \Delta P \equiv \Delta P_0 - \Delta\rho g z \qquad (2.21)$$

where R_1 and R_2 are the principal curvature radii, ΔP is the difference in Laplace pressure across the curved interface, $\Delta\rho$ is the density difference, g is the gravitational acceleration and z is the vertical height of the drop.

3   Interactions between hemicellulose and cellulose

Interactions between hemicellulose and cellulose have been a research topic for many years. This has helped to improve our knowledge about the architecture inside plant cell walls, as well as to design and use these materials in a range of applications. The first part of this chapter is focused on evaluating the nature of the interactions and in the second part the adsorption of hemicellulose to cellulose surface in relation to film crystallinity is discussed.

The discussion in this chapter will involve five hemicellulose samples with varying molecular weight and composition that originate from seeds and spruce. Since these polysaccharides contain mannose as the main constituent, I will refer to them as mannan-based polysaccharides or simply mannans. Spruce hemicelluloses or galactoglucomannans (GGMs) were obtained from thermomechanical pulp process waters (TMP-GGM) and from spruce chips that were subjected to steam extraction (SP-GGM). Seed hemicelluloses or galactomannans (GMs), on the other hand, are commercially available but originate from the seed endosperm of the carob tree *Ceratonia silique L.* (Locust bean gum) and the seed of *Cyamopsis tetragonoloba* (Guar gum). A more detailed description of the extraction and analysis of the samples can be found in Paper 1. A summary of the monomer composition of the samples is shown in Table 3.1.

Table 3.1 Denotation, molecular weight and chemical composition of the mannans studied in this chapter.

Sample	Denotation	Molecular weight [kDa]	Man	Gal	Glc	Acetyl	Ara	Xyl
			Molar ratio					
Guar gum	GG	250.0	67	33				
Locust bean gum	LBG	556.0	78	22				
	LBG*	107.0	78	22				
Galactoglucomannan (GGM)	TMP	14.0	50	15	15	20		
	SP	5.9	40	6	16	2	2	8

3.1 On the interactions of softwood hemicellulose with cellulose surfaces in relation to molecular structure and physicochemical properties of hemicellulose

3.1.1 Hemicellulose properties in solution

The behavior of hemicellulose polysaccharides in solution was investigated with DLS and SLS. In addition, a more detailed characterization of TMP and SP GGM samples was done utilizing SAXS.

Table 3.2 presents the average radius of gyration (R_g), hydrodynamic radius (R_h) and the ratio between the two parameters that gives an indication of the shape that a polymer takes in solution. GGM samples have R_g of 122 nm (TMP) and 87 nm (SP) and R_h of 111 nm (TMP) and 82 nm (SP). However, if we assume that a single sugar monomer has a molecular weight of 0.18 kDa and dimensions of 0.6 nm, then the length of a fully stretched polymer would be 47 nm and 20 nm for 14.0 kDa and 5.9 kDa molecular weight, respectively. These values are significantly smaller than the obtained results from light scattering indicating that the GGMs aggregate in solution. This observation is confirmed by cryo-TEM image of TMP-GGM sample presented in Figure 3.1, where an aggregate of ∼ 200 nm in diameter can be seen. Similar type of aggregated structures but even larger in size, possibly due to a higher molecular weight and sample concentration, were reported in literature for a comparable GGM preparation.[84]
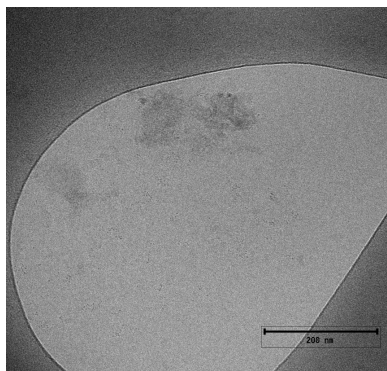
Figure 3.1 Cryo-TEM image of TMP-GGM sample at 1.5 mg mL^{-1}. The scale bar it 200 nm.

The obtained R_g and R_h values for guar gum and locust bean gum are much smaller than the expected contour length (length of a fully stretched polymer) of the corresponding polymers suggesting that the polysaccharides are not in an aggregated state. Comparable R_g have been previously reported in literature.[85,86] Based on the R_g/R_h, both TMP and SP assemble into elongated aggregates while the chains of LBG and GG seem to take a globular shape in solution.[87]

Table 3.2 Molecular weight, radius of gyration (R_g), hydrodynamic radius (R_h) and R_g/R_h of the mannan-based polysaccharides.

		M_W [kDa]	R_g [nm]	R_h [nm]	R_g/R_h
GGM	TMP	14.0	122	111 ± 8	1.10
	SP	5.9	87	82 ± 6	1.07
Locust bean gum	LBG*	107.0	79	95 ± 14	0.75
	LBG	556.0	111	210 ± 39	0.53
Guar gum	GG	250.0	42	93 ± 16	0.61

SAXS measurements were performed to gain more insight into the arrangement of GGM polymers in solution. Figure 3.2 shows SAXS scattering patterns of TMP and SP GGM. Apart from the shift of the power-law decay from -1.85 at low q to -1.0 at high q for TMP and -1.7 to -0.95 for SP, the scattering curves do not present distinct features. Such behavior is characteristic to fractal-like structures (Figure 3.3).
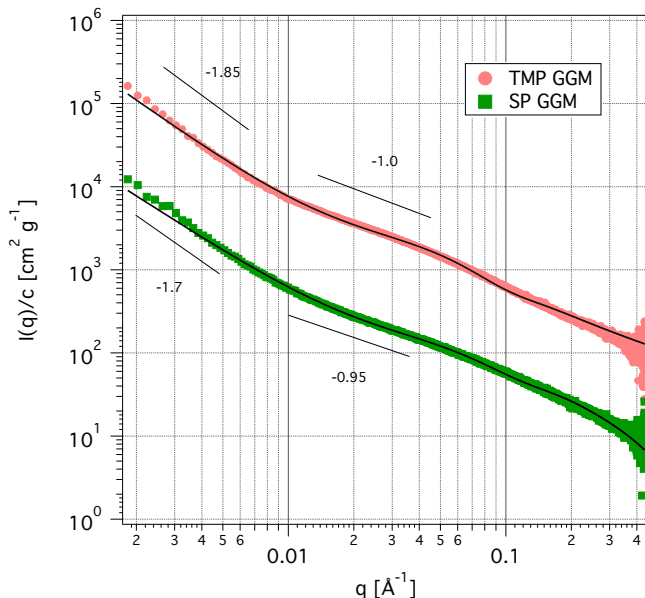
Figure 3.2 SAXS curves of the TMP (light red) and SP (green) at 10 mg mL^{-1}. Solid black lines represent a theoretical fit to the corrected Beaucage model. The scattering curve of the TMP was shifted upwards by a factor of 10 for clarity.

The scattering intensity versus q can therefore be described by a mass fractal model $I(q) \sim q^{-d}$ where d is the exponent of the scattering curve (between -1 and -3, for mass fractals).[88] The exponent of -1 at high q is characteristic to rod-like shape below the persistence length (L_p) of the polymer. Such scattering profiles can be fitted to the corrected Beaucage model that represents fractal morphology formed from flexible cylinders.[88,89]

The Beaucage analysis gives two radii of gyration determined from the low-q or Guiner regime and from the q region where the slope of the scattering curve changes (*i.e.* the transition region). The former radius of gyration (R_g) represents the overall size of the fractal aggregate and the latter (R_{sub}) corresponds to the size of a fractal subunit and can be recalculated into a persistence length (L_p) using Equation 3.1[90]

$$L_p = \frac{\left(\sqrt{12R_g^2} \right)}{2}.$$

(3.1)

Persistence length is an indication of the chain stiffness. For a very flexible polymer, the L_p is very low. For a stiff polymer, however, the L_p is close to a contour length.
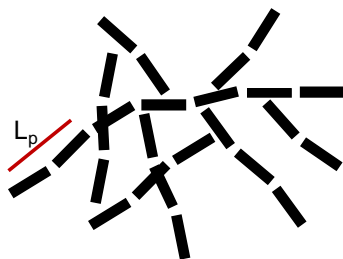
Figure 3.3 Schematic representation of fractal-like aggregates described by persistence length (L_p).

According to the fit, the L_p is 5.6 nm and 4.2 nm for TMP and SP GGM, respectively. The difference in the chain flexibility can be explained by a higher amount of galactose side-groups present in TMP structure that makes the polysaccharide to behave more as comb-like polymers. High branching degree and length of the branches have been shown to considerably decrease flexibility of comb-like polymers.[91] The effect of the side groups on the hemicellulose chain flexibility has also been demonstrated for tamarind seed polysaccharides.[92]

3.1.2 Adsorption studies of hemicellulose on cellulose and hydrophobic surfaces

The adsorption of different hemicellulose samples to cellulose surfaces was studied with the aim to evaluate the impact of the molecular weight and branching degree on the adsorbed amount. In addition, the adsorption to hydrophobic surface was compared in order to shed light on the nature of the interaction between hemicellulose and cellulose. The adsorption studies were performed using ellipsometry on both cellulose and hydrophobic surfaces, as well as QCM-D and neutron reflectometry on hydrophobic surface.

For the adsorption studies using ellipsometry, Avicel microcrystalline cellulose was dissolved in DMAc/LiCl solution and spin-coated on silica wafers (a more detailed protocol can be found in Paper I). Figure 3.4 shows a topographical profile of a typical cellulose film used in ellipsometry measurements imaged with AFM in air. The surface is covered with cellulose fibrils that create a uniform network on Si substrate with the root mean square roughness (rms) of 3 nm.
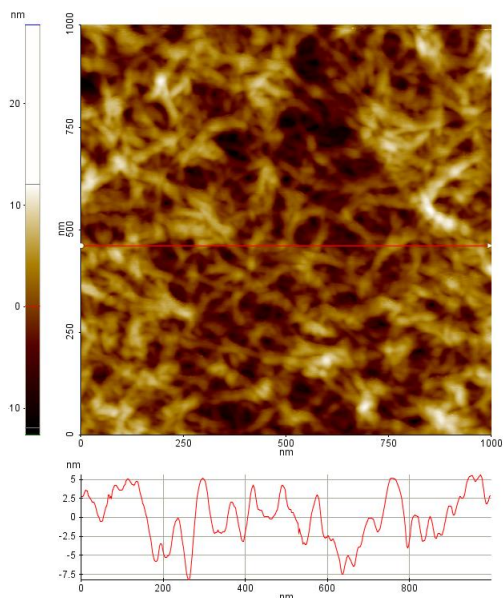
Figure 3.4   AFM topographical image of a cellulose film spin coated on a silica wafer used in the ellipsometry measurements obtained in non-contact mode.

Similar fibrillar topography has been previously reported for Avicel microcrystalline cellulose dissolved in DMAc/LiCl solvent but with a higher rms.[93] However, other sources of cellulose dissolved in a comparable solvent system have been shown to create non-fibrillar surface with spherically shaped cellulose aggregates.[94,95]

The adsorption of the mannan-based polysaccharides to hydrophobic and cellulose surfaces was studied *in situ* with null ellipsometry at low concentration (0.02 mg mL^{-1}). Typical ellipsometry results are shown in Figure 3.5, where also the points of GGM addition and start of flushing the measuring cell with pure buffer are marked.
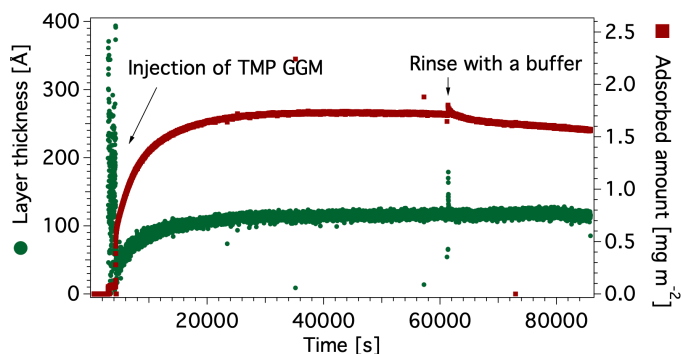
Figure 3.5 A typical ellipsometry measurement set up and results. Adsorbed amount (red) and layer thickness (green) of TMP GGM on a hydrophobic silicon oxide surface.

In general, first the thickness of the silicon oxide was determined by estimating Ψ and Δ values in air and in buffer. After which, a bare hydrophobized substrate or a substrate covered with spin-coated layer of cellulose, was mounted and placed in the sample cell. The average thickness of the oxide layer was ~300 Å with a refractive index of 1.47. The thickness of cellulose layer was typically around 400 Å with a refractive index of around 1.42. Similar refractive index for swollen cellulose films was reported previously with corresponding solvent amount of 68 % based on the refractive index of 1.6 for dry cellulose.[93,96]

Aliquots of mannan stock solution were added to the ellipsometry cell with either a hydrophobic or a cellulose spin-coated silica surface. The adsorption was followed until the plateau was reached and a buffer was flushed through the cell to remove unreacted or loosely attached material. Summary of the obtained adsorbed amount of mannans on two kinds of surfaces is shown in Figure 3.6. All of the mannans demonstrated a significant adsorption to hydrophobic surfaces with the adsorbed amount ranging from 0.8 to 1.53 mg m^{-2} for galactomannans and 1.50 to 1.62 mg m^{-2} for GGMs. This indicates that mannan-based polysaccharides have a relatively hydrophobic character. A generally higher adsorbed amount of GGM samples can possibly be explained by the presence of acetyl groups that are absent in galactomannans. The amphiphilic character of sugars (especially, cellulose) has been widely discussed in literature.[97-99] The hydrophobic character depends on the arrangement of -OH groups in sugar rings, and therefore is different for each type of sugar monomer. The order of the increasing hydrophobicity of sugar units present in mannan-based polysaccharides has been suggested to be: galactose, glucose, mannose.[97] GGMs have a lower galactose substitution degree and, thus, longer unsubstituted sections in the backbone that would facilitate interactions with

the hydrophobic surface.
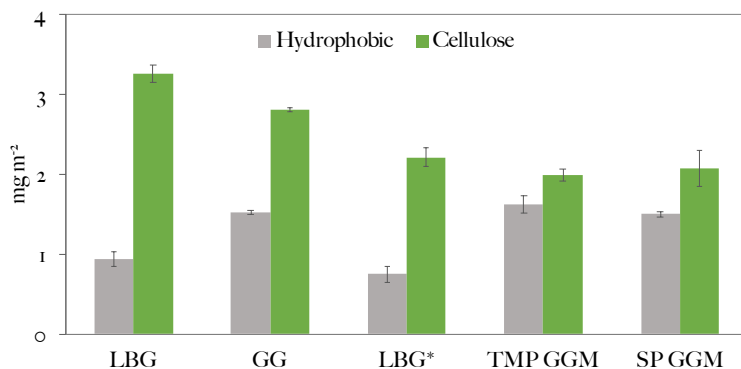
Figure 3.6 Comparison between the adsorbed amount of mannan-based polysaccharides on the cellulose spin-coated film (green) and the hydrophobic surface (gray). Results are arranged in the order of decreasing polysaccharide molecular weight from left to right.

The adsorbed amount is higher on cellulose than on hydrophobic surface for all hemicellulose samples possibly due to specific interactions caused by similarity in structure. It has been shown that bacterial cellulose is able to *co*-crystallise with mannan-based polysaccharides and sugar surfactants have selective attractive interactions between head groups depending on the stereoisomer type.[100-103] In addition, cellulose surface has an open and relatively porous structure providing a larger effective area and, thus, higher number of adsorption sites. This type of surface can accumulate a large amount of water which results in swelling. In such conditions, mannans strive to replace water molecules adsorbed on cellulose surface since the mannan-cellulose surface interactions are more favourable than the water-cellulose interactions. This suggests that the adsorption process is entropy driven.[104]

The adsorbed amount on the cellulose surfaces was found to be dependent on the molecular weight of the mannan polymers. The highest adsorbed amount was obtained with Locust bean gum (556 kDa) and the lowest one with TMP (14.0 kDa) and SP GGM (5.9 kDa). The influence of the molecular weight on the adsorption of hemicellulose has been previously reported in literature, however galactose substitution degree has been suggested to have a stronger impact compared to molecular weight.[11,18,105] Branches might prevent a close contact between the backbone and the surface, however we have not observed such a dependency in our studies.

The adsorption of mannan-based polysaccharides on hydrophobic surface was additionally followed with QCM-D. In comparison to ellipsometry, QCM-D measures the total added "weight" that also includes coupled solvent. By comparing

results from these two techniques, information on the amount of solvent present in the adsorbed layer can be extracted. Table 3.3 presents summary of the adsorbed amount on hydrophobic surface determined with ellipsometry and QCM-D. All of the mannans form a highly hydrated layer with more than 90 % of solvent. Based on the SAXS results, GGM polymer chains are relatively stiff and would lie parallel to the surface stacked on top of each other. However, galactose side groups prevent polymer chains from lying completely flat and cause parts of GGM chains to extend into solution. Such a configuration of polymer chains is open to a large amount of solvent. High content of water has been previously reported for the GG (91 %) and GGM (65 %) adsorbed layers on cellulose but with a lower dry mass than it was obtained here, possibly due to thinner cellulose films.[10,13]

Table 3.3 The summary of the adsorbed amount on hydrophobic surfaces as determined with ellipsometry and QCM-D, and the calculated solvent content in the adsorbed layer.

		LBG	GG	LBG*	TMP GGM	SP GGM
Adsorbed amount [mg m^{-2}]	QCM-D	26 ± 6	30 ± 10	31 ± 4	28 ± 3	28 ± 1
	Ellipsometry	0.94 ± 0.09	0.94 ± 0.09	0.8 ± 0.1	1.6 ± 0.1	1.50 ± 0.03
Solvent content [%]		96	96	97	94	95

Additionally, the adsorption of TMP GGM to hydrophobic surface was studied with neutron reflectometry (NR) which gives the scattering length density profile of the adsorbed layer perpendicular to the surface. The scattering curves of a bare silica and the adsorbed TMP layer in two contrasts are shown in Figure 3.7. A significantly larger difference is seen in the D_2O contrast compared to the H_2O due to a higher scattering contrast between D_2O and TMP. The best fit to the data was obtained by dividing TMP layer into two. The inner layer (closest to hydrophobic surface) is expected to contain GGM moieties with high number of acetyl groups that partially penetrate the hydrophobic layer. Therefore, we denote this layer as the transition layer. The outer layer, on the other hand, is expected to be highly hydrated containing GGM chains with low acetylation degree. Here, the roughness between the transition and the outer GGM layer indicates Gaussian distribution of polymer chains without sharp borders. The scattering length density of GGM used to fit the data was adjusted for the exchangeable hydrogens in sugar monomers.[106]
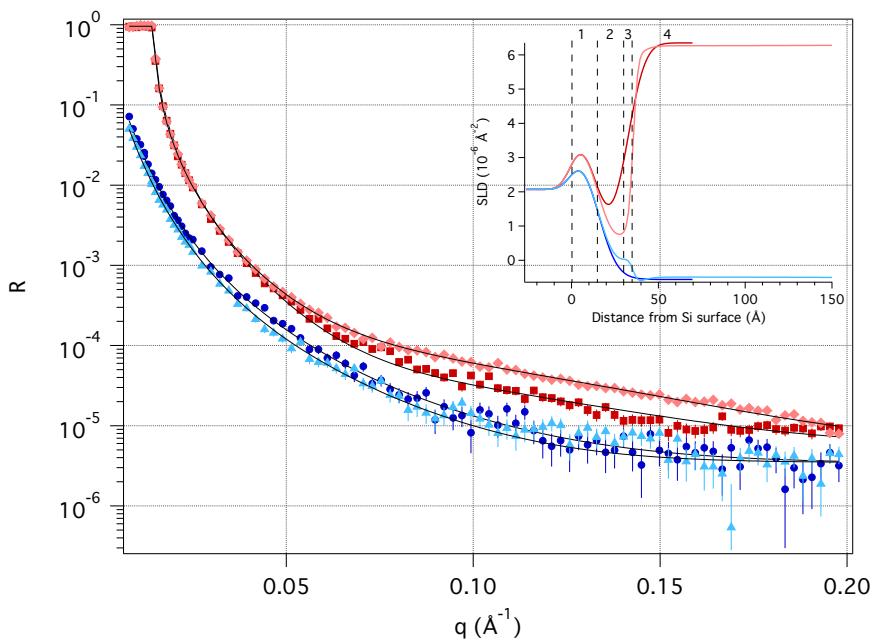
Figure 3.7 Neutron reflectivity curves of pure hydrophobic surface (dark red in D_2O and dark blue in H_2O) and after adsorption of TMP (light red in D_2O and light blue in H_2O). Solid black lines represent the theoretical fit. The inset illustrates the scattering length density (SLD) profile as a function of distance from the Si surface based on the fitting with the numbers indicating layers described in Table 3.4.

According to the fit, the transition layer is 4 Å with 14 % of the coupled solvent. The outer layer, however, is 210 Å. The layer is highly hydrated confirming the results obtained with ellipsometry and QCM-D but much smaller than the measured hydrodynamic radius of the polymer suggesting that TMP takes a relatively flat conformation on the hydrophobic surface.

Table 3.4 Parameters obtained from the fitting of NR data measured in D_2O and H_2O. The numbers correlate to the layer numbers in the SLD profile in Figure 3.7.

	1	2	3		4	
	SiO_x	Hydrophobic layer	Transition layer		GGM	
			D_2O	H_2O	D_2O	H_2O
SLD [10^{-6} Å^{-2}]	3.47	-0.44 ± 0.02	0.68 ± 0.08	0.5 ± 0.4	3.4 ± 0.1	1.9 ± 0.5
Layer thickness [Å]	15.6 ± 0.2	15.8 ± 0.1	4.0 ± 0.2		210 ± 11	
Solvent content [v/v, %]	8.7 ± 0.6	6.9 ± 0.3	14 ± 1		97.1 ± 0.1	
Roughness [Å]	8.2 ± 0.1	8.3 ± 0.1	2.1 ± 0.2		97 ± 13	

3.2 Hemicellulose adsorption to cellulose surfaces in relation to cellulose film crystallinity

3.2.1 Morphology of the bacterial cellulose films in air and liquid environment

In this study the adsorption of the hemicellulose samples to the spin-coated bacterial d-cellulose (d-BC) films was investigated. The morphology of the films was imaged with AFM in air and liquid conditions in order to follow cellulose swelling.

Figure 3.8(a) presents topography features of a typical d-BC surface in air imaged in non-contact mode. A matrix of randomly distributed cellulose fibrils (up to 12 nm in height) uniformly covers the silica substrate. The root mean square surface roughness of the film is 3.6 nm. Topography profile observed here resembles that of the spin-coated microcrystalline cellulose film highlighted in the previous section in Figure 3.4 with the rms of 3 nm.
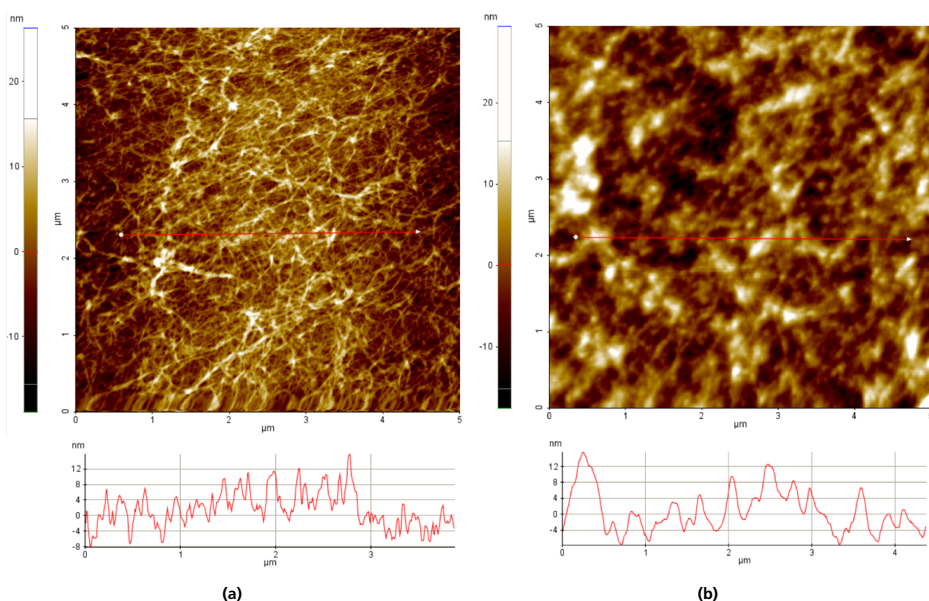
Figure 3.8 AFM topography profile of the bacterial d-cellulose imaged in air **(a)** and liquid **(b)** environment in non-contact mode.

Upon contact with water (Figure 3.8(b)), the lateral dimensions of fibrils increased and subsequently the features of the network became less pronounced. The roughness of the swollen film increased to 4.3 nm as compared to the film imaged in air.

3.2.2 Cellulose film crystallinity

The degree of crystallinity of the spin-coated *d*-cellulose film was evaluated using ATR-FTIR. The dry films were exposed to a saturated D_2O and H_2O vapor environment in order to reveal the number of the non-exchangeable hydroxyl groups. Every sugar unit of the cellulose chains contains three -OH groups at C(2), C(3) and C(6) that in a fully amorphous state once in contact with deuterium atoms are rapidly exchanged. The hydroxyl groups in the crystalline regions, however, are not accessible to the solvent due to a very strong binding between cellulose chains. [107-109] IR technique is sensitive to the atomic mass which makes it a perfect tool to follow the H-D exchange.

The FTIR spectra of the spin-coated non-deuterated and deuterated bacterial cellulose films under various conditions are presented in Figure 3.9 and Figure 3.10, respectively.
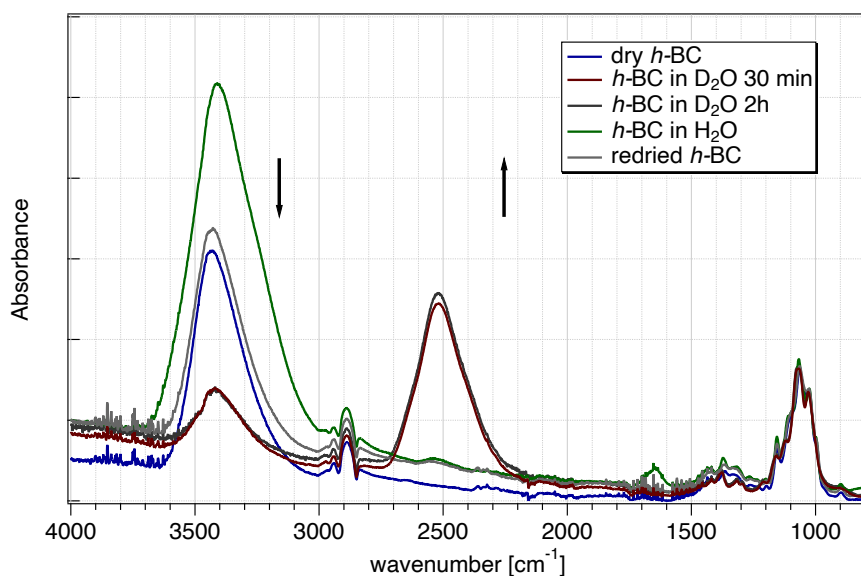
Figure 3.9 FTIR spectra of *h*-BC film in air (dark blue), in D2O vapor after 30 min (dark red), in D2O vapor after 2 hours (dark gray), in H2O vapor (green) and redried (light gray).

The spectra of the films in the dry state contain two main regions: an -OH stretching band between 3600-3200 cm^{-1} and a cellulose fingerprint region between 1550-900 cm^{-1}. The cellulose fingerprint region consists of the overlapping peaks resulting from the stretching vibrations of C-C, C-O, skeletal and ring vibrations. [110-113] The

dry spectrum in Figure 3.9 contains a peak at 2900 cm^{-1} corresponding to the C-H stretching. This peak is shifted to 2100 cm^{-1} frequency in the spectrum of the dry *d*-BC film (Figure 3.10) arising from the C-D stretching instead.[114]
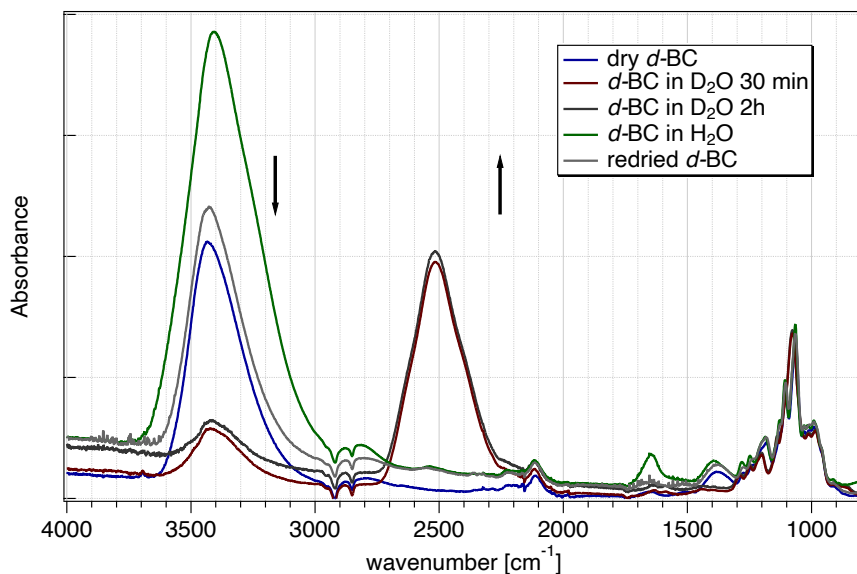
Figure 3.10 FTIR spectra of *d*-BC film in air (dark blue), in D2O vapor after 30 min (dark red), in D2O vapor after 2 hours (dark gray), in H2O vapor (green) and redried (light gray).

Upon contact with a saturated D$_2$O vapor, the intensity of the -OH peak decreased and a new peak at 2500 cm^{-1} appeared corresponding to -OD elongational vibrations. Although, the intensity of the -OH band decreased significantly, the peak did not disappear completely in both types of cellulose films.

D$_2$O vapor was replaced by H$_2$O vapor once the exchange was complete and no further changes were observed in peak intensities of -OH and -OD. A sudden increase in the -OH beyond the initial intensity along with a decrease in -OD peak were observed in the spectra of the deuterated and non-deuterated cellulose. In addition, a new peak appeared at 1635 cm^{-1} corresponding to the presence of free water molecules in both films. Interestingly, not all of the deuterium atoms exchanged back to hydrogen as evidenced by the remaining -OD band even after redrying. The so-called resistant -OD groups have often been reported in literature in relation to the H-D exchange in cellulose. The deuterium atoms are believed to be trapped due to recrystallization during wetting and drying cycles.[109,112,115,116]

The kinetic curves of the H-D exchange in the spin-coated deuterated and non-deuterated cellulose films are presented in Figure 3.11. The reaction was assumed to follow a pseudo-first-order kinetics described by Equation 3.2[117]

$$ln\left\{\frac{[OH]_t}{[OH]_0}\right\} = -kt \qquad (3.2)$$

where $[OH]_0$ and $[OH]_t$ are the area of the -OH peak at 0 and t time point, respectively.

The deuterated and non-deuterated cellulose films follow a similar kinetic trend. The most rapid exchange occurs during the first 1-2 minutes with a slightly faster exchange in the *d*-BC compared to the *h*-BC film possibly due to a less crystalline character of the former. The exchange rate decreases significantly after that and continues to decrease for 2 hours until a steady state of the reaction is reached. The exchange process in cellulose is often described by a two-step model. The first step of the exchange occurs in the amorphous regions of the layer which may take from 15 min to a couple of hours. The second step takes much longer as it occurs on the surface of crystalline planes or at irregularities which are less accessible.[109,112,117-119] Each of the exchange curves presented in Figure 3.11 can be fitted with two exponential decays suggesting that the films contain two regions with distinct kinetic behavior.[119]
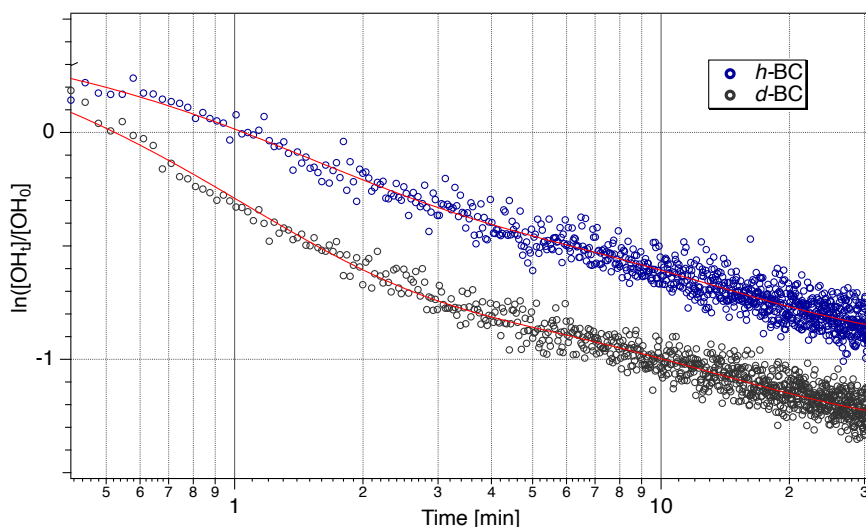
Figure 3.11 The change in the area of the -OH signal with time in *h*-BC (blue circles) and *d*-BC (black circles). Red lines represent fits to the exponential decay.

The number of the exchanged hydroxyl groups (r_{OH}) was estimated according to Equation 2.10 and is equal to 73 % in the deuterated cellulose film and 61 % in the non-deuterated cellulose film. The higher r_{OH} in the d-BC film is expected since the kinetic experiments demonstrated a more rapid exchange to that in the h-BC film. A possible explanation for the difference could be slight variations during the cellulose dissolution or spin-coating step as the deuteration of the cellulose backbone has been shown not to affect the molecular or morphological properties of cellulose.[114] Bacterial cellulose is known to have cellulose I type of crystalline arrangement with chains aligned in a parallel manner. The number of the accessible -OH groups in cellulose I has been reported to be 6 - 21 % depending on the reaction conditions.[109,114] In solution, however, the crystalline network is disrupted, resulting in a higher amount of accessible -OH groups. The solubilization of a bacterial cellulose in N-Methylmorphine-N-oxide monohydrate (NMMO) has been shown to decrease the degree of crystallinity from 79 % to 38 %.[120] Here, a different solvent was used but a comparable degree of crystallinity was observed after the dissolution.

Sugar monomers in the cellulose chains are connected via intra- and intermolecular hydrogen bonds at positions O(2)H$\cdots$O(6), O(3)H$\cdots$O(5) and O(6)H$\cdots$O(3) as demonstrated in Figure 3.12. The molecular stretching of these bonds gives rise to a broad -OH peak. Deconvolution of this peak revealed that it consists of several absorption bands centered at 3460 cm^{-1}, 3340 cm^{-1} and 3230 cm^{-1} corresponding to O(2)H$\cdots$O(6), O(3)H$\cdots$O(5) and O(6)H$\cdots$O(3) bonds, respectively.[112,115]
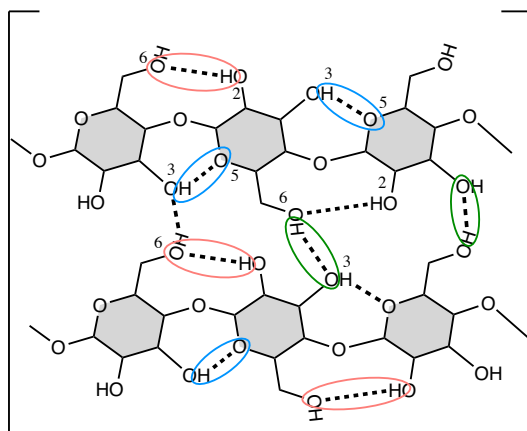
Figure 3.12 Schematic representation of inter- and intramolecular hydrogen bonds in two parallel cellulose chains.

The difference spectra, derived from subtracting the spectrum taken at a first time

point from the spectrum taken at a certain time point, are presented in Figure 3.13. Once the cellulose films were exposed to a D_2O vapor, the reaction started with the exchange on the intramolecular bond $O(2)H\cdots O(6)$. The exchange on this group continued throughout the experiment in both deuterated and non-deuterated cellulose. The exchange on $O(3)H\cdots O(5)$ bond also started early in the experiment but with a lower intensity. The least affected bond was the intermolecular $O(6)H\cdots O(3)$ bond in both deuterated and non-deuterated cellulose films. Hofstetter *et al.* has previously noted that most of the exchange occurs on the intramolecular bonds.[112] Although, the intermolecular bonds have a weaker character and therefore are expected to be more susceptible to the exchange, the hydroxyl groups at O(2) position have been reported to be more reactive.[121-123]
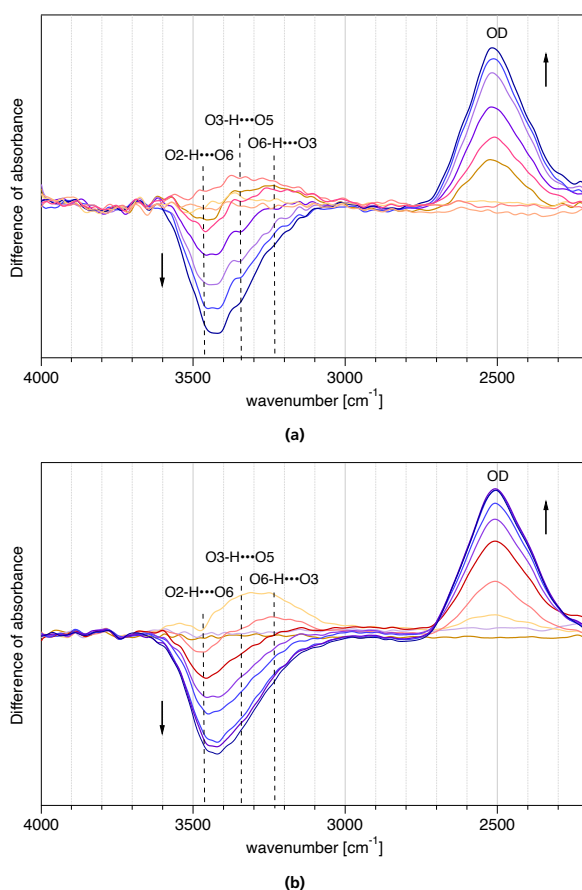
Figure 3.13 Change in difference spectra of *h*-BC **(a)** and *d*-BC **(b)** films in D2O vapor with time with a step of 3 min.

3.2.3   Structure of the cellulose films

The spin-coated cellulose films were probed with neutron reflectometry in order to determine structural properties of the layer. First a bare silicon surface was characterized in three isotopic contrasts: D_2O, H_2O and water contrast matched to silicon (CMSi, SLD=$2.07\text{x}10^{-6}$ Å^{-2}). The obtained data in different contrasts was then fit simultaneously to a model consisting of the SiO_2 (SLD=$3.47\text{x}10^{-6}$ Å^{-2}) layer. The results obtained from the fitting of the bare silicon substrates can be found in the supporting information of Paper II. A cellulose film was then spin-coated on the characterized silicon substrates and the reflectivity curves for the cellulose films were recorded in three isotopic contrasts as for the bare silica. The reflectivity curves of a typical bare silicon substrate and the one with a spin-coated *d*-cellulose film are presented in Figure 3.14. As mentioned earlier, every glucose unit in the cellulose backbone contains three exchangeable hydrogen atoms, therefore, the SLD of cellulose layer is highly dependent on the contrast. The expected SLD of *d*-cellulose in D_2O is $6.85\text{x}10^{-6}$ Å^{-2} which is close to the SLD of D_2O ($6.35\text{x}10^{-6}$ Å^{-2}) resulting in a poor contrast in this solvent and thus almost fully overlapping reflectivity curves from the bare and coated substrate.
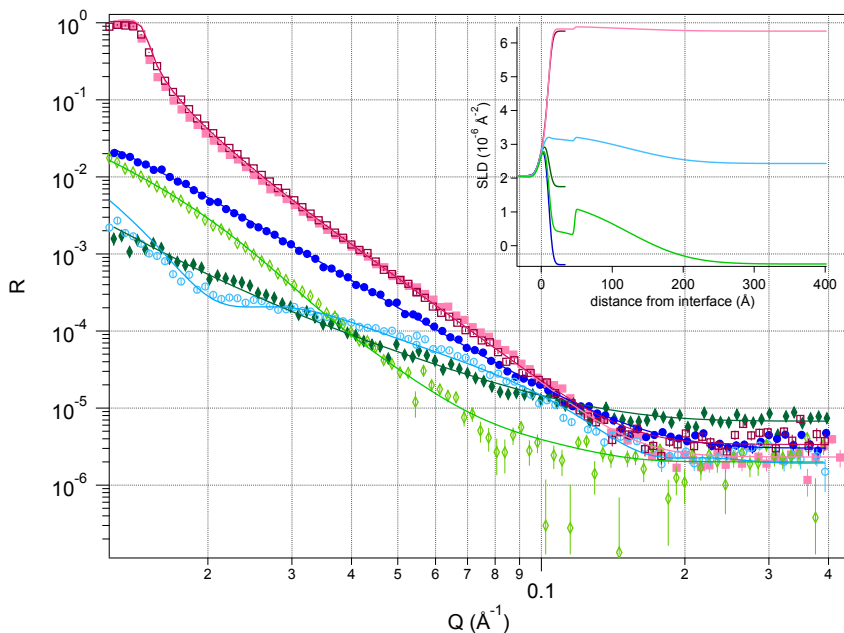
Figure 3.14 Neutron reflectivity as a function of momentum transfer (Q) of bare silica surface (filled symbols) in D_2O (dark red rectangle), H_2O (dark blue circle), CMSi (dark green rhombus) and *d*-cellulose surface (empty symbols) in D_2O (pink rectangle), H_2O (light blue circles), CMSi (light green rhombus). Solid lines represent theoretical fit. The inset illustrates the scattering length density (SLD) profiles as a function of distance from the Si surface.

A multilayer slab model consisting of SiO_2 and two cellulose layers was used to fit the reflectivity data of *d*-cellulose and account for differences perpendicular to the surface of the film (Figure 3.15). This approach has been previously applied to evaluate the structure of bacterial cellulose films.[106] A model with an additional layer next to the silicon surface (Layer 0), i.e. a three layer model was applied to one of the samples (sample 2) which significantly improved the goodness of fit. The Layer 0 was found to be 6 Å thick, with about 4% of trapped H_2O that is inaccessible to the different contrasts. A possible explanation for the presence of trapped water in this layer could be the insufficient drying during the preparation of the film. Due to a highly hydrophilic character, cellulose accumulates water from the surrounding environment. Strongly bound water present in various cellulose samples has been widely reported in literature.[124-126]
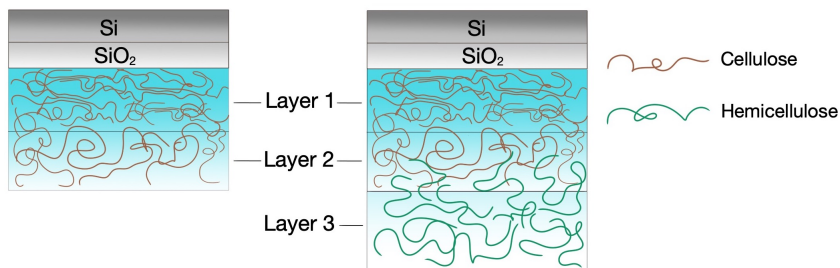
Figure 3.15 Schematic representation of the model used to fit the reflectometry data before and after hemicellulose adsorption on cellulose surface.

The expected SLD of *d*-cellulose in D_2O and H_2O are 6.85×10^{-6} Å^{-2} and 5.33×10^{-6} Å^{-2}, respectively. However, these values are only valid if all of the hydrogen atoms are exchanged with deuterium and vice versa. The higher amount of the inaccessible hydrogen, the lower the SLD of the cellulose layer in the D_2O contrast. In a similar way, the H_2O isotopic contrast would indicate the presence of the trapped deuterium atoms. With this in mind, the SLD values were not fixed to the expected values but instead were fitted within a reasonable margin. The obtained SLD of *d*-cellulose films (samples 1-5) in three isotopic contrasts are demonstrated in Figure 3.16. It should be noted that the film in sample 3 was only characterized in the CMSi and H_2O contrasts due to time constraints.

Indeed, the determined SLD values of *d*-cellulose Layer 1 are lower than the theoretical values indicating the presence of up to 10 % of the inaccessible hydrogen atoms. As it was mentioned earlier the films are almost fully matched out in the D_2O contrast, therefore the observation should be taken with caution. It is worth noting, however, that a similar degree of the non-exchanged hydrogen atoms was observed with ATR-FTIR. The SLD of the outer layer (Layer 2) is slightly higher than it was determined for Layer 1 but still lower than the expected values, suggesting a more crystalline character of the inner layer.

In the H_2O contrast, the SLD values of the cellulose films are higher than the expected ones possibly due to the resistant deuterium atoms since the film was first exposed to the D_2O solvent. The ATR-FTIR studies also showed the presence of the resistant -OD groups in the H_2O vapor environment, as well as in air after contact with D_2O (Figure 3.10).
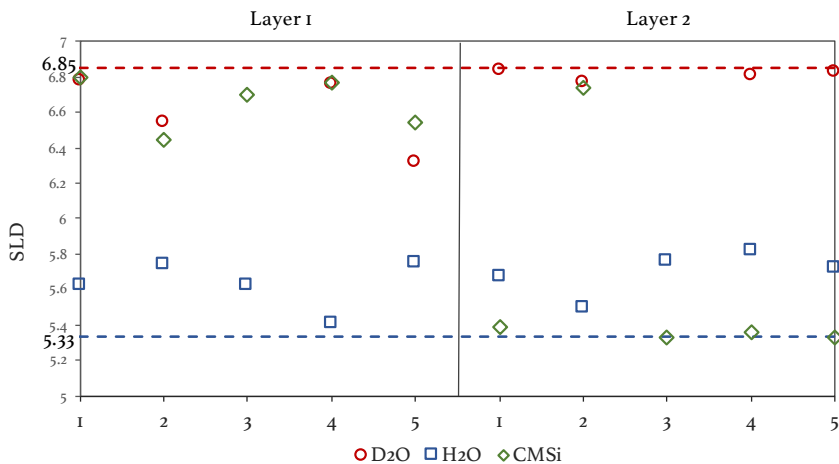
Figure 3.16 Scattering length density (SLD) values obtained from the fit of NR data to the model of Layer 1 and 2 in d-cellulose films (1-5) in D_2O (red circles), CMSi (green rhombus) and H_2O (blue rectangles). Red and blue dash lines represent the theoretical SLD values of d-cellulose in D_2O and H_2O, respectively.

The results obtained from the NR studies of cellulose films are summarized in Table 3.5 along with the results from the hemicellulose adsorption experiments which will be discussed in the following subsection.

The overall thickness of the cellulose films varies between 100 and 150 Å. All films have relatively similar features including a thin and smooth inner layer (Layer 1) and a ticker and rougher outer layer (Layer 2). It should be noted that film 3 has much higher roughness of the inner layer which could be explained by the fact that the film was prepared from a different batch of cellulose solutions as compared to the rest of the samples. Based on these observations and the previous discussion about the SLD values, we can speculate that the inner layer of the spin-coated cellulose films contain a significant number of cellulose crystallites whereas the outer layer mainly comprises amorphous cellulose fibrils. Cellulose films are highly swollen with the solvent penetration above 75 % throughout the film. The ability of cellulose fibrils to accumulate large amounts of water has been widely discussed.[93,95,127-129] High degree of swelling was observed even in the previous section but with a spin-coated microcrystalline cellulose films. Another important feature of the d-cellulose films is the solvent gradient from the inner to the outer layer. The different solvent distribution has been previously observed with the spin coated cellulose films possibly due to a molecular confinement or due to effects of the supporting substrate.[129] Surprisingly, the solvent content is higher in the inner layer despite the higher degree

of crystallinity. However, water accumulation between crystalline plates has been reported in literature in the films prepared with the dispersed cellulose nanocrystals.[95]

Table 3.5 Thickness (T), solvent volume fraction (V) and roughness (R) of cellulose (C) layers before and after addition of the mannan-based polysaccharides obtained from the fitting of a two or three layer model to the NR data. Here SP is steam extraction and TMP is thermomechanical pulp galactoglucomannans, LBG* is 107 kD locust bean gum galactomannan and LBG is the corresponding higher molecular weight sample (556 kD), GG is guar gum galactomannan.

Layer	Parameter	C	SP	C	TMP	C	LBG*	C	GG	C	LBG
		1		**2**		**3**		**4**		**5**	
0	T [Å]			6							
	V [v/v, %]			4							
	R [Å]			1							
1	T [Å]	37		27		58	66	38		39	
	V [v/v, %]	82		83		75	64	81		85	
	R [Å]	1		0.3		37	20	2		1	
2	T [Å]	74	83	87	98	94	103	66	72	78	100
	V [v/v, %]	69	21	72	55	72	67	72	54	73	67
	R [Å]	69	58	45	66	69	57	60	58	69	55
3	T [Å]		178		148		130		122		124
	V [v/v, %]		94		94		81		82		92
	R [Å]		34		45		65		65		43

3.2.4 Hemicellulose adsorption to the bacterial cellulose surfaces

The mannan samples were added to the reflectometry cell after the spin-coated cellulose films were characterized in three isotopic contrasts. As soon as the adsorption reached steady state, the cell was rinsed and the reflectivity was measured once more in three isotopic solvents. The typical reflectivity curves of the hemicellulose adsorbed to the spin-coated d-cellulose surface in the H_2O and the CMSi along with the corresponding neat cellulose curves are presented in Figure 3.17. Similarly to cellulose, hemicellulose contains exchangeable hydrogen atoms yielding a different SLD value depending on the contrast. The expected SLD of hemicellulose in D_2O is 3.19×10^{-6} Å^{-2} whereas in H_2O it is 1.78×10^{-6} Å^{-2}. The largest shift can be seen in the H_2O isotopic contrast, however small changes are noticeable even in the CMSi.
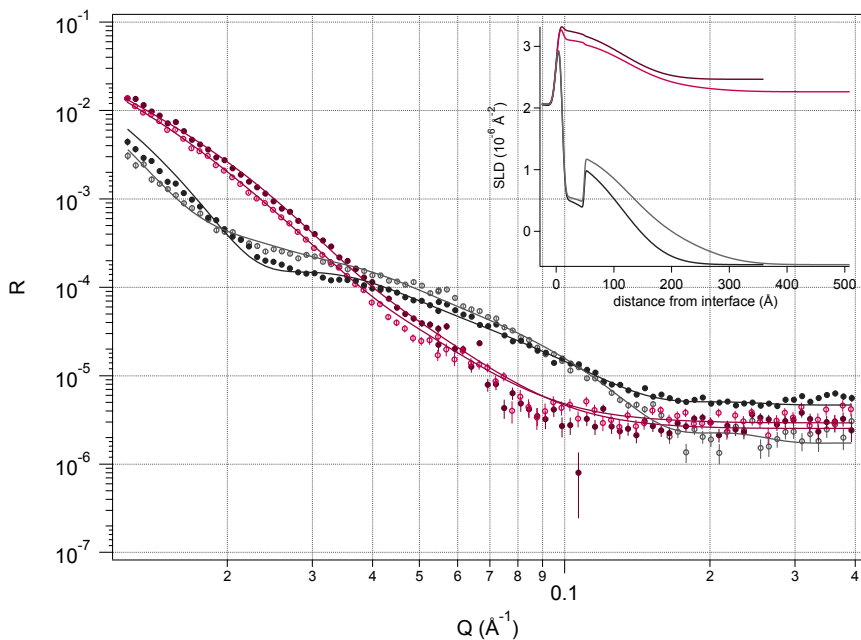
Figure 3.17 Neutron reflectivity as a function of momentum transfer (Q) of *d*-cellulose surface (filled circles) in H_2O (black), CMSi (dark red) and the adsorbed GG (empty circles) in H_2O (gray), CMSi (light red). Solid lines represent theoretical fit. The inset illustrates the scattering length density (SLD) profiles as a function of distance from the Si surface.

A model consisting of the intact cellulose layer and an added hemicellulose layer was fitted to the experimental data. However, the goodness of the fit was unsatisfactory for all of the mannan samples. A new model that allows the penetration of hemicellulose into the outer layer (Layer 2) of the cellulose film (and inner layer, in case of sample 3) was, therefore, used. The summary of the results obtained by applying this model to the reflectivity curves of the hemicellulose samples is presented in Table 3.5.

The mannan-based polysaccharides were found to diffuse into the outer layer of the cellulose film, resulting in a thicker and denser layer as demonstrated by the decreased solvent volume fraction as compared to the pure cellulose layer in Table 3.5. The inner layer of the cellulose, however, remains intact possibly due to a certain degree of crystallinity as discussed earlier. The added layer (Layer 3) is highly solvated (81 - 94 %) which has been observed with these types of mannans adsorbed on a hydrophobic surface in the previous section.[130]
The adsorbed amount (Γ) of the hemicellulose samples in each of the layers was estimated from the SLD of the layer. The results are summarized in Table 3.6. The total Γ of the mannan samples was between 3.3 and 6.6 mg m^{-2}. The adsorption does not seem to follow a similar trend as observed in the previous section in the

ellipsometry experiments. However, once the adsorbed amount was normalized to the cellulose film thickness, the trend relating the mannan properties to the adsorption can be observed. The adsorbed amount in the cellulose film decreases in the following order SP>TMP>LBG*>LBG. The highest adsorbed amount was obtained with SP GGM (89 kg m^{-3}) which has the lowest molecular weight, as well as the galactose substitution degree. The mannan with the highest molecular weight (LBG) and the highest branching degree similar to TMP and LBG* yielded the lowest adsorbed amount (42 kg m^{-3}). Based on these observations, the fairly open and porous nature of the cellulose surfaces (as evidenced by topography profile in Figure 3.4) is likely to allow a higher number of smaller molecules to diffuse into the cellulose layer. In addition, as it has been demonstrated in the previous section, SP is more flexible than the rest of the mannans due to a significantly lower galactose substitution degree which makes it easier to occupy the pores in the cellulose layer.[130] The mannan with the highest substitution degree (GG) yielded a relatively high adsorbed amount despite having the highest substitution degree which suggests that the adsorption was possibly affected by the high polydispersity of the sample or effects of the spin-coating.

Table 3.6 SLD of the layers after addition of hemicellulose obtained from the fitting of NR data and the calculated adsorbed amount of hemicellulose in each layer (Γ_H) the total and normalized adsorbed amount of the hemicellulose, as well as the normalized adsorbed amount of the cellulose layer (Γ_C).

Layer	Parameter	SP	TMP	LBG*	GG	LBG
1	SLD [10^{-6} Å^{-2}]			4.50		
	Γ_H [mg m^{-2}]			1.0		
2	SLD [10^{-6} Å^{-2}]	3.49	3.52	5.12	3.55	4.09
	Γ_H [mg m^{-2}]	5.4	3.4	0.8	2.7	2.0
3	SLD [10^{-6} Å^{-2}]	2.74	2.51	2.56	2.65	2.44
	Γ_H [mg m^{-2}]	1.2	1.1	2.9	2.6	1.2
Total Γ_H [mg m^{-2}]		6.6	4.5	4.7	5.3	3.3
Normalized total Γ_H [kg m^{-3}]		89	52	50	80	42
Normalized Γ_C [kg m^{-3}]		116	41	39	41	40

These results, however, are contradictory with the results demonstrated in the previous section where the mannans with the highest molecular weight yielded the highest adsorbed amount on the cellulose surfaces. Assuming that the type of cellulose used for the preparation of the films did not have a significant effect on the adsorption, it can be speculated that the difference arose from a much higher concentration of the hemicellulose samples (0.6 mg mL^{-1}) used in this study compared to the previous

work (0.02 mg mL^{-1}). This indicates that the adsorption of these mannans on the cellulose surfaces follows contrasting tendencies depending on the concentration. The adsorption of small molecules is less favorable in the low concentration regime due to the loss in translational entropy of these species. The opposite happens in the high concentration regime where small polymers adsorb with a higher intensity to prevent the loss in conformational entropy of large species.[131] Here, the effect is elevated due to the porosity of the cellulose film that restricts diffusion of large molecules inside the film.

4 Physico-chemical properties of compounds derived from hemicellulose

By now you should already be intrigued by the nature of hemicellulose. However, if you are not yet absolutely convinced that hemicellulose is an excellent and versatile material, this chapter is for you. By use of certain tools, hemicellulose can become the basis for a variety of different compounds. Here, I focus on three types of composites that were created by utilising hemicellulose as a raw material: lipid liquid crystalline nanoparticles, thermo-responsive glycopolymers and alkyl mannooligoside surfactants. Since this thesis is written from the physical chemistry point of view, I will not go into details of synthesis but rather focus on the characterisation of structure and physico-chemical properties of these compounds.

4.1 Bicontinuous cubic liquid crystalline phase nanoparticles stabilised by softwood hemicellulose

Lipid self-assembly in water is an intriguing phenomenon that has already found its use in a variety of applications in food and pharmaceutical industries. Glycerol monooleate or simply monoolein (GMO) is the most commonly used lipid for the preparation of cubic phase nanoparticles in water.[33,132,133] However, in order to prevent particles from aggregating and decrease size polydispersity, a stabilizer is often added to the formulation. In this section, I will show how softwood hemicellulose can be used as a stabilizer for such nanoparticles.

4.1.1 Preparation method optimization

For the stabilization of cubic phase nanoparticles two softwood hemicellulose samples were tested - from thermomechanical pulp mill (TMP) and from spent-sulphite liquor (SSL). Table 4.1 shows a summary of the main ingredients in each sample. In the thermomechanical process, the cellulose fibres are mechanically separated under high temperature and pressure, which is fairly ineffective for lignin removal. Therefore process waters usually contain mainly water-soluble hemicelluloses with a very low content of lignin (1.26 % in our case). Spent-sulphite liquor, on the other hand, is the by-product of a chemical process which is much harsher and therefore usually contains a substantial amount of lignin. Samples used in this study were additionally purified with ultrafiltration, diafiltration and anti-solvent precipitation in order to decrease the lignin content, however there was still 7.3 % of lignin present in the SSL extract.

Table 4.1 The chemical composition of the TMP and SSL hemicellulose samples shown as weight percentage of total dry solids (TDS).

	Wt % of TDS	
	TMP	SSL
Ash	0	2.02
Lignin	1.26	7.3
Carbohydrates		
Arabinose	0	1.1
Galactose	10.4	18.7
Glucose	8.8	14.8
Xylose	4.7	7.05
Mannose	76	30.8
Cellobiose	n.d.	1.14
Acids		
Lactic acid	n.d.	1.68
Acetic acid	n.d.	3.99
Formic acid	n.d.	1.63
Levulinic acid	n.d.	2.17
Furfural	n.d.	1.25
Hydroxymethylfurfural	n.d.	0.62

A top-down approach was used to prepare the formulations where first a thin lipid film was created on the walls of a sample vial and then, after adding hemicellulose

solution (3 mg mL^{-1}), the coarse dispersion was sonicated with a tip sonicator to break the film apart and force lipid molecules to self-assemble into cubosomes. Figure 4.1 presents SAXS curves for different preparations of the dispersion with varying concentrations of GMO and sonication times. The Bragg peaks with the highest scattering intensity were observed for the sample with 10 mg mL^{-1} of GMO and sonication time of 12 and 15 min. However, after 15 min of sonication, the Bragg peaks in scattering curve are slightly shifted to lower q values, indicating a larger lattice parameter and water channel radius.
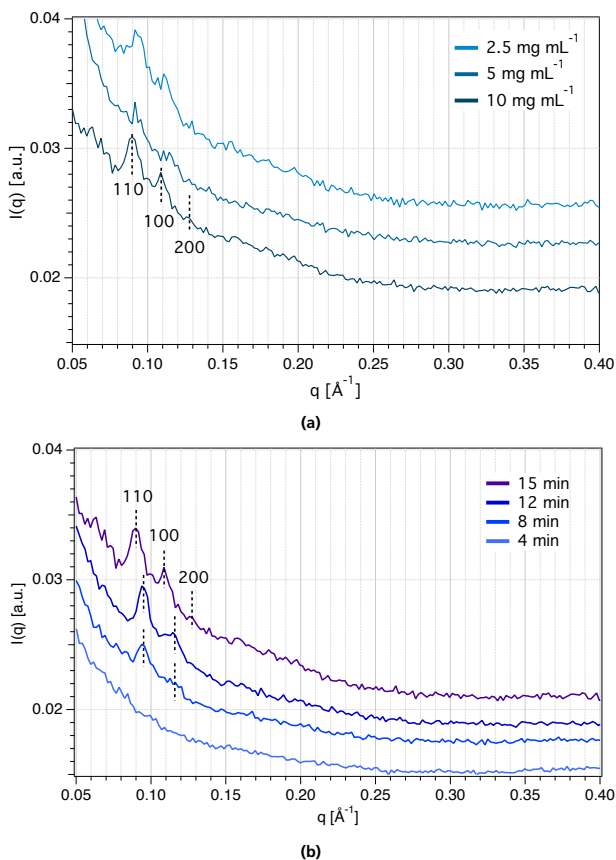
Figure 4.1 SAXS curves of the TMP-NPs at 2.5, 5 and 10 mg mL^{-1} of GMO with 15 min of sonication time **(a)** and after 4, 8, 12 and 15 min of sonication time **(b)** at 10 mg mL^{-1} GMO concentration. Numbers indicate Miller indices.

The DLS results in Figure 4.2 demonstrate that the size and PdI of the nanoparticles is fairly stable after 5 min of sonication. Since larger pores of the nanostructure are more desirable for the encapsulation purpose of hydrophilic drugs, all formulations

were prepared by sonicating for 15 min.
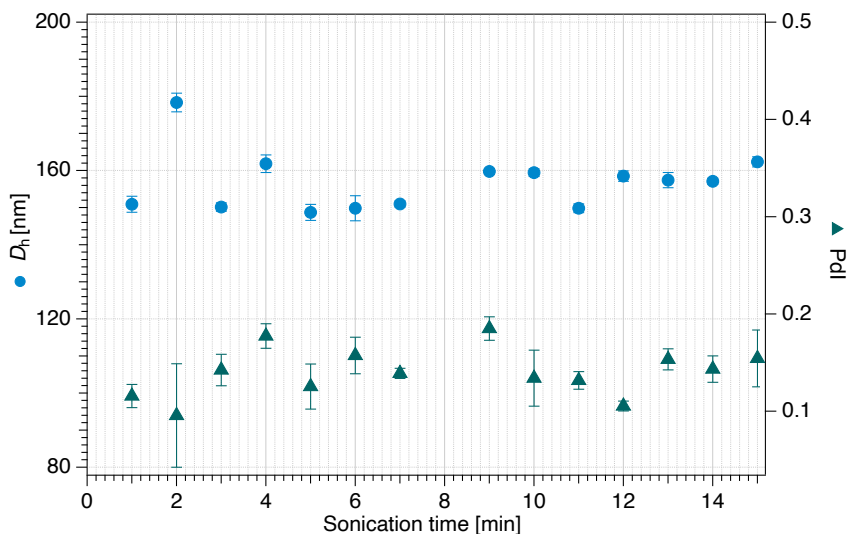
Figure 4.2 Change in D_h (blue circles) and PdI (green triangles) of TMP-NPs with sonication time.

4.1.2 Characterization of the NPs

Structure and morphology of the nanoparticles was studied with SAXS and cryo-TEM. Figure 4.3 shows scattering curves of the TMP- and SSL-stabilized nano-particles. Both of the scattering profiles contain two clearly visible Bragg peaks suggesting a presence of a highly ordered structure. Based on the peak positions, a lattice parameter and water channel radius was determined for each formulation. As indicated in Table 4.2, both of the samples contain Pn3m phase cubosomes with 100 Å lattice parameter and water channels with radius of 22 Å which is similar to the reported data in literature on the cubosomes stabilized with Pluronics.[132,134,135]
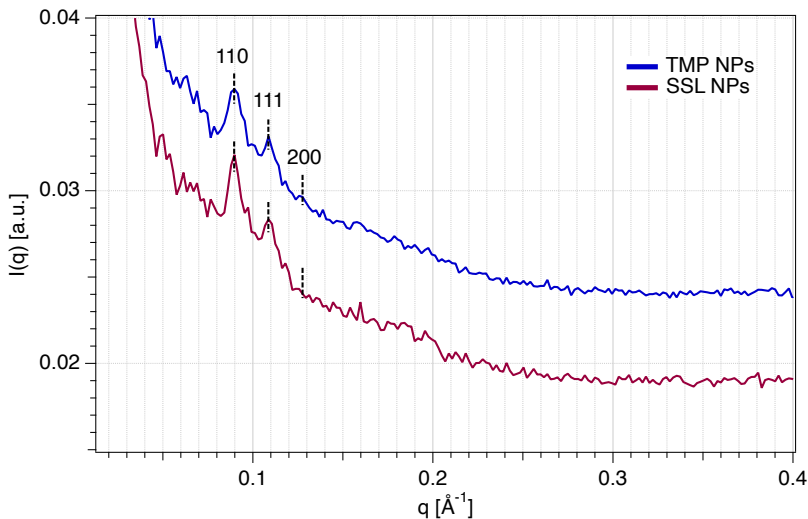
Figure 4.3 SAXS curves of the TMP-NPs (dark blue) and SSL-NPS (red) formulations. Numbers indicate Miller indices.

In excess of water, monoolein is known to assemble into Pn3m cubic phase nanoparticles, however addition of the commonly used Pluronics stabilizers affects the internal structure of the cubosomes resulting in a mixture of Pn3m and Im3m.[34] Cubosomes with the Pn3m phase can be more advantageous as drug delivery systems due to smaller pores if a slower release of small hydrophilic molecules is required.[136]

Table 4.2 Type of the cubic phase, lattice parameter (a) and water channel radius (r_w) of TMP-NPs and SSL-NPs formulations determined from SAXS curves seen in Figure 4.3.

Sample	Phase	$a \pm$ SD [Å]	$r_w \pm$ SD [Å]
TMP-NPs	Pn3m	99.6 ± 0.8	21.9 ± 0.3
SSL-NPs	Pn3m	98.7 ± 0.4	21.6 ± 0.1

The hydrodynamic diameter (D_h) and ζ-potential of the nanoparticles was determined with DLS and electrophoretic mobility measurements, respectively. As shown in Table 4.3, cubosomes in both of the formulations are around 150 nm in diameter with the PdI of 0.2. These parameters correlate well with the cubosome formulations reported in literature using other types of stabilizers.[132,137] Despite the fact that the particles in two dispersions are quite similar in size and PdI, the derived count rate of the SSL-NPs is more than double than that of the TMP-NPs sample. Such a difference indicates a much higher amount of the dispersed phase in the SSL-stabilized formulation. This is not surprising since the SSL-NPs dispersion

has a higher ζ-potential suggesting a better electrostatic stability. However, it has been previously shown that stabilization of emulsion with hemicellulose is mainly driven by steric repulsion.[138] The ζ-potential of hemicellulose extracts is in range with the ones reported in literature.[139] The charge of extracts is believed to be mainly caused by the presence of acidic groups since galactoglucomannans are neutral polysaccharides.[139] Interestingly, ζ-potential of both of the formulations is higher in magnitude compared to the pure hemicellulose extracts. This phenomenon has previously been observed for the monoolein formulations stabilized with non-ionic stabilizers.[137,140] The apparent negative charge is suggested to be caused by a selective adsorption of hydroxide ions at the lipid-water interface.[141]

Table 4.3 Apparent average hydrodynamic diameter (D_h), polydispersity index (PdI), derived count rate, ζ-potential and pH of pure TMP and SSL extract, as well as TMP-NPs and SSL-NPs determined at 25°C.

Sample	$D_h \pm$ SD [nm]	PdI $\pm$ SD	Derived count rate $\pm$ SD	ζ-potential $\pm$ SD [mV]	pH
TMP-NPs	151 ± 1	0.21 ± 0.02	940 ± 3	-37.7 ± 0.8	6.39
SSL-NPs	152.2 ± 0.9	0.19 ± 0.01	2032 ± 20	-49.5 ± 0.6	6.52
TMP	-	-	-	-10 ± 1	6.44
SSL	-	-	-	-14.8 ± 0.2	6.58

Morphology of the nanoparticles was studied with cryo-TEM. Figure 4.4 shows micrographs of the TMP-NPs and SSL-NPs formulations. In both of the samples cubosomes were observed with dimensions similar to the ones obtained with DLS. Insignificant amount of vesicles was also present in the formulations (Figure 4.4B and C). After applying 2D Fourier transform filter to the images of the cubosomes, a lattice parameter of the nanoparticles was determined. Obtained lattice parameters are 89 Å for TMP-NPs and 110 Å for SSL-NPs characteristic to Pn3m phase which agrees well with values calculated based on the SAXS data.

In addition to cubosomes and vesicles, large, irregular fractal-like structures were present in the TMP-NPs dispersion. Structures of similar type have previously been shown to arise from the assembly of a variety of hemicellulose samples including the ones described in Chapter 3 of this thesis.[84,130] We can speculate that since these objects are absent in the SSL-NPs micrographs, most of the hemicellulose is associated with monoolein in cubic phase nanoparticles. The SSL extract contains a larger amount of lignin that is strongly associated or even covalently bound with hemicellulose. Due to its hydrophobic nature, lignin would interact with hydrophobic part of monoolein and the associated hemicellulose would sterically stabilize the nanoparticles.
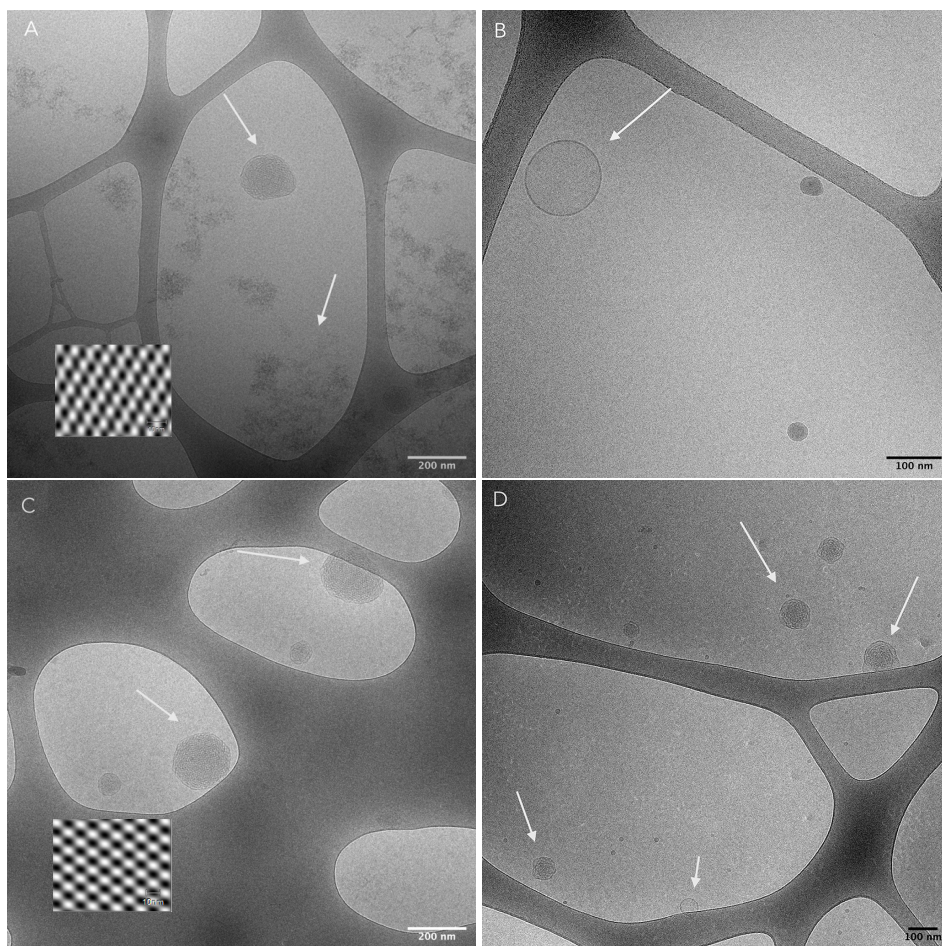
Figure 4.4 Cryo-TEM images of the TMP-NPs (A and B) and SSL-NPs (C and D) sample at 10 mg mL^{-1} of GMO. Insets represent cubosome interanal structure after applying 2D Fourier transform filter to the images. The scale bar is 200 nm (A and C) and 100 nm (B and D).

4.1.3   Stability of the nanoparticles

As was already mentioned before, one of the main potential applications for cubic phase dispersions is drug encapsulation and delivery. Therefore, stability of the formulation under physiological conditions is of utmost importance. For this reason, the size and PdI of the cubosomes was followed for 4 hours after diluting with phosphate buffered saline (PBS, pH 7.4, 0.01 phosphate buffer, 0.0027 M potassium chloride and 0.137 M sodium chloride). Results of the study are summarized in Figure 4.5. The diameter of the nanoparticles in both of the formulations has increased after adding the buffer, however to a much higher extent in the TMP-NPs sample. Similar

trend was observed with polydispersity.
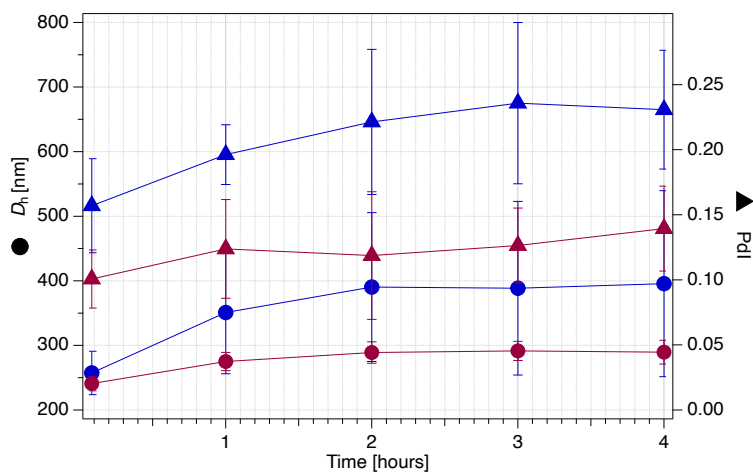
Figure 4.5 Change in hydrodynamic diameter (circles) and polydispersity (triangles) of TMP-NPs (blue) and SSL-NPs (red) in PBS buffer with time.

The difference in the sample behavior under physiological conditions might be explained by the drastic decrease in ζ-potential after diluting with PBS buffer. As shown in Table 4.4, the negative charge of the SSL-NPs has fallen to -7.4 while in case of the TMP-NPs it is almost neutral. Similar change was observed with the hemicellulose extracts.

Table 4.4 ζ-potential of TMP-NPs, SSL-NPs, as well as TMP and SSL extracts in PBS buffer.

Sample	ζ-potential $\pm$ SD [mV]
TMP-NPs	-0.9 ± 0.4
SSL-NPs	-7.4 ± 0.9
TMP	-1 ± 2
SSL	-6 ± 2

The internal structure of the nanoparticles in PBS buffer was evaluated with SAXS since the elevated ionic strength might have caused a change in the phase of the cubosomes as it has been previously reported in literature.[142,143] The scattering profiles (Figure 4.6) demonstrate that the SSL-NPs formulation has retained the internal structure as determined from the positions of the Bragg peaks. The peaks are, however, absent in the scattering curve of the TMP-NPs dispersion indicating that the internal structure has been disrupted. This suggests that stabilization of the cubic phase nanoparticles was mainly caused by the presence of the charged groups.
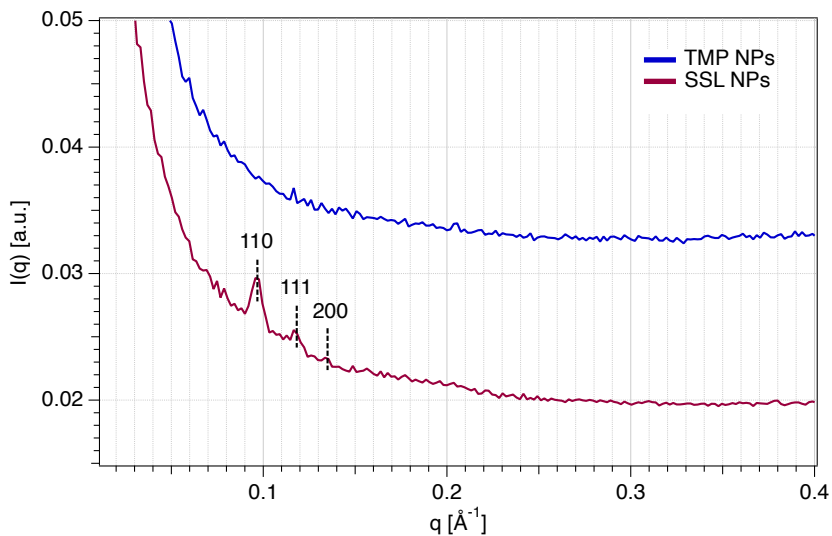
Figure 4.6 SAXS curves of TMP-NPs (dark blue) and SSL-NPs (red) in PBS buffer. Numbers indicate Miller indices. The scattering profile of the TMP-NPs was shifted upwards by a factor of 0.01 for clarity.

In addition, stability of the formulations in water was followed over 42 days time period. Figure 4.7 shows a summary of the results. Both of the dispersions are fairly stable over the whole period of time with an insignificant change in the apparent size and PdI. This only confirms that the TMP and SSL extracts are able to provide colloidal stability to monoolein cubosomes and prevent flocculation with time.
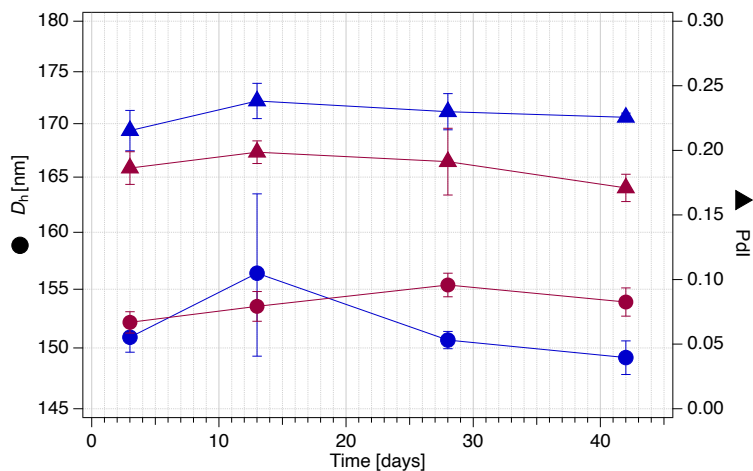
Figure 4.7 Change in hydrodynamic diameter (circles) and polydispersity (triangles) of TMP-NPs (blue) and SSL-NPs (red) with time.

4.2 Thermo-responsive glycopolymers based on *N*-isopropylacrylamide (NIPAm) and β-mannosyl acrylates

NIPAm polymers are widely known for their thermo-responsive behavior with the lower critical solution temperature (LCST) at ~32°C.[144] At this temperature, water becomes a poor solvent leading to a collapse of the polymer backbone. The LCST is sensitive to the molecular weight, as well as the nature and amount of the substituted groups. Introduction of hydrophilic groups in the poly(NIPAm) structure has been shown to lead to a shift in the LCST.[44,45,145]
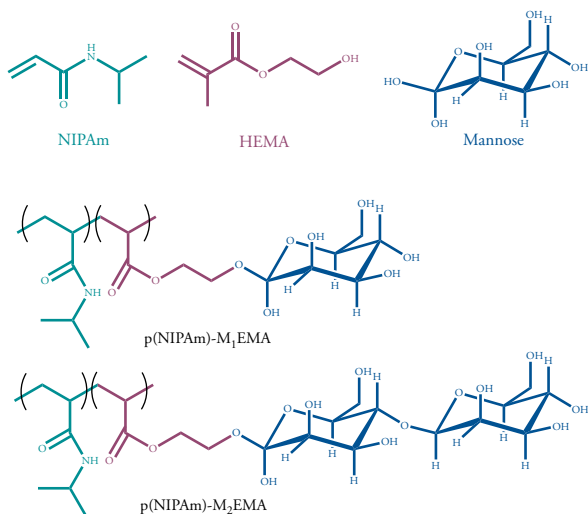
Figure 4.8 Main constituents and the expected molecular structure of the glycopolymers.

Here, the influence of β-mannosyl acrylate side groups (M_nEMA) on the thermo-responsive behavior of the poly(NIPAm) polymers was evaluated. Mainly the impact of two factors was studied: the amount of mannose units in the M_nEMA group (1 or 2) and the degree of substitution. The structure and morphology of the polymers with different amount of either M_1EMA or M_2EMA was compared at different temperatures (see Figure 4.8). Composition and designation of the samples characterised in this section is shown in Table 4.5.

Table 4.5 Polymer composition and designation of the synthesised glycopolymers.

Polymer type	Designation	M_nEMA [mol/mol]
Poly(NIPAM-*co*-M$_1$EMA)	P1M1	0.08
	P2M1	0.18
Poly(NIPAM-*co*-M$_2$EMA)	P1M2	0.03
	P2M2	0.16
	P3M2	0.18

4.2.1 Structure and morphology

Structure of the polymers was studied with SAXS at 25°C and 50°C. Figure 4.9 shows the scattering curves of Poly(NIPAM-*co*-M$_1$EMA) with different M$_1$ substitution degree at two temperatures.
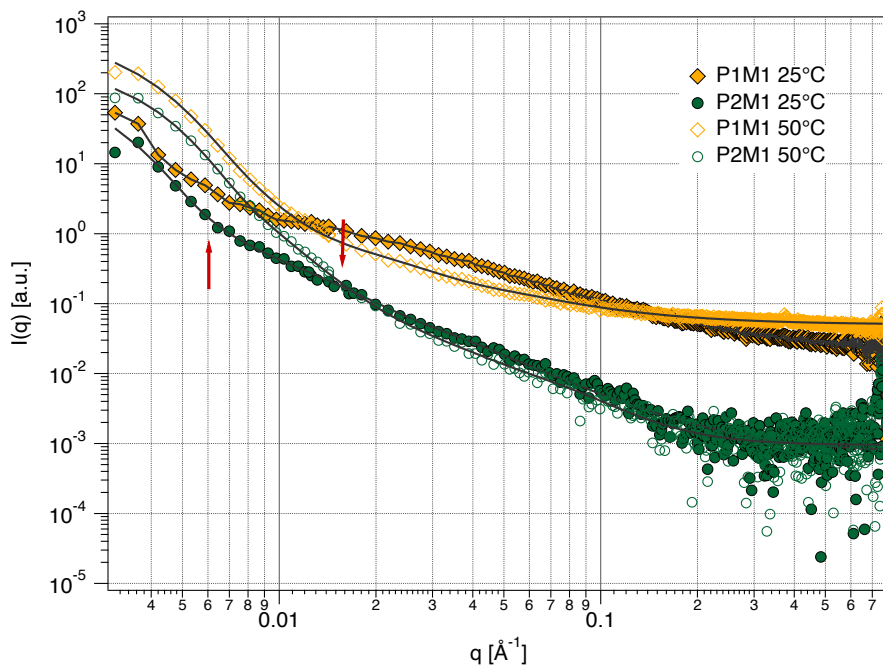
Figure 4.9 SAXS curves of P1M1 (yellow rhombus) and P2M1 (green circles) at the initial concentration at 25°C (filled symbols) and 50°C (empty symbols). Solid lines are fits to the corrected Beaucage model. Red arrows indicate a transition region.

The scattering behavior of the polymers at 25°C exhibits a change in the power-law decay through the extended q-range that results from a self-similarity in the morpho-

logy of the polymer.[146] This kind of behavior has already been observed with GGM samples described in Chapter 3 where the Beaucage model that describes fractal objects as a collection of small connected cylinders was used to fit the scattering curves of the polysaccharides.[88,147] The same model was used to fit the scattering profiles shown in this section.

The glycopolymers exhibit a similar scattering behavior at 50°C to that at 25°C but with higher d values at the transition from an intermediate- to a low-q range. The rapid increase in the intensity ($\sim q^{-4}$) is known as Porod behavior that describes compact objects with sharp interfaces indicating that polymers are collapsed; as expected for p(NIPAm) above the LCST.[148] Similar change in the power-law behavior with temperature has been previously reported for thermo-responsive triblock copolymers containing p(NIPAm) blocks.[149,150]

Along with the increase in the exponent, the transition region shifts to higher q values at 50°C for both polymers indicating a reduction in the size of a subunit or increase in flexibility of the polymer chain. Table 4.6 presents a summary of the results obtained by fitting M1 scattering curves to the Beaucage model. The radius of gyration at 25°C is 89 nm and 75 nm for P1M1 and P2M1, respectively. Despite the fact that R_g decreases with the increased amount of sugar substitution, the persistence length stays constant at 24 nm. This is surprising since bulky sugar side groups tend to render chain less flexible as we have previously observed with softwood hemicellulose and galactose side groups.[130] However, hydrogen bonding or hydrophobic interactions between sugar side groups might enforce a closer contact amongst the p(NIPAm) chains resulting in a more compact morphology. Above the LCST, both the overall size of the particle and the size of the subunit decrease which indicates a collapse of the whole structure.

Table 4.6 Parameters obtained from the fitting of P1M1 and P2M1 SAXS data at 25°C and 50°C to the corrected Beaucage model.

Model	Parameters	25°C		50°C	
		P1M1	P2M1	P1M1	P2M1
	R_g [nm]	89	75	57	55
	d	3.70	4.40	4.70	3.90
Fractal object	R_{sub} [nm]	14	14	8	5
	L_p [nm]	24	24	14	9
	d_{sub}	1.52	2.00	1.60	2.90

Figure 4.10 shows scattering curves of M2 with different di-mannose substitution degree at 25°C and 50°C. Di-mannose substituted glycopolymers have a similar scatter-

ing behavior to the one observed with M1. Therefore, even here the Beaucage model was applied to fit the data with the results are summarised in Table 4.7.
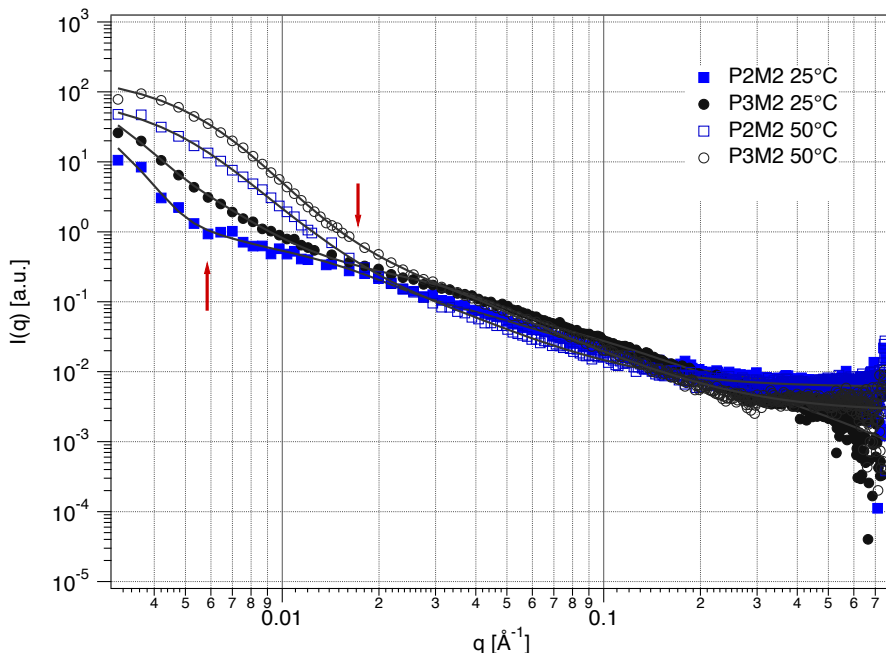
Figure 4.10 SAXS curves of the P2M2 (dark blue square) and P3M2 (black circles) at the initial concentration at 25°C (filled symbols) and 50°C (empty symbols). Solid lines are fits to the corrected Beaucage model and polymer micelle model. Red arrows indicate a transition region.

Based on the results presented in Table 4.7, the R_g and the persistence length of the glycoconjugates with M2 side groups decreases as the degree of substitution increases at 25°C. These observations are in agreement with the assumption that sugars facilitate a closer contact between the polymer chains due to attractive interactions. Similar to M_1EMA, both R_g and R_{sub} of the di-mannose-substitued polymer decrease significantly above LCST.

In addition to the Beaucage model, the scattering curves of M2 at 50°C have also been fitted with a polymer micelle model.[151] This type of model is often used for block copolymers that assemble into spherical particles with a dense core containing polymer head groups and a corona with Gaussian polymer tails.[152] Here, we assume that the core mainly consists of poly(NIPAm) with the SLD of 0.1×10^{-6} Å^{-2} and the corona is made of M2 groups with the SLD of 0.145×10^{-6} Å^{-2}. The results of the fits using the polymer micelle model are also included in Table 4.7. According to the fits from the polymer micelle model, the overall radius of the polymer particles

is 44 nm and 36 nm for P2M2 and P3M2, respectively. Furthermore, both the core and corona are smaller in micelles with a higher amount of di-mannose substitution.

Table 4.7 Parameters obtained from the fitting of P2M2 and P3M2 SAXS data at 25°C and 50°C to the corrected Beaucage model.

		25°C		50°C	
Model	Parameters	P2M2	P3M2	P2M2	P3M2
Fractal object	R_g [nm]	85	80	47	37
	d	3.30	3.20	4.65	3.42
	R_{sub} [nm]	12	5	8	3
	L_p [nm]	21	8	15	5
	d_{sub}	1.54	1.50	2.27	2.15
Polymer micelle	R core [nm]			16	14
	R_g corona [nm]			28	22
	N_{head}			30	41
	V_{head} [nm^3]			22	7
	V_{tail} [nm^3]			322	100

The morphology of the glycoconjugates P1M1 and P2M2 at 25°C and 50°C was studied with cryo-TEM. In addition, P2M2 was imaged at two different concentrations. Figure 4.11 shows cryo-TEM micrographs of the P1M1 glycoconjugate at 25°C and 50°C. The sample was diluted 10 times due to high viscosity.

(a) 25°C

(b) 50°C
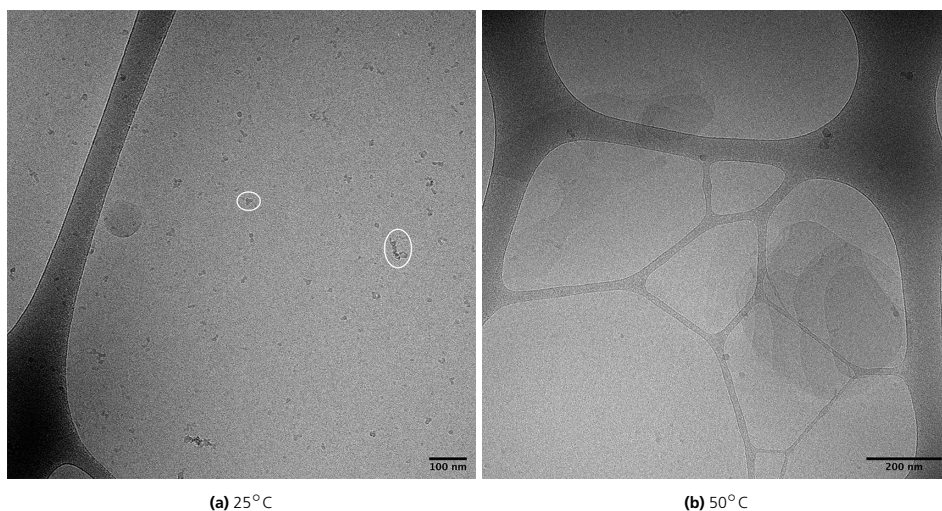
Figure 4.11 Cryo-TEM images of P1M1 at 10x dilution. The scale bar is 100 nm **(a)** and 200 nm **(b)**. Circles highlight pearl shaped aggregates and elongated pearl necklace-like aggregates.

At 25°C, small objects (20-40 nm in diameter) can be seen, where some of them are assembled into elongated structures that resemble pearl necklace type conformation about 80 nm long. These aggregates seem to rearrange and assemble into large irregular disc-like structures above the LCST, as can be seen in Figure 4.11 (b).

The micrographs of the di-mannose substituted copolymer at the initial and diluted concentration at 25°C are shown in Figure 4.12. Pearl-like aggregates that sometimes assemble into elongated structures observed previously with M1 are present even in this sample at both concentrations. However, a higher amount of the elongated particles and even fractal-like structures are seen at higher concentration.

(a)   (b)
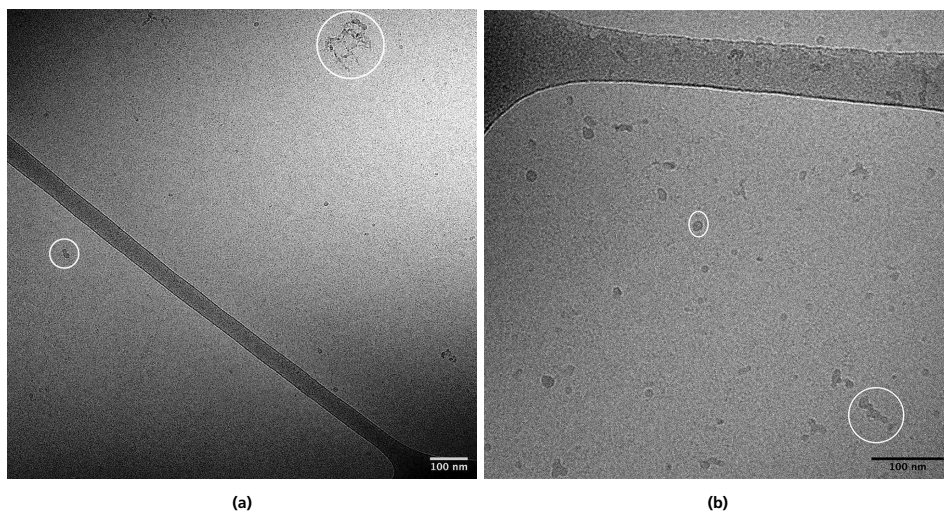
Figure 4.12 Cryo-TEM images of P2M2 at 25°C at the initial concentration **(a)** and 10x dilution **(b)**. The scale bar is 100 nm. Circles highlight pearl shaped aggregates, elongated pearl necklace-like aggregates and fractal-like structures.

Figure 4.13 shows the corresponding behavior of the M2 glycoconjugate at 50°C at two different concentrations. Here, the effect of the concentration is more pronounced than it was at 25°C. For the dilute sample, a large amount of globular aggregates (50-60 nm) are present. Interestingly, even fractal-like structures of similar dimensions can be found. At the initial concentration, however, the polymer is mostly assembled into fractal structures and to a lower extent into globular aggregates. This indicates that at high concentrations, the polymer chains experience crowding effects and self-assemble randomly into fractal aggregates. In the dilute regime, the self-assembly is more controlled and organised.
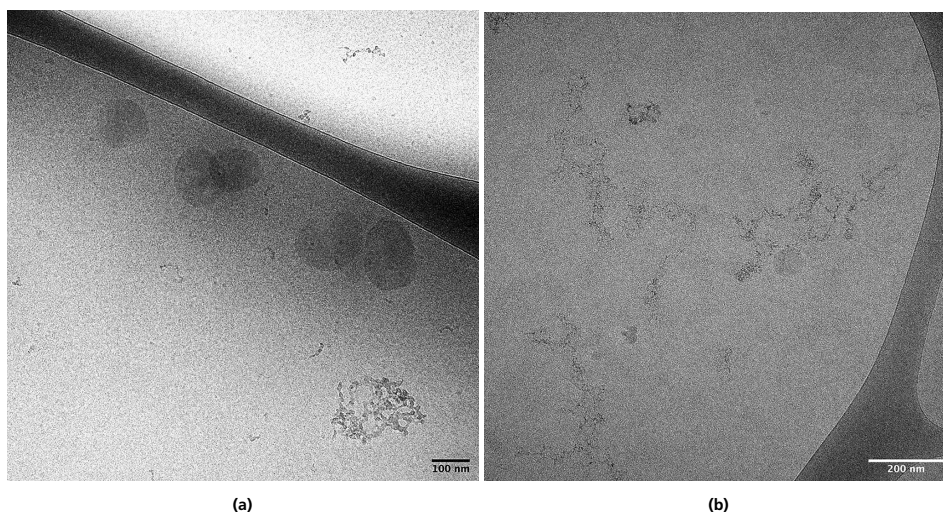
Figure 4.13 Cryo-TEM images of P2M2 at 50°C at 10x dilution **(a)** and at the initial concentration **(b)**. The scale bar is 100 nm **(a)** and 200 nm **(b)**.

4.2.2   Thermo-responsive behavior

The thermo-responsive behavior of the polymers was followed with DLS at temperatures from 25°C to 70°C. Figure 4.14 shows the change in hydrodynamic diameter of di-mannose substituted glycoconjugates and the reference copolymer poly(NIPAm)-HEMA. All of the glycoconjugates show a similar size transition pattern where the size is relatively stable below the LCST. Above the LCST, the hydrodynamic diameter increases sharply until it reaches a maxima followed by a slow decrease in size. This confirms the fact that, with increasing temperature, water becomes a poor solvent for the polymer leading to strong attractive interactions between the NIPAm chains. The collapsed polymers then aggregate into larger structures in order to prevent contact with water. As the temperature is increased even further, the D_{h} starts to decrease indicating that the pNIPAm chains continue contracting. This is confirmed by the SAXS fitting results that showed increased flexibility of the polymers at 50°C. The size of the copolymers stabilizes at around 60°C.
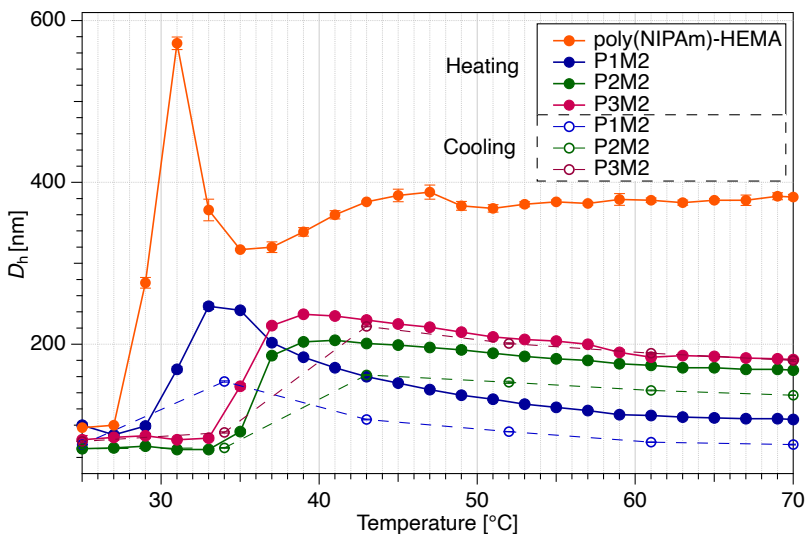
Figure 4.14 Change in D_h with temperature for M2 glycoconjugates and the reference copolymer poly(NIPAm)-HEMA. Heating and cooling process is represented by the curves with filled and empty symbols, respectively.

Among the M2-substituted polymers, P1M2 contracted the most after the maxima possibly due to the lower substitution degree. In fact, P1M2 has the lowest LCST but still slightly higher than that of p(NIPAm)-HEMA confirming the stabilizing effect of the hydrophilic sugars. As the degree of substitution of the M2 glycoconjugates increases, so does the LCST. This increase in transition temperatures has been previously reported for p(NIPAm)-based copolymers with high mannose content. [43]

Figure 4.15 shows the change in D_h of M1 glycoconjugates with temperature. Here, a similar transition pattern to M2 was observed with the exception of P1M1 after 60°C. In this region, the size of the P1M1 increases sharply again, the polymer aggregates become unstable and falls out of the solution. Because the degree of substitution of P1M1 is less than half the degree of P2M1, there may not be sufficient M1EMA to create a protective hydrophilic corona necessary to stabilize the particle.
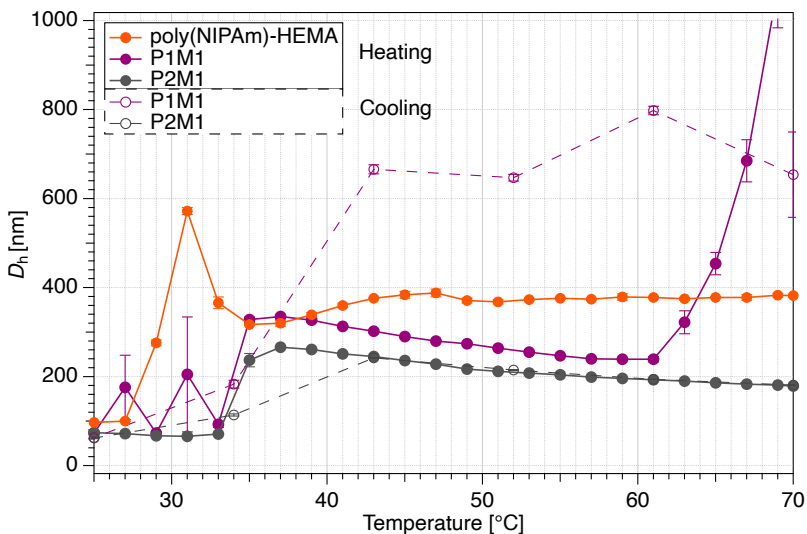
Figure 4.15 Change in D_h M1 glycoconjugates and the reference material poly(NIPAm)-HEMA with temperature. Heating and cooling is represented by filled and empty symbols, respectively.

4.3 Surface active properties of alkyl mannooligosides

β-mannanases were utilized to first produce oligomannans from Locust bean gum and then catalyze transglycosylation with mannotetraose (M_4) as a donor and 1-hexanol as a glycosyl acceptor. A more detailed description of the synthesis can be found in Paper v. The purified mixture contained 1.3 mg of hexyl-mannobiose (hexyl-M_2) and 1.1 mg of hexyl-mannotriose (hexyl-M_3).

Surface tension at different concentrations of the surfactant mixture was determined using pendant drop technique. Due to a limited amount of the sample, the same solution was reused for all of the measurements. Surface tension was recorded for the sample with the highest concentration which was then diluted to obtain a following concentrations. Sample was freeze-dried in between if it was necessary.

In order to estimate critical micelle concentration (CMC), a plot with a surface tension as a function of the surfactant concentration was constructed. As it can be seen from Figure 4.16, there are two inflection points in the curve, at 44 g L^{-1} and 72 g L^{-1}, suggesting that two different types of micelles are formed in the solution. This phenomenon has been previously observed with mixtures containing alkyl polyglucosides with different chain lengths.[153] The minimum around the first break point is caused by the solubilization of the less hydrophobic surfactant in the

micelles when they begin to form leading to the decrease in bulk concentration and thus, decrease in the surface tension of the solution. [154]
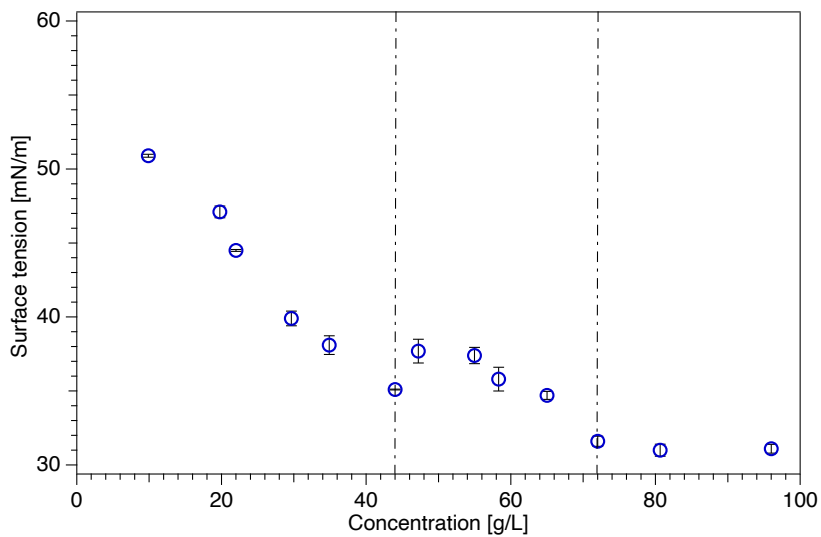
Figure 4.16 Surface tension plot of the purified hexyl mannooligoside mixture. Dash lines represent break points.

5 Epilogue

In this thesis, the structure and behaviour of hemicellulose in solution and at interfaces was investigated with the focus on softwood hemicellulose. The potential of hemicellulose as a raw material for the preparation of several complex materials with an added value was explored.

In the first part, the properties of hemicellulose in solution and their influence on the binding efficiency of hemicellulose to cellulose surfaces was evaluated. A special attention was devoted to the nature of the interaction between hemicellulose and cellulose model surfaces. As it has been mentioned before, both of the polysaccharides occur in plant cell walls forming a strong and functional network. The mechanism behind the formation, although studied thoroughly, is not yet fully understood.

The binding of hemicellulose to cellulose surfaces is believed to partly happen via hydrogen bonding and through an entropy-driven process. Cellulose fibrils form a porous network on a surface which entraps a significant amount of water molecules in solution. Due to more favourable hemicellulose-cellulose interactions than water-cellulose, hemicellulose molecules adsorb to the cellulose surface, thereby releasing water molecules. In addition, sugars (especially, cellulose) are known to have a certain degree of hydrophobicity. The adsorption studies of different kinds of hemicellulose to hydrophobic surfaces have confirmed that hemicellulose polysaccharides posses a hydrophobic character. The presence of the acetyl side groups results in an elevated hydrophobic properties of GGMs as compared to GMs and thus a higher adsorbed amount on the hydrophobized silica surface. Neutron reflectometry measurements revealed that hemicellulose chains orient themselves with the acetyl groups towards the hydrophobic surface.

Hemicelluloses are branched polymers that tend to aggregate in solution. The high galactose substitution degree reduces the flexibility of the polymer chains

leading to a formation of bulky and highly solvated layers on a surface.

The adsorption of hemicellulose samples is higher on the cellulose surface compared to the hydrophobic silica indicating that specific interactions are involved facilitated by the similarity in the backbone structure of the two polysaccharides. The results showed that the adsorption of hemicellulose samples to cellulose surfaces is concentration dependant. In the low concentration regime, hemicellulose molecules with a higher molecular weight adsorb to a higher extent since the adsorption of smaller molecules is less favourable due to the loss in the translational entropy of these species. The opposite happens in the high concentration regime, where the decrease in the conformational entropy prevents larger hemicelluloses from adsorbing to the surface. In addition, smaller and more flexible molecules are able to diffuse inside the cellulose layer much easier leading to a higher adsorbed amount.

In the second part of the thesis, the properties of hemicellulose-based LLC nanoparticles, thermo-responsive glycopolymers and alkyl glycosides were evaluated.

Monoolein cubic phase nanoparticles were successfully stabilized with softwood hemicellulose (TMP and SSL) resulting in the monodispersed formulations with Pn3m phase cubosomes. The highest amount of the dispersed phase was obtained using hemicellulose extract containing a higher content of lignin (SSL) indicating that the presence of lignin facilitates the stabilizing effect due to its hydrophobic properties. The hemicellulose-stabilized dispersions were electrostatically stable in milli-Q water, however, the negative charge has dropped significantly in physiological conditions leading to the loss of the internal structure in the TMP-stabilized particles. The Pn3m phase structure was retained in the SSL-stabilized formulation despite the increase in the size of particles which demonstrates a better applicability of this preparation as a drug delivery system. Both dispersions were stable over the period of 42 days in terms of hydrodynamic size and polydispersity.

The introduction of β-mannosyl acrylate side groups in the structure of thermo-responsive p(NIPAm) copolymers caused the shift in the transition temperature to higher values. Hydrophilic side groups are believed to create a protective shell which provides the stabilizing effect for the hydrophobic backbone. This was confirmed by the presence of stable particles above the LCST with no precipitation up to 70°C (except for P1M1 samples).

Mannan branches enforce a closer contact between the glycopolymer chains due attractive interactions among sugars rendering the chain more flexible and the particle more compact. Glycopolymers aggregate into small globular objects

(20-40 nm) and some even assemble into elongated pearl necklace type structures at room temperature. Above the LCST, the particles rapidly contract and aggregate similarly to unsubstituted p(NIPAm) due to the unfavourable interactions with water at higher temperatures. Interestingly, the size of the copolymer particles reaches a certain maximum followed by a gradual decrease suggesting that the polymers continue to collapse as the temperature increases until the equilibrium is reached at around 60°C.

The self-assembly of the glycopolymers above the LCST is the concentration dependant process. In the low concentration regime, copolymers mainly assemble into globular disc-shaped aggregates. At high concentration, due to the crowding effect, the aggregation is more random and sharp where polymers assemble into fractal-like structures.

Finally, the third type of hemicellulose-based conjugates studied in this thesis was hexyl mannooligosides. Surface tension measurements of the mixture containing hexyl-mannobiose and hexyl-mannotriose demonstrated that glycosides possesed surface active properties and assembled into two separate types of micelles as indicated by the two inflection points in the surface tension curve.

Hemicellulose is a great material that can be utilized as versatile building blocks tailored according to the potential applications. The results summarized in this thesis demonstrate that hemicellulose can be used in the preparation of drug delivery systems. However, there are still few factors that should be considered. In order to use hemicellulose-based nanoparticles for drug delivery, the ability of the particles to encapsulate and release drugs should be tested with both hydrophilic and hydrophobic drugs. If the encapsulation is successful, it would be important to evaluate the cytotoxicity of the formulations. A specific binding of the sugars present in the structure of the nanoparticles and glycopolymers is an interesting aspect that should be evaluated.

In addition, the question about intriguing interactions between hemicellulose and cellulose has many directions to follow. The hemicellulose samples with different molecular weights and substitution degree were studied in this thesis. However, the variety in the structural properties of these samples to made it challenging to determine which factor affected the adsorption the most. It would be interesting to evaluate adsorption of the same kind of hemicellulose but modified to either gradually decrease the number of side groups or molecular weight. The thickness of the cellulose layer is an important factor that could be studied more, especially with neutron reflectometry to track how hemicellulose is distributed inside the layer.

Both the ordinary and deuterated cellulose were used in this thesis to prepare films in separate studies, however the effect of the deuteration degree on the adsorption of hemicellulose has not been followed explicitly.

References

[1] Höfte, H.; Voxeur, A. Plant Cell Walls. *Current Biology* **2017**, *27*, R865–R870.

[2] Scheller, H. V.; Ulvskov, P. Hemicelluloses. *Annual Review of Plant Biology* **2010**, *61*, 263–289.

[3] Ebringerová, A.; Hromádková, Z.; Heinze, T. In *Polysaccharides I: Structure, Characterization and Use*; Heinze, T., Ed.; Springer Berlin Heidelberg: Berlin, Heidelberg, 2005; pp 1–67.

[4] Ek, M.; Gellerstedt, G.; Henriksson, G. *Wood Chemistry and Biotechnology*; Walter de Gruyter, 2009.

[5] Sjostrom, E. *Wood Chemistry: Fundamentals and Applications*; Gulf Professional Publishing, 1993.

[6] Timell, T. E. Recent Progress in the Chemistry of Wood Hemicelluloses. *Wood Sci. Technol.* **1967**, *1*, 45–70.

[7] Lundqvist, J.; Jacobs, A.; Palm, M.; Zacchi, G.; Dahlman, O.; Stålbrand, H. Characterization of Galactoglucomannan Extracted from Spruce (Picea Abies) by Heat-Fractionation at Different Conditions. *Carbohydrate Polymers* **2003/02/01/**, *51*, 203–211.

[8] Lucia, L. A., Rojas, O. J., Eds. *The Nanoscience and Technology of Renewable Biomaterials*; John Wiley & Sons, Ltd: Chichester, UK, 2009.

[9] Hannuksela, T.; Holmbom, B.; Lachenal, D. Effect of Sorbed Galactoglucomannans and Galactomannans on Pulp and Paper Handsheet Properties, Especially Strength Properties. *Nordic Pulp & Paper Research Journal* **2004**, *19*, 237–244.

[10] Eronen, P.; Junka, K.; Laine, J.; Österberg, M. Interaction between Water Soluble Polysaccharides and Native Nanofibrillar Cellulose Thin Films. *BioResources* **2011**, *6*, 4200–4217.

[11] Hannuksela, T.; Tenkanen, M.; Holmbom, B. Sorption of Dissolved Galactoglucomannans and Galactomannans to Bleached Kraft Pulp. *Cellulose* **2002**, *9*, 251–261.

[12] Hannuksela, T.; Fardim, P.; Holmbom, B. Sorption of Spruce O-Acetylated Galactoglucomannans onto Different Pulp Fibres. *Cellulose* **2003**, *10*, 317–324.

[13] Eronen, P.; Österberg, M.; Heikkinen, S.; Tenkanen, M.; Laine, J. Interactions of Structurally Different Hemicelluloses with Nanofibrillar Cellulose. *Carbohydrate Polymers* **2011**, *86*, 1281–1290.

[14] Karaaslan, M. A.; Tshabalala, M. A.; Yelle, D. J.; Buschle-Diller, G. Nanoreinforced Biocompatible Hydrogels from Wood Hemicelluloses and Cellulose Whiskers. *Carbohydrate Polymers* **2011**, *86*, 192–201.

[15] Liu, J.; Chinga-Carrasco, G.; Cheng, F.; Xu, W.; Willför, S.; Syverud, K.; Xu, C. Hemicellulose-Reinforced Nanocellulose Hydrogels for Wound Healing Application. *Cellulose* **2016**, *23*, 3129–3143.

[16] Berglund, J.; Mikkelsen, D.; Flanagan, B. M.; Dhital, S.; Gaunitz, S.; Henriksson, G.; Lindström, M. E.; Yakubov, G. E.; Gidley, M. J.; Vilaplana, F. Wood Hemicelluloses Exert Distinct Biomechanical Contributions to Cellulose Fibrillar Networks. *Nature Communications* **2020**, *11*, 4692.

[17] Lucenius, J.; Parikka, K.; Österberg, M. Nanocomposite Films Based on Cellulose Nanofibrils and Water-Soluble Polysaccharides. *Reactive and Functional Polymers* **2014**, *85*, 167–174.

[18] Lucenius, J.; Valle-Delgado, J. J.; Parikka, K.; Österberg, M. Understanding Hemicellulose-Cellulose Interactions in Cellulose Nanofibril-Based Composites. *Journal of Colloid and Interface Science* **2019**, *555*, 104–114.

[19] Lopez-Sanchez, P.; Schuster, E.; Wang, D.; J. Gidley, M.; Strom, A. Diffusion of Macromolecules in Self-Assembled Cellulose/Hemicellulose Hydrogels. *Soft Matter* **2015**, *11*, 4002–4010.

[20] Oinonen, P.; Krawczyk, H.; Ek, M.; Henriksson, G.; Moriana, R. Bioinspired Composites from Cross-Linked Galactoglucomannan and Microfibrillated Cellulose: Thermal, Mechanical and Oxygen Barrier Properties. *Carbohydrate Polymers* **2016**, *136*, 146–153.

[21] Al-Rudainy, B.; Galbe, M.; Arcos Hernandez, M.; Jannasch, P.; Wallberg, O. Impact of Lignin Content on the Properties of Hemicellulose Hydrogels. *Polymers* **2019**, *11*, 35.

[22] Roos, A. A.; Edlund, U.; Sjöberg, J.; Albertsson, A.-C.; Stålbrand, H. Protein Release from Galactoglucomannan Hydrogels: Influence of Substitutions and Enzymatic Hydrolysis by β-Mannanase. *Biomacromolecules* **2008**, *9*, 2104–2110.

[23] Lindblad, M. S.; Ranucci, E.; Albertsson, A.-C. Biodegradable Polymers from Renewable Sources. New Hemicellulose-Based Hydrogels. *Macromolecular Rapid Communications* **2001**, *22*, 962–967.

[24] Zhao, W.; Odelius, K.; Edlund, U.; Zhao, C.; Albertsson, A.-C. In Situ Synthesis of Magnetic Field-Responsive Hemicellulose Hydrogels for Drug Delivery. *Biomacromolecules* **2015**, *16*, 2522–2528.

[25] Gao, C.; Ren, J.; Zhao, C.; Kong, W.; Dai, Q.; Chen, Q.; Liu, C.; Sun, R. Xylan-Based Temperature/pH Sensitive Hydrogels for Drug Controlled Release. *Carbohydrate Polymers* **2016**, *151*, 189–197.

[26] Edlund, U.; Albertsson, A.-C. A Microspheric System: Hemicellulose-Based Hydrogels. *Journal of Bioactive and Compatible Polymers* **2008**, *23*, 171–186.

[27] Israelachvili, J. N.; Mitchell, D. J.; Ninham, B. W. Theory of Self-Assembly of Hydrocarbon Amphiphiles into Micelles and Bilayers. *J. Chem. Soc., Faraday Trans. 2* **1976**, *72*, 1525–1568.

[28] Hill, K.; Rhode, O. Sugar-Based Surfactants for Consumer Products and Technical Applications. *Lipid / Fett* **1999**, *101*, 25–33.

[29] Bouxin, F.; Marinkovic, S.; Bras, J. L.; Estrine, B. Direct Conversion of Xylan into Alkyl Pentosides. *Carbohydrate Research* **2010**, *345*, 2469–2473.

[30] Ludot, C.; Estrine, B.; Hoffmann, N.; Bras, J. L.; Marinkovic, S.; Muzart, J. Manufacture of Decyl Pentosides Surfactants by Wood Hemicelluloses Transglycosidation: A Potential Pretreatment Process for Wood Biomass Valorization. *Industrial Crops and Products* **2014**, *58*, 335–339.

[31] Seguin, A.; Marinkovic, S.; Estrine, B. New Pretreatment of Wheat Straw and Bran in Hexadecanol for the Combined Production of Emulsifying Base, Glucose and Lignin Material. *Carbohydrate Polymers* **2012**, *88*, 657–662.

[32] Morrill, J.; Manberger, A.; Rosengren, A.; Naidjonoka, P.; von Freiesleben, P.; Krogh, K.; Bergquist, K. E.; Nylander, T.; Karlsson, E. N.; Adlercreutz, P.; Stalbrand, H. Beta-Mannanase-Catalyzed Synthesis of Alkyl Mannooligosides.

[33] Kulkarni, C. V.; Wachter, W.; Iglesias-Salto, G.; Engelskirchen, S.; Ahualli, S. Monoolein: A Magic Lipid? *Phys. Chem. Chem. Phys.* **2011**, *13*, 3004–3021.

[34] Nakano, M.; Sugita, A.; Matsuoka, H.; Handa, T. Small-Angle X-Ray Scattering and 13C NMR Investigation on the Internal Structure of "Cubosomes". *Langmuir* **2001**, *17*, 3917–3922.

[35] Valoppi, F.; H. Lahtinen, M.; Bhattarai, M.; J. Kirjoranta, S.; K. Juntti, V.; J. Peltonen, L.; O. Kilpeläinen, P.; S. Mikkonen, K. Centrifugal Fractionation of Softwood Extracts Improves the Biorefinery Workflow and Yields Functional Emulsifiers. *Green Chemistry* **2019**, *21*, 4691–4705.

[36] Lahtinen, M. H.; Valoppi, F.; Juntti, V.; Heikkinen, S.; Kilpeläinen, P. O.; Maina, N. H.; Mikkonen, K. S. Lignin-Rich PHWE Hemicellulose Extracts Responsible for Extended Emulsion Stabilization. *Front. Chem.* **2019**, *7*.

[37] Mikkonen, K. S.; Tenkanen, M.; Cooke, P.; Xu, C.; Rita, H.; Willför, S.; Holmbom, B.; Hicks, K. B.; Yadav, M. P. Mannans as Stabilizers of Oil-in-Water Beverage Emulsions. *LWT - Food Science and Technology* **2009**, *42*, 849–855.

[38] Mikkonen, K. S.; Xu, C.; Berton-Carabin, C.; Schroën, K. Spruce Galactoglucomannans in Rapeseed Oil-in-Water Emulsions: Efficient Stabilization Performance and Structural Partitioning. *Food Hydrocolloids* **2016**, *52*, 615–624.

[39] Lehtonen, M.; Merinen, M.; Kilpeläinen, P. O.; Xu, C.; Willför, S. M.; Mikkonen, K. S. Phenolic Residues in Spruce Galactoglucomannans Improve Stabilization of Oil-in-Water Emulsions. *Journal of Colloid and Interface Science* **2018**, *512*, 536–547.

[40] Uyama, M.; Nakano, M.; Yamashita, J.; Handa, T. Useful Modified Cellulose Polymers as New Emulsifiers of Cubosomes. *Langmuir* **2009**, *25*, 4336–4338.

[41] Almgren, M.; Borné, J.; Feitosa, E.; Khan, A.; Lindman, B. Dispersed Lipid Liquid Crystalline Phases Stabilized by a Hydrophobically Modified Cellulose. *Langmuir* **2007**, *23*, 2768–2777.

[42] Spicer, P. T.; Small, W. B.; Small, W. B.; Lynch, M. L.; Burns, J. L. Dry Powder Precursors of Cubic Liquid Crystalline Nanoparticles (Cubosomes). *Journal of Nanoparticle Research* **2002**, *4*, 297–311.

[43] Paul, T. J.; Strzelczyk, A. K.; Feldhof, M. I.; Schmidt, S. Temperature-Switchable Glycopolymers and Their Conformation-Dependent Binding to Receptor Targets. *Biomacromolecules* **2020**, *21*, 2913–2921.

[44] Quan, J.; Shen, F.-W.; Cai, H.; Zhang, Y.-N.; Wu, H. Galactose-Functionalized Double-Hydrophilic Block Glycopolymers and Their Thermoresponsive Self-Assembly Dynamics. *Langmuir* **2018**, *34*, 10721–10731.

[45] Zhang, Q.; Wilson, P.; Anastasaki, A.; McHale, R.; Haddleton, D. M. Synthesis and Aggregation of Double Hydrophilic Diblock Glycopolymers via Aqueous SET-LRP. *ACS Macro Lett.* **2014**, *3*, 491–495.

[46] Chen, Z.; Boyd, S. D.; Calvo, J. S.; Murray, K. W.; Mejia, G. L.; Benjamin, C. E.; Welch, R. P.; Winkler, D. D.; Meloni, G.; D'Arcy, S.; Gassensmith, J. J. Fluorescent Functionalization across Quaternary Structure in a Virus-like Particle. *Bioconjugate Chem.* **2017**, *28*, 2277–2283.

[47] Rosengren, A.; J. Butler, S.; Arcos-Hernandez, M.; Bergquist, K.-E.; Jannasch, P.; Stålbrand, H. Enzymatic Synthesis and Polymerisation of β-Mannosyl Acrylates Produced from Renewable Hemicellulosic Glycans. *Green Chemistry* **2019**, *21*, 2104–2118.

[48] Landgren, M.; Jönsson, B. Determination of the Optical Properties of Si/SiO2 Surfaces by Means of Ellipsometry, Using Different Ambient Media. *Journal of Physical Chemistry* **1993**, *97*, 1656–1660.

[49] Azzam, R. M. A.; Bashara, N. M.; Ballard, S. S. Ellipsometry and Polarized Light. *Physics Today* **1978**, *31*, 72.

[50] Jenkins, T. E. Multiple-Angle-of-Incidence Ellipsometry. *J. Phys. D: Appl. Phys.* **1999**, *32*, R45–R56.

[51] Tompkins, H.; Irene, E. A. *Handbook of Ellipsometry*; William Andrew, 2005.

[52] Robinson, G.; Ross-Murphy, S. B.; Morris, E. R. Viscosity-Molecular Weight Relationships, Intrinsic Chain Flexibility, and Dynamic Solution Properties of Guar Galactomannan. *Carbohydrate Research* **1982/09/01/**, *107*, 17–32.

[53] Xu, C.; Pranovich, A.; Vähäsalo, L.; Hemming, J.; Holmbom, B.; Schols, H. A.; Willför, S. Kinetics of Acid Hydrolysis of Water-Soluble Spruce O-Acetyl Galactoglucomannans. *Journal of Agricultural and Food Chemistry* **2008**, *56*, 2429–2435.

[54] Ono, Y.; Ishida, T.; Soeta, H.; Saito, T.; Isogai, A. Reliable Dn/Dc Values of Cellulose, Chitin, and Cellulose Triacetate Dissolved in LiCl/N,N-Dimethylacetamide for Molecular Mass Analysis. *Biomacromolecules* **2016**, *17*, 192–199.

[55] Penfold, J.; Thomas, R. K. The Application of the Specular Reflection of Neutrons to the Study of Surfaces and Interfaces. *J. Phys.: Condens. Matter* **1990**, *2*, 1369–1412.

[56] Zhou, X.-L.; Chen, S.-H. Theoretical Foundation of X-Ray and Neutron Reflectometry. *Physics Reports* **1995**, *257*, 223–348.

[57] Nelson, A. Co-Refinement of Multiple-Contrast Neutron/X-Ray Reflectivity Data Using MOTOFIT. *Journal of Applied Crystallography* **2006**, *39*, 273–276.

[58] Nelson, A. Motofit– Integrating Neutron Reflectometry Acquisition, Reduction and Analysis into One, Easy to Use, Package. *J. Phys.: Conf. Ser.* **2010**, *251*, 012094.

[59] Abelès, F. Sur la propagation des ondes dans les milieux stratifiés. *Nuovo Cim* **2008**, *9*, 214.

[60] Höök, F.; Kasemo, B. In *Piezoelectric Sensors*; Janshoff, A., Steinem, C., Eds.; Springer Series on Chemical Sensors and Biosensors; Springer: Berlin, Heidelberg, 2007; pp 425–447.

[61] Sauerbrey, G. The Use of Quarts Oscillators for Weighing Thin Layers and for Microweighing. *Z. Phys.* **1959**, *155*, 206–222.

[62] Voinova, M. V.; Rodahl, M.; Jonson, M.; Kasemo, B. Viscoelastic Acoustic Response of Layered Polymer Films at Fluid-Solid Interfaces: Continuum Mechanics Approach. *Physica Scripta* **1999**, *59*, 391.

[63] Binnig, G.; Quate, C. F.; Gerber, C. Atomic Force Microscope. *Phys. Rev. Lett.* **1986**, *56*, 930–933.

[64] Dufrêne, Y. F.; Ando, T.; Garcia, R.; Alsteens, D.; Martinez-Martin, D.; Engel, A.; Gerber, C.; Müller, D. J. Imaging Modes of Atomic Force Microscopy for Application in Molecular and Cell Biology. *Nature Nanotechnology* **2017**, *12*, 295–307.

[65] Haugstad, G. *Atomic Force Microscopy: Understanding Basic Modes and Advanced Applications*; John Wiley & Sons, 2012.

[66] McIntire, T. M.; Brant, D. A. Imaging of Individual Biopolymers and Supramolecular Assemblies Using Noncontact Atomic Force Microscopy. *Biopolymers* **1997**, *42*, 133–146.

[67] Ismail, A. A.; van de Voort, F. R.; Sedman, J. *Techniques and Instrumentation in Analytical Chemistry*; Elsevier, 1997; Vol. 18; pp 93–139.

[68] Ramer, G.; Lendl, B. *Encyclopedia of Analytical Chemistry*; American Cancer Society, 2013.

[69] Leboucher, J.; Bazin, P.; Goux, D.; El Siblani, H.; Travert, A.; Barbulée, A.; Bréard, J.; Duchemin, B. High-Yield Cellulose Hydrolysis by HCl Vapor: Co-Crystallization, Deuterium Accessibility and High-Temperature Thermal Stability. *Cellulose* **2020**, *27*, 3085–3105.

[70] Horikawa, Y.; Clair, B.; Sugiyama, J. Varietal Difference in Cellulose Microfibril Dimensions Observed by Infrared Spectroscopy. *Cellulose* **2009**, *16*, 1–8.

[71] Thybring, E. E.; Thygesen, L. G.; Burgert, I. Hydroxyl Accessibility in Wood Cell Walls as Affected by Drying and Re-Wetting Procedures. *Cellulose* **2017**, *24*, 2375–2384.

[72] Zemb, T.; Lindner, P. *Neutron, X-Rays and Light. Scattering Methods Applied to Soft Condensed Matter*; NORTH HOLLAND, 2002.

[73] Jeu, W. H. D. *Basic X-Ray Scattering for Soft Matter*, illustrated edition ed.; Oxford University Press: Oxford, 2016.

[74] Skoog, D. A.; Holler, F. J.; Crouch, S. R. *Principles of Instrumental Analysis*; Cengage Learning, 2017.

[75] Kulkarni, C. V.; Tomšič, M.; Glatter, O. Immobilization of Nanostructured Lipid Particles in Polysaccharide Films. *Langmuir* **2011**, *27*, 9541–9550.

[76] Schätzel, K. Correlation Techniques in Dynamic Light Scattering. *Appl. Phys. B* **1987**, *42*, 193–213.

[77] Koppel, D. E. Analysis of Macromolecular Polydispersity in Intensity Correlation Spectroscopy: The Method of Cumulants. *J. Chem. Phys.* **1972**, *57*, 4814–4820.

[78] Adrian, M.; Dubochet, J.; Lepault, J.; McDowall, A. W. Cryo-Electron Microscopy of Viruses. *Nature* **1984**, *308*, 32–36.

[79] Kuntsche, J.; Horst, J. C.; Bunjes, H. Cryogenic Transmission Electron Microscopy (Cryo-TEM) for Studying the Morphology of Colloidal Drug Delivery Systems. *International Journal of Pharmaceutics* **2011**, *417*, 120–137.

[80] Bhella, D. Cryo-Electron Microscopy: An Introduction to the Technique, and Considerations When Working to Establish a National Facility. *Biophys Rev* **2019**, *11*, 515–519.

[81] Williams, D. B.; Carter, C. B. *Transmission Electron Microscopy: A Textbook for Materials Science*, 2nd ed.; Springer US, 2009.

[82] Berry, J. D.; Neeson, M. J.; Dagastine, R. R.; Chan, D. Y. C.; Tabor, R. F. Measurement of Surface and Interfacial Tension Using Pendant Drop Tensiometry. *Journal of Colloid and Interface Science* **2015**, *454*, 226–237.

[83] Javadi, A.; Mucic, N.; Karbaschi, M.; Won, J.; Lotfi, M.; Dan, A.; Ulaganathan, V.; Gochev, G.; Makievski, A.; Kovalchuk, V.; Kovalchuk, N.; Krägel, J.; Miller, R. Characterization Methods for Liquid Interfacial Layers. *Eur. Phys. J. Spec. Top.* **2013**, *222*, 7–29.

[84] Kishani, S.; Vilaplana, F.; Xu, W.; Xu, C.; Wågberg, L. Solubility of Softwood Hemicelluloses. *Biomacromolecules* **2018**, *19*, 1245–1255.

[85] Picout, D. R.; Ross-Murphy, S. B.; Errington, N.; Harding, S. E. Pressure Cell Assisted Solution Characterization of Polysaccharides. 1. Guar Gum. *Biomacromolecules* **2001**, *2*, 1301–1309.

[86] Picout, D. R.; Ross-Murphy, S. B.; Jumel, K.; Harding, S. E. Pressure Cell Assisted Solution Characterization of Polysaccharides. 2. Locust Bean Gum and Tara Gum. *Biomacromolecules* **2002**, *3*, 761–767.

[87] Burchard, W. Static and Dynamic Light Scattering Approaches to Structure Determination of Biopolymers. *Laser light scattering in biochemistry* **1992**, 3–22.

[88] Hammouda, B. Analysis of the Beaucage Model. *J Appl Cryst* **2010**, *43*, 1474–1478.

[89] Beaucage, G. Small-Angle Scattering from Polymeric Mass Fractals of Arbitrary Mass-Fractal Dimension. *Journal of Applied Crystallography* **1996**, *29*, 134–146.

[90] Mansel, B.; Chu, C.-Y.; Leis, A.; Chen, H.-L.; Lundin, L.; Williams, M. Zooming In: Structural Investigations of Rheologically Characterized Hydrogen-Bonded Low-Methoxyl Pectin Networks. *Biomacromolecules* **2015**, *16*.

[91] Nakamura, Y.; Norisuye, T. Backbone Stiffness of Comb-Branched Polymers. *Polymer Journal* **2001**, *33*, 874–878.

[92] Gidley, M. J.; Lillford, P. J.; Rowlands, D. W.; Lang, P.; Dentini, M.; Crescenzi, V.; Edwards, M.; Fanutti, C.; Grant Reid, J. Structure and Solution Properties of Tamarind-Seed Polysaccharide. *Carbohydrate Research* **1991**, *214*, 299–314.

[93] Eriksson, J.; Malmsten, M.; Tiberg, F.; Callisen, T. H.; Damhus, T.; Johansen, K. S. Enzymatic Degradation of Model Cellulose Films. *Journal of Colloid and Interface Science* **2005**, *284*, 99–106.

[94] Eriksson, M.; Notley, S. M.; Wågberg, L. Cellulose Thin Films: Degree of Cellulose Ordering and Its Influence on Adhesion. *Biomacromolecules* **2007**, *8*, 912–919.

[95] Aulin, C.; Ahola, S.; Josefsson, P.; Nishino, T.; Hirose, Y.; Österberg, M.; Wågberg, L. Nanoscale Cellulose Films with Different Crystallinities and Mesostructures—Their Surface Properties and Interaction with Water. *Langmuir* **2009**, *25*, 7675–7685.

[96] Knill, C.; Kennedy, J. Polymer Handbook (4th Edition): J. Brandrup, E.H. Immergut, E.A. Grulke (Eds.); Wiley, New York, 1999. *Carbohydrate Polymers* **2001**, *46*, 295.

[97] Janado, M.; Yano, Y. Hydrophobic Nature of Sugars as Evidenced by Their Differential Affinity for Polystyrene Gel in Aqueous Media. *Journal of Solution Chemistry* **1985**, *14*, 891–902.

[98] Yamane, C.; Aoyagi, T.; Ago, M.; Sato, K.; Okajima, K.; Takahashi, T. Two Different Surface Properties of Regenerated Cellulose Due to Structural Anisotropy. *Polymer Journal* **2006**, *38*, 819–826.

[99] Lindman, B.; Karlström, G.; Stigsson, L. On the Mechanism of Dissolution of Cellulose. *Journal of Molecular Liquids* **2010/09/15/**, *156*, 76–81.

[100] Larsson, J.; Sanchez-Fernandez, A.; Mahmoudi, N.; Barnsley, L. C.; Wahlgren, M.; Nylander, T.; Ulvenlund, S. Effect of the Anomeric Configuration on the Micellization of Hexadecylmaltoside Surfactants. *Langmuir* **2019**, *35*, 13904–13914.

[101] Uhlin, K. I.; Atalla, R. H.; Thompson, N. S. Influence of Hemicelluloses on the Aggregation Patterns of Bacterial Cellulose. *Cellulose* **1995**, *2*, 129–144.

[102] Iwata, T.; Indrarti, L.; Azuma, J.-I. Affinity of Hemicellulose for Cellulose Produced by Acetobacter Xylinum. *Cellulose* **1998**, *5*, 215–228.

[103] Whitney, S. E. C.; Brigham, J. E.; Darke, A. H.; Reid, J. S. G.; Gidley, M. J. Structural Aspects of the Interaction of Mannan-Based Polysaccharides with Bacterial Cellulose. *Carbohydrate Research* **1998/02/01/**, *307*, 299–309.

[104] Benselfelt, T.; Cranston, E. D.; Ondaral, S.; Johansson, E.; Brumer, H.; Rutland, M. W.; Wågberg, L. Adsorption of Xyloglucan onto Cellulose Surfaces of Different Morphologies: An Entropy-Driven Process. *Biomacromolecules* **2016**, *17*, 2801–2811.

[105] Kabel, M. A.; van den Borne, H.; Vincken, J.-P.; Voragen, A. G. J.; Schols, H. A. Structural Differences of Xylans Affect Their Interaction with Cellulose. *Carbohydrate Polymers* **2007/05/01/**, *69*, 94–105.

[106] Raghuwanshi, V. S.; Su, J.; Garvey, C. J.; Holt, S. A.; Raverty, W.; Tabor, R. F.; Holden, P. J.; Gillon, M.; Batchelor, W.; Garnier, G. Bio-Deuterated Cellulose Thin Films for Enhanced Contrast in Neutron Reflectometry. *Cellulose* **2017**, *24*, 11–20.

[107] Marrinan, H. J.; Mann, J. A Study by Infra-Red Spectroscopy of Hydrogen Bonding in Cellulose. *Journal of Applied Chemistry* **1954**, *4*, 204–211.

[108] Marrinan, H.; Mann, J. Infrared Spectra of the Crystalline Modifications of Cellulose. *Journal of Polymer Science* **1956**, *21*, 301–311.

[109] Jeffries, R. An Infra-Red Study of the Deuteration of Cellulose and Cellulose Derivatives. *Polymer* **1963**, *4*, 375–389.

[110] Kondo, T.; Sawatari, C. A Fourier Transform Infra-Red Spectroscopic Analysis of the Character of Hydrogen Bonds in Amorphous Cellulose. *Polymer* **1996**, *37*, 393–399.

[111] Garside, P.; Wyeth, P. Identification of Cellulosic Fibres by FTIR Spectroscopy - Thread and Single Fibre Analysis by Attenuated Total Reflectance. *Studies in Conservation* **2003**, *48*, 269–275.

[112] Hofstetter, K.; Hinterstoisser, B.; Salmén, L. Moisture Uptake in Native Cellulose – the Roles of Different Hydrogen Bonds: A Dynamic FT-IR Study Using Deuterium Exchange. *Cellulose* **2006**, *13*, 131–145.

[113] Hinterstoisser, B.; Salmén, L. Application of Dynamic 2D FTIR to Cellulose. *Vibrational Spectroscopy* **2000**, *22*, 111–118.

[114] Bali, G.; Foston, M. B.; O'Neill, H. M.; Evans, B. R.; He, J.; Ragauskas, A. J. The Effect of Deuteration on the Structure of Bacterial Cellulose. *Carbohydrate Research* **2013**, *374*, 82–88.

[115] Lindh, E. L.; Salmén, L. Surface Accessibility of Cellulose Fibrils Studied by Hydrogen–Deuterium Exchange with Water. *Cellulose* **2017**, *24*, 21–33.

[116] Nelson, M. L.; O'Connor, R. T. Relation of Certain Infrared Bands to Cellulose Crystallinity and Crystal Latticed Type. Part I. Spectra of Lattice Types I, II, III and of Amorphous Cellulose. *Journal of Applied Polymer Science* **1964**, *8*, 1311–1324.

[117] Hishikawa, Y.; Togawa, E.; Kataoka, Y.; Kondo, T. Characterization of Amorphous Domains in Cellulosic Materials Using a FTIR Deuteration Monitoring Analysis. *Polymer* **1999**, *40*, 7117–7124.

[118] Jeffries, R. The Amorphous Fraction of Cellulose and Its Relation to Moisture Sorption. *Journal of Applied Polymer Science* **1964**, *8*, 1213–1220.

[119] Hishikawa, Y.; Inoue, S.-i.; Magoshi, J.; Kondo, T. Novel Tool for Characterization of Noncrystalline Regions in Cellulose: A FTIR Deuteration Monitoring and Generalized Two-Dimensional Correlation Spectroscopy. *Biomacromolecules* **2005**, *6*, 2468–2473.

[120] Shanshan, G.; Jianqing, W.; Zhengwei, J. Preparation of Cellulose Films from Solution of Bacterial Cellulose in NMMO. *Carbohydrate Polymers* **2012**, *87*, 1020–1025.

[121] Nishiyama, Y.; Langan, P.; Chanzy, H. Crystal Structure and Hydrogen-Bonding System in Cellulose Iβ from Synchrotron X-Ray and Neutron Fiber Diffraction. *J. Am. Chem. Soc.* **2002**, *124*, 9074–9082.

[122] Rowland, S. P.; Roberts, E. J. The Nature of Accessible Surfaces in the Microstructure of Cotton Cellulose. *Journal of Polymer Science Part A-1: Polymer Chemistry* **1972**, *10*, 2447–2461.

[123] Pérez, S.; Mazeau, K. Conformations, Structures, and Morphologies of Celluloses. *Polysaccharides: Structural diversity and functional versatility* **2005**, *2*.

[124] Garvey, C. J.; Parker, I. H.; Simon, G. P.; Whittaker, A. K. The Hydration of Paper Studied with Solid-State Magnetisation-Exchange 1H NMR Spectroscopy. *Holzforschung* **2006**, *60*, 409–416.

[125] Radloff, D.; Boeffel, C.; Spiess, H. W. Cellulose and Cellulose/Poly(Vinyl Alcohol) Blends. 2. Water Organization Revealed by Solid-State NMR Spectroscopy. *Macromolecules* **1996**, *29*, 1528–1534.

[126] L. Lindh, E.; Terenzi, C.; Salmén, L.; Furó, I. Water in Cellulose: Evidence and Identification of Immobile and Mobile Adsorbed Phases by 2 H MAS NMR. *Physical Chemistry Chemical Physics* **2017**, *19*, 4360–4369.

[127] Eckelt, J.; Wolf, B. A. Cellulose/Water: Liquid/Gas and Liquid/Liquid Phase Equilibria and Their Consistent Modeling. *Biomacromolecules* **2007**, *8*, 1865–1872.

[128] Kontturi, E.; Suchy, M.; Penttilä, P.; Jean, B.; Pirkkalainen, K.; Torkkeli, M.; Serimaa, R. Amorphous Characteristics of an Ultrathin Cellulose Film. *Biomacromolecules* **2011**, *12*, 770–777.

[129] Cheng, G.; Liu, Z.; Murton, J. K.; Jablin, M.; Dubey, M.; Majewski, J.; Halbert, C.; Browning, J.; Ankner, J.; Akgun, B.; Wang, C.; Esker, A. R.; Sale, K. L.; Simmons, B. A.; Kent, M. S. Neutron Reflectometry and QCM-D Study of the Interaction of Cellulases with Films of Amorphous Cellulose. *Biomacromolecules* **2011**, *12*, 2216–2224.

[130] Naidjonoka, P.; Arcos Hernandez, M.; K. Pálsson, G.; Heinrich, F.; Stålbrand, H.; Nylander, T. On the Interaction of Softwood Hemicellulose with Cellulose Surfaces in Relation to Molecular Structure and Physicochemical Properties of Hemicellulose. *Soft Matter* **2020**, *16*, 7063–7076.

[131] Janardhan, R.; Gedam, P.; Sampathkumaran, P. The Effect of Polymer Molecular Weight in the Adsorption Process. *Journal of Colloid and Interface Science* **1990**, *140*, 391–400.

[132] Murgia, S.; Falchi, A. M.; Meli, V.; Schillén, K.; Lippolis, V.; Monduzzi, M.; Rosa, A.; Schmidt, J.; Talmon, Y.; Bizzarri, R.; Caltagirone, C. Cubosome Formulations Stabilized by a Dansyl-Conjugated Block Copolymer for Possible Nanomedicine Applications. *Colloids and Surfaces B: Biointerfaces* **2015**, *129*, 87–94.

[133] Borné, J.; Nylander, T.; Khan, A. Effect of Lipase on Monoolein-Based Cubic Phase Dispersion (Cubosomes) and Vesicles. *J. Phys. Chem. B* **2002**, *106*, 10492–10500.

[134] Caltagirone, C.; Falchi, A. M.; Lampis, S.; Lippolis, V.; Meli, V.; Monduzzi, M.; Prodi, L.; Schmidt, J.; Sgarzi, M.; Talmon, Y.; Bizzarri, R.; Murgia, S. Cancer-Cell-Targeted Theranostic Cubosomes. *Langmuir* **2014**, *30*, 6228–6236.

[135] Murgia, S.; Falchi, A. M.; Mano, M.; Lampis, S.; Angius, R.; Carnerup, A. M.; Schmidt, J.; Diaz, G.; Giacca, M.; Talmon, Y.; Monduzzi, M. Nanoparticles from Lipid-Based Liquid Crystals: Emulsifier Influence on Morphology and Cytotoxicity. *J. Phys. Chem. B* **2010**, *114*, 3518–3525.

[136] Aleandri, S.; Mezzenga, R. The Physics of Lipidic Mesophase Delivery Systems. *Physics Today* **2020**, *73*, 38–44.

[137] Fornasier, M.; Biffi, S.; Bortot, B.; Macor, P.; Manhart, A.; Wurm, F. R.; Murgia, S. Cubosomes Stabilized by a Polyphosphoester-Analog of Pluronic F127 with Reduced Cytotoxicity. *Journal of Colloid and Interface Science* **2020**, *580*, 286–297.

[138] S. Mikkonen, K.; Merger, D.; Kilpeläinen, P.; Murtomäki, L.; S. Schmidt, U.; Wilhelm, M. Determination of Physical Emulsion Stabilization Mechanisms of Wood Hemicelluloses via Rheological and Interfacial Characterization. *Soft Matter* **2016**, *12*, 8690–8700.

[139] Bhattarai, M.; Valoppi, F.; Hirvonen, S.-P.; Hietala, S.; Kilpeläinen, P.; Aseyev, V.; Mikkonen, K. S. Time-Dependent Self-Association of Spruce Galactoglucomannans Depends on pH and Mechanical Shearing. *Food Hydrocolloids* **2020**, *102*, 105607.

[140] Akhlaghi, S. P.; Ribeiro, I. R.; Boyd, B. J.; Loh, W. Impact of Preparation Method and Variables on the Internal Structure, Morphology, and Presence of Liposomes in Phytantriol-Pluronic(®) F127 Cubosomes. *Colloids Surf B Biointerfaces* **2016**, *145*, 845–853.

[141] Kim, J.-Y.; Song, M.-G.; Kim, J.-D. Zeta Potential of Nanobubbles Generated by Ultrasonication in Aqueous Alkyl Polyglycoside Solutions. *Journal of Colloid and Interface Science* **2000**, *223*, 285–291.

[142] Muir, B. W.; Zhen, G.; Gunatillake, P.; Hartley, P. G. Salt Induced Lamellar to Bicontinuous Cubic Phase Transitions in Cationic Nanoparticles. *J. Phys. Chem. B* **2012**, *116*, 3551–3556.

[143] Hartnett, T. E.; Ladewig, K.; O'Connor, A. J.; Hartley, P. G.; McLean, K. M. Size and Phase Control of Cubic Lyotropic Liquid Crystal Nanoparticles. *J. Phys. Chem. B* **2014**, *118*, 7430–7439.

[144] Heskins, M.; Guillet, J. E. Solution Properties of Poly(N-Isopropylacrylamide). *Journal of Macromolecular Science: Part A - Chemistry* **1968**, *2*, 1441–1455.

[145] Luo, Y.; Liu, L.; Wang, X.; Shi, H.; Lv, W.; Li, J. Sugar-Installed Thermoresponsive Micellar Aggregates Self-Assembled from "Coil-Comb-Coil" Triblock Glycopolymers: Preparation and Recognition with Concanavalin A. *Soft Matter* **2012**, *8*, 1634–1642.

[146] Hernandez-Cerdan, P.; Mansel, B.; Leis, A.; Lundin, L.; Williams, M. On the Structural Analysis of Polysaccharide-Networks by Transmission Electron-Microscopy: Comparison with SAXS. *Biomacromolecules* **2018**, *19*.

[147] Beaucage, G. Approximations Leading to a Unified Exponential/Power-Law Approach to Small-Angle Scattering. *Journal of Applied Crystallography* **1995**, *28*, 717–728.

[148] Porod, G. X-Ray Low Angle Scattering of Dense Colloid Systems. *Kolloid-Zeitschrift und Zeitschrift fuer Polymere* **1953**, *133*, 51.

[149] Cook, M. T.; Filippov, S. K.; Khutoryanskiy, V. V. Synthesis and Solution Properties of a Temperature-Responsive PNIPAM–b-PDMS–b-PNIPAM Triblock Copolymer. *Colloid Polym Sci* **2017**, *295*, 1351–1358.

[150] Papagiannopoulos, A.; Zhao, J.; Zhang, G.; Pispas, S.; Radulescu, A. Thermoresponsive Aggregation of PS–PNIPAM–PS Triblock Copolymer: A Combined Study of Light Scattering and Small Angle Neutron Scattering. *European Polymer Journal* **2014**, *56*, 59–68.

[151] Pedersen, J. S. Form Factors of Block Copolymer Micelles with Spherical, Ellipsoidal and Cylindrical Cores. *Journal of Applied Crystallography* **2000**, *33*, 637–640.

[152]   Schillén, K.; Galantini, L.; Du, G.; Giudice, A. D.; Alfredsson, V.; Carnerup, A. M.; Pavel, N. V.; Masci, G.; Nyström, B. Block Copolymers as Bile Salt Sequestrants: Intriguing Structures Formed in a Mixture of an Oppositely Charged Amphiphilic Block Copolymer and Bile Salt. *Phys. Chem. Chem. Phys.* **2019**, *21*, 12518–12529.

[153]   Balzer, D.; Luders, H. *Nonionic Surfactants: Alkyl Polyglucosides*; Taylor & Francis, 2000.

[154]   Lin, S.-Y.; Lin, Y.-Y.; Chen, E.-M.; Hsu, C.-T.; Kwan, C.-C. A Study of the Equilibrium Surface Tension and the Critical Micelle Concentration of Mixed Surfactant Solutions. *Langmuir* **1999**, *15*, 4370–4376.

Scientific Publications

Paper 1

On the interaction of softwood hemicellulose with cellulose surfaces in relation to molecular structure and physicochemical properties of hemicellulose

P. Naidjonoka, M. Arcos Hernandez, G. K. Pálsson, F. Heinrich, H. Stålbrand, T. Nylander

On the interaction of softwood hemicellulose with cellulose surfaces in relation to molecular structure and physicochemical properties of hemicellulose†

Polina Naidjonoka, [ID] *[a] Monica Arcos Hernandez,[b] Gunnar K. Pálsson,[cd] Frank Heinrich,[ef] Henrik Stålbrand [ID] *[g] and Tommy Nylander [ID] *[ahi]

The substantial part of the water-soluble hemicellulose fraction, obtained when processing cellulose to produce paper and other products, has so far been discarded. The aim of this work is to reveal the interfacial properties of softwood hemicellulose (galactoglucomannan, GGM) in relation to their molecular and solution structure. In this study the sugar composition of GGM was characterised by chemical analysis as well as 1D and 2D NMR spectroscopy. Previously it has been demonstrated that hemicellulose has high affinity towards cellulose and has the ability to alter the properties of cellulose based products. This study is focused on the interactions between hemicellulose and the cellulose surface. Therefore, adsorption to hydrophobized silica and cellulose surfaces of two softwood hemicellulose samples and structurally similar seed hemicelluloses (galactomannans, GMs) was studied with ellipsometry, QCM-D and neutron reflectometry. Aqueous solutions of all samples were characterized with light scattering to determine how the degree of side-group substitution and molecular weight affect the conformation and aggregation of these polymers in the bulk. In addition, hemicellulose samples were studied with SAXS to investigate backbone flexibility. Light scattering results indicated that GM polymers form globular particles while GGMs were found to form rod-like aggregates in the solution. The polysaccharides exhibit higher adsorption to cellulose than on hydrophobic surfaces. A clear correlation between the increase in molecular weight of polysaccharides and increasing adsorbed amount on cellulose was observed, while the adsorbed amount on the hydrophobic surface was fairly independent of the molecular weight. The obtained layer thickness was compared with bulk scattering data and the results indicated flat conformation of the polysaccharides on the surface.

Introduction

The interactions between hemicellulose and another major wood polysaccharide, cellulose, are of key importance for the organization and structure of the plant cell walls as well as for a range of applications. The major components of softwood hemicellulose are galactoglucomannans (GGM). Their content varies both in different parts of the tree, as well as between plant species with GGM, reaching up to 20% w/w of dry wood.[1–4] Today a significant part of the softwood GGM is discarded together with the waste stream during processes like thermo-mechanical pulp production.[5] However, it is now possible to recover this highly valuable polymer from such waste streams.[6–8] While other mannan-based polysaccharides like Locust bean gum (LBG) and Guar gum (GG) are used in the industry, mostly in food related applications,[9–12] GGMs from softwood are not yet fully exploited in spite of the large amount produced during pulp processing. However, numerous potential applications have been suggested and tested for GGMs in therapeutic reagents,[13] as a raw material for biodegradable films[14–16] and novel anticoagulants.[17] Therefore, this study focuses on the interfacial interactions between cellulose and softwood hemicellulose and how it relates to the aggregation and molecular architecture in comparison to other mannan-based polysaccharides.

a Physical Chemistry, Department of Chemistry, Lund University, Lund, Sweden. E-mail: polina.naidjonoka@fkem1.lu.se, tommy.nylander@fkem1.lu.se
b Polymer & Materials Chemistry, Department of Chemistry, Lund University, Lund, Sweden
c Department of Physics & Astronomy, Uppsala University, Uppsala, Sweden
d Institut Laue Langevin, Grenoble, France
e Department of Physics, Carnegie Mellon University, Pittsburgh, PA, USA
f NIST Center for Neutron Research, Gaithersburg, MD, USA
g Biochemistry and Structural Biology, Department of Chemistry, Lund University, Lund, Sweden. E-mail: henrik.stalbrand@biochemistry.lu.se
h NanoLund, Lund University, Lund, Sweden
i Lund Institute of Advanced Neutron and X-ray Science LINXS, Lund, Sweden
† Electronic supplementary information (ESI) available. See DOI: 10.1039/d0sm00264j

Hemicellulose has a large number of side groups and their role for interaction with cellulose and to what extent they prevent the polysaccharide to assemble into larger aggregates is not clear. GGMs consist of a β-(1→4)-D-mannopyranose backbone that is partially interrupted by β-(1→4)-D-glucopyranose units.[1,18,19] The backbone carries side-groups of α-(1→6)-D-galactopyranose and acetyl side groups.[18] The degree of side-group substitution may vary between sources and preparations. Galactoglucomannans are mainly present in the secondary cell walls of conifer plants, however, small amounts are also found in dicot cell walls.[3] Locust bean gum is produced in the seed endosperm of the carob tree *Ceratonia silique L.* and Guar gum in the seed of *Cyamopsis tetragonoloba.* Both LBG and GG contain only β-(1→4)-mannopyranose in the backbone and galactopyranose side-groups attached *via* α-(1→6) linkages.

In wood, cellulose forms microfibrils that are well organized with chains of hemicellulose located either on the surface of or in between the fibrils.[20] The nature of the binding of hemicellulose is still under debate, however, it is believed that the polysaccharides interact with each other *via* hydrogen bonding.[21,22] Benselfelt *et al.*[23] showed that the adsorption of xyloglucan, the main hemicellulose in primary plant cell walls, onto cellulose surfaces is an entropy-driven process. An increase in entropy is caused by the release of water molecules from the cellulose layer as hemicellulose is adsorbed.

Several approaches have been used to reveal the nature of the interaction between cellulose and hemicellulose. Hayashi *et al.*[20,24] studied the influence of the polymerization degree on the adsorption of xyloglucan on dispersed cellulose. They demonstrated that xyloglucans adsorb to the microfibrils of cellulose as a monolayer with highly branched parts extending into solution. The adsorption per weight unit was found to be larger on microcrystalline cellulose compared to amorphous cellulose. Similar results were obtained by Vincken *et al.*[22] where xyloglucan was found to bind more efficiently to microcrystalline cellulose Avicel than to cellulose from cotton linters. Avicel has a 10 times smaller exposed surface-to-weight ratio than bacterial cellulose, but the per-area-adsorption of the polymeric xyloglucans is similar.[25] Uhlin *et al.*[26] used *Acetobacter xylinum* as a model system to produce cellulose in the presence of carboxymethyl cellulose (CMC), xylan, xyloglucan and ivory nut mannan. These polysaccharides were shown to affect cellulose structure in different ways. Xyloglucans and xylans showed the largest effect on the aggregation of cellulose due to a similarity in the backbone unit conformation with cellulose. Cellulose produced in the presence of mannans and CMC was found to have a very similar aggregation pattern but with a lower degree of cellulose crystallinity in comparison to a control grown without the polysaccharides. The charge of hemicellulose was found to be more crucial than the molecular weight for the adsorption to nanofibrillated cellulose (NFC). The adsorbed amount of Guar gum before and after hydrolysis showed comparable results in similar conditions. The adsorption of the anionic CMC showed strong dependence on the pH of the buffer, with irreversible adsorption at low pH but not at pH 8 where the carboxylic groups of both CMC and cellulose are deprotonated.[27,28]

The sorption of glucomannans to cellulose is affected by the presence of side groups that prevent a close contact of the polysaccharide with the cellulose fibre surface. In addition, by removing the side groups, solubility of the chains of the polysaccharides chain decreases[29–31] and promotes binding to a surface. Deacetylation generates new hydroxyl groups that can take part in hydrogen bonding[5,32] and at least 15 unsubstituted xylosyl units are required for adsorption.[25]

It is clear that the increasing use of hemicelluloses requires knowledge on how their molecular structure affect bulk solution behaviour and the adsorption to different types of surfaces. Here we compared the results of two types of GGMs, with different molecular weight and degree of side-group substitution, with those from seed hemicelluloses (LBG and GG). The LBG and GG samples are commonly used in industrial applications. Solution behaviour of the polysaccharides was characterized with light and small angle X-ray scattering, which gave information on the size, shape and stiffness, as well as the aggregation state of the polysaccharides. The knowledge gained from the polysaccharide molecular structure, conformation and aggregation was related to the results from adsorption studies on two relevant surfaces for applications, *i.e.* hydrophobic and spin-coated cellulose films. The combination of *in situ* ellipsometry, quartz crystal microbalance with dissipation (QCM-D) and neutron reflectometry (NR) allowed us not only to quantify the adsorption in terms of surface excess and adsorption kinetics, but by comparing the adsorption onto a cellulose surface with that on a hydrophobic surface we were able to gain insight into the nature of the surface interactions of hemicellulose.

Experimental

Materials

Galactomannans. Galactomannan polysaccharides Guar gum and Locust bean gum were obtained from Megazyme International (Bray, Ireland).

Preparation of GGM. Two types of GGM-enriched preparations originating from spruce were used in the study. The first one (TMP-GGM) was obtained from the process water from termomechanical pulp processing and GGM was purified using ultrafiltration and four rounds of diafiltration as described in detail by Andersson *et al.*[6] To prepare SP-GGM, steam extraction of GGM from spruce chips in 0.025% NaOH was performed at 190 °C for 5 minutes according to Lundqvist *et al.*[2] The liquid phase was then filtered and GGM purified by size-exclusion chromatography (SEC) with recovery of the ''F1-fraction'' as described by Palm and Zacchi.[33] The GGM preparations were freeze-dried and stored under dry conditions at room temperature.

Chemical analysis of GGM samples. The GGM preparations were analysed for sugar monomer composition, acetyl content and weight-average molecular weight (M_w) as described by Lundqvist *et al.*[2] The sugar monomer composition was determined after hydrolysis in an autoclave at 120 °C in 0.25 M sulphuric acid. Monomer sugar analysis (mannose, galactose, glucose, xylose, arabinose) was performed using high-performance liquid

chromatography with pulsed amperometric detection (HPAEC-PAD), using a Carbo Pac Pa10 guard and analytical column (Dionex/Thermofischer Scientific). The acetyl content was analysed after treatment in 1% NaOH for 12 h at room temperature and quantification of acetic acid by high-performance liquid chromatography (HPLC) using an Aminex HPX-87H (BIO-RAD) column and refractive-index (RI) detection. M_w was estimated using SEC (RI-detection) with water as eluent and using GGM mass-standards analysed by matrix-assisted laser ionization/desorption time-of-light (MALDI-TOF).[2] The lignin content was estimated by measuring the absorbance at 280 nm of water-dissolved samples and using an extinction coefficient of 17.8 L g^{-1} cm^{-1} (for milled wood lignin) previously suggested applicable for water soluble spruce lignin from mechanical pulp processing.[34]

1D and 2D NMR spectroscopy. Dried samples were dissolved in 0.6 mL of 99.9% deuterium oxide (Sigma Aldrich Co., MO, USA) to a concentration of 10 mg mL^{-1}. ^{1}H and ^{13}C spectra as well as heteronuclear single quantum coherence (HSQC) NMR spectra were recorded at 25 °C, 12 or 70 °C on a Bruker Avance III spectrometer (Bruker, Billerica, MA, USA) at 500.17 MHz for ^{1}H and at 125.77 MHz for ^{13}C. Chemical shifts were referenced to the C-1 signal of glucopyranose (103.548 ppm) and the H-2 signal of the 2-O-acetylated mannopyranose (5.423 ppm).[19,35] The chosen temperatures for spectra acquisition were different to room temperature in order to induce a shift of the residual internal solvent (HDO) to reveal or improve the resolution of the anomeric signals arising from the sugar units. HSQC was acquired at 25 °C using the same method as described in Al-Rudainy et al.[8] with minor adjustment for specific samples (adjustment of SR, sweep width and O 1p and O 2p parameters). Data was processed with Topspin (Bruker) or MestreNova (Mestrelab Research). Baseline and phase correction were applied in both directions. ^{1}H NMR was used for quantification as described in Rosengren et al. using an external standard[36] as well as using the module ERETIC 2 for quantification which is based on PULCON,[37] an internal standard method which correlates the absolute intensities of two different spectra (Topspin, Bruker).

Microcrystalline cellulose. Microcrystalline cellulose (Avicel PH101, Sigma-Aldrich, Sweden) with an average particle size of 50 μm, N,N-dimethylacetamide (DMAc), lithium chloride (99.0% LiCl) and dimethyloctylchlorosilane (DMOCS, 97%) were purchased from Sigma-Aldrich, Sweden. LiCl$_2$ was dried at 200 °C overnight and used immediately. Purified water (18 MΩ cm) was obtained by passing deionized water through a Milli-Q® Water Purification system (MerckMillipore, Darmstadt, Germany) was used for the preparation of all solutions. All other solvents and reagents were of analytical grade and were used as received.

Sample preparation. GG and LBG solutions (5 mg mL^{-1}) in sodium citrate buffer (0.05 M, pH 5.9) were prepared by adding 1.0 g of powder to 180 mL of buffer. The mixture was then homogenized with Heidolph DIAX 900 homogenizer (Heidolph Instruments GmbH, Schwabach, Germany) (using 5 pulses at a setting 1) at 80 °C and heated to the boiling point under

agitation. The obtained viscous solution was cooled down to a room temperature while continuing agitation overnight at 4 °C. The solution was then centrifuged (5338 × g, 20 min) to remove impurities and diluted with the buffer to 200 mL. Aliquots of clear solution were stored at −20 °C until further use. After thawing, the solution was vigorously stirred.

LvLBG was dissolved by wetting 1 g of powder with 2 mL of 95% ethanol followed by the addition of 90 mL sodium citrate buffer (0.05 M, pH 5.9) and stirring overnight at 4 °C. Thereafter, the solution was heated to 120 °C in a beaker covered with aluminium foil and under vigorous stirring with an IKA RCT basic magnetic stirrer. Stirring continued without heating for approximately 20 min until complete dissolution. The solution was then centrifuged (5338 × g, 10 min) to remove impurities and diluted with buffer to a final volume of 100 mL.[38]

GGM samples (10 mg mL^{-1}) were dissolved directly in 0.05 M citrate buffer and stored at +4 °C for maximum 1 week until further use. Cellulose solutions were prepared according to Sczech et al.[39] Microcrystalline cellulose powder (1 g) was first left to swell for 1 h in 10 mL of deionized water at 40 °C. Excess of water was then removed from the hydrated cellulose by centrifugation (2616 × g, 15 min). This was followed by an exchange with 10 mL of methanol, after which the mixture was incubated during stirring for 45 min, followed by centrifugation at 2616 × g for 15 min to remove the excess of the solvent. The same procedure was repeated once more with methanol and then twice with the anhydrous DMAc. After the last incubation, the mixture was centrifuged, and the cellulose pellet was then dissolved in 100 mL of 7% (w/v) LiCl/DMAc solution under stirring at room temperature for 15 h. The cellulose solution was then placed at 4 °C under stirring until the cellulose was completely dissolved.

Substrate preparation. Substrates used for the ellipsometry measurements were polished silicon wafers (p-type, boron-doped, resistivity of 1–20 Ω cm) which were obtained from SWI (Semiconductor Wafer, Inc., Taiwan). The wafers were thermally oxidized at 920 °C in an oxygen atmosphere to yield a 300 Å thick SiO$_2$ layer.

Silicon wafers were cut into 2 × 1 cm pieces and cleaned according to Chang et al.[40] Silica substrates were placed in a base mixture of 25% NH$_4$OH, 30% H$_2$O$_2$, and H$_2$O (1/1/5 by volume) at 80 °C for 5 min, rinsed with deionized water, and cleaned in an acid mixture of 32% HCl, 30% H$_2$O$_2$ and H$_2$O (1/1/5 by volume) at 80 °C for 5 min. The substrates were thoroughly rinsed with water and ethanol, and stored in ethanol (99.7%) until further use.

Polished silicon substrates (Siltronix, Archamps-France) of 5 × 5 × 1.5 cm^3 capped with a silicon oxide layer were used for Neutron Reflectometry (NR) measurements. Surfaces were cleaned as described above.

The substrates used for Quartz Crystal Microbalance with Dissipation (QCM-D, Q-Sense Analyzer, Biolin Scientific, Gothenburg, Sweden) measurements were quartz crystals (Q-Sense QSX 303) coated with gold and a top layer of SiO$_2$ exposed to the solution. The fundamental frequency of the

crystals was 4.95 MHz. The quartz QCM crystals were cleaned for 5 min in 2% (v/v) Hellmanex III® while sonicating and rinsed with water and 99.7% ethanol.

Hydrophobized silica substrates were prepared by first treating cleaned silica surfaces in an air plasma for 5 min at 0.02 mbar using a plasma cleaner (Harrick Scientific Corp, model PDC-3XG, New York, USA). The samples were then immediately placed in a desiccator under vacuum with 1 mL of DMOCS overnight. The hydrophobized silicon wafers were subsequently sonicated for 20 min in tetrahydrofuran and ethanol and stored in ethanol. Substrates were carefully rinsed with ethanol and water, and dried with nitrogen gas before each experiment.

Cellulose surfaces were prepared by spin-coating a few drops of clear cellulose solution on the silica surface (spin coater module LabSpin6/8, SUSS MicroTec SE, Germany) at 6000 rpm for 60 s. The spin-coated wafers were annealed at 100 °C for 10 min, cooled down to room temperature, placed into deionized water for 20 min, dried in a nitrogen flow and heated at 150 °C for 15 min. The cellulose covered substrates were used immediately. The cellulose film thickness was roughly 40 nm for all the substrates used for the ellipsometry measurements.

Dynamic and static light scattering (DLS and SLS). Both static and dynamic light scattering experiments were performed on an ALV/DLS/SLS-5022F, CGH-8F-based compact goniometer system (ALV-GmbH, Langen, Germany) with a 22 mW He–Ne-laser (632.8 nm) light source. The instrument was equipped with an automatic attenuator, controlled via software. The sample holder consists of a cell housing filled with a refractive index matched liquid (cis-decahydronaphtalene) in which the cuvette was placed.

Light scattering data from GGM samples were recorded at a concentration of 1.5 mg mL^{-1} and from galactomannans at 3 mg mL^{-1} dissolved in 0.05 M citrate buffer (pH 5.9). All samples were filtered with a 0.45 μm-pore-size filter and transferred to clean borosilicate NMR tubes prior to the measurements. For SLS, angles from 40° to 140° were used with a step size of 2° for 6 s. The intensity autocorrelation functions were obtained for angles from 60° to 130° with steps of 10° for at least 300 s. All the measurements were performed at 25 °C.

For the static light scattering, the obtained scattering intensity $I(q)$ was corrected for background scattering ($\Delta I(q)$) and brought to an absolute scale according to eqn (1)[41]

$$I(q) = \frac{\Delta I(q)}{I_{ref}(q)}\left(\frac{n}{n_{ref}}\right)^2 RR_{ref} \qquad (1)$$

where n is the refractive index of the solution, and $I_{ref}(q)$, n_{ref} and RR_{ref} are the scattered intensity, refractive index, and Rayleigh ratio, of the reference (toluene), respectively. q is the magnitude of the scattering vector:

$$q = \frac{4\pi n}{\lambda_0}\sin\left(\frac{\theta}{2}\right) \qquad (2)$$

where λ_0 is the laser wavelength, n is the refractive index of the solution and θ is the scattering angle. The radius of gyration R_G was determined using Zimm plots.

The decay rate (Γ) was obtained from the second order cumulative expansion,[42] which was plotted at different scattering vectors. The slope of such a plot gives the translational diffusion coefficient D. The hydrodynamic radius R_H was calculated according to the Stokes–Einstein equation:

$$D = \frac{k_B T}{6\pi\eta R_H} \qquad (3)$$

where k_B is the Boltzmann constant, T is the temperature and η is the solvent viscosity.

Small-angle X-ray scattering (SAXS). SAXS measurements were performed at the SWING beamline at the SOLEIL Synchrotron (Gif-sur-Yvette, France). The instrument was equipped with an Eiger 4M (Dectris) detector. The X-ray wavelength was 1.54 Å^{-1}. Small-Angle X-ray Scattering curves were recorded for SP and TMP samples in 0.05 M citrate buffer (pH 5.9) at three different concentrations: 5 mg mL^{-1}, 10 mg mL^{-1} and 20 mg mL^{-1}. A flow capillary set up was used for all the samples. Buffer was flushed through the capillary and measured before and after each sample to ensure a clean capillary and to account for fluctuations in the beam intensity. The data were collected for two different q-ranges (0.0049–0.44 Å^{-1} and 0.0027–0.24 Å^{-1}) with an exposure time of 500 ms. Collected scattering curves were reduced and stitched together using the Foxtrot Software (https://www.synchrotron-soleil.fr/en/beamlines/swing). The reduced data was evaluated with SasView.[43] The scattering curves for both samples were fitted to the Unified Exponential/Power-law model developed by Beaucage[44–46] that describes fractal-like behavior of polymers in solution.

Cryogenic-transmission electron microscopy (Cryo-TEM). Samples for Cryo-TEM at a concentration of 1.5 mg mL^{-1} were filtered through a 0.45 μm-pore-size filter. A 4 μL-sample drop was placed on a lacey carbon coated formvar grid (Ted Pella Inc., Redding, CA, USA) and gently blotted with a filter paper to create a thin film. The grid was then prepared for imaging using an automatic plunge-freezer system (Leica Em GP, Leica Microsystems, Wetzlar, Germany) with the environmental chamber operated at 25 °C and 90% relative humidity to prevent evaporation from the specimen. The vitrification of the specimen was performed by rapid plunging of the grid into liquid ethane (−183 °C). Thereafter, samples were stored in liquid nitrogen (−196 °C) and transferred into the microscope using a cryo transfer tomography holder (Fischione, Model 2550, E. A. Fischione Instruments, Inc., Corporate Circle Export, PA, USA). The grids were examined with a Jeol JEM-2200FS transmission electron microscope (JEOL, Tokyo, Japan) equipped with a field-emission electron source, a cryopole piece in the objective lens and an in-column energy filter (omega filter). Zero-loss images were recorded under low-dose conditions at an acceleration voltage of 200 kV on a bottom-mounted TemCam-F416 camera (TVIPS-Tietz Video and Image Processing Systems GmbH, Gauting, Germany) using SerialEM.

Atomic force microscopy (AFM). AFM was performed with a Park XE-100 (Park Systems Corp., Suwon, Korea) in a non-contact mode. Samples were probed in dry state under ambient conditions. A silicon cantilever with a 42 N m^{-1} spring constant

and 330 kHz resonance frequency was used. The image analysis was done with the XEI software (Park Systems Corp., Suwon, Korea).

Ellipsometry. The main technique used to study the interfacial behavior of GGM is ellipsometry with complimentary information obtained by QCM-D and neutron reflectometry. The adsorption of hemicellulose to cellulose and hydrophobic surfaces were measured *in situ* using null ellipsometry as described previously.[47] This method is based on the changes in the polarization state when elliptically polarized light is reflected from a surface. A Rudolph Research ellipsometer (type 43603-200E) equipped with a xenon arc lamp light source was used for the adsorption study. All measurements were performed at 4015 Å wavelength and an incidence angle of 68.00°. The silicon substrates were placed inside a trapezoid cuvette with volume of 5 mL that was held at 25 °C.

The optical properties of the silicon substrates were characterized before each experiment in two different media, air and aqueous buffer. To minimize the effect caused by imperfections of the optical components, the average positions of polarizer and analyzer in four zones were used to calculate the ellipsometric angles, ψ and Δ. Here, ψ represents the change in the relative amplitude and Δ, the phase shift of polarized light upon reflection at the interface. From the ellipsometric angles, the refractive index and layer thickness of the adsorbed layer were determined using a three or four layer optical model.[47] The adsorbed amount Γ was calculated using the de Feijter equation[48]

$$\Gamma = \frac{(n_f - n_0)d_f}{dn/dc} \qquad (4)$$

where n_0, n_f, d_f and dn/dc are the refractive index of the medium, the mean refractive index of the adsorbed layer, the optical thickness of the layer and the specific refractive index increment, respectively. The dn/dc values used for the calculations and the references are summarized in Table 1.

After the characterization of the bare surface, a polysaccharide solution was added to the ellipsometry cuvette to a final concentration of 0.02 mg mL^{-1}. For the experiments with cellulose surfaces, pre-characterized silicon wafers were spin-coated with the cellulose solution before the addition of the sample.

As soon as the system reached an equilibrium, the cuvette was flushed with fresh buffer solution to remove the polysaccharide solution. This allowed to estimate the extent of reversible mannan binding to the substrate.

Quartz crystal microbalance with dissipation (QCM-D). QCM-D is an acoustic technique that measures changes in the resonance frequency of a quartz crystal due to adsorption or deposition of material on its surface. The change in

frequency is recorded as a function of time while a substance is adsorbing to the substrate. The dissipation energy is measured by monitoring the decay of the signal amplitude when switching off the potential across the crystal and yields viscoelastic properties of the surface layer.[52] A QSense E4 system with four flow cells (Biolin Scientific, Gothenburg, Sweden) was used.

Hydrophobized crystals were placed in the flow cell and ethanol was passed through the system with peristaltic pump (Ismatec IPC-N 4, Zürich, Switzerland), followed by purging with 0.05 M citrate buffer (pH 5.9). The crystals were left to stabilize in the buffer for at least 30 min. The fundamental frequencies and dissipation energies for each overtone were determined before samples were injected at 150 μL min^{-1} at a concentration of 0.02 mg mL^{-1}. All measurements were performed at 25 °C. The obtained data was treated and fitted with a Voigt viscoelastic model[53] using Dfind software (QSense, Biolin Scientific).

Neutron reflectometry (NR). Neutron reflectometry is a technique, where a neutron beam is directed towards a surface and the intensity of the reflected radiation as a function of scattering vector q (see eqn (5)) is measured.

$$q = \frac{4\pi}{\lambda_0}\sin(\theta_{in}) \qquad (5)$$

where λ_0 is the neutron wavelength and θ_{in} is the angle of incidence.

Here we used specular NR, *i.e.* the angle of reflection is equal to the incident beam angle.[54] Measurements were performed at NIST Center For Neutron Research (NCNR, Gaithersburg, MD) on the NGD-MAGIK reflectometer over a q-range of 0.005–0.2 Å^{-1}.[55]

Adsorption of TMP GGM was studied with NR on a hydrophobic surface. TMP was dissolved in deuterated 0.05 M citrate buffer (pH 5.9) at a concentration of 0.2 mg mL^{-1}. First, the specular reflectivity of the bare surface immersed in deuterated (D$_2$O) and protonated (H$_2$O) buffer was measured *versus* q. The sample in D$_2$O buffer was then injected and left for 1 hour to adsorb. Thereafter, two NR curves were measured after rinsing with D$_2$O and H$_2$O-based buffers, respectively. The raw data was reduced with the online data reduction service *reductus*.[56] The reduced data was evaluated with the Motofit software, which uses the Abeles matrix method to calculate the reflectivity from a stratified interfaces.[57,58] The best fit was obtained applying 4 layers as follows: Si–SiO$_2$, hydrophobic layer, the transition layer containing acetyl groups of GGM interconnected with the hydrophobic layer and the top layer mainly consisting of the GGM sugar units. The layer thickness, roughness, solvent penetration and Scattering length density (SLD) were found for each layer by simultaneously fitting the model to the data from H$_2$O and D$_2$O contrasts. Attempt was also made to measure the interaction between GGM and the cellulose layer using neutron reflectometry. However, the poor SLD contrast between GGM and cellulose made modelling uncertain and we therefore prefer not to discuss these data. We are at the moment working on neutron reflectometry study where we use deuterated cellulose to enhance the SLD contrast.

Table 1 dn/dc values of polysaccharides

Polysaccharide	dn/dc [mL g^{-1}]	Ref.
LBG, LvLBG, GG	0.135	49
GGMs	0.148	50
Cellulose	0.131	51

Results and discussion

Chemical analysis

The results from the chemical analysis are summarized in Table 2. Assuming polymeric mannose, galactose, glucose and acetyl content comprise acetylated GGM (AcGGM), this component accounted for 77% and 83% of the dry-weight for the TMP-GGM and SP-GGM preparations, respectively. The SP-GGM preparation contained arabinoxylan, estimated from the acid released xylose and arabinose as described above (Table 2). No detectable arabinoxylan was present in TMP-GGM. The lignin content was estimated to be 3.0% (TMP-GGM) and 3.3% (SP-GGM) of the dry weight, based on simple UV light absorption measurements.

1D and 2D NMR spectroscopy

Expansions of the 2D-NMR data in the anomeric region of SP and TMP preparations are shown in Fig. 1. The proton NMR resonances in the anomeric region were assigned based on HSQC and confirmed by comparison with literature.[18,19,59–61] The spectra recorded for both samples are similar confirming the similarity of the two samples. Hence, the SP is used as a template to describe assignments of the peaks. Table 3 shows the assignation in the anomeric area for SP

using HSQC (the corresponding data for TMP are shown in the ESI†).

Spectra analysis showed that the studied hemicelluloses (TMP and SP) mainly contain mannose, glucose and galactose thus can be described as galactoglucomannan (GGM). HSQC showed no resonances in the aromatic region characteristic of lignin and these samples could be considered as fairly pure in terms of lignin contamination, which is also consistent with the UV spectroscopy analyses. However, a fair amount of arabino glucuronoxylan is also part of the SP sample as previously reported for a similar preparation by Palm and Zacchi.[33] Sample TMP also contains arabino glucuronoxylan but in much lower amount. Traces of 4-O-methylglucoronic acid (4-O-Me-GlcA) were present in the SP sample, which was also reported by Palm and Zacchi.[33]

The 1D proton spectra of both samples at 70 °C is shown in Fig. 2 and corresponds to the general assignments in the anomeric region from Table 3. Apart from the anomeric signals assigned in the fingerprint region (4.4–5.5 ppm), signals at 2.1–2.24 ppm indicate presence of acetylated saccharides. This was further confirmed in HSQC, where typical cross peak for acetyl group is clearly seen in the insert of Fig. 1 at δ_H/δ_C 2.2–1.9/21.56–21.4. Of these acetylated saccharides, HSQC shows that they correspond to β-(1–4)-linked mannopyranosyl

Table 2 Structural properties of different mannans. The GGM chemical analysis is from present work and the reference is for the method of preparation. The guar gum and locust bean gum data is from supplier[38]

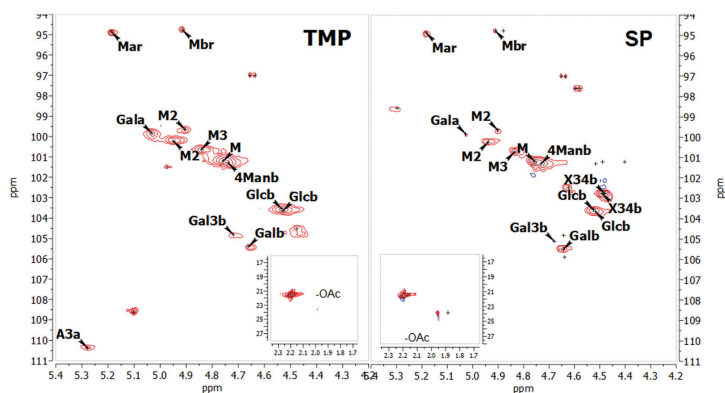| Sample | | Molecular weight [kDa] | Molar ratio | | | | | | Ref. |
			Man	Gal	Glc	Acetyl	Ara	Xyl	
Guar gum (GG)		250.0	67	33					38
Locust bean gum	LBG	556.0	78	22					
	LvLBG	107.0	78	22					
Spruce galactoglucomannan (GGM)	TMP	14.0	50	15	15	20			2, 6 and 33
	SP	5.9	40	6	16	2	2	8	

Fig. 1 2D NMR spectra of the anomeric region for the TMP (on the left) and SP (on the right) samples at 25 °C.
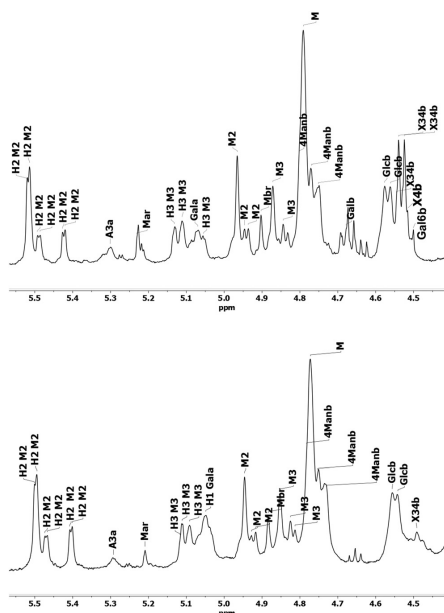
Fig. 2 Anomeric region of ¹H NMR spectra of *O*-acetyl-GGM SP (top) and TMP (bottom). Table 3 describes assignations.

Table 3 ¹H and ¹³C NMR data of the anomeric region for the SP-GGM

Constituent	Annotation	Fig. key	¹H (ppm)	¹³C (ppm)
Mannose	α-ManpR	Mar	5.18	94.87
	-4)-β-Manp-(1-, 2-*O*-Ac	M2	4.94	100.23
	-4)-β-Manp-(1-, 2-*O*-Ac	M2	4.9	99.65
	β-ManpR	Mbr	4.88,	94.77
			4.91	
	-4)-β-Manp-(1-, 3-*O*-Ac	M3	4.83	100.72
	β-Manp-(1-	M	4.76	101.21
	-4)-β-Manp-(1-	4Manb	4.73	101.3
Glucose	-4)-β-Glcp-(1-	Glcb	4.53	103.55
	-4)-β-Glcp-(1-	Glcb	4.52	103.65
Galactose	αGalp-(1-	Gala	5.03	99.84
Other polysacharides				
Arabino-xylan	-4,3)-β-Xylp-(1-	X34b	4.48,	102.77
			4.49	
	α-Araf-(1-3	A3a	5.28*a*	
β-Galactan	-4)-β-Galp-(1-	Galb	4.64	105.5
Arabino-galactan	-3)-β-Galp-(1-	Gal3b	4.68	105.11

a From ¹H NMR.

residues at C-2 and C-3 as previously reported.[19,59,61] For both acetylated saccharides HSQC showed multiple cross peaks as

well as several resonances in the 1D proton spectra (compare with inserts in Fig. 1). This reflects the random distribution of the acetylated residues along the backbone and was also observed by Lundqvist *et al.*[18]

Ratios of the different sugars were estimated using a semi-quantitative approach based on the volume integration[60,62] from HSQC as well as integration from 1D ¹H. The limitation of using volume integrals from HSQC is that the phase in the directly detected dimension varies between the different cross-peaks, with different amounts of the dispersive component contributing, thereby affecting their integral. The disadvantage of using ¹H is that with the overlap of peaks the accuracy of the integration is no more than 95% in some cases, this error would propagate when calculating ratios as they involve more than two integrals. Nevertheless, these methods are established and have been extensively used previously.[35,59] Quantification of molar fraction an estimation of masses was also calculated as done in Rosengren *et al.*,[36] using and external standard and using ERETIC 2 method as described previously. Given that the results from all the methods are comparable here we present the results from the ERETIC 2 based calculations in Tables 4 and 5. We have made the utmost effort to describe the correct assignation of all peaks.

Table 4 shows a summary of the composition estimates for both samples using NMR. The Man : Glu : Gal was estimated to be 100 : 22 : 9 and 100 : 18 : 5 for TMP and SP, respectively. Both samples are fairly similar except in the galactose molar content. Here it should be noted that galactose content is calculated based on α-galactose, the presence of galactan would up this number. GGM in softwood is described usually as substituted with only αGalp units.[19] Furthermore, the galactose peak is not well-resolved (*cf.* Fig. 2) and the integration is likely to substantial error. We also note that the chemical analysis (Table 2) gives a larger galactose content. The degree of acetylation (DSAc) was estimated by comparing the integrals of the acetylated regions and the GGM sugars in the anomeric region.[60]

Table 4 Total sugar composition of GGM samples

% mol	Man	Glc	αGal	AraXyl	Acetyl	DSAc*a*
TMP	64	14	6	5	12	0.15
SP	61	11	3	15	11	0.15

Man – mannose, Gal – galactose, Glc – glucose, AraXyl – arabino xylan. *a* The degree of acetylation was determined as the molar ratio of –OAc groups linked to the GGM sugars.

Table 5 Sugar composition of GGM samples in relation to mannose content

% mol	Man	αGal-Man*a*	OAc-Man	2-OAc Man	3-OAc Man
TMP	59	1	40	57	43
SP	59	5	36	58	42

Man – (unsubstituted) mannose, Gal – galactose, OAc-Man = 2-OAc + 3-OAc. *a* Molar fraction of non-acetylated mannose with galactose substituents assuming that mannose is either substituted with an –OAc or an αGal.

Table 4 shows that the main difference between both samples is the presence of higher amounts of arabino glucurunoxylan constituents in the SP sample (see Table S2, detailed SP NMR peak assignments are shown in ESI†). The given values include the two major residues of arabino glucuronxylan-3,4)-β-Xylp-(1- and α-Araf-(1–3 because they are the major constituents identified unequivocally from the spectra. Other components related to other polysaccharides such as arabinogalactan were not possible to use for quantification given their small area, ambiguity in peak assignation and/or overlapping with other peaks. Based on the values given in Table 4, the ratio of Man : AraXyl of ~1 : 0.24 was calculated for SP compared to 1 : 0.07 in TMP. Arabino glucuronoxylan is also a hemicellulose common in spent sulfite liquor (SSL) from spruce.[62] It has been shown that small amounts of arabinose and xylose can be covalent constituents of GGM.[63] Nevertheless, the presence of these polysaccharides may be due to hemicellulose contaminants. Other cross peaks related to arabino glucuronoxylan could be assigned to β-Xylp (4.13, 3.38/64.04) as well as the residue 3,4-Xylp in sample SP. Characteristic peaks of α-glucuronic acid were also detected. The cross peaks at 3.47/61.02 and 3.3/73.8 ppm indicate that a fraction of these residues carry the 4-O-methyl substituent.[19]

Table 5 shows the sugar composition in relation to the mannose content. The degree of acetylation (DSAc) was 0.15 in relation to the Manp units for both of the samples. As discussed above, the NMR spectra suggest that the acetylated residues are randomly distributed along the backbone. It is interesting to note that the molar fraction of non-acetylated mannose with galactose substituents is higher for the SP sample, however this can be related to the difficulties in determining the galactose content with NMR.

Dynamic and static light scattering (DLS and SLS). The combination of static and dynamic light scattering gives a measure of the overall shape and size of particles, molecules or aggregates in solution. The ratio between R_G and R_H indicates whether a polymer behaves as a random coil, forms a spherical particle ($R_G/R_H > 0.778$) or has a long rod-like conformation ($R_G/R_H > 2.0$) in solution.[64] Table 6 shows the average R_G and R_H of LBG, GG, LvLBG, TMP and SP GGM. All samples were filtered with 0.45 μm-pore filter to remove larger aggregates and dust that have disproportionally large impact on the scattering data due to their higher scattering power. The correlation functions are listed in the ESI† (Fig. S2).

The molecular weight and dimensions of the GGM monomer estimated from individual sugar groups are 0.18 kDa and 0.6 nm,

respectively. Therefore, fully stretched linear polymer in a mono-disperse sample with molecular weights of 14.0 kDa and 5.9 kDa, would be 47 nm and 20 nm long, respectively, which is almost three times lower than the obtained values. Thus, the GGM samples are likely to be aggregated. This conclusion is consistent with cryo-TEM images of TMP GGM at the same concentration (Fig. S4, in the ESI†) and with a recent study of a comparable GGM preparation that shows similar aggregated structures but larger in size,[65] likely due to a higher molecular weight and solution concentration of the sample. The expected contour length of the locust bean gum and guar gum samples, calculated based on the molecular weight of the corresponding linear polymer, is about 10 times larger than the measured value. This suggests that these polysaccharides are not aggregated but form separate polymer chains in solution. Furthermore, both GGMs have a R_G/R_H slightly higher than 1 (Table 6) which suggests that the aggregates have an elongated shape. With a R_G/R_H of around 0.7, LBG and GG chains seems to adopt a globular shape in solution. The radius of gyration for the GG and LBG are similar to literature values.[66,67]

Small-angle X-ray scattering. Fig. 3 shows the scattering curves obtained with SAXS for TMP and SP GGM samples with different molecular weights, as well as branching degree. Samples were characterized at three concentrations 5 mg mL^{-1}, 10 mg mL^{-1} and 20 mg mL^{-1} (Fig. S3, in the ESI†) but no significant difference in scattering was observed for either sample when taking into account the polymer concentration. Therefore, we show only the scattering curves recorded at 10 mg mL^{-1} for each sample. This study is focused on GGM and the galacto-mannans are to be considered as important reference samples. A detailed SAXS analyses for this type of samples require

Fig. 3 SAXS curves of the TMP (light red) and SP GGM (green) at a concentration of 10 mg mL^{-1}. Solid lines are fits to the corrected Beaucage model. The scattering curve of the TMP was shifted upwards by a factor of 10 for clarity.

Table 6 Molecular weight and the results obtained from DLS and SLS of the mannan-based polysaccharides

		M_w [kDa]	R_G [nm]	R_H [nm]	R_G/R_H
GGM	TMP	14.0	122	111 ± 8	1.10
	SP	5.9	87	82 ± 6	1.07
Locust bean gum	LvLBG	107.0	79	95 ± 14	0.75
	LBG	556.0	111	210 ± 39	0.53
Guar gum	GG	250.0	42	93 ± 16	0.61

synchrotron X-rays, and unfortunately, we only got limited beam time that was enough to fully characterize the GGM samples.

The scattering curves show no distinct features other than a shift of the power-law decay from -1.85 at low q to -1.0 at high q for TMP GGM (-1.7 to -0.95 for SP GGM) as indicated in Fig. 3. The lack of a drastic change in the slope through the extended q-range indicates self-similarity or fractal-like behaviour of the polymer molecules in solution. The scattering from such a polymer chain can be described by using a mass fractal model, *i.e.* the scattering intensity, $I(q) \sim q^{-d}$. Such a model is valid as the exponents ($-d$) are between -1 and -3.[45] The exponent of -1 at high q-values indicates rod-like shape of the polymer below its persistence length. Based on these observations, the scattering data was fitted to a corrected Beaucage model that describes fractal morphology with flexible cylinders as building blocks.[45,46] This model gives two radii of gyration that were determined from the low-q region and the transition region between two slopes of the scattering curve indicated in Fig. 3. The slope at low-q, *i.e.* in the regime where the Guiner model is valid, R_G represents the overall size of the polymer particle. However, in the case of (large) polymers, it can be challenging to reach the Guinier regime due to limited q-range of most instruments. The second R_G, however, can be converted to a Kuhn length l by using the eqn (6)[68,69]

$$l = \sqrt{12 R_G^2} \qquad (6)$$

The Kuhn length is twice the persistence length and a measure of the polymer chain stiffness. For the data shown in Fig. 3, we obtained $l = 8.4$ and $l = 11.2$ nm for SP and TMP GGM, respectively. This demonstrates a decreased chain flexibility due to branching, as TMP GGM has a higher galactose substitution degree than SP GGM according to the chemical analysis results (Table 2). This is not shown by NMR though, but here as discussed above the quantification of galactose is a bit uncertain. Another factor that can affect the results is the presence of higher amounts of arabino glucuronoxylan constituents in the SP sample.

Due to a high density of short galactose branches on the polysaccharide backbone, we expect the GGMs to behave as comb-like polymers. A computational study showed that branching considerably stiffens the backbone of comb-like polymers and the Kuhn segment length increases with increasing side chain length due to excluded volume interactions between side chains.[70]

AFM of cellulose film. The microcrystalline cellulose Avicel used in this study for the film formation has a crystalline structure characteristic to a native cellulose I. In order to solubilize cellulose, the strong inter and intramolecular hydrogen bonds need to be broken. This is achieved in LiCl/DMAc solvent as Li$^-$ anions form even stronger hydrogen bonds with the hydroxyl group protons of cellulose.[71] By breaking the hydrogen bonding network, cellulose fibres disintegrate into individual polymer chains or smaller bundles that can be dispersed in solution. Thus, it is likely to expect a change of cellulose crystal structure, when the cellulose is recrystallized at

surface from the LiCl/DMAc solvent. In fact after dissolution, the crystallinity index usually decreases to a value typical for a semicrystalline matrix (cellulose III).[72] Different aspects of crystallinity of cellulose and quantification has been thoroughly discussed by Krässig.[73] Important also to consider is the size of the crystalline domains, which can be estimated from broadening of the X-ray powder pattern.[74] Aulin *et al.* has used small incidence angle X-ray diffraction to estimate the crystallinity of thin films of cellulose prepared using different methods and sources.[75] They estimated the crystallinity of the type of surface films used in the present study to be about 15% or less.

Films from dissolved cellulose were characterized with AFM in non-contact mode in air before the ellipsometry and neutron reflectometry experiments. Fig. 4 shows the topographical features of the spin-coated cellulose surface. The surface is uniformly covered with cellulose fibrils associated in random network giving a fairly smooth layer and the root mean square roughness of the film is 3 nm.

We note that the applied protocol gives high reproducibility when it comes to surface structures as observed with AFM in air. Unfortunately, it is not possible to determine the crystallinity of the film with AFM. It was also not possible to image the surfaces under water with the used AFM set-up. This is partly due to swelling of the surface layer as observed by ellipsometry and described further below. Swelling of the cellulose film in water has also been observed by Aulin *et al.*[75]

Ellipsometry. The adsorption of mannans at low concentration (0.02 mg mL^{-1}) were studied *in situ* with null ellipsometry.
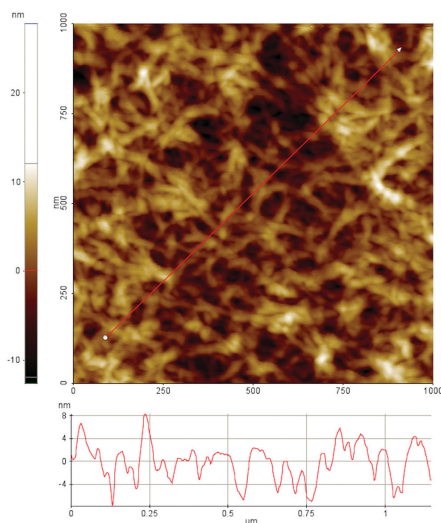

Fig. 4 AFM topography image of a cellulose film spin coated on silica substrate.
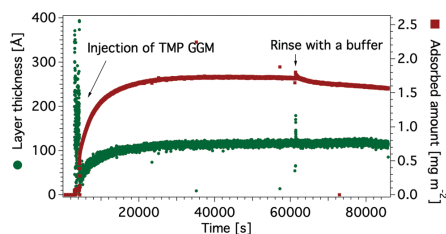
Fig. 5 Adsorbed amount (red) and layer thickness (green) of TMP GGM on a hydrophobic silicon oxide surface.

Fig. 5 shows the results from a typical adsorption measurement. The sample was added to the cuvette after the substrate had been equilibrated in the buffer. The kinetics of the adsorbed amount was then followed and after the plateau in adsorption is reached, the cuvette was rinsed with a neat buffer solution to reveal the reversibility of the adsorption.

Fig. 6 summarizes ellipsometry results for mannans on hydrophobic and cellulose coated surfaces. The adsorption *versus* time data are shown in Fig. S6 and S7, in the ESI.† The adsorbed amount is higher on cellulose surfaces than on hydrophobic surfaces for all studied polysaccharides. This suggests a stronger attractive interaction of mannans to the cellulose surface. One might speculate that this is due to a specific interaction between the two types of polysaccharides, *i.e.* mannans and cellulose. It is known that simple sugar surfactants, *i.e.* hexadecyl maltosides, show strongly attractive head group interactions, which is different for different stereoisomers and have large effect on the assembly behaviour.[76]

Similar tendency has also been observed with bacterial cellulose produced in the presence of mannan-based polysaccharides leading to a *co*-crystallisation of polysaccharides.[26,32,77] A contributing factor could also be that the rougher cellulose substrate gives a larger effective area and hence a larger number of adsorption sites.

We note that the ellipsometry data has been analysed with a model comprised of individual homogenous layers, *i.e.* silicon, silicon oxide and a top layer consisting of cellulose that also includes mannans after adsorption. We have used an alternative model with a separate mannan layer on top of the cellulose layer (Table S3, ESI†). We would like to remind that the cellulose films prepared with the above described method is expected to have a semicrystalline structure. We also note from the AFM image in Fig. 4 that the film has a rather open structure and we can expect that such a structure can entrap a significant amount of water, leading to swelling of the film. This was also observed with ellipsometry (Fig. S5, in the ESI†). Since the mannan–cellulose surface interaction is more favourable than the water–cellulose surface interaction, mannan polymers adsorb on surface replacing the water molecules.[23] Under such conditions we can regard the adsorption process as entropically driven. Compared to a flat and smooth hydrophobic surface the rougher cellulose surface has also a larger effective area to which hemicellulose can bind.

The adsorbed amount of the mannans to the cellulose surface is dependent on the molecular weight of polymer chains as the highest value was obtained with the 556 kDa Locust bean gum (3.4 ± 0.2 mg m^{-2}) and the lowest one with the 5.9 kDa SP (2.1 ± 0.3 mg m^{-2}) and 14 kDa TMP GGM (2.1 ± 0.1 mg m^{-2}). The effect of the molecular weight on the adsorption of polysaccharides was previously noted by Kabel *et al.*[25] who compared the adsorption of xylans with different molecular weights to bacterial cellulose. However, a study by Hannuksela *et al.*[5] on the interaction between enzymatically modified guar gum and bleached kraft pulp found that the galactose substitution degree has a stronger impact on the adsorbed amount to cellulose than molecular weight. The highest adsorption was found for mannans with lower density of galactose units for both high and low molecular weight samples. The authors suggested that a close contact between mannan backbone and cellulose surface is necessary to obtain high adsorbed amount and a large density of side groups prevents this close contact.

We can conclude that all studied mannan polymers have fairly hydrophobic character based on the ellipsometry results that show significant adsorption on the hydrophobic surface. GGMs give higher adsorbed amount on hydrophobic surfaces than galactomannans. A plausible explanation is the acetylation carried by the GGM backbone but not by the galactomannans (Table 2). The NMR spectra indicated that the acetylation is randomly distributed along the polysaccharide chain. An additional contributing factor may be the amphiphilic character of sugar monomers, displaying a hydrophobic surface that makes hydrophobic interactions favourable[78] as described *e.g.* for cellulose.[79,80] The hydrophobicity of mannoses is suggested to be similar or even slightly higher than for glucose.[78] With the lower degree of galactosylation of the used GGM (Table 2) it could be argued that the GGM on average have longer unsubstituted backbone regions which potentially, in addition to acetyls, could be responsible for interactions with the hydrophobic surface. All the polysaccharides have higher adsorbed amount on the cellulose surface than on the hydrophobic surface. This is possibly due to attractive interaction between
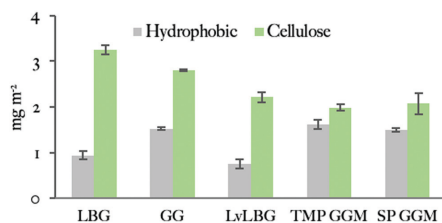

Fig. 6 Adsorbed amounts of mannan-based polysaccharides on hydrophobic and cellulose surfaces studied by ellipsometry. Data is represented in the order of decreasing polysaccharide molecular weight. Measurements were repeated at least once.

Table 7 The summary of the adsorbed amounts on hydrophobic surfaces as followed with ellipsometry and QCM-D, and the calculated solvent content in the adsorbed layer

		LBG	GG	LvLBG	TMP GGM	SP GGM
Adsorbed amount (mg m^{-2})	QCM-D	26 ± 6	30 ± 10	31 ± 4	28 ± 3	28 ± 1
	Ellipsometry	0.94 ± 0.09	1.53 ± 0.03	0.8 ± 0.1	1.6 ± 0.1	1.50 ± 0.03
Solvent content [%]		96	95	97	94	95

the carbohydrate groups of the adsorbing polymer and those in the cellulose surface. Although this cannot be the driving force of the hemicellulose attachment, it can possibly make the adsorption less reversible. In this respect, it can lead to an apparently higher adsorption. In addition, the more open structure of the cellulose film will lead to higher specific area as discussed above. The adsorption was found to increase with the molecular weight and in contrast to the study of Hannuksela *et al.*,[5] we did not find a correlation between difference in branching as indicated by the chemical analysis (Table 2) and adsorption.

Quartz crystal microbalance with dissipation. The adsorption of mannan-based polysaccharides on hydrophobic surface was studied using QCM-D. The adsorbed amount on hydrophobic surfaces was obtained from fitting the data to the Voigt viscoelastic model, see ESI† (Fig. S8, in the ESI†). The adsorbed amounts recorded by QCM-D (Table 7) are significantly higher than those obtained with ellipsometry. This is because QCM-D measures the wet mass of the adsorbed layer that includes coupled water. The combined results from ellipsometry and QCM-D show that the adsorbed mannan layer is highly hydrated with the solvent amount above 90%. Here is noteworthy that the SAXS data suggest that the GGM polymer chains are quite stiff, presumably due to the presence of galactose side chains. Unless the GGM chain is parallel to the surface, portions of the GGM molecules will extend into solution and contribute to the large added amount as revealed with QCM-D, *i.e.* larger amount of coupled water. The high content of water in the adsorbed layers of mannans have already been reported previously with 91% for GG and 65% for GGM.[28,81] However, the dry mass of the added layer of GG and GGM on cellulose (0.26 mg m^{-2} and 0.6 mg m^{-2}) is much lower than the one obtained in the current study (2.8 mg m^{-2} and 2.0 mg m^{-2}) with the ellipsometry. This could be explained by the difference in the thickness of the cellulose layer. As shown in Fig. S9 (in the ESI†), the thickness of a cellulose layer has a significant effect on the adsorbed amount of the mannan.

Neutron reflectometry. Neither ellipsometry nor QCM-D allows for a determination of the density profile of the adsorbed biopolymer layer perpendicular to the surface; the adsorption of TMP GGM on hydrophobic surface was therefore studied with neutron reflectometry. The reflectivity curves and modelling results are shown in Fig. 7. The model fit parameters are summarized in Table 8.

A significant change in the measured reflectivity is observed after the addition of TMP GGM compared to the bare surface, although the changes in the measurements with H$_2$O solvent
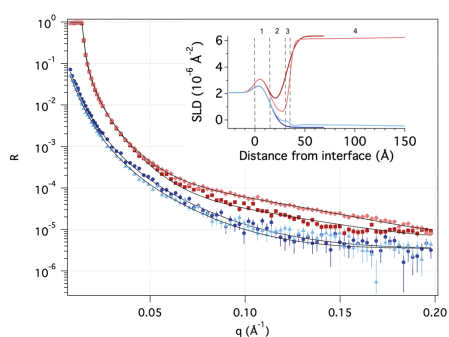

Fig. 7 Neutron reflectivity as a function of momentum transfer (*q*) of pure hydrophobic surface (dark red in D$_2$O and dark blue in H$_2$O) and after adsorption of TMP (light red in D$_2$O and light blue in H$_2$O). Solid black lines represent the theoretical fit. The inset illustrates the scattering length density (SLD) profile as a function of distance from the Si surface based on the fitting with the numbers indicating layers described in Table 8.

are smaller due to the comparatively low scattering contrast between H$_2$O and TMP GGM.

The best fit to the data with a χ^2 of 3.6 was obtained by using a simple optical model where the TMP GGM layer is divided into two. Here, the layer closest to the hydrophobic surface is expected to have more of GGM moieties with acetyl groups and parts of the hydrophobic layer *i.e.* the transition layer. The top layer is expected to be much more hydrated with more of the non-acetylated sugar moieties. The roughness takes care of the fact there are no sharp borders between the layers, but rather a (Gaussian) distribution of matter.

The transition layer is around 4 Å with the scattering length density (SLD) equal to 0.7×10^{-6} Å^{-2} in D$_2$O and 0.5×10^{-6} Å^{-2} in H$_2$O. This suggests that there is very little water in this layer. The top layer is 210 Å with the SLD of 3.4×10^{-6} Å^{-2} and 1.9×10^{-6} Å^{-2} in D$_2$O and H$_2$O, respectively. According to Raghuwanshi *et al.*[82] every glucose unit in cellulose contains three hydrogens that are instantly exchanged with deuterium, therefore SLD of the polysaccharide is different in D$_2$O and H$_2$O. The top layer is much thinner than expected from the hydrodynamic radius (see Table 6), indicating that the polymer takes a flat conformation on the hydrophobic surface. As we have shown previously by combining the results obtained with ellipsometry and QCM-D, the top layer is highly hydrated with the solvent amount of 97%.

Table 8 Parameters obtained from the fitting of NR data measured in D_2O and H_2O. The numbers correlate to the layer numbers in the SLD profile in Fig. 7

	1	2	3		4	
	SiO_x	Hydrophobic layer	Transition layer		GGM	
			D_2O	H_2O	D_2O	H_2O
SLD [10^{-6} Å^{-2}]	3.47	-0.44 ± 0.02	0.68 ± 0.08	0.5 ± 0.4	3.4 ± 0.1	1.9 ± 0.5
Layer thickness [Å]	15.6 ± 0.2	15.8 ± 0.1	4.0 ± 0.2		210 ± 11	
Solvent [v/v, %]	8.7 ± 0.6	6.9 ± 0.3	14 ± 1		97.1 ± 0.1	
Roughness [Å]	8.2 ± 0.1	8.3 ± 0.1	2.1 ± 0.2		97 ± 13	

Conclusions

The nature of the interactions between hemicellulose and cellulose is important for both understanding the processes inside plant cell walls, as well as a tool for development of various sustainable materials to replace fossil-based ones. Although these interactions have been studied since 1980s, the nature of the interactions are still not fully understood due to lack of access to well-defined samples and challenges when it comes to preparation of samples and characterisation techniques.

The main aim of this work was to reveal the structural properties of softwood hemicellulose that controls their affinity to cellulose surfaces. The adsorption of softwood hemicellulose (GGM) and similar galactomannans was studied with ellipsometry, QCM-D and neutron reflectometry. To provide further understanding of the forces that control the interaction between hemicellulose and cellulose, the adsorption was also performed on the hydrophobised silica. The combined results from these measurements show:

1. All polymers showed a higher adsorbed amount on the cellulose surface than on the hydrophobic one. This can be related to the larger specific area of the cellulose layer. In addition, attractive interaction between the adsorbing polymer sugar groups and corresponding groups in the cellulose layer might contribute to anchoring the polymer to the surface.

2. The substantial adsorption to the hydrophobic surface indicates that the polysaccharides have a fairly hydrophobic character. The results also suggest that GGM samples are more hydrophobic as shown by NR possibly due to the presence of acetyl side groups in the GGM structure that interact with the hydrophobic surface.

Cellulose films prepared in this study are expected to have a semi-crystalline nature with amorphous regions entrapping large amount of water molecules. The interaction between mannan and cellulose molecules are more favourable than cellulose–water interaction due to relatively hydrophobic nature of both polymers. We therefore expect that increase of entropy due to the release of water upon adsorption is one of the driving forces.

Mannans form a diffuse monolayer with parts extending into the solution as observed by QCM-D and NR. This is supported by the SAXS data showing that GGMs are quite stiff, likely due to bulky galactose side groups. DLS, SLS and Cryo-TEM indicate that polymers are present in the solution in the aggregated state. However, the observed thickness of the layer is smaller, which indicates that they rearrange and take flat conformation at the interface.

The adsorption to cellulose coated surface increases with the molecular weight, however, no clear impact of the galactose substitution degree was found.

Conflicts of interest

There are no conflicts to declare.

Acknowledgements

References

1 E. Sjostrom, *Wood chemistry: fundamentals and applications*, Gulf professional publishing, 1993.

2 J. Lundqvist, A. Jacobs, M. Palm, G. Zacchi, O. Dahlman and H. Stålbrand, *Carbohydr. Polym.*, 2003, **51**, 203–211.

3 H. V. Scheller and P. Ulvskov, *Annu. Rev. Plant Biol.*, 2010, **61**, 263–289.

4 S. Willför, K. Sundberg, M. Tenkanen and B. Holmbom, *Carbohydr. Polym.*, 2008, **72**, 197–210.

5 T. Hannuksela, M. Tenkanen and B. Holmbom, *Cellulose*, 2002, **9**, 251–261.

6 A. Andersson, T. Persson, G. Zacchi, H. Stålbrand and A.-S. Jönsson, *Appl. Biochem. Biotechnol.*, 2007, **137**, 971–983.

7 B. Al-Rudainy, M. Galbe and O. Wallberg, *Sep. Purif. Technol.*, 2017, **187**, 380–388.

8 B. Al-Rudainy, M. Galbe, H. Schagerlöf and O. Wallberg, *Holzforschung*, 2018, **72**, 839–850.

9 B. Ünal, S. Metin and N. D. Işikli, *Int. Dairy J.*, 2003, **13**, 909–916.

10 P. K. Soma, P. D. Williams and Y. M. Lo, *Front. Chem. Eng. China*, 2009, **3**, 413–426.

11 M. A. Cerqueira, A. I. Bourbon, A. C. Pinheiro, J. T. Martins, B. W. S. Souza, J. A. Teixeira and A. A. Vicente, *Trends Food Sci. Technol.*, 2011, **22**, 662–671.

12 S. Parija, M. Misra and A. K. Mohanty, *J. Macromol. Sci., Rev. Macromol. Chem. Phys.*, 2001, **41**, 175–197.

13 A. Ebringerová, Z. Hromádková, V. Hříbalová, C. Xu, B. Holmbom, A. Sundberg and S. Willför, *Int. J. Biol. Macromol.*, 2008, **42**, 1–5.

14 K. S. Mikkonen, M. I. Heikkilä, H. Helén, L. Hyvönen and M. Tenkanen, *Carbohydr. Polym.*, 2010, **79**, 1107–1112.

15 J. Hartman, A. C. Albertsson, M. S. Lindblad and J. Sjöberg, *J. Appl. Polym. Sci.*, 2006, **100**, 2985–2991.

16 J. Hartman, A. C. Albertsson and J. Sjöberg, *Biomacromolecules*, 2006, **7**, 1983–1989.

17 A. Doliška, S. Willför, S. Strnad, V. Ribitsch, K. S. Kleinschek, P. Eklund and C. Xu, *Holzforschung*, 2012, **66**, 149–154.

18 J. Lundqvist, A. Teleman, L. Junel, G. Zacchi, O. Dahlman, F. Tjerneld and H. Stålbrand, *Carbohydr. Polym.*, 2002, **48**, 29–39.

19 T. Hannuksela and C. Herve du Penhoat, *Carbohydr. Res.*, 2004, **339**, 301–312.

20 T. Hayashi, K. Ogawa and Y. Mitsuishi, *Plant Cell Physiol.*, 1994, **35**, 1199–1205.

21 Å. Linder, R. Bergman, A. Bodin and P. Gatenholm, *Langmuir*, 2003, **19**, 5072–5077.

22 J.-P. Vincken, A. de Keizer, G. Beldman and A. G. J. Voragen, *Plant Physiol.*, 1995, **108**, 1579–1585.

23 T. Benselfelt, E. D. Cranston, S. Ondaral, E. Johansson, H. Brumer, M. W. Rutland and L. Wågberg, *Biomacromolecules*, 2016, **17**, 2801–2811.

24 T. Hayashi, T. Takeda, K. Ogawa and Y. Mitsuishi, *Plant Cell Physiol.*, 1994, **35**, 893–899.

25 M. A. Kabel, H. van den Borne, J.-P. Vincken, A. G. J. Voragen and H. A. Schols, *Carbohydr. Polym.*, 2007, **69**, 94–105.

26 K. I. Uhlin, R. H. Atalla and N. S. Thompson, *Cellulose*, 1995, **2**, 129–144.

27 S. Ahola, P. Myllytie, M. Osterberg, T. Teerinen and J. Laine, *BioResources*, 2008, **3**, 1315–1328.

28 P. Eronen, K. Junka, J. Laine and M. Österberg, *BioRes*, 2011, **6**, 4200–4217.

29 S. Gao and K. Nishinari, *Biomacromolecules*, 2004, **5**, 175–185.

30 S. Gao and K. Nishinari, *Colloids Surf., B*, 2004, **38**, 241–249.

31 J.-y. Liu, H.-c. Wang, Y. Yin, N. Li, P.-l. Cai and S.-l. Yang, *Carbohydr. Polym.*, 2012, **89**, 158–162.

32 T. Iwata, L. Indrarti and J. I. Azuma, *Cellulose*, 1998, **5**, 215–228.

33 M. Palm and G. Zacchi, *Sep. Purif. Technol.*, 2004, **36**, 191–201.

34 F. Örså, B. Holmbom and J. Thornton, *Wood Sci. Technol.*, 1997, **31**, 279–290.

35 R. Schröder, P. Nicolas, S. J. Vincent, M. Fischer, S. Reymond and R. J. Redgwell, *Carbohydr. Res.*, 2001, **331**, 291–306.

36 A. Rosengren, S. J. Butler, M. Arcos-Hernandez, K.-E. Bergquist, P. Jannasch and H. Stålbrand, *Green Chem.*, 2019, **21**, 2104–2118.

37 G. Wider and L. Dreier, *J. Am. Chem. Soc.*, 2006, **128**, 2571–2576.

38 Megazyme, https://www.megazyme.com, accessed December 2017.

39 R. Sczech and H. Riegler, *J. Colloid Interface Sci.*, 2006, **301**, 376–385.

40 D. P. Chang, J. Jankunec, J. Barauskas, F. Tiberg and T. Nylander, *ACS Appl. Mater. Interfaces*, 2012, **4**, 2643–2651.

41 T. Zemb and P. Lindner, *Neutron, X-Rays and Light. Scattering Methods Applied to Soft Condensed Matter*, North Holland, 2002.

42 D. E. Koppel, *J. Chem. Phys.*, 1972, **57**, 4814–4820.

43 SasView, https://www.sasview.org/, accessed February 2019.

44 G. Beaucage, *J. Appl. Crystallogr.*, 1995, **28**, 717–728.

45 B. Hammouda, *J. Appl. Crystallogr.*, 2010, **43**(6), 1474–1478.

46 G. Beaucage, *J. Appl. Crystallogr.*, 1996, **29**, 134–146.

47 F. Tiberg and M. Landgren, *Langmuir*, 1993, **9**, 927–932.

48 J. A. De Feijter, J. Benjamins and F. A. Veer, *Biopolymers*, 1978, **17**, 1759–1772.

49 G. Robinson, S. B. Ross-Murphy and E. R. Morris, *Carbohydr. Res.*, 1982, **107**, 17–32.

50 C. Xu, A. Pranovich, L. Vähäsalo, J. Hemming, B. Holmbom, H. A. Schols and S. Willför, *J. Agric. Food Chem.*, 2008, **56**, 2429–2435.

51 Y. Ono, T. Ishida, H. Soeta, T. Saito and A. Isogai, *Biomacromolecules*, 2016, **17**, 192–199.

52 M. V. Voinova, M. Jonson and B. Kasemo, *Spectroscopy*, 2004, **18**(4), 537–544.

53 M. V. Voinova, M. Rodahl, M. Jonson and B. Kasemo, *Phys. Scr.*, 1999, **59**, 391.

54 J. Penfold and R. Thomas, *J. Phys.: Condens. Matter*, 1990, **2**, 1369–1412.

55 J. A. Dura, D. J. Pierce, C. F. Majkrzak, N. C. Maliszewskyj, D. J. McGillivray, M. Lösche, K. V. O'Donovan, M. Mihailescu, U. Perez-Salas, D. L. Worcester and S. H. White, *Rev. Sci. Instrum.*, 2006, **77**(7), 74301–7430111.

56 B. Maranville, W. Ratcliff II and P. Kienzle, *J. Appl. Crystallogr.*, 2018, **51**, 1500–1506.

57 A. Nelson, *J. Appl. Crystallogr.*, 2006, **39**, 273–276.

58 A. Nelson, *J. Phys.: Conf. Ser.*, 2010, **251**, 012094.

59 B. Al-Rudainy, M. Galbe, M. Arcos Hernandez, P. Jannasch and O. Wallberg, *Polymers*, 2019, **11**, 35.

60 J. Berglund, S. Achar, M. Lawoko, M. Lindström, F. Vilaplana, J. Wohlert and G. Henriksson, *Cellulose*, 2019, **26**, 2155–2175.

61 H. Lindqvist, J. Holmback, A. Rosling, K. Salminen, B. Holmbom, M. Auer and A. Sundberg, *BioResources*, 2013, **8**, 994–1010.

62 B. Al-Rudainy, M. Galbe, F. Lipnizki and O. Wallberg, *Membranes*, 2019, **9**, 99.

63 I. M. Sims, D. J. Craik and A. Bacic, *Carbohydr. Res.*, 1997, **303**, 79–92.

64 W. Burchard, *Laser light scattering in biochemistry*, 1992, pp. 3–22.

65 S. Kishani, F. Vilaplana, W. Xu, C. Xu and L. Wågberg, *Biomacromolecules*, 2018, **19**, 1245–1255.

66 D. R. Picout, S. B. Ross-Murphy, N. Errington and S. E. Harding, *Biomacromolecules*, 2001, **2**, 1301–1309.

67 D. R. Picout, S. B. Ross-Murphy, K. Jumel and S. E. Harding, *Biomacromolecules*, 2002, **3**, 761–767.

68 B. W. Mansel, C.-Y. Chu, A. Leis, Y. Hemar, H.-L. Chen, L. Lundin and M. A. K. Williams, *Biomacromolecules*, 2015, **16**, 3209–3216.

69 P. Hernandez-Cerdan, B. Mansel, A. Leis, L. Lundin and M. A. K. Williams, *On the Structural Analysis of Polysaccharide-Networks by Transmission Electron-Microscopy: Comparison with SAXS*, 2018.

70 Y. Nakamura and T. Norisuye, *Polym. J.*, 2001, **33**, 874–878.

71 C. Zhang, R. Liu, J. Xiang, H. Kang, Z. Liu and Y. Huang, *J. Phys. Chem. B*, 2014, **118**, 9507–9514.

72 A. L. Da Róz, F. L. Leite, L. V. Pereiro, P. A. P. Nascente, V. Zucolotto, O. N. Oliveira and A. J. F. Carvalho, *Carbohydr. Polym.*, 2010, **80**, 65–70.

73 H. A. Krässig, *Cellulose, structure, accessibility and reactivity*, Gordon and Breach Publishers, Philadelphia, PA, 1993.

74 C. J. Garvey, I. H. Parker and G. P. Simon, *Macromol. Chem. Phys.*, 2005, **206**, 1568–1575.

75 C. Aulin, S. Ahola, P. Josefsson, T. Nishino, Y. Hirose, M. Österberg and L. Wågberg, *Langmuir*, 2009, **25**, 7675–7685.

76 J. Larsson, A. Sanchez-Fernandez, N. Mahmoudi, L. C. Barnsley, M. Wahlgren, T. Nylander and S. Ulvenlund, *Langmuir*, 2019, **35**(43), 13904–13914.

77 S. E. C. Whitney, J. E. Brigham, A. H. Darke, J. S. G. Reid and M. J. Gidley, *Carbohydr. Res.*, 1998, **307**, 299–309.

78 M. Janado and Y. Yano, *J. Solution Chem.*, 1985, **14**, 891–902.

79 C. Yamane, T. Aoyagi, M. Ago, K. Sato, K. Okajima and T. Takahashi, *Polym. J.*, 2006, **38**, 819–826.

80 B. Lindman, G. Karlström and L. Stigsson, *J. Mol. Liq.*, 2010, **156**, 76–81.

81 P. Eronen, M. Österberg, S. Heikkinen, M. Tenkanen and J. Laine, *Carbohydr. Polym.*, 2011, **86**, 1281–1290.

82 V. S. Raghuwanshi, J. Su, C. J. Garvey, S. A. Holt, W. Raverty, R. F. Tabor, P. J. Holden, M. Gillon, W. Batchelor and G. Garnier, *Cellulose*, 2017, **24**, 11–20.

Electronic Supplementary information

On the interaction of softwood hemicellulose with cellulose surfaces in relation to molecular structure and physicochemical properties of hemicellulose

Polina Naidjonoka,[*a] **Monica Arcos Hernandez**[b]**, Gunnar K. Pálsson** [c,d]**, Frank Heinrich** [e,f]**, Henrik Stålbrand**[*g]**, Tommy Nylander**[*a,h,i]

[a.] *Physical Chemistry, Department of Chemistry, Lund University, Lund, Sweden.*

[b.] *Polymer & Materials Chemistry, Department of Chemistry, Lund University, Lund, Sweden*

[c.] *Department of Physics & Astronomy, Uppsala University, Uppsala, Sweden.*

[d.] *Institut Laue Langevin, Grenoble, France.*

[e.] *Department of Physics, Carnegie Mellon University, Pittsburgh PA, USA*

[f.] *NIST Center for Neutron Research, Gaithersburg MD, USA*

[g.] *Biochemistry and Structural Biology, Department of Chemistry, Lund University, Lund, Sweden*

[h.] *NanoLund, Lund University, Lund Sweden*

[i.] *Lund Institute of Advanced Neutron and X-ray Science LINXS, Lund, Sweden.*

*polina.naidjonoka@fkem1.lu.se

*tommy.nylander@fkem1.lu.se

*henrik.stalbrand@biochemistry.lu.se

TMP anomeric assignation:

Table S1 ^{1}H and ^{13}C NMR data of the anomeric region for the TMP GGM

Constituent	^{1}H (ppm)	^{13}C (ppm)	Annotation	Figure Key
	5.19	94.86	α-ManpR	Mar
	4.94	100.23	-4)-β-Manp-(1-, 2-O-Ac	M2
	4.90	99.64	-4)-β-Manp-(1-, 2-O-Ac	M2
mannose	4.91	94.77	β-ManpR	Mbr
	4.84	100.62	-4)-β-Manp-(1-, 3-O-Ac	M3
	4.76	101.20	β-Manp-(1-	M
	4.74	101.30	-4)-β-Manp-(1-	4Manb
glucose	4.53	103.55	-4)-β-Glcp-(1-	Glcb
	4.52	103.65	4)-β-Glcp-(1-	Glcb
galactose	5.03	99.84	αGalp-(1-	Gala
Other polysaccharides				
arabino glucuronoxylan	4.49	102.76	-3,4)-β-Xylp-(1-	X34b
	5.28	110.37	α-Araf-(1-3	Ara3
arabinogalactan	5.10	108.62		Ara3
β-Galactan	4.64	105.50	-4)-β-Galp-(1-	Galb

Table S2. NMR spectra peak assignment for SP Sample

Constituent	Annotation	Figure Key	1 1H (ppm)	1 13C (ppm)	2 1H (ppm)	2 13C (ppm)	3 1H (ppm)	3 13C (ppm)	4 1H (ppm)	4 13C (ppm)	5 1H (ppm)	5 13C (ppm)	6a 1H (ppm)	6a 13C (ppm)	6b 1H (ppm)	6b 13C (ppm)
mannose	α-ManpR	Mar	5.18	94.87												
	-4)-β-Manp-(1-, 2-O-Ac	M2	4.94	100.23	5.49	72.82										
	-4)-β-Manp-(1-, 2-O-Ac	M2	4.9	99.65	5.42, 5.52	72.72	4.04	71.16	3.82	77.6	3.53	76.14				
	β-ManpR	Mbr	4.88, 4.91	94.77												
	-4)-β-Manp-(1-, 3-O-Ac	M3	4.83	100.72	4.12, 4.2	69.8	5.11	74.48	4.04	74.28						
	β-Manp-(1-	M	4.76	101.21	4.07	71.55	3.64	73.89	3.57	67.75	3.43	77.5	3.94	61.99	4	61.31
	-4)-β-Manp-(1-	4Manb	4.73	101.3	4.13	71.06	3.79, 3.82	72.53	3.77, 3.81	78.48	3.45	75.94	3.75, 3.9	61.6	3.81	61.8
glucose	-4)-β-Glcp-(1-	Glcb	4.53	103.55	3.36	73.89	3.69	74.97	3.62	79.55	3.79	77.5				
	4)-β-Glcp-(1-	Glcb	4.52	103.65					3.69	79.55						
galactose	αGalp-(1-	Gala	5.03	99.84	3.82	69.5	3.94	70.48	4.01	70.28	3.91	71.94	3.75	62.29		
Other polysaccharides																
arabino glucuronoxylan	-3,4)-β-Xylp-(1-	X34b	4.48, 4.49	102.77												
	-4)-β-Xylp-(1-	X4b					3.56	73.8			3.36, 4.13	64.04				
	α-GlcpA-(1-2	aGlc			3.56	72.33										
	α-Araf-(1-3	Ara3	5.28[1]													
β-Galactan	-4)-β-Galp-(1-	Galb	4.64	105.5					4.18	78.77						
Arabinogalactan	-3)-β-Galp-(1-	Gal3b	4.68	105.11												

[1]from 1D 1H spectrum

SP Mannose region assignation:
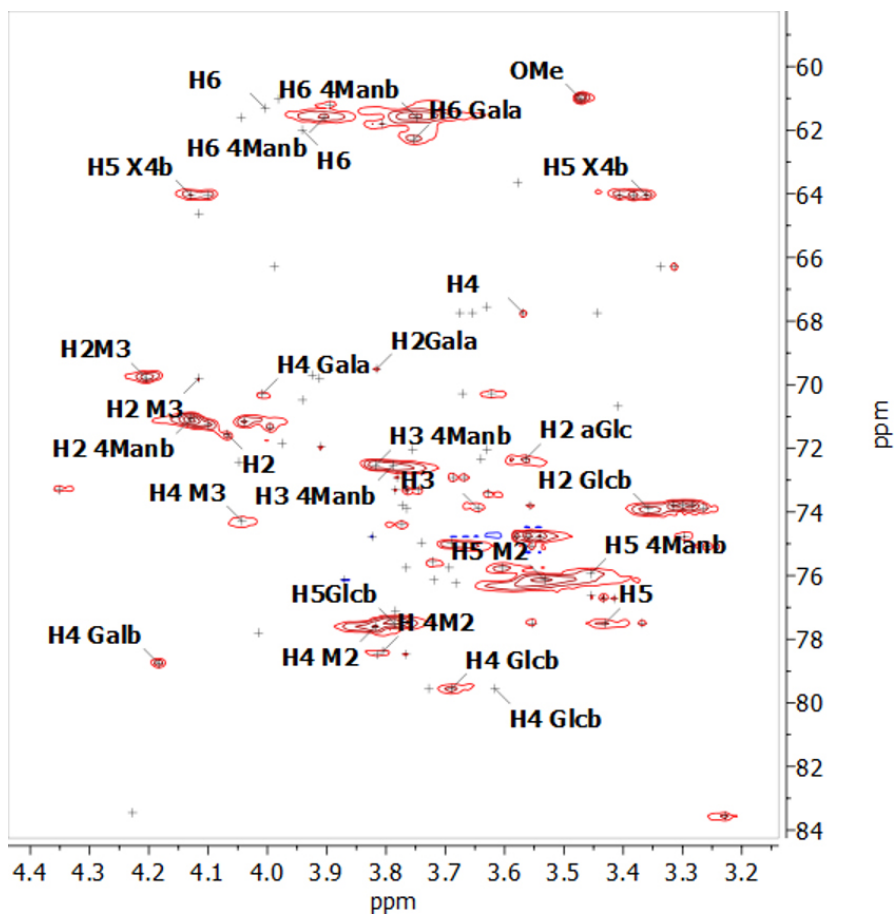
Figure S1 Assignment of cross peaks for mannose in HSQC (Table S2).

DLS autocorrelation functions:
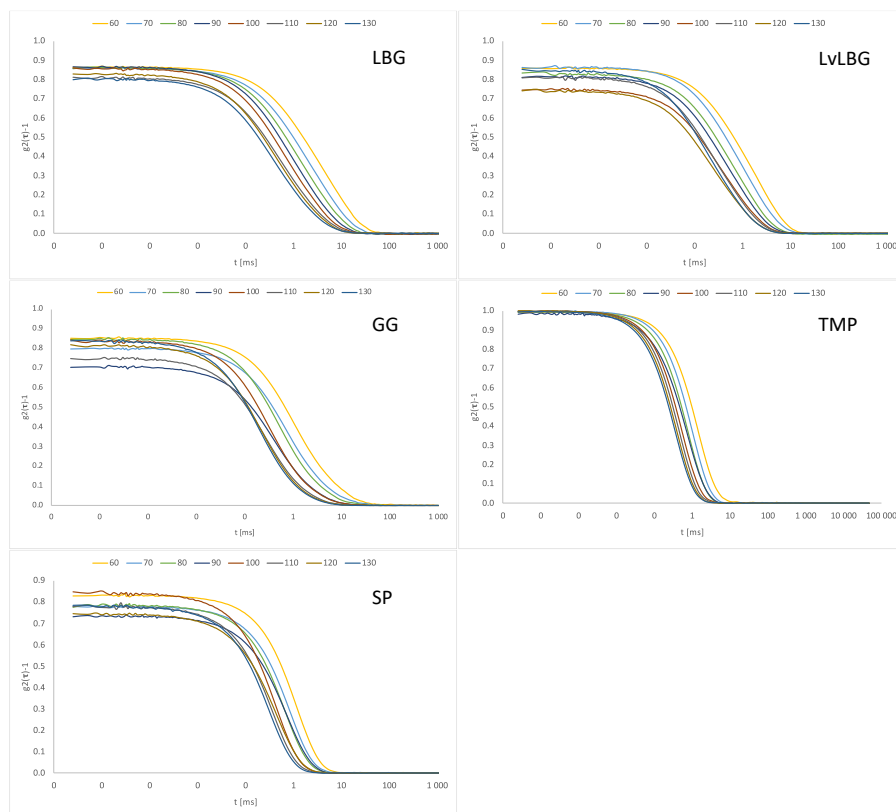
Figure S2 Dynamic light scattering correlation functions of mannans obtained for different angles.

SAXS scattering curves:
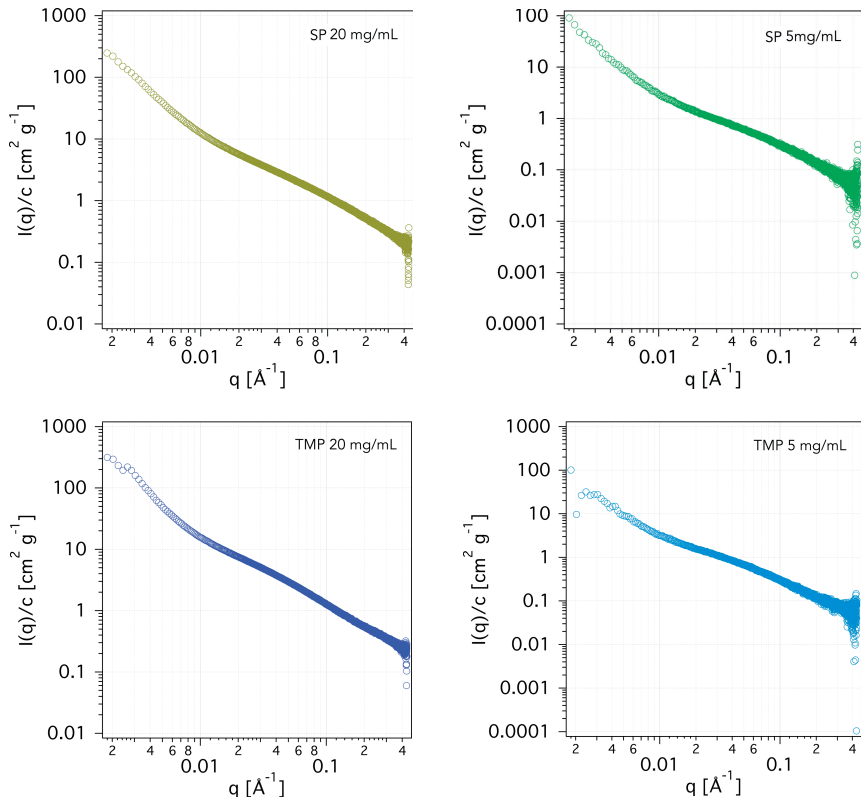
Figure S3 Scattering curves of TMP and SP GGM samples at concentrations of 5 mg/mL and 20 mg/mL.
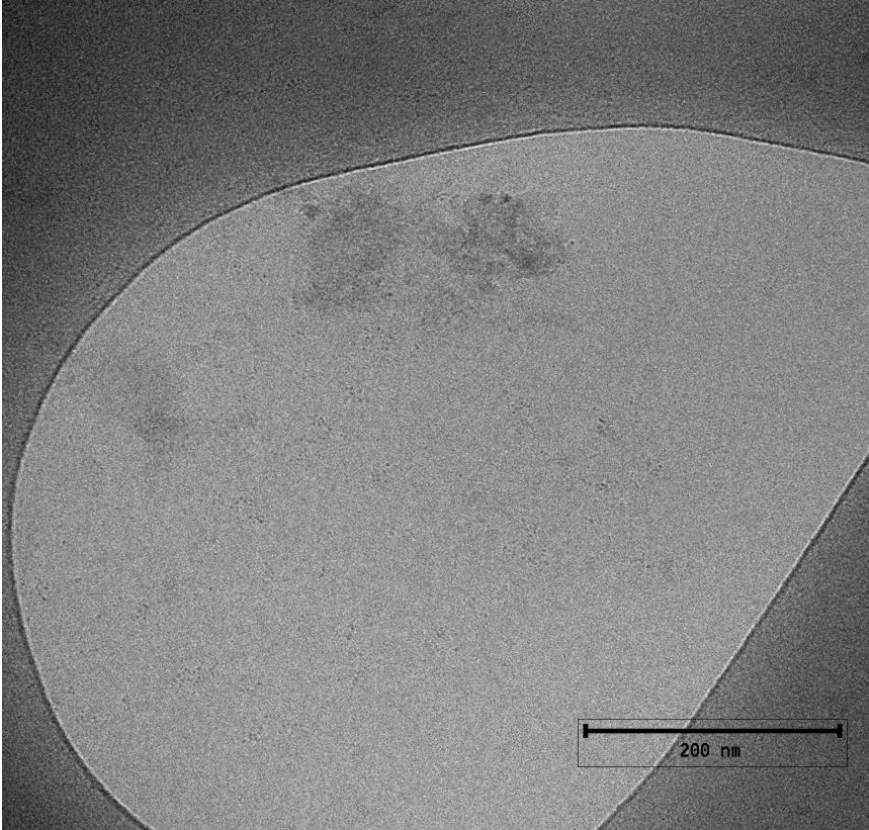
Figure S4 Cryo-TEM image of TMP GGM

Table S3 Ellipsometry results obtained by fitting experimental data on cellulose surface to a 3-layer model.

	Layer	Refractive index	Thickness [Å]	Adsorbed amount [mg/m²]
1	LBG	1.416	57	3.1
	Cellulose	1.424	450	28.1
	SiOn	1.470	274	
	Si	5.512		
2	LBG	1.408	50	2.4
	Cellulose	1.420	460	27.4
	SiOn	1.466	279	
	Si	5.475		
1	GG	1.418	44	2.5
	Cellulose	1.423	460	28.4
	SiOn	1.467	297	
	Si	5.515		
2	GG	1.413	56	2.9
	Cellulose	1.421	414	24.9
	SiOn	1.465	270	
	Si	5.470		
1	LvLBG	1.421	37	2.2
	Cellulose	1.425	394	24.9
	SiOn	1.472	268	
	Si	5.478		
2	LvLBG	1.418	35	2.0
	Cellulose	1.423	439	27.1
	SiOn	1.471	267	
	Si	5.479		
1	TMP	1.417	38	1.9
	Cellulose	1.413	438	23.7
	SiOn	1.472	278	
	Si	5.478		
2	TMP	1.417	39	2.0
	Cellulose	1.423	486	30.0
	SiOn	1.471	260	
	Si	5.477		
1	SP	1.416	41	2.0
	Cellulose	1.42	411	24.4
	SiOn	1.468	276	
	Si	5.478		
2	SP	1.412	37	1.7
	Cellulose	1.417	432	24.7
	SiOn	1.468	261	
	Si	5.481		
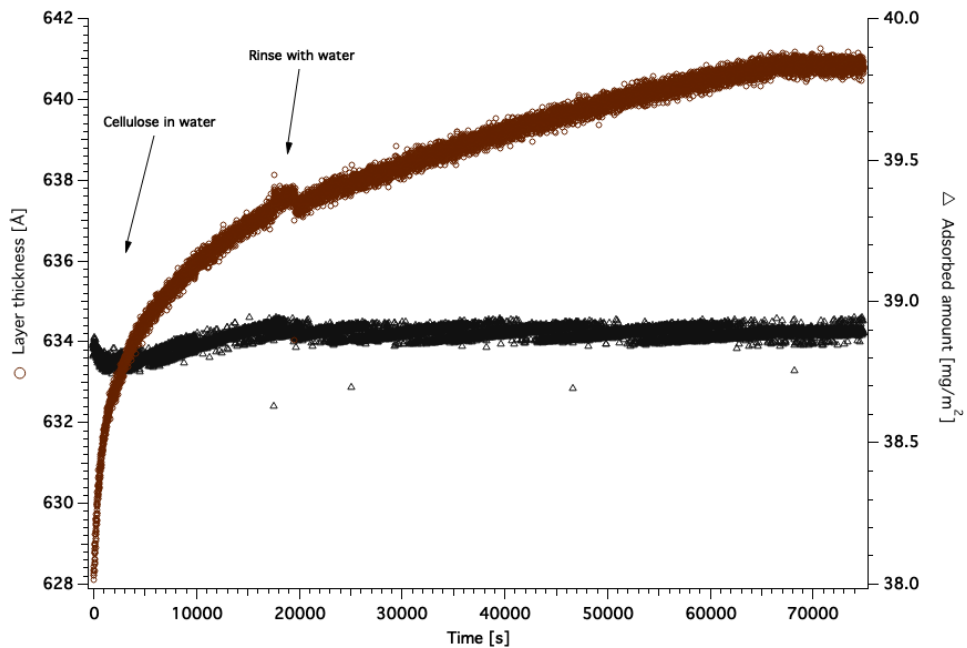
Figure S5 Cellulose film swelling in water as observed with null ellipsometry
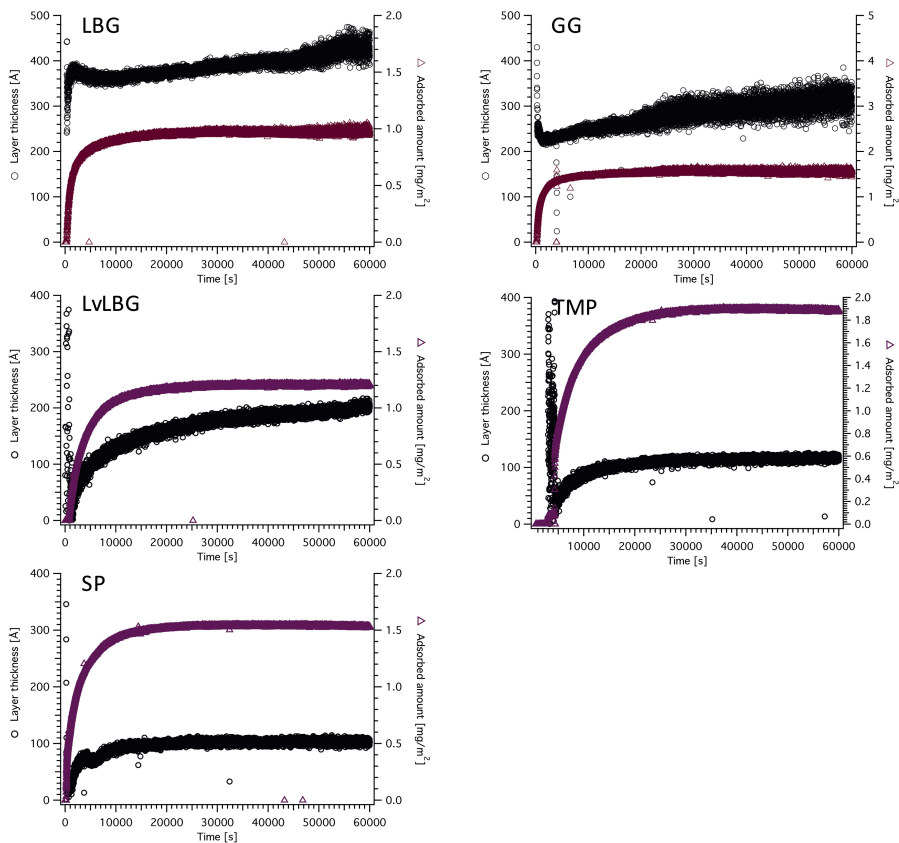
Figure S6 Mannan adsorption on hydrophobic surface measured with ellipsometry
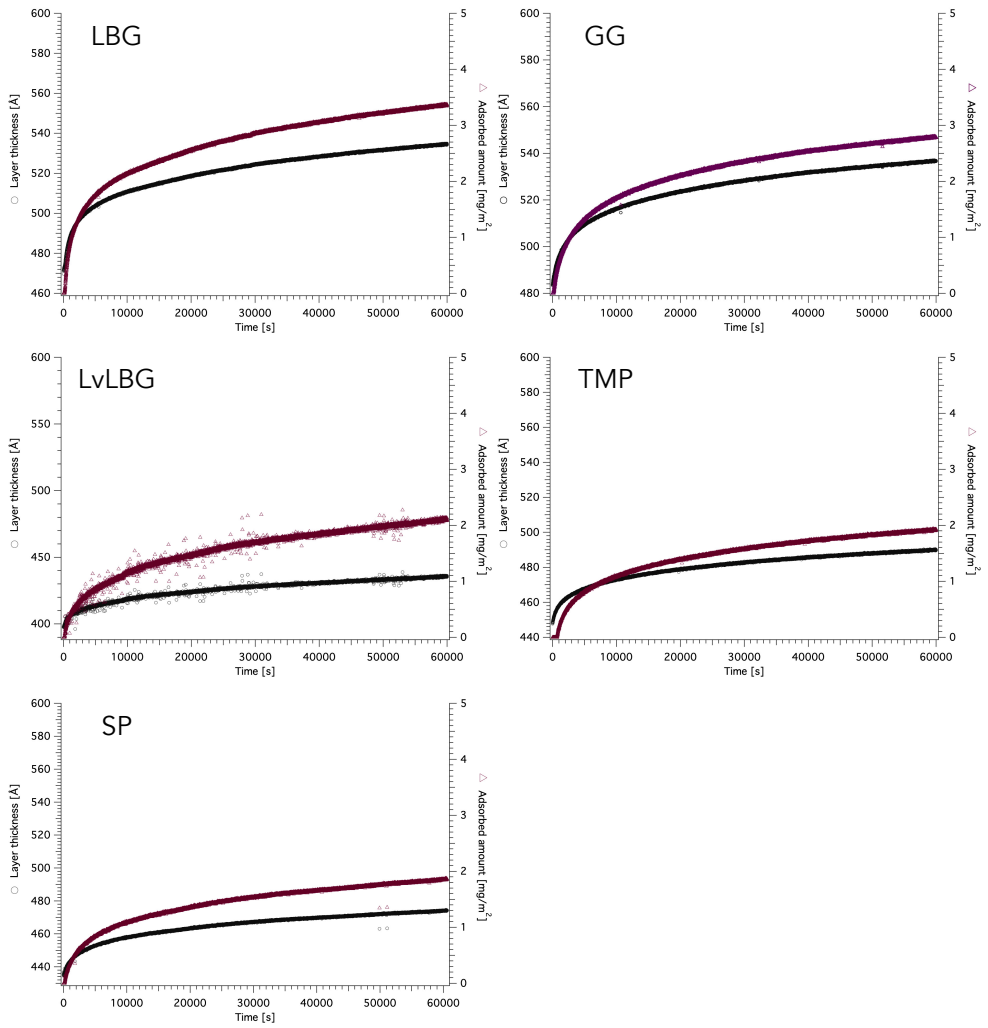
Figure S7 Mannan adsorption on cellulose surface measured with ellipsometry

QCM-D data and fitting:
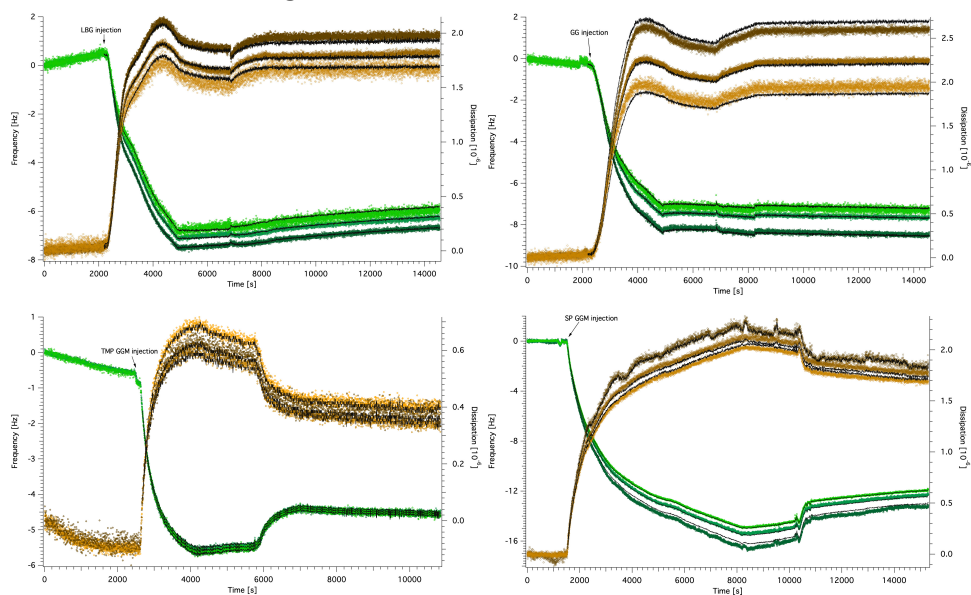
Figure S8 Mannan adsorption on hydrophobic surface measured with QCM-D. Results were fitted to the Voigt viscoelastic model using at least three overtones. Theoretical fit is represented by solid lines.
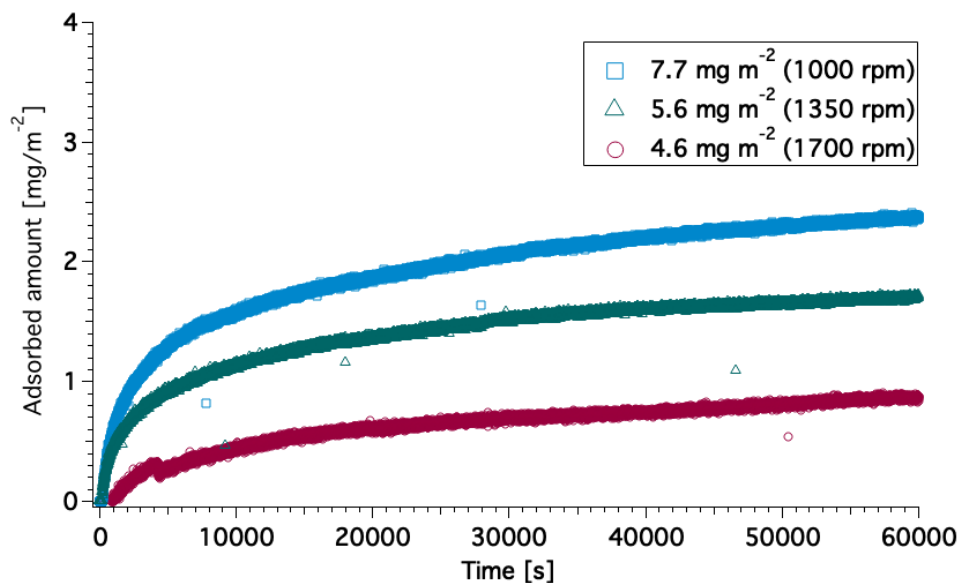
Figure S9 The adsorbed amount of GG on the cellulose films spin coated at different speeds determined with ellipsometry

Paper II

Adsorption of hemicellulose to cellulose films and cellulose crystallinity

P. Naidjonoka, C. Dicko, C. J. Garvey, J. Gilbert, C. J. Kinane, A. Caruana, A. Vorobiev, R. Russell, S. Holt, H. Stålbrand, T. Nylander

Manuscript

Adsorption of hemicellulose to cellulose films and cellulose crystallinity

Polina Naidjonoka[a], Cedric Dicko[b], Christopher J. Garvey[a,c,k], Jennifer Gilbert[a], Christy J. Kinane[d], Andrew Caruana[d], Alexei Vorobiev[e], Robert Russell[f], Stephen Holt[c], Henrik Stålbrand[g], Tommy Nylander[a,j,k]

[a]*Division of Physical Chemistry, Department of Chemistry, Lund University, P.O. Box 124, Lund, SE-221 00, Sweden*
[b]*Division of Pure and Applied Biochemistry, Department of Chemistry, Lund University, P.O. Box 124, Lund, SE-221 00, Sweden*
[c]*The Australian Nuclear Science and Technology Organisation, Sydney, Australia*
[d]*ISIS-STFC, Rutherford Appleton Laboratory, Didcot, OX11 0QX, UK*
[e]*Division for Materials Physics, Department of Physics and Astronomy, Uppsala University, Box 516*
[f]*National Deuteration Facility, ANSTO, Australia*
[g]*Biochemistry and Structural Biology, Department of Chemistry, Lund University, Lund, Sweden*
[j]*NanoLund, Lund University, Lund Sweden*
[k]*Lund Institute of Advanced Neutron and X-ray Science LINXS, Lund, Sweden.*

Abstract

Cellulose and hemicellulose form complexes inside plant cell walls in order to protect the cells from deformation and provide stability. This study aims to further improve the knowledge regarding the interactions between these two polysaccharides, to aid in the design of novel materials, as well as provide insight into the mechanisms of formation of the complex structures inside plants. Here we investigate the adsorption of wood- and seed-based β-mannans to model cellulose films. The properties of the cellulose films, e.g. crystallinity, were first evaluated with attenuated total reflectance Fourier transform infrared spectroscopy, based on quantification of the unexchangeable hydroxyl groups in a D_2O environment. The spin-coated bacterial cellulose films contained both crystalline and amorphous regions with around 8% of inaccessible hydrogen atoms. The films were characterized with neutron reflectometry before and after adsorption of hemicellulosic heteromannans to determine their thickness and solvent content. The spin-coated cellulose films were rather thin (10 to 15 nm) and highly hydrated with the solvent penetration above 75%. β-Mannan chains were found to penetrate the cellulose film for all hemicellulose samples. The highest adsorbed amount of hemicellulose was obtained for the sample with the lowest content of galactose side chains and with the lowest molecular weight, as these smaller and more flexible molecules are able to diffuse into the cellulose layer more extensively.

Introduction

Cellulose is the primary polysaccharide that makes up plant cell walls. Cellulose chains assemble to form crystalline and amorphous fibrillar networks that provide mechanical strength to plants. Hemicellulose is the largest non-cellulosic polysaccharide found in plant cell walls. Hemicelluloses have higher aqueous solubility and provide additional strength and elasticity to the cell walls, as well as controlling the aggregation of cellulose microfibrils. Some hemicelluloses are stored in the secondary plant cell walls as an energy source.[1] Both of these polysaccharides have garnered a lot of attention as a potential replacements for fossil-based matter due to their biodegradable nature and vast abundance of the raw material. Wood consists of about 40-50 wt% cellulose but other plant tissue e.g. in cotton, consists of more than 90 wt% of cellulose.[2] Hemicellulose content varies not only in different plants but also between different cell wall types (primary or secondary).

Hemicelluloses are often divided into xyloglycans, mannoglycans, xyloglucans and β-glucans with mixed linkages, based on the types of sugar and sugar linkages they contain.[3] Xyloglucans are the major hemicelluloses in primary cell walls with the highest amount found in dicotyl plants (20-25%). Xyloglucans have a similar backbone to cellulose, containing (1→4)-β-D-glucopyranan and α-D-xylopyranose branches at the C-6 position. It often also contains other monosugars. Xyloglucans are also stored in the seeds of nasturtium and tamarind plants. In the secondary cell walls of dicotyl plants, however, the predominant hemicelluloses are xyloglycans or xylans (20-30%). Grass cell walls contain up to 50% xyloglycans.[4] Xylans consist of a (1→4)-β-D-xylopyranan backbone alone or with branches containing various oligosaccharides, D-glucuronic acid or its 4-*O*-methyl ether. β-D-glucans containing 1→3 and 1→4 linkages occur only in Poales plants such as cereal grasses. Mannoglycans consist of (1→4)-β-D-mannopyranan with (1→6)-β-D-galactopyranose side groups, therefore they are often called galactomannans (GMs). Galactomannans with low galactose substitution degree (around 4% galactose) are present in the seed endosperm of ivory nut (*Phytelephas macrocarpa*), date (*Phoenix dactylifera*) and in the green arabica coffee beans. Highly substituted galactomannans are mainly found in the storage tissue cell walls of seeds e.g. guar (*Cyanopsis tetragonoloba*), locust bean gum (*Ceratonia siliqua*) and tara gum (*Caesalpinia spinosa*). In some mannoglycans, the mannan backbone is partially substituted with (1→4)-β-D-glucopyranose. Such mannoglycans are often called galactoglucomannans (GGMs) and they are the primary non-cellulosic components in the secondary cell walls of softwood such as spruce, pine and poplar. In addition to galactose side groups, GGMs contain acetyl groups attached at the C-2 and C-3 positions.[3]

The role of hemicellulose inside plant cell walls is well understood, the nature of the interaction with cellulose, however, remains unclear. The binding of hemicellulose to cellulose is believed to occur partly via hydrogen bonding, but the process has been reported to be mainly driven by the gain in entropy upon the release of water molecules when hemicellulose chains attach to cellulose. [5–7] In addition, the composition and structure of hemicellulose, as well as cellulose type and crystallinity, is expected to control the strength of the attractive interaction. The adsorption of hemicellulose to cellulose has been studied extensively. For instance, the backbone unit conformation of hemicellulose has been shown to affect the aggregation behavior of the bacterial cellulose when produced in the presence of different types of hemicelluloses. [8] The absence of the axial hydroxyl groups in xylan-based hemicelluloses and cellulose allowed a closer contact between the backbones resulting in co-crystallization of the components. β–Mannans, on the other hand, decrease the crystallinity of the composite as compared to the pure bacterial cellulose. The branching degree has been shown to impact the adsorption behavior of different kinds of hemicellulose.[9–14] A large side group content disrupts the intimate alignment between the backbones, leading to a lower contact area between the polysaccharides. It has been shown that at least 15 consecutive unsubstituted xylosyl or 4 glucosyl units are necessary for efficient binding.[10,15] Cleaving off the side groups from the backbone reduces the solubility of the

hemicellulose and has been shown to facilitate its adsorption to cellulose surfaces.[11–13] High galactose substitution degree has been shown to decrease the flexibility of the hemicellulose backbone which in turn hinders the ability of the polysaccharide to penetrate cellulose pores.[6,16,17]

Interestingly, when considering the effect of molecular weight on the adsorption, contrasting results have been reported. A higher molecular weight of oat spelt xylans has been shown to significantly increase their adsorption to cellulose surfaces.[15] A study performed on enzymatically modified guar gum samples demonstrated that their adsorption to a bleached kraft pulp is affected by molecular weight but more so by the degree of branching.[18] However, it has also been highlighted that polysaccharides with lower molecular weight are able to penetrate the cellulose layer and occupy smaller pores.[6,16]

We have previously shown how solution properties of several types of hemicelluloses affect their adsorption to spin-coated microcrystalline cellulose surfaces. In this study, we focus on the properties of cellulose films, mainly crystallinity, and the distribution of hemicellulose across the cellulose layer. The crystallinity of the deuterated bacterial cellulose film was determined from the amount of the inaccessible hydroxyl groups present in a D_2O environment. The adsorption of hemicellulose samples originating from various sources to the *d*-cellulose surfaces was monitored using neutron reflectometry (NR), which provides information about the scattering density profile of the layer and, therefore, its composition perpendicular to the substrate surface.

Experimental

Materials

N,N-dimethylacetamide (DMAc), lithium chloride (99.0% LiCl) and dimethyloctylchlorosilane (DMOCS, 97%) were purchased from Sigma-Aldrich, Sweden. $LiCl_2$ was dried at 200°C overnight and used immediately. Purified water (18 MΩ cm) was obtained by passing deionized water through a Milli-Q® Water Purification system (MerckMillipore, Darmstadt, Germany) and was used for the preparation of all solutions. All other solvents and reagents were of analytical grade and were used as received.

Hemicellulosic β−mannan samples. Galactomannan polysaccharides, guar gum (GG) and locust bean gum (LBG) were obtained from Megazyme International (Bray, Ireland). Spruce galactoglucomannan samples were obtained from the spruce thermomechanical pulp process waters (TMP) and spruce chips that were subjected to steam extraction (SP) according to Lundqvist *et al.*[19] TMP was purified using ultrafiltration and diafiltration as described in detail by Andersson *et al.*[20] whereas the purification of SP was performed with size exclusion chromatography as described by Palm and Zacchi.[21] The GGM preparations were freeze-dried and stored under dry conditions at room temperature. Detailed NMR analysis of the samples is described in Naidjonoka *et al.*[17] Carbohydrate composition and molar weight of all the polysaccharides used in this study are summarized in Table 1.

Table 1. Denotation, molecular weight and molar ratio of different β−mannan based polysaccharides. The GGM chemical analysis is from Naidjonoka *et al.*[17] and the reference is for the method of preparation. The guar gum and locust bean gum data is from the supplier[22]

Sample		Molecular weight [kDa]	Man	Gal	Glc	Acetyl	Ara	Xyl	Reference
Guar gum (GG)		250.0	67	33					
Locust bean gum	LBG	556.0	78	22					22
	LBG*	107.0	78	22					
Spruce galactoglucomannan (GGM)	TMP	14.0	50	15	15	20			19–21
	SP	5.9	40	6	16	28	2	8	

Bacterial cellulose. Deuterated bacterial cellulose was provided by the National Deuteration Facility (ANSTO, Australia) and non-deuterated bacterial cellulose was kindly provided by Cedric Dicko (Lund University). Deuterated bacterial cellulose was produced by Gluconacetobacter. *xylinus* (ATCC53524) bacteria grown on D_2O medium with d8-glycerol as the carbon source.[23]

Sample preparation. Hemicellulose samples were solubilized according to the protocols described in Naidjonoka *et al.*[17] and diluted with 0.05 M citrate buffer to a concentration of 0.6 mg mL^{-1}.

Cellulose solutions were prepared using a DMAc/LiCl solvent system according to the method described in Naidjonoka *et al.*[17]

Substrate preparation. Substrates used for the neutron reflectometry measurements were polished silicon substrates (Siltronix, Archamps-France) of 9 x 5 x 1.5 cm^3 capped with a silicon oxide layer. Surfaces were cleaned according to Chang *et al.*[24] The surfaces were first placed in a base mixture of 25% NH_4OH, 30% H_2O_2, and H_2O (1:1:5 by volume) at 80°C for 5 min and then rinsed with deionized water, and placed in an acid mixture of 32% HCl, 30% H_2O_2 and H_2O (1:1:5 by volume) at 80°C for 5 min. The silica substrates were thoroughly rinsed with water and ethanol, then stored in ethanol (99.7%) until further use.

Diamond crystal was used for the ATR-FTIR measurements. The crystal was cleaned with 2% Hellmanex solution and rinsed thoroughly with milli-Q water and ethanol.

Cellulose films were prepared by spin-coating a few drops of clear cellulose solution on the silica surface or FTIR crystal (spin coater module LabSpin6/8, SUSS MicroTec SE, Germany) at 1700 rpm for 5s. The spin-coated wafers were annealed at 100°C for 10 min, cooled down to room temperature, placed into deionized water for 20 min, dried in a nitrogen flow and heated at 100°C for 10 min. The cellulose covered substrates were used immediately.

Atomic Force Microscopy (AFM). Park XE—100 (Park Systems Corp., Suwon, Korea) was utilized for the AFM measurements in a non-contact mode. Samples were probed in a dry and liquid state under ambient conditions. A silicon cantilever with a 42 N/m spring constant and 330 kHz resonance frequency was used for imagining in the dry state. Images in liquid were obtained using tapping mode with a silicon cantilever with a 3 N/m spring constant and 75 kHz resonance frequency. The image analysis was performed with the XEI software (Park Systems Corp., Suwon, Korea).

Attenuated Total Reflectance Fourier Transform Infrared Spectroscopy (ATR-FTIR). A Thermo Scientific Nicolet 6700 spectrometer equipped with a MIRacle single reflection ATR accessory (Pike Technologies) was used for these measurements. The crystal of the ATR accessory was diamond. ATR-FTIR was used to determine the amount of inaccessible hydroxyl groups present in the spin-coated cellulose films. This was done by passing D_2O vapor flow through a flow through cover cell for single bounce ATR-FTIR crystal (Pike Technologies). The D_2O vapor was produced by gently bubbling nitrogen gas in a D_2O containing tube. First, the background spectrum of the clean diamond crystal was taken. After that, the crystal was spin-coated with cellulose solution as described above. The cellulose film was then dried by passing N_2 through the FTIR flow through cover cell for at least an hour. Once the film was dry, the kinetics measurement was set for 30 min with continuous flow of D_2O vapor. The spectrum was taken once more after 2 and 3 hours from the beginning of the experiment. The cell was then purged with H_2O vapor for 30 min and dried with N_2 gas. High resolution spectra were taken with 512 scans for the film in dry state, after 30 min, 2 and 3 hours of D_2O exchange, after 30 min of H_2O exchange and after final redrying. Kinetics measurement was done for 30 min with a sampling interval of 1.44 sec and 8 scans per sampling. For all data collection, the spectral resolution was set to 2 cm^{-1}. ATR correction was performed using OMNIC (Thermo Scientific proprietary software). The kinetic

analysis, including background subtraction and peak integration, was performed in custom written Matlab (The Mathworks Inc.) scripts.

Neutron reflectometry (NR). Adsorption of the β−mannans was studied with NR on the spin-coated *d*-cellulose surface. In specular neutron reflectometry, a neutron beam is directed towards a substrate and the intensity of the radiation reflected at the same angle as the incident beam angle is measured as a function of the scattering vector Q (see Eq. 1)

$$Q = \frac{4\pi}{\lambda_0}\sin(\theta_{in})$$ (1)

where λ_0 is the neutron wavelength and θ_{in} is the angle of incidence.

Measurements were performed at Australian Nuclear Science and Technology Organization (ANSTO) on the Platypus reflectometer over a Q - range of $0.001 – 0.4$ Å^{-1} and at ISIS Rutherford Appleton laboratory on the POLREF reflectometer over a Q - range of $0.0085 – 0.25$ Å^{-1}.

The specular reflectivity of the bare silica surface in deuterated (D_2O), protonated (H_2O) and contrast matched silicon (CMSi) buffer was measured versus Q, after which the substrate was covered with a cellulose layer by spin coating, as described above, and the layer was characterized in all three solvent contrasts. The β−mannan sample in D_2O buffer was then injected and left for 1 hour to adsorb, after which, NR curves were measured after rinsing with D_2O-, CMSi- and H_2O-based buffers, respectively. The reduced data was evaluated with the Motofit software, which uses the Abeles matrix method to calculate the reflectivity from a stratified interfaces.[25,26] The best fit for the reflectivity curves of the cellulose films was obtained with a model containing the following layers: SiO_2-(Cellulose0)-Cellulose1-Cellulose2. The model to fit the reflectivity curves of the cellulose layer with the adsorbed β−mannan polysaccharides consisted of SiO_2, modified Cellulose1 and Cellulose2 layers (to account for hemicellulose penetration) and an extra layer representing adsorbed hemicellulose (Layer 3).

The adsorbed amount (Γ) of the hemicellulose on the cellulose films was calculated using Eq. 2

$$\Gamma = \frac{\Phi \cdot T}{V_p}$$ (2)

where Φ is the volume fraction of hemicellulose in the film, T is the layer thickness and V_p is the partial specific volume (V_p of cellulose acetate = 0.68 was used here).

Results and Discussion

Morphology of the cellulose films in air and liquid environments

Spin-coated cellulose films were imaged using AFM in non-contact mode in air. A typical image is presented in Figure 1 and shows that the film consists of cellulose microfibrils randomly arranged on the surface. The height profile of the cellulose fibril layer reaches a maximal value of 12 nm in height with the root mean square (rms) surfaces roughness of 3.6 nm and shows that the layer uniformly covers the surface. Similar topography has been observed for films prepared with microcrystalline cellulose dissolved in the DMAc/LiCl solvent system but for these layers a higher rms surface roughness was observed.[27] Dissolving grade pulp solubilized in a similar solvent has been reported to create a non-fibrillar spherically shaped topography.[28,29]
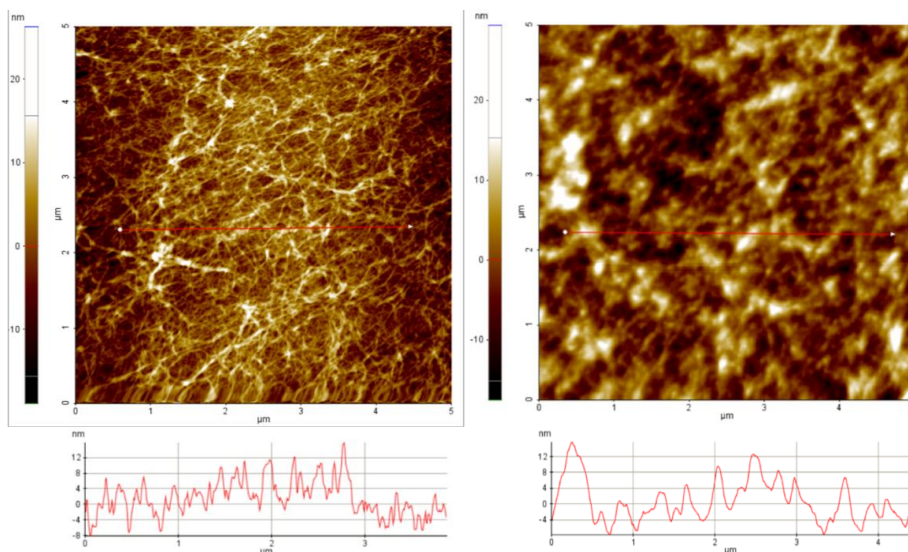
Figure 1. AFM topography profile of a spin-coated *d*-cellulose layer on silicon imaged in air (left) and in liquid (right).

The fibrillar network is less pronounced once the cellulose film is submerged into water due to a substantial swelling of the cellulose (Figure 1). The height profile of the fibril layer shows a similar maximum height, but significantly different lateral dimensions. Swelling of the cellulose fibrils also resulted in a higher rms surface roughness (4.3 nm) as compared to that of the dry film.

ATR-FTIR of deuterated and non-deuterated bacterial cellulose

The spin-coated cellulose films were characterized using ATR-FTIR in order to reveal the crystallinity of the cellulose. For this purpose, the substrates with cellulose layers were exposed to a saturated D_2O and H_2O vapor environments in order to determine the amount of non-exchangeable -OH groups. The cellulose sugar unit ring contains three -OH groups at $C(2)$, $C(3)$ and $C(6)$, with protons that are easily exchangeable with deuterium atoms provided that cellulose chains are entirely amorphous. In crystalline regions, these groups are not accessible to the solvent and this property can be used to evaluate cellulose crystallinity.[30–32]

Figure 2 presents FTIR spectra of the spin-coated bacterial *d*-cellulose (*d*-BC) and non-deuterated (*h*-BC) cellulose film under different conditions. The spectra recorded under dry conditions represent the initial state of the spin-coated films, in which two main regions can be observed: an -OH stretching band between 3600-3200 cm^{-1} and the cellulose fingerprint region at 1550-900 cm^{-1}, which comprises bands resulting from the stretching vibrations of C-C, C-O, skeletal and ring vibrations.[33–36] The peak observed at 2900 cm^{-1} in the dry *h*-BC spectra corresponds to C-H stretching. This peak is absent in the *d*-BC spectra, which contains a signal between 2100 cm^{-1} arising from C-D stretching instead.[37] Once the film was exposed to a D_2O vapor, the -OH signal decreased and simultaneously a new band at around 2500 cm^{-1} appeared, that corresponds to -OD elongational vibrations. The spectra in Figure 2 demonstrate that, although, the intensity of the -OH peak in both deuterated and non-deuterated film decreased significantly, it did not disappear completely.

Once there were no further changes in -OH and -OD signal intensities, the D_2O vapor in the FTIR cell was replaced with H_2O vapor. The presence of free water molecules in the cellulose film is evident from the appearance of a new peak at 1635 cm^{-1}. Along with the water signal, an increase in -OH and decrease in -OD peak intensities were observed. Surprisingly, the -OD signal did not disappear completely and

persisted even after redrying. This phenomenon of the resistant -OD groups has been widely reported in literature and is believed to occur due to recrystallization during drying and wetting cycles. [32,35,38,39]
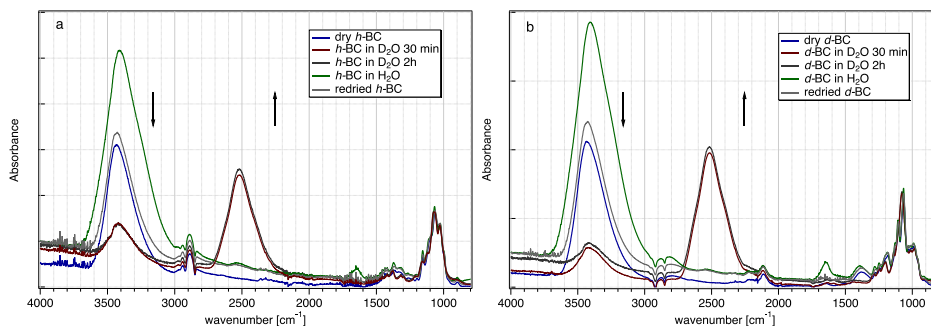
Figure 2. FTIR spectra of *h*-BC (a) and *d*-BC (b) films in air (dark blue), in D_2O vapor after 30 min (dark red), in D_2O vapor after 2 hours (dark grey), in H_2O vapor (green) and redried (light grey).

The kinetic behavior of the exchange between -OH and -OD groups in the spin-coated cellulose layers was followed during the first 30 min of the reaction. Figure 3 shows the change in the -OH groups with time in both deuterated and non-deuterated cellulose films. It was assumed that the exchange rate followed a pseudo-first-order kinetics[40]

$$\ln\left\{\frac{[OH]_t}{[OH]_0}\right\} = -kt \tag{2}$$

where $[OH]_0$ is the initial area of the -OH peak and $[OH]_t$ is the area of the signal at a time point *t*.

The profile of the kinetic curves of the two cellulose films appeared very similar with the most rapid exchange happening during the first 1-2 minutes of the reaction, after which it slowed down considerably and continued to decrease throughout the whole experiment at a much lower rate until it completely stopped after 2 hours.
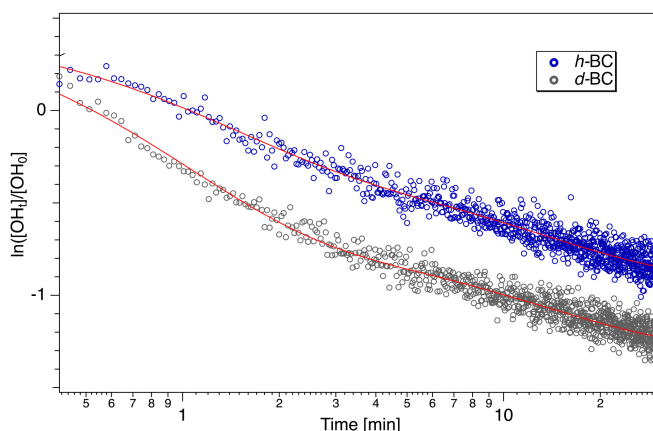
Figure 3. The change in the area of the -OH peak with time in *h*-BC (blue circles) and *d*-BC (black circles). Red lines represent fits to the exponential decay.

Generally, the exchange process has been described by a two-step model, wherein the exchange first occurs in the amorphous regions. Depending on the sample and the setup conditions, the time for this process may vary from 15 min to a couple of hours. The second step may take up to several days since

the exchange occurs with less accessible parts of the layer like the surface of the crystallites or at irregularities.[32,35,40–42] Hishikawa *et al.* suggested that every region where the kinetic curve follows a straight line corresponds to a domain in the cellulose film with a distinct exchange behavior.[40] The curve in Figure 3 can be fitted with two exponential decays suggesting a presence of two distinct regions as described above. The initial exchange is faster in the *d*-BC film suggesting a less crystalline character. The amount of the exchanged -OH groups (r_{OH}) was estimated using Equation 3[43–45]

$$r_{OH} = \frac{1.34 \cdot A_{OD}}{1.34 \cdot A_{OD} + A_{OH}} \tag{3}$$

where A_{OD} and A_{OH} are the integrated areas of the signals between 2260-2700 cm^{-1} and 3050-3680 cm^{-1}, respectively. Based on this calculation, the proportion of the -OH groups, that are accessible, is 73% in the deuterated cellulose film and 61% in the *h*-BC film. This result supports the observations from the kinetic measurements, which showed a more rapid exchange in the *d*-BC film. Considering that the replacement of protons by deuterium in the backbone of cellulose does not affect the molecular and morphological properties of cellulose,[37] the difference in r_{OH} between the deuterated and non-deuterated cellulose film should arise solely during the cellulose dissolution or spin-coating step. Bacterial cellulose is known to be highly crystalline, with chains arranged in a parallel manner characteristic of cellulose I, which has previously been reported to have 6% to 21% accessible -OH groups depending on the reaction conditions.[32,37] In this work, however, the crystalline network of cellulose fibers has been disrupted to achieve complete dissolution, therefore a higher amount of the accessible -OH groups is expected. Shanshan *et al.* found that, by solubilizing bacterial cellulose in *N*-Methylmorphine-*N*-oxide monohydrate (NMMO), the crystallinity of cellulose decreases from 79% to 38%.[46] Even though a different solvent system was used in this study, a similar level of crystallinity after dissolution was observed.
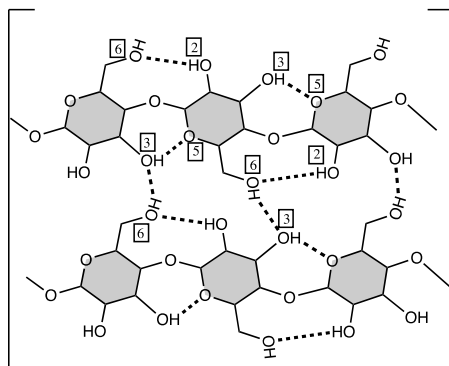
Figure 4. Schematic representation of inter- and intramolecular hydrogen bonds in two parallel cellulose chains.

The -OH stretching signal consists of overlapping bands arising from intramolecular O(2)H···O(6) at 3460 cm^{-1}, O(3)H···O(5) at 3340 cm^{-1} and intermolecular bond O(6)H···O(3) at 3230 cm^{-1} (see Figure 4).[35,38] Figure 5 shows difference spectra derived from the first time point and the following points in the kinetics measurement.
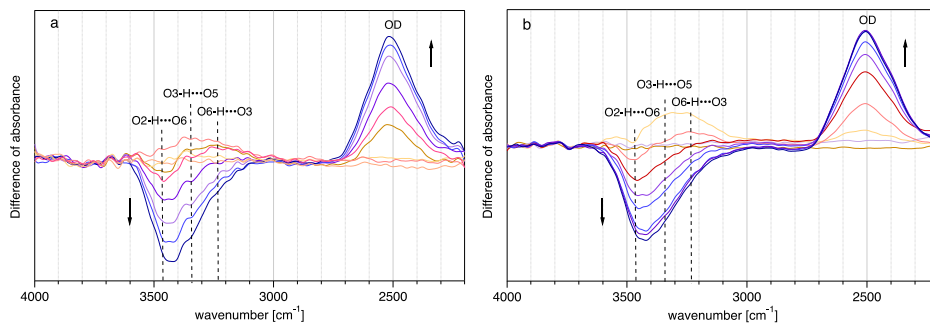
Figure 5. Change in difference spectra of *h*-BC (a) and *d*-BC (b) films in D_2O vapor with time with a step of 3 min.

As soon as D_2O vapor penetrated the film, in both deuterated and non-deuterated cellulose, the exchange began on the intramolecular bond $O(2)H\cdots O(6)$ and continued until the end of the experiment. The exchange at $O(3)H\cdots O(5)$ bond was less active and started later in the reaction. The least affected bond seems to be the intermolecular $O(6)H\cdots O(3)$ bond. The fact that most of the exchange happens on the intramolecular bonds has been observed before by Hofstetter *et al.*[35] Even though $O(6)H\cdots O(3)$ is an interchain bond and therefore has a weaker character, -OH groups at $O(2)$ are more reactive.[47–49]

Structure of the cellulose films probed by NR

The spin-coated cellulose films were further characterized with neutron reflectometry using three isotopic contrasts: D_2O, H_2O and CMSi (SLD = 6.35×10^{-6}, -0.55×10^{-6} and 2.07×10^{-6} $Å^{-2}$, respectively). First a bare silicon substrate was characterized in three contrasts and the data fitted to a model consisting of a SiO_2 layer (SLD=3.47×10^{-6} $Å^{-2}$). The simultaneous fit of the model to data recorded in three solvent contrasts, allowed accurate determination of the substrate's properties. The results obtained from the fitting of the bare silicon substrate can be found in Table S1 (ESI).

Considering that every glucose unit in the cellulose backbone contains three exchangeable hydrogens, the expected SLD of *d*-cellulose in D_2O is 6.85×10^{-6} $Å^{-2}$ resulting in a poor contrast in D_2O. This is apparent from Figure 6, where the reflectivity profile of the bare silica and the spin-coated *d*-cellulose in D_2O almost fully overlap.
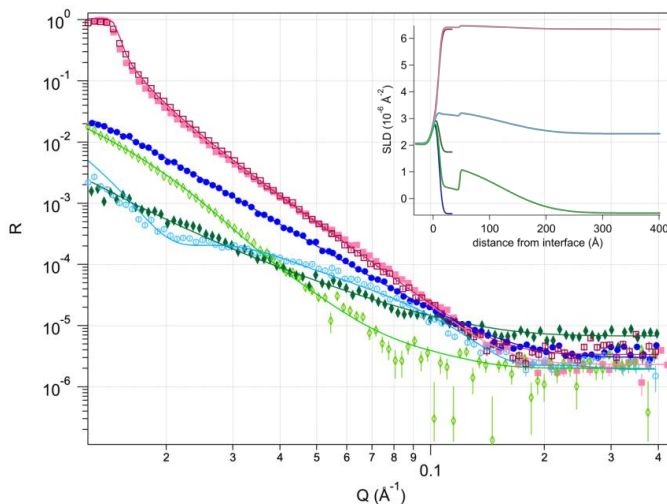
Figure 6. Neutron reflectivity as a function of momentum transfer (Q) of bare silica surface (filled symbols) in D_2O (dark red rectangle), H_2O (dark blue circle), CMSi (dark green rhombus) and *d*-cellulose surface (empty symbols) in D_2O (pink rectangle), H_2O (light blue circles), CMSi (light green rhombus). Solid lines represent the fit to the data. The inset illustrates the scattering length density (SLD) profiles as a function of distance from the Si surface.

As for the bare silica, a multilayer slab model was applied and fitted simultaneously to data from *d*-cellulose measurements in three isotopic solvent contrasts. The multilayer model used for the cellulose film consisted of two layers, as this was found to give a better fit than a single layer (see Figure 7). The two layer model has previously been applied before to describe bacterial cellulose films.[50] For one of the samples, sample 2 (see Table 2), using a model with an additional layer (layer 0), i.e. a three layer model, significantly improved the goodness of the fit. The 6 Å thick layer 0 for this sample, next to the silicon surface, was found to be dense and to include about 4% of trapped H_2O that is non-exchangeable in different contrasts, possibly due to remaining water from the drying step in the film preparation. Cellulose is a hydrophilic polymer that accumulates a large amount of moisture from the surrounding environment. The presence of bound water in cellulose samples even after extensive drying has been widely reported and investigated.[51–53]
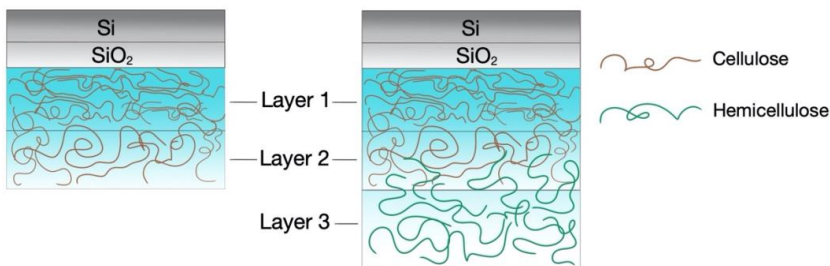
Figure 7. Schematic representation of the model used to fit the reflectometry data before and after hemicellulose adsorption on cellulose surface.

Table 2 summarizes of the results obtained from the NR investigation of cellulose films before and after adsorption of hemicellulose (discussed in the following section).

As it can be seen from the data presented in Table 2, layers 1 and 2 have very distinct features. The thickness of layer 1 (inner layer) ranges from 27 to 58 Å with a very low roughness that varies slightly between the samples. All of the samples, however, have a very high solvent content in layer 1 (above

75%). Extreme swelling behavior of cellulose in water has been widely reported in literature with up to 89% of solvent uptake in the amorphous films.[27,29,54–56] The DMAc/LiCl solvent system is known to achieve complete dissolution of the cellulose fibrils, therefore cellulose films prepared from such system often demonstrate the highest degree of swelling.[29] It should be noted that the roughness of layer 1 in sample 3 is much higher than that of the other samples, which can be attributed to the fact that it was prepared from a different batch of the cellulose solutions.

Table 2. Thickness (T), solvent volume fraction (V) and roughness (R) of cellulose (C) layers before and after addition of the β–mannan-based polysaccharides obtained from the fitting of a two or three layer model to the NR data. Here SP is steam extraction and TMP is thermomechanical pulp galactoglucomannans, LBG* is 107 kD locust bean gum galactomannan and LBG is the corresponding higher molecular weight sample (556 kD), GG is guar gum galactomannan.

Sample		1		2		3		4		5	
Layer	Parameter	C	SP	C	TMP	C	LBG*	C	GG	C	LBG
0	T [Å]			6							
	V [%]			4							
	R [Å]			1							
1	T [Å]	37		27		58	66	38		39	
	V [%]	82		83		75	64	81		85	
	R [Å]	1		0.3		37	20	2		1	
2	T [Å]	74	83	87	98	94	103	66	72	78	100
	V [%]	69	21	72	55	72	67	72	54	73	67
	R [Å]	69	58	46	66	69	57	60	58	69	55
3	T [Å]		178		148		130		122		124
	V [%]		94		94		81		82		92
	R [Å]		34		45		65		65		43

Layer 2 seems to be thicker and rougher than layer 1, with a slightly lower solvent content. Solvent gradients in the spin coated cellulose films have been reported in literature and could arise from molecular confinement or due to effects of the supporting surface.[56] Based on these observations, it can be can speculated that spin-coated cellulose films have a thin and more crystalline inner layer next to the silica surface and a thicker outer layer with cellulose microfibrils extending into solution. The presence of more crystalline regions in the film next to the supporting surface is consistent with the ATR-FTIR showing that d-cellulose contains 27% inaccessible hydroxyl groups or 8% of all hydrogens in the cellulose structure. It is noteworthy that this layer has a high solvent uptake in spite of the relative crystallinity of the cellulose. However, water penetration between crystalline planes has been noted before in films prepared with cellulose nanocrystals.[29] The overall thicknesses of the cellulose films vary from 10 to 15 nm.

As it was mentioned above, the SLD of cellulose is different in D_2O and H_2O contrasts, due to the exchangeable hydrogens in the structure. The expected SLD of d-cellulose is 6.85×10^{-6} Å^{-2} and 5.33×10^{-6} Å^{-2} in D_2O and H_2O, respectively. However, the model fit was quite poor when the SLD values were fixed to the theoretical ones, therefore, the SLD values were also fitted within a reasonable margin. Table 3 shows a summary of the obtained SLD values of d-cellulose in different samples from the fit in various contrasts. It should be noted that the cellulose film in sample 3 was only characterized in CMSi and H_2O contrast due to time constraints.

The obtained SLD values for d-cellulose in D_2O are slightly lower than the theoretical ones indicating that the layer contains up to 10% of non-exchanged hydrogens. This observation should be taken with

caution since the layer is almost completely matched out in the isotopic solvent, but it should be noted that a similar result was obtained with ATR-FTIR.

As opposed to the D_2O contrast, the SLD values of cellulose layer in H_2O are slightly higher than the theoretical ones. According to the fitting results, both the inner and the outer layer contain non-exchangeable deuterium atoms as it has also been observed in the ATR-FTIR spectra (Figure 2).

Table 3. Scattering length density (SLD) of *d*-cellulose obtained from fitting the neutron reflectivity curves of layer 1 and 2 in *d*-cellulose films (1-5) in D_2O, H_2O and CMSi.

Sample	Layer 1			Layer 2		
	D_2O	CMSi	H_2O	D_2O	CMSi	H_2O
1	6.78	6.8	5.62	6.84	5.39	5.67
2	6.54	6.44	5.74	6.77	6.74	5.49
3		6.7	5.62		5.31	5.76
4	6.76	6.77	5.41	6.81	5.36	5.82
5	6.32	6.54	5.75	6.83	5.33	5.72

Hemicellulose adsorption to cellulose films

Figure 8 shows neutron reflectivity curves of the *d*-cellulose films before and after addition of β−mannan-based polysaccharides in H_2O and CMSi citrate buffer. The largest difference can be seen in the H_2O isotopic contrast, however small shifts are also noticeable in the CMSi contrast. Initially, a model with an intact cellulose layer and an added hemicellulose layer was used to fit the data, however this gave a poor fit to the data for all of the samples. Upon noting that the AFM images in Figure 1 indicate a fairly open structure in the cellulose layer, the reflectivity data was fitted to a new model that allows the penetration of hemicellulose into the outer layer of the cellulose film. In the case of sample 3, the hemicellulose even reaches even the inner layer of cellulose due to a high roughness of the cellulose film.

It was observed that all of the β−mannans penetrate the outer layer but not the inner layer of the cellulose film (with the exception of sample 3), possibly due to the presence of crystalline regions (Table 2). As the hemicellulose penetrates cellulose, the layer becomes thicker and denser, which can be noted from the increased volume fraction of polysaccharides in the layer. The added layer (layer 3), however, contains an extremely high amount of solvent (81 - 94%). Similarly high hydration has been previously observed with these types of β−mannans on hydrophobic surfaces.[17]
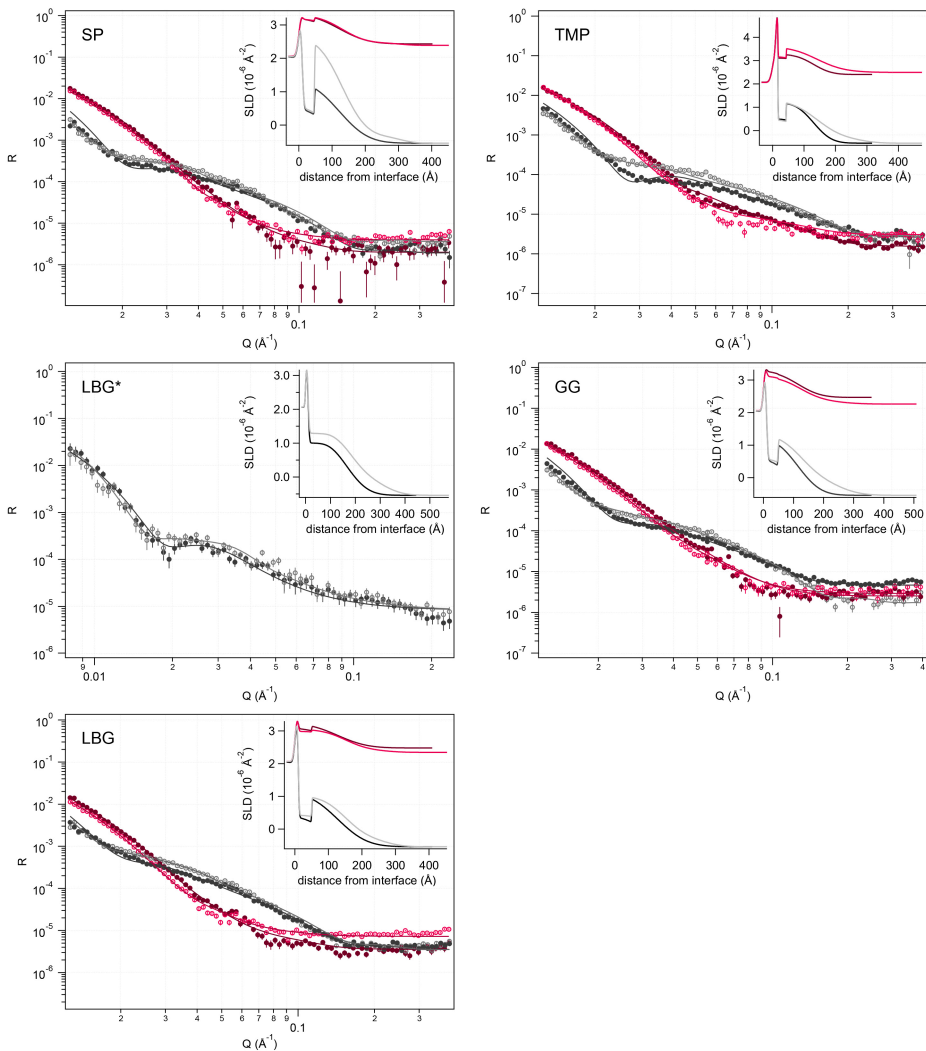
Figure 8. Neutron reflectivity as a function of momentum transfer (Q) of *d*-cellulose surface (filled circles) in H_2O (black), CMSi (dark red) and the layer with adsorbed hemicelluloses (empty circles) in H_2O (gray), CMSi (light red). Solid lines represent theoretical fit. The inset illustrates the scattering length density (SLD) profiles as a function of distance from the Si surface.

The amount of hemicellulose present in each of the cellulose layers was determined from the calculated SLD of the layers (the results are summarized in Table 4). The total adsorbed amount of the β–mannans varies from 3.3 to 6.6 mg m^{-2}. The adsorption does not follow a general trend according to the molecular weight or branching degree. It is interesting to note that the highest adsorbed amount was obtained for SP, which has both the lowest molecular weight and galactose substitution degree. A β–mannan backbone with lower degree of galactosylation could potentially lead to more favorable cellulose interaction.[57] Perhaps more important in the current case, the SP mannan is smaller in size and less rigid compared to the other hemicellulose samples. SP molecules were, therefore, able to penetrate the

cellulose layer more easily. TMP, with a slightly larger molecular weight but a significantly higher galactosylation, adsorbed to a much lower extent. The lowest adsorbed amount was obtained with LBG, which has the highest molecular weight among the studied β–mannans, but a similar galactose substitution degree to TMP and LBG*. This observation indicates that TMP and SP molecules, with much lower molecular weights, are able to penetrate smaller pores in the cellulose films, resulting in a higher adsorbed amount. However, the adsorption of LBG* is slightly higher than that of TMP despite the larger molecular weight. This could be attributed to the difference in the cellulose films. The higher roughness and thickness of the cellulose film in sample 3 allowed a deeper penetration of LBG*. Once the adsorbed amount was divided by the cellulose layer thickness (Normalized Γ), it can be observed that there is a decrease in the adsorbed amount with increasing molecular weight of hemicellulose (except for GG). These results confirm our hypothesis that molecules with smaller dimensions are able to occupy a larger area as they penetrate the cellulose layer. The second highest adsorbed amount was obtained with GG, the most extensively substituted mannan and with a relatively large molecular weight. The adsorption of GG does not follow the trend observed with the other samples possibly due to the high sample polydispersity or the properties of the spin-coated cellulose layer.

Table 4. SLD of the layers after addition of hemicellulose obtained from the fitting of NR data. The calculated adsorbed amount of hemicellulose in each layer (Γ_H), and the total and normalized adsorbed amount of the hemicellulose, as well as the normalized adsorbed amount of the cellulose layer (Γ_C) are also presented here.

Layer	Parameter	SP	TMP	LBG*	GG	LBG
1	SLD [10^{-6} Å^{-2}]			4.50		
	Γ_H [mg m^{-2}]			1.0		
2	SLD [10^{-6} Å^{-2}]	3.49	3.52	5.12	3.55	4.09
	Γ_H [mg m^{-2}]	5.4	3.4	0.8	2.7	2.0
3	SLD [10^{-6} Å^{-2}]	2.74	2.51	2.56	2.65	2.44
	Γ_H [mg m^{-2}]	1.2	1.1	2.9	2.6	1.2
Total Γ_H [mg m^{-2}]		6.6	4.5	4.7	5.3	3.3
Normalized total Γ_H [kg m^{-3}]		89	52	50	80	42
Normalized Γ_C [kg m^{-3}]		116	41	39	41	40

In our previous work, where the adsorption of these types of hemicelluloses on the spin-coated microcrystalline cellulose films was investigated, we have demonstrated that molecules with larger molecular weight yield a higher adsorbed amount. However, the hemicellulose concentration used (0.02 mg mL^{-1}) was significantly lower than that used in the current study (0.6 mg mL^{-1}). This indicates that the hemicellulose concentration was not high enough to saturate the porous cellulose films. We can speculate that the adsorption of hemicellulose on cellulose surfaces follows contrasting tendencies. In the low concentration regime, the adsorption of small molecules is less favorable due to a loss in translational entropy. In the high concentration regime, on the other hand, small polymers adsorb more rapidly to avoid the loss in conformational entropy of large species.[58] The effect is even more pronounced here due to the porous nature of the cellulose surface, which acts as a filter, restricting the penetration of large molecules into the layer.

Conclusions

In this study we used ATR-FTIR in a D$_2$O environment to show that the spin-coated bacterial *d*-cellulose films recrystallize on the surface with around 8% of inaccessible hydrogens. These findings are also confirmed by neutron reflectometry measurements, which demonstrate that the limited

exchange also leads to the entrapment of deuterium atoms in the cellulose layer. The neutron reflectometry data showed that the spin-coated layers were 10-15 nm thick with a gradient of solvent penetration. Cellulose films seem to have more crystalline regions closer to the silicon oxide substrate surface with a slightly higher solvent content, compared to the outer layer, that is possibly caused by a solvent penetration and accumulation between the crystalline planes. The adsorption experiments have revealed that hemicellulose penetrates the amorphous cellulose outer layer, which confirms a strong affinity between these two polysaccharides. The penetration was found to be dependent on the molecular weight of the hemicellulose, with the highest adsorbed amount obtained for the sample with the lowest molecular weight. The adsorption, however, might have been affected by the increased rigidity of chains with higher galactose substitution degree.

Acknowledgements

References

(1) Höfte, H.; Voxeur, A. Plant Cell Walls. *Current Biology* **2017**, *27* (17), R865–R870. https://doi.org/10.1016/j.cub.2017.05.025.

(2) *The Nanoscience and Technology of Renewable Biomaterials*; Lucia, L. A., Rojas, O. J., Eds.; John Wiley & Sons, Ltd: Chichester, UK, 2009. https://doi.org/10.1002/9781444307474.

(3) Ebringerová, A.; Hromádková, Z.; Heinze, T. Hemicellulose. In *Polysaccharides I: Structure, Characterization and Use*; Heinze, T., Ed.; Springer Berlin Heidelberg: Berlin, Heidelberg, 2005; pp 1–67.

(4) Henrik Vibe Scheller; Peter Ulvskov. Hemicelluloses. *Annual Review of Plant Biology* **2010**, *61* (1), 263–289. https://doi.org/10.1146/annurev-arplant-042809-112315.

(5) Linder, Å.; Bergman, R.; Bodin, A.; Gatenholm, P. Mechanism of Assembly of Xylan onto Cellulose Surfaces. *Langmuir* **2003**, *19* (12), 5072–5077.

(6) Vincken, J.-P.; de Keizer, A.; Beldman, G.; Voragen, A. G. J. Fractionation of Xyloglucan Fragments and Their Interaction with Cellulose. *Plant Physiology* **1995**, *108* (4), 1579–1585.

(7) Benselfelt, T.; Cranston, E. D.; Ondaral, S.; Johansson, E.; Brumer, H.; Rutland, M. W.; Wågberg, L. Adsorption of Xyloglucan onto Cellulose Surfaces of Different Morphologies: An Entropy-Driven Process. *Biomacromolecules* **2016**, *17* (9), 2801–2811. https://doi.org/10.1021/acs.biomac.6b00561.

(8) Uhlin, K. I.; Atalla, R. H.; Thompson, N. S. Influence of Hemicelluloses on the Aggregation Patterns of Bacterial Cellulose. *Cellulose* **1995**, *2* (2), 129–144. https://doi.org/10.1007/BF00816385.

(9) Hayashi, T.; Ogawa, K.; Mitsuishi, Y. Characterization of the Adsorption of Xyloglucan to Cellulose. *Plant and Cell Physiology* **1994**, *35* (8), 1199–1205. https://doi.org/10.1093/oxfordjournals.pcp.a078714.

(10) Hayashi, T.; Takeda, T.; Ogawa, K.; Mitsuishi, Y. Effects of the Degree of Polymerization on the Binding of Xyloglucans to Cellulose. *Plant and Cell Physiology* **1994**, *35* (6), 893–899.

(11) Gao, S.; Nishinari, K. Effect of Degree of Acetylation on Gelation of Konjac Glucomannan. *Biomacromolecules* **2004**, *5* (1), 175–185. https://doi.org/10.1021/bm034302f.

(12) Gao, S.; Nishinari, K. Effect of Deacetylation Rate on Gelation Kinetics of Konjac Glucomannan. *Colloids and Surfaces B: Biointerfaces* **2004**, *38* (3-4 SPEC. ISS.), 241–249. https://doi.org/10.1016/j.colsurfb.2004.02.026.

(13) Liu, J.; Wang, H.; Yin, Y.; Li, N.; Cai, P.; Yang, S. Controlled Acetylation of Water-Soluble Glucomannan from Bletilla Striata. *Carbohydrate Polymers* **2012**, *89* (1), 158–162. https://doi.org/10.1016/j.carbpol.2012.02.065.

(14) Lucenius, J.; Valle-Delgado, J. J.; Parikka, K.; Österberg, M. Understanding Hemicellulose-Cellulose Interactions in Cellulose Nanofibril-Based Composites. *Journal of Colloid and Interface Science* **2019**, *555*, 104–114. https://doi.org/10.1016/j.jcis.2019.07.053.

(15) Kabel, M. A.; van den Borne, H.; Vincken, J.-P.; Voragen, A. G. J.; Schols, H. A. Structural Differences of Xylans Affect Their Interaction with Cellulose. *Carbohydrate Polymers* **2007**, *69* (1), 94–105. https://doi.org/10.1016/j.carbpol.2006.09.006.

(16) Gidley, M. J.; Lillford, P. J.; Rowlands, D. W.; Lang, P.; Dentini, M.; Crescenzi, V.; Edwards, M.; Fanutti, C.; Grant Reid, J. S. Structure and Solution Properties of Tamarind-Seed Polysaccharide. *Carbohydrate Research* **1991**, *214* (2), 299–314. https://doi.org/10.1016/0008-6215(91)80037-N.

(17) Naidjonoka, P.; Arcos Hernandez, M.; K. Pálsson, G.; Heinrich, F.; Stålbrand, H.; Nylander, T. On the Interaction of Softwood Hemicellulose with Cellulose Surfaces in Relation to Molecular Structure and Physicochemical Properties of Hemicellulose. *Soft Matter* **2020**, *16* (30), 7063–7076. https://doi.org/10.1039/D0SM00264J.

(18) Hannuksela, T.; Tenkanen, M.; Holmbom, B. Sorption of Dissolved Galactoglucomannans and Galactomannans to Bleached Kraft Pulp. *Cellulose* **2002**, *9* (3), 251–261. https://doi.org/10.1023/A:1021178420580.

(19) Lundqvist, J.; Teleman, A.; Junel, L.; Zacchi, G.; Dahlman, O.; Tjerneld, F.; Stålbrand, H. Isolation and Characterization of Galactoglucomannan from Spruce (Picea Abies). *Carbohydrate Polymers* **2002**, *48* (1), 29–39. https://doi.org/10.1016/S0144-8617(01)00210-7.

(20) Andersson, A.; Persson, T.; Zacchi, G.; Stålbrand, H.; Jönsson, A.-S. Comparison of Diafiltration and Size-Exclusion Chromatography to Recover Hemicelluloses from Process Water from Thermomechanical Pulping of Spruce. *Applied Biochemistry and Biotechnology* **2007**, *137* (1), 971–983. https://doi.org/10.1007/s12010-007-9112-9.

(21) Palm, M.; Zacchi, G. Separation of Hemicellulosic Oligomers from Steam-Treated Spruce Wood Using Gel Filtration. *Separation and Purification Technology* **2004**, *36* (3), 191–201. https://doi.org/10.1016/S1383-5866(03)00215-6.

(22) Carbohydrates https://www.megazyme.com/shop-all-products/carbohydrates (accessed Nov 22, 2017).

(23) Russell, R. A.; Garvey, C. J.; Darwish, T. A.; Foster, L. J. R.; Holden, P. J. Chapter Five - Biopolymer Deuteration for Neutron Scattering and Other Isotope-Sensitive Techniques. In *Methods in Enzymology*; Kelman, Z., Ed.; Isotope Labeling of Biomolecules - Labeling Methods; Academic Press, 2015; Vol. 565, pp 97–121. https://doi.org/10.1016/bs.mie.2015.06.015.

(24) Chang, D. P.; Jankunec, M.; Barauskas, J.; Tiberg, F.; Nylander, T. Adsorption of Lipid Liquid Crystalline Nanoparticles on Cationic, Hydrophilic, and Hydrophobic Surfaces. *ACS Applied Materials & Interfaces* **2012**, *4* (5), 2643–2651. https://doi.org/10.1021/am300301b.

(25) Nelson, A. Motofit– Integrating Neutron Reflectometry Acquisition, Reduction and Analysis into One, Easy to Use, Package. *J. Phys.: Conf. Ser.* **2010**, *251*, 012094. https://doi.org/10.1088/1742-6596/251/1/012094.

(26) Nelson, A. Co-Refinement of Multiple-Contrast Neutron/X-Ray Reflectivity Data Using MOTOFIT. *J Appl Cryst* **2006**, *39* (2), 273–276. https://doi.org/10.1107/S0021889806005073.

(27) Eriksson, J.; Malmsten, M.; Tiberg, F.; Callisen, T. H.; Damhus, T.; Johansen, K. S. Enzymatic Degradation of Model Cellulose Films. *Journal of Colloid and Interface Science* **2005**, *284* (1), 99–106. https://doi.org/10.1016/j.jcis.2004.10.041.

(28) Eriksson, M.; Notley, S. M.; Wågberg, L. Cellulose Thin Films: Degree of Cellulose Ordering and Its Influence on Adhesion. *Biomacromolecules* **2007**, *8* (3), 912–919. https://doi.org/10.1021/bm061164w.

(29) Aulin, C.; Ahola, S.; Josefsson, P.; Nishino, T.; Hirose, Y.; Österberg, M.; Wågberg, L. Nanoscale Cellulose Films with Different Crystallinities and Mesostructures—Their Surface Properties and Interaction with Water. *Langmuir* **2009**, *25* (13), 7675–7685. https://doi.org/10.1021/la900323n.

(30) Marrinan, H. J.; Mann, J. A Study by Infra-Red Spectroscopy of Hydrogen Bonding in Cellulose. *Journal of Applied Chemistry* **1954**, *4* (4), 204–211. https://doi.org/10.1002/jctb.5010040408.

(31) Marrinan, H.; Mann, J. Infrared Spectra of the Crystalline Modifications of Cellulose. *Journal of Polymer Science* **1956**, *21* (98), 301–311. https://doi.org/10.1002/pol.1956.120219812.

(32) Jeffries, R. An Infra-Red Study of the Deuteration of Cellulose and Cellulose Derivatives. *Polymer* **1963**, *4*, 375–389. https://doi.org/10.1016/0032-3861(63)90044-2.

(33) Kondo, T.; Sawatari, C. A Fourier Transform Infra-Red Spectroscopic Analysis of the Character of Hydrogen Bonds in Amorphous Cellulose. *Polymer* **1996**, *37* (3), 393–399. https://doi.org/10.1016/0032-3861(96)82908-9.

(34) Garside, P.; Wyeth, P. Identification of Cellulosic Fibres by FTIR Spectroscopy - Thread and Single Fibre Analysis by Attenuated Total Reflectance. *Studies in Conservation* **2003**, *48* (4), 269–275. https://doi.org/10.1179/sic.2003.48.4.269.

(35) Hofstetter, K.; Hinterstoisser, B.; Salmén, L. Moisture Uptake in Native Cellulose – the Roles of Different Hydrogen Bonds: A Dynamic FT-IR Study Using Deuterium Exchange. *Cellulose* **2006**, *13* (2), 131–145. https://doi.org/10.1007/s10570-006-9055-2.

(36) Hinterstoisser, B.; Salmén, L. Two-dimensional Step-scan FTIR: A Tool to Unravel the OH-valency-range of the Spectrum of Cellulose I. *Cellulose* **1999**, *6* (3), 251–263. https://doi.org/10.1023/A:1009225815913.

(37) Bali, G.; Foston, M. B.; O'Neill, H. M.; Evans, B. R.; He, J.; Ragauskas, A. J. The Effect of Deuteration on the Structure of Bacterial Cellulose. *Carbohydrate Research* **2013**, *374*, 82–88. https://doi.org/10.1016/j.carres.2013.04.009.

(38) Lindh, E. L.; Salmén, L. Surface Accessibility of Cellulose Fibrils Studied by Hydrogen–Deuterium Exchange with Water. *Cellulose* **2017**, *24* (1), 21–33. https://doi.org/10.1007/s10570-016-1122-8.

(39) Nelson, M. L.; O'Connor, R. T. Relation of Certain Infrared Bands to Cellulose Crystallinity and Crystal Latticed Type. Part I. Spectra of Lattice Types I, II, III and of Amorphous Cellulose. *Journal of Applied Polymer Science* **1964**, *8* (3), 1311–1324. https://doi.org/10.1002/app.1964.070080322.

(40) Hishikawa, Y.; Togawa, E.; Kataoka, Y.; Kondo, T. Characterization of Amorphous Domains in Cellulosic Materials Using a FTIR Deuteration Monitoring Analysis. *Polymer* **1999**, *40* (25), 7117–7124. https://doi.org/10.1016/S0032-3861(99)00120-2.

(41) Jeffries, R. The Amorphous Fraction of Cellulose and Its Relation to Moisture Sorption. *Journal of Applied Polymer Science* **1964**, *8* (3), 1213–1220. https://doi.org/10.1002/app.1964.070080314.

(42) Hishikawa, Y.; Inoue, S.; Magoshi, J.; Kondo, T. Novel Tool for Characterization of Noncrystalline Regions in Cellulose: A FTIR Deuteration Monitoring and Generalized Two-Dimensional Correlation Spectroscopy. *Biomacromolecules* **2005**, *6* (5), 2468–2473. https://doi.org/10.1021/bm050032k.

(43) Leboucher, J.; Bazin, P.; Goux, D.; El Siblani, H.; Travert, A.; Barbulée, A.; Bréard, J.; Duchemin, B. High-Yield Cellulose Hydrolysis by HCl Vapor: Co-Crystallization, Deuterium Accessibility and High-Temperature Thermal Stability. *Cellulose* **2020**, *27* (6), 3085–3105. https://doi.org/10.1007/s10570-020-03002-2.

(44) Horikawa, Y.; Clair, B.; Sugiyama, J. Varietal Difference in Cellulose Microfibril Dimensions Observed by Infrared Spectroscopy. *Cellulose* **2009**, *16* (1), 1–8. https://doi.org/10.1007/s10570-008-9252-2.

(45) Thybring, E. E.; Thygesen, L. G.; Burgert, I. Hydroxyl Accessibility in Wood Cell Walls as Affected by Drying and Re-Wetting Procedures. *Cellulose* **2017**, *24* (6), 2375–2384. https://doi.org/10.1007/s10570-017-1278-x.

(46) Shanshan, G.; Jianqing, W.; Zhengwei, J. Preparation of Cellulose Films from Solution of Bacterial Cellulose in NMMO. *Carbohydrate Polymers* **2012**, *87* (2), 1020–1025. https://doi.org/10.1016/j.carbpol.2011.06.040.

(47) Nishiyama, Y.; Langan, P.; Chanzy, H. Crystal Structure and Hydrogen-Bonding System in Cellulose Iβ from Synchrotron X-Ray and Neutron Fiber Diffraction. *J. Am. Chem. Soc.* **2002**, *124* (31), 9074–9082. https://doi.org/10.1021/ja0257319.

(48) Rowland, S. P.; Roberts, E. J. The Nature of Accessible Surfaces in the Microstructure of Cotton Cellulose. *Journal of Polymer Science Part A-1: Polymer Chemistry* **1972**, *10* (8), 2447–2461. https://doi.org/10.1002/pol.1972.150100819.

(49) Pérez, S.; Mazeau, K. Conformations, Structures, and Morphologies of Celluloses. *Polysaccharides: Structural diversity and functional versatility* **2005**, *2*.

(50) Raghuwanshi, V. S.; Su, J.; Garvey, C. J.; Holt, S. A.; Raverty, W.; Tabor, R. F.; Holden, P. J.; Gillon, M.; Batchelor, W.; Garnier, G. Bio-Deuterated Cellulose Thin Films for Enhanced Contrast in Neutron Reflectometry. *Cellulose* **2017**, *24* (1), 11–20. https://doi.org/10.1007/s10570-016-1108-6.

(51) Radloff, D.; Boeffel, C.; Spiess, H. W. Cellulose and Cellulose/Poly(Vinyl Alcohol) Blends. 2. Water Organization Revealed by Solid-State NMR Spectroscopy. *Macromolecules* **1996**, *29* (5), 1528–1534. https://doi.org/10.1021/ma950405h.

(52) L. Lindh, E.; Terenzi, C.; Salmén, L.; Furó, I. Water in Cellulose: Evidence and Identification of Immobile and Mobile Adsorbed Phases by 2 H MAS NMR. *Physical Chemistry Chemical Physics* **2017**, *19* (6), 4360–4369. https://doi.org/10.1039/C6CP08219J.

(53) Garvey, C. J.; Parker, I. H.; Simon, G. P.; Whittaker, A. K. The Hydration of Paper Studied with Solid-State Magnetisation-Exchange 1H NMR Spectroscopy. *Holzforschung* **2006**, *60* (4), 409–416. https://doi.org/10.1515/HF.2006.064.

(54) Eckelt, J.; Wolf, B. A. Cellulose/Water: Liquid/Gas and Liquid/Liquid Phase Equilibria and Their Consistent Modeling. *Biomacromolecules* **2007**, *8* (6), 1865–1872. https://doi.org/10.1021/bm070174+.

(55) Kontturi, E.; Suchy, M.; Penttilä, P.; Jean, B.; Pirkkalainen, K.; Torkkeli, M.; Serimaa, R. Amorphous Characteristics of an Ultrathin Cellulose Film. *Biomacromolecules* **2011**, *12* (3), 770–777. https://doi.org/10.1021/bm101382q.

(56) Cheng, G.; Liu, Z.; Murton, J. K.; Jablin, M.; Dubey, M.; Majewski, J.; Halbert, C.; Browning, J.; Ankner, J.; Akgun, B.; Wang, C.; Esker, A. R.; Sale, K. L.; Simmons, B. A.; Kent, M. S. Neutron Reflectometry and QCM-D Study of the Interaction of Cellulases with Films of Amorphous Cellulose. *Biomacromolecules* **2011**, *12* (6), 2216–2224. https://doi.org/10.1021/bm200305u.

(57) Hult, E.-L.; Larsson, P. T.; Iversen, T. A CP/MAS 13C-NMR Study of Supermolecular Changes in the Cellulose and Hemicellulose Structure during Kraft Pulping. *Nordic Pulp & Paper Research Journal* **2001**, *16* (1), 33–39. https://doi.org/10.3183/npprj-2001-16-01-p033-039.

(58) Janardhan, R.; Gedam, P. H.; Sampathkumaran, P. S. The Effect of Polymer Molecular Weight in the Adsorption Process. *Journal of Colloid and Interface Science* **1990**, *140* (2), 391–400. https://doi.org/10.1016/0021-9797(90)90359-V.

Adsorption of hemicellulose to cellulose films and cellulose crystallinity

Polina Naidjonoka[a], Cedric Dicko[b], Christopher J. Garvey[a,c,k], Jennifer Gilbert[a], Christy J. Kinane[d], Andrew Caruana[d], Alexei Vorobiev[e], Robert Russell[f], Stephen Holt[c], Henrik Stålbrand[g], Tommy Nylander[a,j,k]

[a]*Division of Physical Chemistry, Department of Chemistry, Lund University, P.O. Box 124, Lund, SE-221 00, Sweden*
[b]*Division of Pure and Applied Biochemistry, Department of Chemistry, Lund University, P.O. Box 124, Lund, SE-221 00, Sweden*
[c]*The Australian Nuclear Science and Technology Organisation, Sydney, Australia*
[d]*ISIS-STFC, Rutherford Appleton Laboratory, Didcot, OX11 0QX, UK*
[e]*Institut Laue-Langevin, Grenoble, France*
[f]*National Deuteration Facility, ANSTO, Australia*
[g]*Biochemistry and Structural Biology, Department of Chemistry, Lund University, Lund, Sweden*
[j]*NanoLund, Lund University, Lund Sweden*
[k]*Lund Institute of Advanced Neutron and X-ray Science LINXS, Lund, Sweden.*
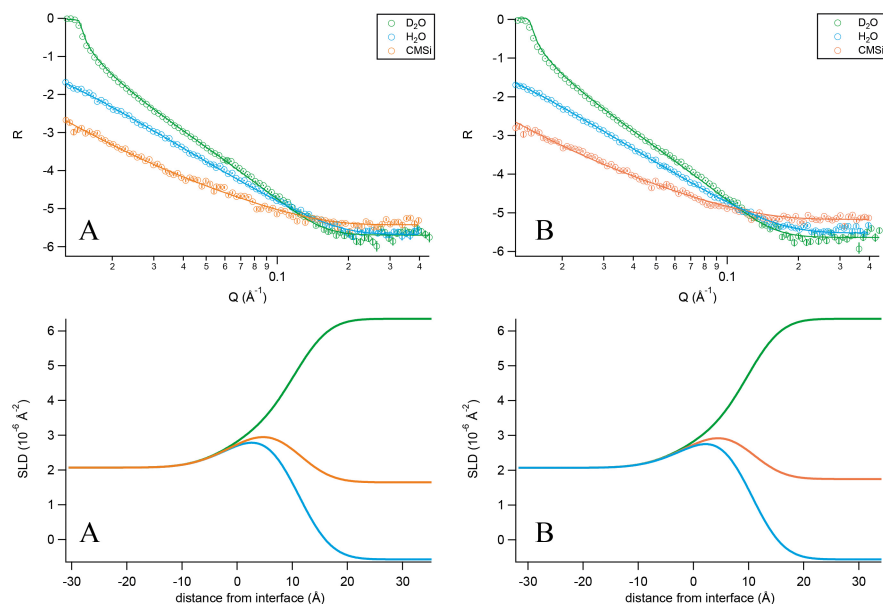
Figure S1 Reflectivity curves and SLD profiles of two silica blocks

Table S1 Thickness (T), solvent content (V), scattering length density (SLD) and roughness (R) of silicon oxide layer obtained from fitting neutron reflectivity curves of bare silica substrates presented in Figure S1 measured in three isotopic contrasts

Sample	1	2
T [Å]	10.1	10.3
V [%]	0.2	1.25
SLD [10^{-6} Å^{-2}]	3.47	3.47
R [Å]	3.2	1.4

Paper III

Bicontinuous cubic liquid crystalline phase nanoparticles stabilized by softwood hemicellulose

P. Naidjonoka, M. Fornasier, D. Pålsson, G. Rudolph, B. Al-Rudainy, S. Murgia, T. Nylander

Bicontinuous cubic liquid crystalline phase nanoparticles stabilized by softwood hemicellulose

Polina Naidjonoka,[a,$,*] Marco Fornasier,[a,b,$,*] David Pålsson,[a,$] Gregor Rudolph,[c] Basel Al-Rudainy,[c] Sergio Murgia,[b] Tommy Nylander[a,d,e]

[a]*Division of Physical Chemistry, Department of Chemistry, Lund University, P.O. Box 124, Lund, SE-221 00, Sweden*
[b]*Department of Chemical and Geological Sciences, University of Cagliari, s.s 554 bivio Sestu, Monserrato I-09042, Italy*
[c]*Department of Chemical Engineering, Lund University, SE-221 00, Lund, Sweden*
[d]*NanoLund, Lund University, Lund Sweden*
[e]*Lund Institute of Advanced Neutron and X-ray Science LINXS, Lund, Sweden.*

**$These authors equally contributed to this work.**

Corresponding Authors:
Polina Naidjonoka (polina.naidjonoka@fkem1.lu.se)
Marco Fornasier (mfornasier@unica.it)

Abstract

The colloidal stability of lipid based cubosomes, aqueous dispersion of inverse bicontinuous cubic phase, can be significantly increased by a stabilizer. The most commonly used are non-ionic tri-block copolymers, poloxamers, which adsorb at the lipid-water interface and hence sterically stabilize the dispersion. One of the challenges with these synthetic polymers is the effect on the internal structure of the cubosomes and the potential toxicity when these nanoparticles are applied as nanomedicine platforms. The natural polysaccharide, softwood hemicellulose, has been proved to be an excellent stabilizer for oil-in-water emulsions, partially due to the hydrophobic lignin which to some extent is associated to hemicellulose.

Herein, we reported for the first time cubosomes stabilized by two types of softwood hemicelluloses, where one is extracted through thermomechanical pulping (TMP, low lignin content) and the other from sodium-based sulfite liquor (SSL, high lignin content). The effect of the two hemicellulose samples on the colloidal stability and structure of GMO-based cubosomes have been investigated via DLS, SAXS, AFM and cryo-TEM. The data obtained suggest that both types of the hemicelluloses stabilize GMO based cubosomes in water without significantly affecting their size, morphology and inner structure. SSL-extracted hemicellulose yields the most stable cubosomes, likely due to the higher content of lignin in comparison to TMP-stabilized ones. In addition, the stability of these particles was tested under physiological conditions relevant to possible application as drug carriers.

Keywords

Introduction

Non-lamellar Lipid Liquid Crystalline Nanoparticles (LLCNPs) have been widely studied in the last decades due to their intriguing structure and morphology. Examples of these kind of aggregates are cubosomes,[1,2] hexosomes[2,3] and the dispersion of sponge phase (spongosomes).[4,5]

Cubosomes are dispersions of an inverse bicontinuous cubic phase in which a curved non-intersecting bilayer forms two continuous and unconnected system water channels. The curved bilayer can be described by an infinite periodic minimal surface (IPMS), such as the primitive (Im3m), the gyroid (Ia3d) and the double-diamond (Pn3m). Monoolein (GMO) and phytantriol are among the most studied lipids that form cubic phase,[1,6] nevertheless other lipids can be adopted to formulate the particles.[7,8]

The preparation of the LLCNPs is based on a top-down, bottom-up or microfluidic approach. Lipid Liquid Crystalline (LLC) cubic bulk phase can be fragmented with e.g. homogenization involving high-energy input often with the help of an emulsifier. The most common bottom-up method yields the aggregates *via* dissolution of the lipid components in solvent and thereafter mixing of the lipid solution with an aqueous solution of additives to obtain the dispersion.

Colloidally stable cubosome dispersions require a stabilizing agent, such as tri-block copolymers, to a larger extent than their lamellar counterpart, liposomes. Here, poloxamers (poly(ethylene oxide)-poly(propylene oxide)-poly(ethylene oxide)), i.e. Pluronics F127 and F108, are the most common stabilizers, where the hydrophobic PPO moiety interacts with the lipid bilayer and the PEO units form a hydrophilic corona that prevents NPs from aggregating. The biocompatibility and biodegradability of the components of the formulations are crucial parameters for application of cubosomes in drug delivery and imaging.[9–14] Although the GMO-based carriers are less cytotoxic compared to those based on phytantriol,[1,6] the intrinsic cytotoxicity of the stabilizer could prevent the application of the system.[15] Therefore, stabilizing the cubic dispersion and at the same time providing a "safe" formulation can be challenging.

Recently, a polyphosphoester (PPE) tri-block copolymer, a structural analog of Pluronic F127, was shown to be able to stabilize GMO-based cubosomes.[16] Biocompatibility assay on Human umbilical vein endothelial cells (HUVEC) and blood cells showed that the PPE-stabilized NPs were less cytotoxic at the same concentration in comparison to the cubosomes stabilized with Pluronic F127. These new formulations were also shown to have less tendency to activate the complement system, which our body employs to remove anything foreign from the blood stream.

The cytotoxic effect can be reduced by mimicking natural molecular structures and thereby improving the efficacy of the therapy. For this reason, natural polysaccharides are of great interest as potential nanoparticle stabilizers. In addition, they can remain functional as stabilizers over a relatively broad range of temperatures and pH. However, lack of clear and structured amphiphilic character brings a variety of challenges to the table. Several studies have been published where monoolein cubosomes have been stabilized by different polysaccharides like starch and cellulose.[17–19] These polysaccharides were, however, modified by introducing hydrophobic groups in their structure. This is a promising alternative to commonly used

Pluronic F127 that is believed to have some unwanted physiological side effects when ingested or inhaled,[19] and also has shown to affect the internal structure of monoolein based cubosomes. Here we have explored the stabilizing potential of hemicellulose that along with cellulose and lignin is one of the main polymer constituents of plant cell walls. Hemicelluloses are heteropolysaccharides that vary in structure and size depending on the plant type. Lignin, on the other hand, is a highly hydrophobic group of aromatic polyphenol compounds that are strongly associated with hemicelluloses and help to provide mechanical strength to the cell walls.[20] Hemicelluloses have been shown to have excellent emulsifying properties in several applications.[21–26]

The chemical composition of hemicellulose is dependent on the plant type and is often affected by the extraction method. A great variety of methods have been developed in order to obtain high purity extracts. However, one of the biggest challenges still remains the removal of lignin since it is covalently bound to hemicellulose sugar groups via glycosidic, ester or ether bonds.[25] Interestingly, when it comes to stabilizing oil in water emulsions, lignin plays an impartial role as it is believed to interact with the hydrophobic moiety of lipids and anchor hemicellulose chains on the interface. Hemicellulose in turn provides steric stabilization mechanism due to chains with high molecular weight.

The most abundant hemicellulose in spruce and pine is galactoglucomannan (GGM). It accounts for 25 – 35 % of dry wood mass.[27,28] Galactoglucomannans, often acetylated, have a linear (1→4)-linked β-D-mannopyranosyl (Man$p$) backbone partially substituted with (1→4)-linked β-D-glucopyranosyl (Glc$p$) units and α-galactopyranosyl (Gal$p$) side groups that are (1→6)-linked to the backbone.[29,30]

In this study, we investigate the ability of two different softwood hemicellulose preparations to stabilize monoolein cubic nanoparticles. One is the TMP (thermomechanical pulping) hemicellulose, which has been isolated from thermomechanical pulp and contains a very low amount of lignin, whereas the SSL (spent-sulfite-liquor) preparation originates from a sodium-based sulphite liquor with high lignin concentration. The effect of these stabilizing agents on the structure, morphology and colloidal stability of the lipid based cubosome was studied in order to identify their possible application as components to prepare future drug carriers.

Experimental section

Materials

The main component of the cubosomes, glycerol monooleate (MO, 1-monooleoylglycerol, RYLO MG 19 PHARMA, 98.1 wt% monoglycerides) was kindly provided by Danisco A/S (Denmark). Fresh distilled water purified using a Milli-Q® Water Purification system (MerckMillipore, Darmstadt, Germany) was used for preparing each sample and it was filtered with a 0.22 μm pore size hydrophilic filter prior to any use. Chloroform (99.8% purity) and phosphate buffered saline (PBS) tablets were purchased from Sigma-Aldrich (0.01 M phosphate buffer, 0.0027 M potassium chloride and 0.137 M sodium chloride).

The TMP hemicellulose sample was obtained from Stora Enso Kvarnsvedens bruk (Kvarnsveden, Sweden) and was purified by filtration and anti-solvent precipitation as described by Thuvander et al.[31] and Zasadowski et al.[32] The sample was characterized according to the National Renewable Energy Laboratory (NREL) procedure.[33] The SSL hemicellulose sample was provided by Domsjö Fabriker (Örnsköldsvik, Sweden) which was further ultrafiltrated and the components used in the study were precipitated with acetone. Details of the extraction procedure and analysis can be found at Al-Rudainy et al.[34] Table 1 shows a summary of the main components present in each of the samples.

Table 1. The chemical composition of the TMP and SSL hemicellulose extracts shown as weight percentage of total dry solids (TDS).[34] Acidic components were not determined for TMP extract indicated as n.d.

	Wt % of TDS	
	TMP	SSL
Ash	0	2.02
Lignin	1.26	7.3
Carbohydrates		
Arabinose	0	1.11
Galactose	10.4	18.7
Glucose	8.8	14.85
Xylose	4.7	7.05
Mannose	76	30.78
Cellobiose	n.d.	1.14
Lactic acid	n.d.	1.68
Acetic acid	n.d.	3.99
Formic acid	n.d.	1.63
Levulinic acid	n.d.	2.17
Furfural	n.d.	1.25
Hydroxymethylfurfural	n.d.	0.62

Methods

Sample preparation

Cubosome formulations were prepared by first dissolving 10 mg of monoolein in 1 mL of chloroform in a vial. The chloroform was then evaporated under a gentle stream of nitrogen to yield a lipid film, which was left to dry under vacuum overnight at room temperature to remove any trace of chloroform. 1 mL of GGM aqueous solution with a concentration of 3 mg mL^{-1} was then added to the vial with the monoolein film. The sample was vortexed for a few seconds and left to equilibrate at room temperature for one hour. After that, the mixture was placed in an ice bath and sonicated with a tip sonicator (equipped with a controller Sonics Vibra Cells, both from Chemical Instruments AB, Sweden) for 15 min at 70% amplitude with 10 s pulses in 10 s intervals. The samples were characterized within 48 hours after preparation.

Dynamic Light Scattering (DLS) and Electrophoretic Mobility (EM)

Dynamic light scattering experiments were performed on a Zetasizer Nano ZS (Malvern Instruments Ltd, Worshestershire, UK) at a set angle of 173° using the non-invasive backscatter technology. The instrument was equipped with a 4 mW He-Ne laser with a 632.8 nm wavelength and an Avalanche photodiode detection unit. The electrophoretic mobility measurements were performed using M3-PALS technology at 13°. The obtained correlation functions were analyzed using the cumulants method available in the Malvern software.

The cubosome formulations were diluted 500 times with either Milli-Q water or PBS buffer, placed in the Zetasizer measurement cell and equilibrated at 25°C for 2 minutes before starting the measurement.

Small Angle X-ray Scattering (SAXS)

SAXS measurements were performed at the SAXSLab instrument (JJ-Xray, Denmark) available at Lund University. The instrument was equipped with a 30 W Cu X-RAY TUBE for GeniX 3D and a 2D 300 K Pilatus detector (Dectris). The X-ray wavelength was 1.54 Å^{-1} and the sample-to-detector distance was 480 nm, yielding a q-range of 0.012 – 0.67 Å^{-1}. The measurements were recorded at 25°C. The temperature was controlled using a Julabo T Controller CF41 from Julabo Labortechnik GmbH (Germany).

The magnitude of the scattering vector is defined by $q = 4\pi/(\lambda \cdot \sin\theta)$, where the wavelength λ equals to 1.54 Å, Cu Kα wavelength, and θ is half of the scattering angle.

The repeat distance or d spacing was obtained using the following expression:

$$d = \frac{2\pi}{q} \qquad \text{(eq. 1)}$$

Then, the cubic phase lattice parameter (a) is given by eq. 2:

$$a = d \cdot \sqrt{h^2 + k^2 + l^2} \qquad \text{(eq. 2)}$$

Here, h, k and l are the Miller indexes that describe the crystalline planes into the liquid crystalline lattice. The lattice parameter was used to estimate the water channel radius (r_w) of the bicontinuous cubic phase (eq. 3)[35]:

$$r_w = (a - l) \cdot \sqrt{\frac{A_0}{-2\pi\chi}} \qquad \text{(eq. 3)}$$

where χ and A_0 are the Euler characteristic and the surface area of the IPMS geometry (Pn3m, $\chi = -2$, $A_0 = 1.919$), respectively, and l is the MO hydrophobic chain length at 25 °C (17 Å). The formulations in PBS buffer were prepared by diluting the aqueous stock of cubosome dispersion 10 times with the buffer.

Cryogenic-TEM (cryo-TEM)

A 4 µL drop of the formulations at the initial concentration was placed on a lacey carbon coated formvar grid (Ted Pella Inc, Redding, CA, USA). A thin film was then created by gently blotting the grid with a filter paper. After that the grid was prepared for imaging using an automatic plunge-freezer system (Leica Em GP, Leica Microsystems, Wetzlar, Germany). The environmental chamber was operated at 25 °C and 90% relative humidity to prevent evaporation from the sample. The specimen was vitrified by rapidly plunging the grid into liquid ethane (-183 °C) and the samples were stored in liquid nitrogen (-196 °C) and transferred into the microscope using a cryo transfer tomography holder (Fischione, Model 2550, E.A. Fischione Instruments, Inc., Corporate Circle Export, PA, USA). The grids were imaged with a Jeol JEM-2200FS transmission electron microscope (JEOL, Tokyo, Japan) equipped with a field-emission electron source, a cryo-pole piece in the objective lens and an in-column energy filter (omega filter). Zero-loss images were recorded with a bottom-mounted TemCam F416 digital camera (TVIPS-Tietz Video and Image Processing Systems GmbH, Gauting, Germany) using SerialEM under low-dose conditions at an acceleration voltage of 200 kV.
Gwyddion software[36] was used to apply 2D Fourier transform filter to cryo-TEM micrographs and extract lattice parameter.

Atomic Force Microscopy (AFM)

AFM was performed with a Park XE—100 (Park Systems Corp., Suwon, Korea) in a non-contact mode. Samples were probed in a liquid state under ambient conditions. A silicon cantilever with a 3 N/m spring constant and 75 kHz resonance frequency was used. The image analysis was done with the XEI software (Park Systems Corp., Suwon, Korea). A hydrophobized silicon wafer was covered with 90 µL of SSL-NPs formulation and left to adsorb for 4 hours before rinsing with Milli-Q water. The wafer with a drop liquid sample was then placed in the AFM liquid cell and Milli-Q water was added, after which the imaging was performed. The preparation was done in this way in order to avoid passing the sample surface film through the air/water interface.

Results and Discussion

Preparation of the NPs and their bulk characterization

Formulations stabilized by softwood hemicellulose extracted with two different methods were prepared and characterized in a similar manner using ultrasonication. This approach has been found effective to reduce the size of the aggregates and inducing a good size distribution.[1,6]

After preparation, both formulations appeared homogeneous and milky, however the SSL-stabilized solution was less translucent than the TMP-stabilized sample. The DLS and ζ-potential results, reported in Table 2, indicate that the formulations contain negatively charged, electrostatically stable particles of relatively low polydispersity.

Table 2. Apparent average hydrodynamic diameter (d_H), polydispersity index (PdI), derived count rate, as well as phase, lattice parameter (a) and water channel radius (r_w) determined from the SAXS curves for the TMP and SSL formulations. Additionally, ζ-potential and pH of pure TMP and SSL extract, as well as of TMP-NPs and SSL-NPs determined at 25 °C.

Parameters	TMP-NPs	SSL-NPs	TMP	SSL
$d_H \pm$ SD [nm]	151 ± 1	152.2 ± 0.9	-	-
PdI ± SD	0.21 ± 0.02	0.19 ± 0.01	-	-
Derived count rate ± SD	940 ± 3	2032 ± 20	-	-
Phase	Pn3m	Pn3m	-	-
a ± SD [Å]	99.6 ± 0.8	98.7 ± 0.4	-	-
r_w ± SD [Å]	21.9 ± 0.3	21.6 ± 0.1	-	-
ζ-potential [mV]	-37.7 ± 0.8	-49.5 ± 0.6	-10 ± 1	-14.8 ± 0.2
pH	6.39	6.52	6.44	6.58

The ζ-potential of the TMP- and SSL- stabilized cubosomes was -37.7 and -49.5 mV, respectively. Negative charge of the nanoparticles could partially be explained by a negative ζ-potential of their respective hemicellulose extracts (-10 and -14.8 mV for TMP and SSL, respectively). We note that the charge is highly dependent on the extraction method and the purity of the sample. Galactoglucomannans are neutral polysaccharides, the charge is believed to be caused by the presence of acidic groups.[22] The amount of acidic groups present in the TMP sample was not determined, however, the SSL extract contains at least 10% as shown in Table 1. Interestingly, the apparent negative charge is a common feature of the GMO-based dispersions: this phenomenon is not fully understood, but it has been reported for other lipid formulations stabilized with non-ionic block-copolymers.[16,37] A possible reason could be related to an adsorption of hydroxide ions at the lipid-water interface, resulting in a polarized outer layer surrounding the NPs and an apparent negative surface potential.[38]

Dispersions formulated with both GGMs exhibited the same size, around 150 nm in diameter, with relatively low polydispersity. Similar size and polydispersity have been previously reported in literature for cubosomes stabilized with different kinds of polymers.[11,16] The

intensity of the scattering from the dispersion of the SSL-stabilized NPs is more than twice as high (2032 ± 20) as from the TMP-NPs formulation (940 ± 3), indicating a larger number of particles present in the solution. This finding correlates with the less translucent appearance of the former sample.

It has previously been shown that the presence of lignin in GGM strongly increases their capability in stabilizing oil in water emulsions.[21,23–25] Lignin consists of phenolic compounds that are usually associated or even covalently bound to hemicellulose sugar units via glycosidic, ester or ether bonds.[25] Due to their hydrophobic nature, phenolic residues interact with the hydrophobic part of the lipids and thus anchor bound hemicellulose chains that in turn provide steric stabilization of the oil/water interface. Consequently, a larger amount of nanoparticles in the sample could be stabilized by the SSL hemicellulose preparation, given its higher content of lignin. In addition, the SSL-NPs have a more negative ζ-potential than the corresponding TMP-NPs. This could contribute to the electrostatic stabilization of the nanoparticles, although it has been suggested that emulsion stabilization with hemicellulose is mainly due to steric repulsion.[39]

SAXS was used to reveal internal NP structure. Figure 1 shows SAXS data TMP- and SSL-stabilized nanoparticles. Lyotropic GMO-based aqueous dispersions show a rich polymorphism depending on the water content.[40] In excess of water, monoolein is expected to form a Pn3m cubic phase. The presence of a stabilizer can affect monoolein self-assembly as reported by e.g. Nakano *et al.*[41] in cubosome dispersions stabilized by Pluronic F127. The interaction between the PPO lipophilic moiety of the stabilizer locally affects the organization of the lipid bilayer, giving two types bicontinuous cubic phases, Im3m and Pn3m, depending on the amount of added stabilizer. In the case of GGM-stabilized formulations, both of the SAXS curves have similar patterns with at least two clearly visible Bragg peaks, which corresponds to a Pn3m. This is highlighting that the GGM is covering the surface of the NPs without affecting the internal structure in water. This is in contrast to formulations stabilized with Pluronics. This finding represents a crucial point for a possible application of these aggregates as drug delivery systems. The diffusion coefficient of small hydrophilic molecules in Pn3m phase has been observed to be larger than in Im3m phase, which has been attributed to the higher porosity of the former.[42]
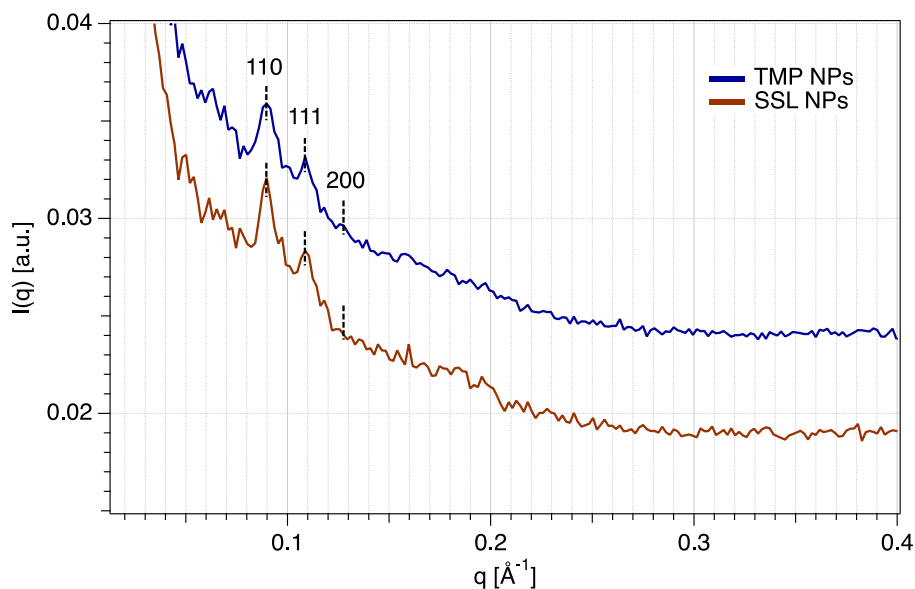
Figure 1. SAXS curves of the TMP (dark blue) and SSL (brown) nanoparticles. The scattering profile of the TMP was shifted upwards by a factor of 0.01 for clarity. The Miller indices for the Pn3m type of cubic phase are indicated for the corresponding Bragg peaks. The corresponding lattice parameters (a) and water channel radius (r_w) of TMP-NPs and SSL-NPs are shown in Table 1.

Lattice parameter and water channel radius could be determined from the position of the Bragg peaks in scattering curves. As reported in Table 2, formulations contain particles with a lattice parameter characteristic to Pn3m phase cubosomes equal to 99.6 Å and 94.7 Å for TMP- and SSL-NPs, respectively.

These values of lattice parameters are in line with the ones already reported for Pluronic-stabilized cubosomes, with no significant difference between the two types of hemicellulose stabilizers.[11,43,44]

In order to assess the morphology of the aggregates, the samples were imaged with cryo-TEM and the results of the two different formulations are shown in Figure 2. In all of the micrographs, aggregates with a defined internal structure can be observed. In order to confirm internal structure of the nanoparticles, 2D Fourier transform filter was applied to the cryo-TEM images and lattice parameter was extracted. The Fourier transform filtered images of the cubosome internal structure are shown as insets in Figure 2. Obtained lattice parameters are 89 Å for TMP-NPs and 110 Å for SSL-NPs which agrees well with values extracted based on SAXS patterns.

The TMP-NPs sample contains 200 – 250 nm large cubosomes, in addition to fractal-like aggregates (Figure 2). Different types of softwood hemicellulose have previously been shown to assemble into similar structures and therefore the aggregates observed in Figure 2 can be attributed to the excess hemicellulose that is not incorporated in the cubic nanoparticles.[45,46] Additionally, the TMP-stabilized sample contains a small amount of vesicles that are approximately 150 nm large (Figure 2B).
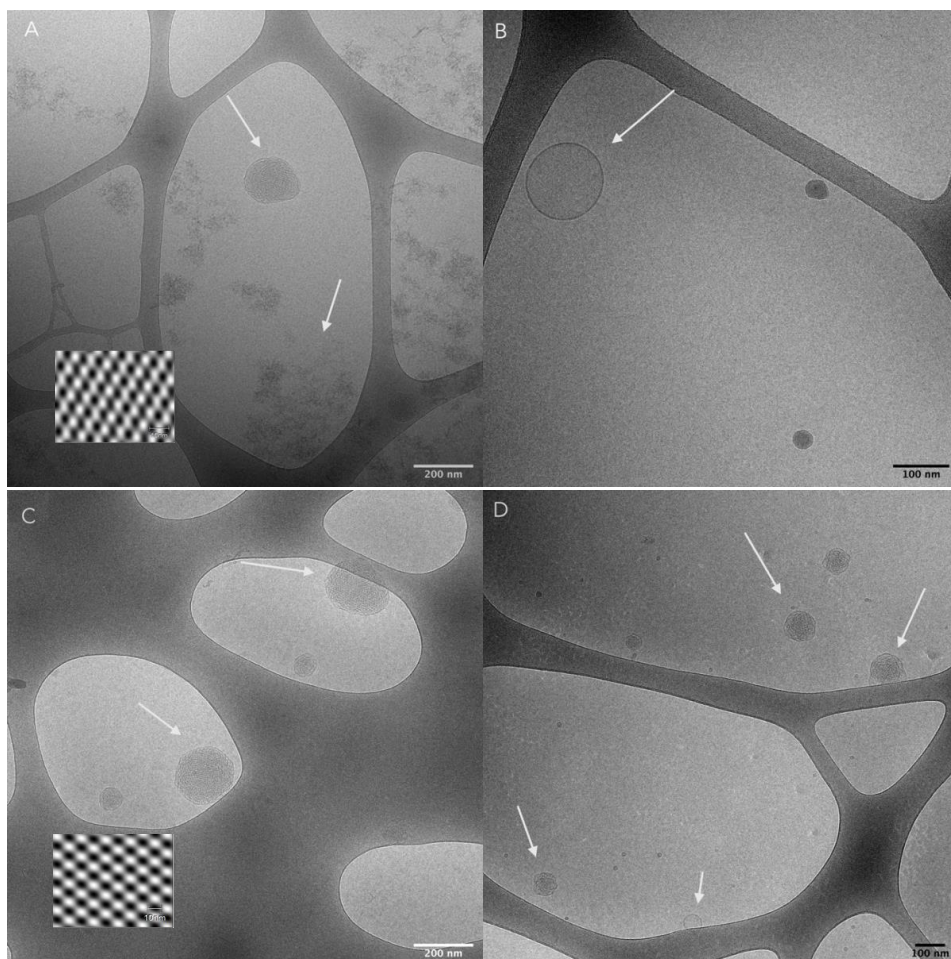
Figure 2. Cryo-TEM images of TMP-NPs (A and B) and SSL-NPs (C and D) at 10mg mL^{-1} concentration incubated at 25 °C prior to blotting. The insets represent micrographs after applying 2D Fourier transform filter.

Figure 2 (C, D) shows the cryo-TEM images of SSL-stabilized sample. This sample looks more homogenous without the presence of hemicellulose fractal structures. This indicates that most of the hemicellulose is associated with monoolein in the cubosomes. The cubosomes range in diameter from 50 – 200 nm that agrees well with the DLS results. Similar to the TMP-NPs, a low amount of vesicles is present in this sample as well (Figure 2D).

Since at this concentration, monoolein gives a Pn3m cubic phase with excess water, the presence of vesicles in the sample confirms that hemicellulose interacts with the monoolein lipid bilayer. This result is not surprising, since other studies have highlighted the effect that stabilizers can have on the morphology of cubosomes.[16,37,47,48] Here we note that in our study we observed a small or negligible fraction of vesicles.

Imaging of the nanoparticles on hydrophobic surface liquid AFM

In addition to cryo-TEM, SSL-NPs were imaged with AFM on a hydrophobized silica surface in liquid mode in order to emulate their interaction with interfaces, which is relevant for delivery applications.[49] As it can be seen in Figure 3, the nanoparticles are generally 30 - 60 nm in height and 250 – 600 nm in diameter. The fact that the diameter is much larger than we have observed both with DLS and cryo-TEM, indicates that the cubosomes partly spread on the surface and adopt a flatter conformation.
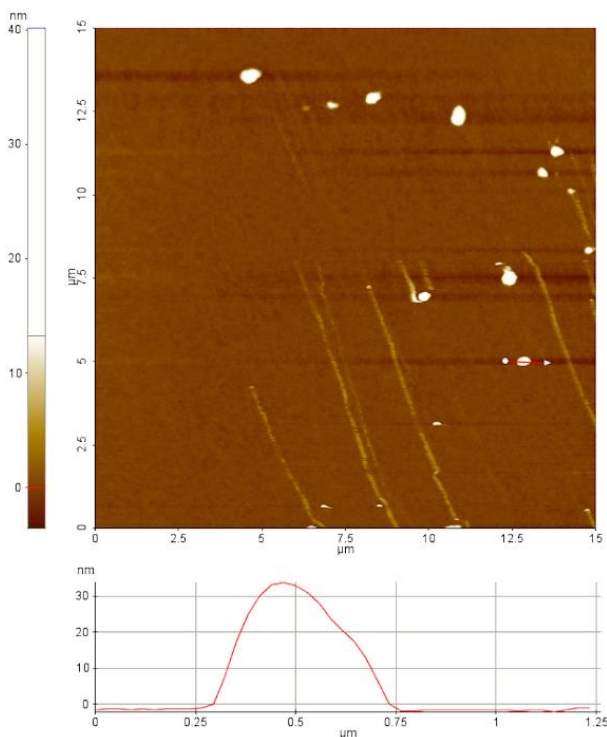
Figure 3. AFM images of SSL-NPs on hydrophobic silica in liquid obtained in tapping mode.

Stability of the nanoparticles in water

The shelf-life presents a critical feature of a formulation, therefore understanding the colloidal stability over time is fundamental in applying these aggregates as drug carriers. The cubosomes dispersion colloidal stability over time has been investigated by DLS and the results are summarized in Figure 4. Both formulations are stable in terms of apparent hydrodynamic diameter and polydispersity index for at least 42 days at room temperature. These results show that both TMP and SSL extracts are stabilizing the lipid-water interface is such a way that they provide colloidal stability of the dispersion and preventing the system from flocculating.

146
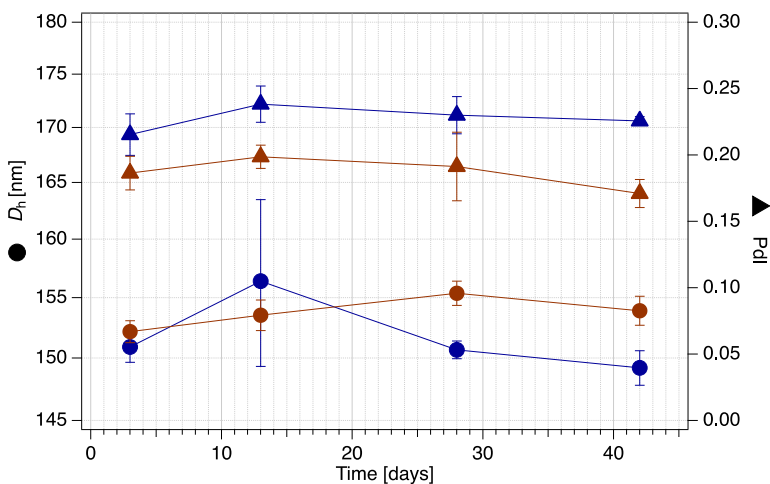
Figure 4 Hydrodynamic diameter (circles) and polydispersity (triangles) over time of TMP-NPs (dark blue) and SSL-NPs (brown).

Effect of physiological environment

The application of cubosomes for drug delivery and other biomedical applications make their colloidal and structural stability in a physiological environment a crucial requirement. Indeed, pH and salt concentration can affect lipid self-assembly in terms of size, charge and structure.[50] Taking these factors into account, 10 mM phosphate saline buffer (PBS) pH 7.4 has been used to mimic the physiological environment.

First, an aliquot of the formulations was diluted 500 times in PBS in order to follow the changes in the size and polydispersity of the nanoparticles under these conditions. The size of the nanoparticles of both formulations increases significantly (to 250 nm) at the start of the incubation but remains stable in case of SSL-NPs (Figure 5B). However, the size of the TMP-NPs continues to increase for the next two hours until it reaches 400 nm. The polydispersity is relatively stable in SSL-stabilized sample over the whole investigated time span, while it increases from 0.15 to 0.25 during the first 3 hours in the TMP-stabilized formulation. These changes might indicate aggregation of particles due to screening effect caused by increasing the ionic strength with the added buffer.

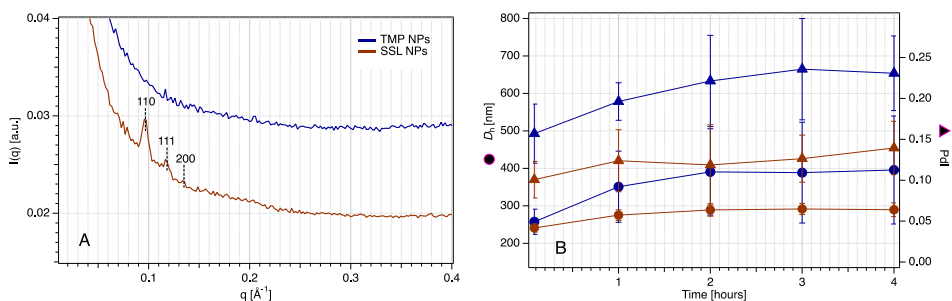**Figure 5.** SAXS curves of TMP-NPs (blue) and SSL-NPs (brown) seen in A and change in hydrodynamic diameter (circles) and polydispersity (triangles) seen in B in PBS buffer. The scattering curve of the TMP-NPs was shifted upwards by a factor of 0.01 for clarity.

Indeed, the electrophoretic mobility measurements showed that the negative potential has decreased significantly explaining the reduction of the cubosome colloidal stability, which in particular for TMP-NPs causes aggregation (see Table 3).

Table 3. ζ-potential of TMP-NPs, SSL-NPs, as well as TMP and SSL extracts in PBS buffer determined at 25 °C.

Sample	ζ-potential ± SD [mV]
TMP-NPs	-0.9 ± 0.4
SSL-NPs	-7.4 ± 0.9
TMP	-1 ± 2
SSL	-6 ± 2

The effect of PBS on the internal structure of the two GGMs stabilized cubosomes was evaluated through SAXS measurements. It has previously been reported that the change in ionic strength can trigger shift from one phase to another.[51,52]

Figure 5A shows the scattering curves of the TMP- and SSL-stabilized samples after dilution in PBS buffer 0.1 times.

The TMP-stabilized nanoparticles precipitated as soon as the buffer was added. The precipitation was observed with the SSL-stabilized sample as well, however to a lower extent and the sample still appeared milky after dilution. Indeed, the SAXS patterns confirm that the SSL-NPs retain Pn3m phase with no significant change in terms of lattice parameter and water channel radius after addition of the PBS buffer. The lattice parameter and water channel radius of the SSL-NPs in PBS buffer was 93.1 ± 0.4 Å and 19.4 ± 0.1 Å, respectively. On the other hand, the Bragg peaks completely disappear in case of the TMP-NPs indicating that it appears as the internal structure is at least partly lost. Partly this can be explained by the precipitation of the particles and hence a significantly lower number of particles. Similar tendency was observed with DLS: due to a much lower concentration, the aggregation of the TMP-NPs could not be monitored beyond a size of 400 nm.

The fact that the SSL-NPs formulation is more stable at an elevated ionic strength might be due to the higher ζ-potential as shown in Table 2. Moreover, a larger amount of monoolein is dispersed in the SSL-NPs sample than in the TMP-NPs one.

Conclusions

Softwood hemicellulose is an underutilized and abundant resource that can be used for a variety of applications thanks to its unique properties.[23,26,53–55] Its application as a stabilizer has already been proven in previous studies for oil-in-water emulsions. Indeed, other hemicelluloses such as xylan have found application in several field, given their promising biological features.[56]

The ability of two softwood hemicellulose extracts, with different amount of lignin, to stabilize monoolein-based cubosomes was demonstrated in this study, where the higher lignin content in the SSL-extract facilitated stabilization of a larger fraction of the dispersed lipid phase. The presence of the hemicellulose extracts did not affect the self-assembly structure of monoolein

in aqueous dispersions, giving a Pn3m bicontinuous cubic structure. Moreover, both formulations were stable over the period of at least 42 days with no significant changes in size or polydispersity. The results show that the physiological environment did not affect the structure for the SSL-stabilized cubosomes.

Indeed, the SSL-hemicellulose provided a better colloidal stability in comparison with the TMP-extract. This study shows that hemicellulose can be used as natural substitute to Pluronics to stabilize lipid liquid crystalline nanoparticles. Further studies are needed to reveal the biological effect of these aggregates, hence *in vitro* investigations will be performed as a future perspective.

References

(1) Barriga, H. M. G.; Holme, M. N.; Stevens, M. M. Cubosomes: The Next Generation of Smart Lipid Nanoparticles? *Angew. Chem. Int. Ed. Engl.* **2019**, *58* (10), 2958–2978. https://doi.org/10.1002/anie.201804067.

(2) Neto, C.; Aloisi, G.; Baglioni, P.; Larsson, K. Imaging Soft Matter with the Atomic Force Microscope: Cubosomes and Hexosomes. *J. Phys. Chem. B* **1999**, *103* (19), 3896–3899. https://doi.org/10.1021/jp984551b.

(3) Meli, V.; Caltagirone, C.; Sinico, C.; Lai, F.; Falchi, A. M.; Monduzzi, M.; Obiols-Rabasa, M.; Picci, G.; Rosa, A.; Schmidt, J.; Talmon, Y.; Murgia, S. Theranostic Hexosomes for Cancer Treatments: An in Vitro Study. *New Journal of Chemistry* **2017**, *41* (4), 1558–1565. https://doi.org/10.1039/c6nj03232j.

(4) Chen, Y.; Angelova, A.; Angelov, B.; Drechsler, M.; M. Garamus, V.; Willumeit-Römer, R.; Zou, A. Sterically Stabilized Spongosomes for Multidrug Delivery of Anticancer Nanomedicines. *Journal of Materials Chemistry B* **2015**, *3* (39), 7734–7744. https://doi.org/10.1039/C5TB01193K.

(5) Gilbert, J.; Valldeperas, M.; K. Dhayal, S.; Barauskas, J.; Dicko, C.; Nylander, T. Immobilisation of β-Galactosidase within a Lipid Sponge Phase: Structure, Stability and Kinetics Characterisation. *Nanoscale* **2019**, *11* (44), 21291–21301. https://doi.org/10.1039/C9NR06675F.

(6) Murgia, S.; Biffi, S.; Mezzenga, R. Recent Advances of Non-Lamellar Lyotropic Liquid Crystalline Nanoparticles in Nanomedicine. *Current Opinion in Colloid & Interface Science* **2020**, *48*, 28–39. https://doi.org/10.1016/j.cocis.2020.03.006.

(7) Magana, J. R.; Homs, M.; Esquena, J.; Freilich, I.; Kesselman, E.; Danino, D.; Rodríguez-Abreu, C.; Solans, C. Formulating Stable Hexosome Dispersions with a Technical Grade Diglycerol-Based Surfactant. *Journal of Colloid and Interface Science* **2019**, *550*, 73–80. https://doi.org/10.1016/j.jcis.2019.04.084.

(8) Prajapati, R.; Salentinig, S.; Yaghmur, A. Temperature Triggering of Kinetically Trapped Self-Assemblies in Citrem-Phospholipid Nanoparticles. *Chemistry and Physics of Lipids* **2018**, *216*, 30–38. https://doi.org/10.1016/j.chemphyslip.2018.09.003.

(9)   Bazylińska, U.; Kulbacka, J.; Schmidt, J.; Talmon, Y.; Murgia, S. Polymer-Free Cubosomes for Simultaneous Bioimaging and Photodynamic Action of Photosensitizers in Melanoma Skin Cancer Cells. *Journal of Colloid and Interface Science* **2018**, *522*, 163–173. https://doi.org/10.1016/j.jcis.2018.03.063.

(10) Biffi, S.; Andolfi, L.; Caltagirone, C.; Garrovo, C.; Falchi, A. M.; Lippolis, V.; Lorenzon, A.; Macor, P.; Meli, V.; Monduzzi, M.; Obiols-Rabasa, M.; Petrizza, L.; Prodi, L.; Rosa, A.; Schmidt, J.; Talmon, Y.; Murgia, S. Cubosomes Forin Vivofluorescence Lifetime Imaging. *Nanotechnology* **2016**, *28* (5), 055102. https://doi.org/10.1088/1361-6528/28/5/055102.

(11) Murgia, S.; Falchi, A. M.; Meli, V.; Schillén, K.; Lippolis, V.; Monduzzi, M.; Rosa, A.; Schmidt, J.; Talmon, Y.; Bizzarri, R.; Caltagirone, C. Cubosome Formulations Stabilized by a Dansyl-Conjugated Block Copolymer for Possible Nanomedicine Applications. *Colloids and Surfaces B: Biointerfaces* **2015**, *129*, 87–94. https://doi.org/10.1016/j.colsurfb.2015.03.025.

(12) Alcaraz, N.; Liu, Q.; Hanssen, E.; Johnston, A.; Boyd, B. J. Clickable Cubosomes for Antibody-Free Drug Targeting and Imaging Applications. *Bioconjugate Chem.* **2018**, *29* (1), 149–157. https://doi.org/10.1021/acs.bioconjchem.7b00659.

(13) Boge, L.; Umerska, A.; Matougui, N.; Bysell, H.; Ringstad, L.; Davoudi, M.; Eriksson, J.; Edwards, K.; Andersson, M. Cubosomes Post-Loaded with Antimicrobial Peptides: Characterization, Bactericidal Effect and Proteolytic Stability. *International Journal of Pharmaceutics* **2017**, *526* (1), 400–412. https://doi.org/10.1016/j.ijpharm.2017.04.082.

(14) Mendozza, M.; Montis, C.; Caselli, L.; Wolf, M.; Baglioni, P.; Berti, D. On the Thermotropic and Magnetotropic Phase Behavior of Lipid Liquid Crystals Containing Magnetic Nanoparticles. *Nanoscale* **2018**, *10* (7), 3480–3488. https://doi.org/10.1039/C7NR08478A.

(15) Azmi, I. D. M.; Wibroe, P. P.; Wu, L.-P.; Kazem, A. I.; Amenitsch, H.; Moghimi, S. M.; Yaghmur, A. A Structurally Diverse Library of Safe-by-Design Citrem-Phospholipid Lamellar and Non-Lamellar Liquid Crystalline Nano-Assemblies. *J Control Release* **2016**, *239*, 1–9. https://doi.org/10.1016/j.jconrel.2016.08.011.

(16) Fornasier, M.; Biffi, S.; Bortot, B.; Macor, P.; Manhart, A.; Wurm, F. R.; Murgia, S. Cubosomes Stabilized by a Polyphosphoester-Analog of Pluronic F127 with Reduced Cytotoxicity. *Journal of Colloid and Interface Science* **2020**, *580*, 286–297. https://doi.org/10.1016/j.jcis.2020.07.038.

(17) Uyama, M.; Nakano, M.; Yamashita, J.; Handa, T. Useful Modified Cellulose Polymers as New Emulsifiers of Cubosomes. *Langmuir* **2009**, *25* (8), 4336–4338. https://doi.org/10.1021/la900386q.

(18) Almgren, M.; Borné, J.; Feitosa, E.; Khan, A.; Lindman, B. Dispersed Lipid Liquid Crystalline Phases Stabilized by a Hydrophobically Modified Cellulose. *Langmuir* **2007**, *23* (5), 2768–2777. https://doi.org/10.1021/la062482j.

(19) Spicer, P. T.; Small, W. B.; Small, W. B.; Lynch, M. L.; Burns, J. L. Dry Powder Precursors of Cubic Liquid Crystalline Nanoparticles (Cubosomes). *Journal of Nanoparticle Research* **2002**, *4* (4), 297–311. https://doi.org/10.1023/A:1021184216308.

(20) Fengel, D.; Wegener, G. *Wood: Chemistry, Ultrastructure, Reactions*; Walter de Gruyter, 2011.

(21) Mikkonen, K. S.; Xu, C.; Berton-Carabin, C.; Schroën, K. Spruce Galactoglucomannans in Rapeseed Oil-in-Water Emulsions: Efficient Stabilization Performance and Structural Partitioning. *Food Hydrocolloids* **2016**, *52*, 615–624. https://doi.org/10.1016/j.foodhyd.2015.08.009.

(22) Bhattarai, M.; Valoppi, F.; Hirvonen, S.-P.; Hietala, S.; Kilpeläinen, P.; Aseyev, V.; Mikkonen, K. S. Time-Dependent Self-Association of Spruce Galactoglucomannans Depends on PH and Mechanical Shearing. *Food Hydrocolloids* **2020**, *102*, 105607. https://doi.org/10.1016/j.foodhyd.2019.105607.

(23) Valoppi, F.; H. Lahtinen, M.; Bhattarai, M.; J. Kirjoranta, S.; K. Juntti, V.; J. Peltonen, L.; O. Kilpeläinen, P.; S. Mikkonen, K. Centrifugal Fractionation of Softwood Extracts Improves the Biorefinery Workflow and Yields Functional Emulsifiers. *Green Chemistry* **2019**, *21* (17), 4691–4705. https://doi.org/10.1039/C9GC02007A.

(24) Lahtinen, M. H.; Valoppi, F.; Juntti, V.; Heikkinen, S.; Kilpeläinen, P. O.; Maina, N. H.; Mikkonen, K. S. Lignin-Rich PHWE Hemicellulose Extracts Responsible for Extended Emulsion Stabilization. *Front. Chem.* **2019**, *7*. https://doi.org/10.3389/fchem.2019.00871.

(25) Lehtonen, M.; Merinen, M.; Kilpeläinen, P. O.; Xu, C.; Willför, S. M.; Mikkonen, K. S. Phenolic Residues in Spruce Galactoglucomannans Improve Stabilization of Oil-in-Water Emulsions. *Journal of Colloid and Interface Science* **2018**, *512*, 536–547. https://doi.org/10.1016/j.jcis.2017.10.097.

(26) Mikkonen, K. S.; Kirjoranta, S.; Xu, C.; Hemming, J.; Pranovich, A.; Bhattarai, M.; Peltonen, L.; Kilpeläinen, P.; Maina, N.; Tenkanen, M.; Lehtonen, M.; Willför, S. Environmentally-Compatible Alkyd Paints Stabilized by Wood Hemicelluloses. *Industrial Crops and Products* **2019**, *133*, 212–220. https://doi.org/10.1016/j.indcrop.2019.03.017.

(27) Lundqvist, J.; Teleman, A.; Junel, L.; Zacchi, G.; Dahlman, O.; Tjerneld, F.; Stålbrand, H. Isolation and Characterization of Galactoglucomannan from Spruce (Picea Abies). *Carbohydrate Polymers* **2002**, *48* (1), 29–39. https://doi.org/10.1016/S0144-8617(01)00210-7.

(28) Hannuksela, T.; Tenkanen, M.; Holmbom, B. Sorption of Dissolved Galactoglucomannans and Galactomannans to Bleached Kraft Pulp. *Cellulose* **2002**, *9* (3), 251–261. https://doi.org/10.1023/A:1021178420580.

(29) Henrik Vibe Scheller; Peter Ulvskov. Hemicelluloses. *Annual Review of Plant Biology* **2010**, *61* (1), 263–289. https://doi.org/10.1146/annurev-arplant-042809-112315.

(30) Willför, S.; Sjöholm, R.; Laine, C.; Roslund, M.; Hemming, J.; Holmbom, B. Characterisation of Water-Soluble Galactoglucomannans from Norway Spruce Wood and Thermomechanical Pulp. *Carbohydrate Polymers* **2003**, *52* (2), 175–187. https://doi.org/10.1016/S0144-8617(02)00288-6.

(31) Thuvander, J.; Jönsson, A.-S. Extraction of Galactoglucomannan from Thermomechanical Pulp Mill Process Water by Microfiltration and Ultrafiltration—Influence of Microfiltration Membrane Pore Size on Ultrafiltration Performance. *Chemical Engineering Research and Design* **2016**, *105*, 171–176. https://doi.org/10.1016/j.cherd.2015.12.003.

(32) Zasadowski, D.; Yang, J.; Edlund, H.; Norgren, M. Antisolvent Precipitation of Water-Soluble Hemicelluloses from TMP Process Water. *Carbohydrate Polymers* **2014**, *113*, 411–419. https://doi.org/10.1016/j.carbpol.2014.07.033.

(33) Biomass Compositional Analysis Laboratory Procedures | Bioenergy | NREL https://www.nrel.gov/bioenergy/biomass-compositional-analysis.html (accessed Oct 15, 2020).

(34) Al-Rudainy, B.; Galbe, M.; Schagerlöf, H.; Wallberg, O. Antisolvent Precipitation of Hemicelluloses, Lignosulfonates and Their Complexes from Ultrafiltrated Spent Sulfite Liquor (SSL). *Holzforschung* **2018**, *72* (10), 839–850. https://doi.org/10.1515/hf-2017-0218.

(35) Kulkarni, C. V.; Wachter, W.; Iglesias-Salto, G.; Engelskirchen, S.; Ahualli, S. Monoolein: A Magic Lipid? *Phys. Chem. Chem. Phys.* **2011**, *13* (8), 3004–3021. https://doi.org/10.1039/C0CP01539C.

(36) Gwyddion – Free SPM (AFM, SNOM/NSOM, STM, MFM, …) data analysis software http://gwyddion.net/ (accessed Oct 29, 2020).

(37) Akhlaghi, S. P.; Ribeiro, I. R.; Boyd, B. J.; Loh, W. Impact of Preparation Method and Variables on the Internal Structure, Morphology, and Presence of Liposomes in Phytantriol-Pluronic(®) F127 Cubosomes. *Colloids Surf B Biointerfaces* **2016**, *145*, 845–853. https://doi.org/10.1016/j.colsurfb.2016.05.091.

(38) Kim, J.-Y.; Song, M.-G.; Kim, J.-D. Zeta Potential of Nanobubbles Generated by Ultrasonication in Aqueous Alkyl Polyglycoside Solutions. *Journal of Colloid and Interface Science* **2000**, *223* (2), 285–291. https://doi.org/10.1006/jcis.1999.6663.

(39) S. Mikkonen, K.; Merger, D.; Kilpeläinen, P.; Murtomäki, L.; S. Schmidt, U.; Wilhelm, M. Determination of Physical Emulsion Stabilization Mechanisms of Wood Hemicelluloses via Rheological and Interfacial Characterization. *Soft Matter* **2016**, *12* (42), 8690–8700. https://doi.org/10.1039/C6SM01557C.

(40) Qiu, H.; Caffrey, M. The Phase Diagram of the Monoolein/Water System: Metastability and Equilibrium Aspects. *Biomaterials* **2000**, *21* (3), 223–234. https://doi.org/10.1016/S0142-9612(99)00126-X.

(41) Nakano, M.; Sugita, A.; Matsuoka, H.; Handa, T. Small-Angle X-Ray Scattering and 13C NMR Investigation on the Internal Structure of "Cubosomes." *Langmuir* **2001**, *17* (13), 3917–3922. https://doi.org/10.1021/la010224a.

(42) Aleandri, S.; Mezzenga, R. The Physics of Lipidic Mesophase Delivery Systems. *Physics Today* **2020**, *73*, 38–44. https://doi.org/10.1063/PT.3.4522.

(43) Caltagirone, C.; Falchi, A. M.; Lampis, S.; Lippolis, V.; Meli, V.; Monduzzi, M.; Prodi, L.; Schmidt, J.; Sgarzi, M.; Talmon, Y.; Bizzarri, R.; Murgia, S. Cancer-Cell-Targeted Theranostic Cubosomes. *Langmuir* **2014**, *30* (21), 6228–6236. https://doi.org/10.1021/la501332u.

(44) Murgia, S.; Falchi, A. M.; Mano, M.; Lampis, S.; Angius, R.; Carnerup, A. M.; Schmidt, J.; Diaz, G.; Giacca, M.; Talmon, Y.; Monduzzi, M. Nanoparticles from Lipid-Based Liquid Crystals: Emulsifier Influence on Morphology and Cytotoxicity. *J. Phys. Chem. B* **2010**, *114* (10), 3518–3525. https://doi.org/10.1021/jp9098655.

(45) Naidjonoka, P.; Arcos Hernandez, M.; K. Pálsson, G.; Heinrich, F.; Stålbrand, H.; Nylander, T. On the Interaction of Softwood Hemicellulose with Cellulose Surfaces in Relation to Molecular Structure and Physicochemical Properties of Hemicellulose. *Soft Matter* **2020**. https://doi.org/10.1039/D0SM00264J.

(46) Kishani, S.; Vilaplana, F.; Xu, W.; Xu, C.; Wågberg, L. Solubility of Softwood Hemicelluloses. *Biomacromolecules* **2018**, *19* (4), 1245–1255. https://doi.org/10.1021/acs.biomac.8b00088.

(47) Murgia, S.; Bonacchi, S.; Falchi, A. M.; Lampis, S.; Lippolis, V.; Meli, V.; Monduzzi, M.; Prodi, L.; Schmidt, J.; Talmon, Y.; Caltagirone, C. Drug-Loaded Fluorescent Cubosomes: Versatile Nanoparticles for Potential Theranostic Applications. *Langmuir* **2013**, *29* (22), 6673–6679. https://doi.org/10.1021/la401047a.

(48) Jenni, S.; Picci, G.; Fornasier, M.; Mamusa, M.; Schmidt, J.; Talmon, Y.; Sour, A.; Heitz, V.; Murgia, S.; Caltagirone, C. Multifunctional Cubic Liquid Crystalline Nanoparticles for Chemo- and Photodynamic Synergistic Cancer Therapy. *Photochemical & Photobiological Sciences* **2020**, *19* (5), 674–680. https://doi.org/10.1039/C9PP00449A.

(49) Chang, D. P.; Barauskas, J.; Dabkowska, A. P.; Wadsäter, M.; Tiberg, F.; Nylander, T. Non-Lamellar Lipid Liquid Crystalline Structures at Interfaces. *Advances in Colloid and Interface Science* **2015**, *222*, 135–147. https://doi.org/10.1016/j.cis.2014.11.003.

(50) Liu, Q.; Dong, Y.-D.; Hanley, T. L.; Boyd, B. J. Sensitivity of Nanostructure in Charged Cubosomes to Phase Changes Triggered by Ionic Species in Solution. *Langmuir* **2013**, *29* (46), 14265–14273. https://doi.org/10.1021/la402426y.

(51) Muir, B. W.; Zhen, G.; Gunatillake, P.; Hartley, P. G. Salt Induced Lamellar to Bicontinuous Cubic Phase Transitions in Cationic Nanoparticles. *J. Phys. Chem. B* **2012**, *116* (11), 3551–3556. https://doi.org/10.1021/jp300239g.

(52) Hartnett, T. E.; Ladewig, K.; O'Connor, A. J.; Hartley, P. G.; McLean, K. M. Size and Phase Control of Cubic Lyotropic Liquid Crystal Nanoparticles. *J. Phys. Chem. B* **2014**, *118* (26), 7430–7439. https://doi.org/10.1021/jp502898a.

(53) Hartman, J.; Albertsson, A. C.; Lindblad, M. S.; Sjöberg, J. Oxygen Barrier Materials from Renewable Sources: Material Properties of Softwood Hemicellulose-Based Films. *Journal of Applied Polymer Science* **2006**, *100* (4), 2985–2991. https://doi.org/10.1002/app.22958.

(54) Mikkonen, K. S.; Tenkanen, M.; Cooke, P.; Xu, C.; Rita, H.; Willför, S.; Holmbom, B.; Hicks, K. B.; Yadav, M. P. Mannans as Stabilizers of Oil-in-Water Beverage Emulsions. *LWT - Food Science and Technology* **2009**, *42* (4), 849–855. https://doi.org/10.1016/j.lwt.2008.11.010.

(55) Willför, S.; Sundberg, K.; Tenkanen, M.; Holmbom, B. Spruce-Derived Mannans – A Potential Raw Material for Hydrocolloids and Novel Advanced Natural Materials. *Carbohydrate Polymers* **2008**, *72* (2), 197–210. https://doi.org/10.1016/j.carbpol.2007.08.006.

(56) Li, X.; Shi, X.; Wang, M.; Du, Y. Xylan Chitosan Conjugate - A Potential Food Preservative. *Food Chemistry* **2011**, *126* (2), 520–525. https://doi.org/10.1016/j.foodchem.2010.11.037.

Paper IV

Thermoresponsive glycopolymers based on *N*-isopropyl acrylamide and enzymatically synthesized β-mannosyl acrylates

M. Arcos-Hernandez, **P. Naidjonoka**, S. J. Butler, T. Nylander, H. Stålbrand, P. Jannasch

Thermoresponsive Glycopolymers Based on Enzymatically Synthesized β-Mannosyl Acrylates and N-Isopropylacrylamide

Monica Arcos-Hernandez[a]*, Polina Naidjonoka[b‡], Samuel J. Butler[c‡], Tommy Nylander[b], Henrik Stålbrand[c]*, Patric Jannasch[a]*

[a]Centre for Analysis and Synthesis, Department of Chemistry, Lund University, PO Box 124, S-221 00 Lund, Sweden

[b]Physical Chemistry, Department of Chemistry, Lund University, PO Box 124, S-221 00 Lund, Lund, Sweden.

[c]Department of Biochemistry and Structural Biology, Department of Chemistry, Lund University, PO Box 124, S-221 00 Lund, Sweden.

*monica.arcos_hernandez@chem.lu.se

*patric.jannasch@chem.lu.se

*henrik.stalbrand@biochemistry.lu.se

‡These authors contributed equally.

Abstract

We here present a series of thermoresponsive glycopolymers in the form of poly(N-isopropyl acrylamide)-*co*-(2-[β-manno[oligo]syloxy] ethyl methacrylate)s. These copolymers were prepared from β-mannosyl acrylates that were synthesized through enzymatic catalysis, and were subsequently investigated with respect to their aggregation and phase behavior in aqueous solution using a combination of ^{1}H NMR spectroscopy, dynamic light scattering, cryogenic transmission electron microscopy and small angle X-ray scattering. The thermoresponsive glycopolymers were prepared by copolymerizations of different mixtures of 2-(β-manno[oligo]syloxy)ethyl methacrylates (with either one or two saccharide units) and N-isopropyl acrylamide (NIPAm) to tune the thermoresponsiveness. The results showed that at temperatures below the low critical solution temperature (LCST) of poly(NIPAm), the glycopolymers readily aggregate into nanoscale structures due to attractive interaction between sugar moieties. Above the LCST of poly(NIPAm), the glycopolymers rearrange into fractal and disc/globular aggregates. Cryo-TEM and SAXS data demonstrated that the presence of the β-mannosyl pendant moieties in the glycopolymers induces a gradual conformational change over a wide temperature range which offers improved control of

temperature-dependent properties in comparison to poly(NIPAm) with a sharp coil-to-globule transition. In addition, the thermoresponsiveness can be conveniently tuned by varying the sugar unit-length and content of the β-mannosyl acrylates.

1. Introduction

Glycopolymers are synthetic biobased polymers that have sugar groups as pendant moieties. They have attracted great attention because of their function as biomimetic analogues of glycolipids and glycoproteins.[1,2] Glycopolymers have affinity for specific proteins that are responsible for interactions at the cellular level which are the basis of important biological phenomena[3,4]. As such, glycopolymers can be used as biomaterials in drug delivery, tissue engineering, biosensors and medicine.[5] Responsive polymers, are polymers that undergo conformational changes when exposed to an external stimuli (temperature, pH, light, etc.). This type of polymers are valuable in applications where such changes are advantageous under certain conditions[6], for example in food, cosmetics[7], paints, oil recovery[8], as well as in biomedical applications for injectable hydrogels and controlled drug release.[9,10] In particular, temperature responsive polymers undergo a lower critical solution temperature (LCST) transition, resulting in a conformational coil-to-globule transformation upon exceeding a certain temperature.[11] At this temperature the polymer chain contracts as water becomes a poor solvent for the polymer.[12] Hence the polymer changes its character from hydrophilic to more hydrophobic, and is therefore prone to aggregation. One of the most widely studied thermoresponsive polymers is poly(N-isopropylacrylamide) [poly(NIPAm)] due to its temperature dependent phase transition in aqueous solution at ~32 °C, close to body temperature. The LCST behavior of poly(NIPAm) is frequently modulated by copolymerization with other hydrophilic or hydrophobic monomers such as 2-hydroxy ethyl methacrylate (HEMA).[13]

Glycopolymers that can undergo conformational changes under certain conditions, such as changes in temperature are of great interest. Sugar moieties have previously been incorporated into thermal responsive glycopolymers.[14–16] For example, thermoresponsive double hydrophilic diblock (TDHD) glycopolymers from poly(NIPAm) and an α-linked mannose-containing acrylate[15] and galactose-functionalized have been reported.[15] Recently, a set of temperature-switchable glycopolymers from NIPAm and α-mannose ligands were chemically synthesized.[17] These remarkable glycopolymers are mostly based on glycomonomers that contain mono-substituted pendant sugar units and have commonly been synthesized through multi-step pathways.

We have previously shown that β-mannanases, a type of glycoside hydrolases, can catalyze the synthesis of 2-(β-manno[oligo]syloxy) ethyl methacrylates (M_nEMAs) (i.e., mannosyl-EMA [M_1EMA] and mannobiosyl-EMA [M_2EMA]) that were subsequently used to synthesize glycopolymers.[18] The enzyme catalyzed synthesis of glycomonomers presents several advantages compared to traditional chemical synthesis, including the avoidance of cumbersome protection-deprotection steps and of toxic chemicals, as well as the possibility to use low temperature.[18] Although other glycopolymers containing enzymatically synthesized monomers (glycomonomers)

have been previously prepared[2,4,19], our glycomonomers (M$_n$EMAs) feature an equatorial (β) linkage at the anomeric position with the acceptor and between mannose residues, making these monomers quite unique. This linkage occurs widely within plants, hemicelluloses and storage glycans but has been shown to be very difficult to synthesize chemically.[20]

In the present work the transglycosylation capacity of the β-mannanase *TrMan5A* was utilized for glycomonomer synthesis using locust bean galactomannan as donor glycan, providing a cocktail of functionalized acrylate monomers bearing one to three β-mannose units in a one pot reaction in water at 37 °C.[18] Subsequently we were able to separate and purify the different M$_n$EMAs for polymer synthesis at microscale. We then used these monomers to synthesize thermoresponsive glycopolymers with NIPAm in conventional radical polymerizations in water at ambient temperature. In order to influence the solubility properties and the transition temperature of the copolymers in aqueous solution, we varied the molar fraction and the sequence of the sugar units. As mentioned above, M$_n$EMAs are glycomonomers with a hydrophilic biodegradable mannosylated part and a polymerizable acrylate part. By incorporating the glycomonomers in copolymers with NIPAm, we expected to modulate the LCST thanks to the mannosyl moieties, concurrently increasing the biodegradability and biocompatibility. We then studied the thermoresponsive behavior of the glycopolymers using dynamic light scattering (DLS), combined with ^{1}H nuclear magnetic resonance (NMR) spectroscopy, small angle X-ray scattering (SAXS) and cryogenic transmission electron microscopy (cryo-TEM).

2. Experimental section

2.1 Materials

Sodium acetate (molecular biology grade), acetic acid, diethyl ether (anhydrous, ≥ 99.7%, with 1ppm BHT as inhibitor), hydroquinone (HQ, ≥ 99%), acetonitrile (ACN, ≥ 99.9%, HPLC gradient grade), 2,5–dihydro benzoic acid (DHB), N-isopropylacrylamide (NIPAm), deuterated water (D$_2$O), 2,2'-azobis(isobutyronitrile) (AIBN), potassium persulfate (KPS) and N,N,N',N'-tetramethylethylenediamine (TEMED), HPLC grade ethanol, 2,2'-azobis(isobutyronitrile) (AIBN), diethyl ether, 2-hydroxyethyl methacrylate (HEMA) 97% containing 200 ppm hydroquinone (HQ) were all obtained from Sigma-Aldrich (St. Louis, MO, USA).

Low viscosity locust bean gum (LBG, >94% (dry weight basis)) was supplied by Megazyme (Bray, Ireland) (LOT 150901a) (galactose:mannose ratio, 24:76).

All chemicals were used as received except for HEMA, which was passed through an alumina column prior to polymerization to remove the inhibitor.[18]

TrMan5A

GH5 β-mannanase Man5A from *Trichoderma reesei* (TrMan5A) was prepared as previously described.[21] An amount of 20 mg of freeze-dried enzyme was dissolved in 50mM Sodium acetate buffer (50mM), pH 5.3. The solution was concentrated thrice, from 10 ml to 0.2 ml, in Sartorius VivaSpin 20 columns with a 10 kDa cut-off (Sartorius, Göttingen, Germany), refilling the column

with fresh buffer between each concentration step. The concentration was performed at 4 °C, 5000 rpm, 30 min, in VivaSpin 20 centrifugal concentrators (10000 MWCO PES membrane).

2.2 Methods

Synthesis of 2-(β-manno[oligos]yloxy) ethyl methacrylates) [M_nEMAs]

Enzymatic synthesis of the target glycomonomers, M_nEMAs, denoted with n=1 and 2 respectively, was done using the method developed in our previous work, except the volume of the reaction was 500 ml instead of 50 ml.[18] In short, the reaction was carried out in 500 ml 30 mM sodium-acetate buffer, pH 5.3. The donor substrate was galactomannan in the form of low viscosity locust bean gum (LBG) (3 w.v%) and the acceptor substrate, HEMA (20 vol%). The reaction was catalyzed by 0.2 µM of the β-mannanase *TrMan5A* at 37 °C, for 48 h, in a stirred, covered glass beaker, with intermittent sampling to enable reaction progression analysis. The glycomonomers were purified, screened, quantified and characterized using methods described previously.[18] [1]H and ^{13}C shift assignment has been extensively described previously.[18]

Synthesis of poly(N-isopropyl acrylamide)-*co*-(2-[β-manno[oligo]syloxy] ethyl methacrylate)s [poly(NIPAm-*co*-M_nEMA)s]

A total of eight different polymers were prepared in solution via conventional radical polymerization as previously described[18], three glycopolymers (P1M1-P3M1) based on M_1EMA and two (P1M2 and P2M2) with M_2EMA. Additionally, two reference samples were prepared, i.e. a homopolymer of NIPAm (PR1) and a copolymer of NIPAm and HEMA (PR2). Details of the experimental design of the polymerizations are found as supporting information (SI) part A and Table S1.

The copolymers of NIPAm and M_nEMAs (P1M1-P2M1 and P1M2-P3M2) and the homopolymer of NIPAm (PR1) were synthesized in D_2O with KPS as initiator and TEMED as accelerator. The reactions were performed at room temperature in an NMR spectroscopy tube as previously reported.[18] Sample PR2 was prepared in ethanol with AIBN as initiator at 60 °C similar to literature.[22] Scheme 1 summarizes the synthesis of the glycomonomers and their subsequent co-polymerization with NIPAm.

A

Poly-mannose + **HEMA** → (β-mannanase) → **MₙEMA**

B

MₙEMA + **NIPAm** → (D₂O, RT) → **Poly(NIPAm-co-MₙEMA)**
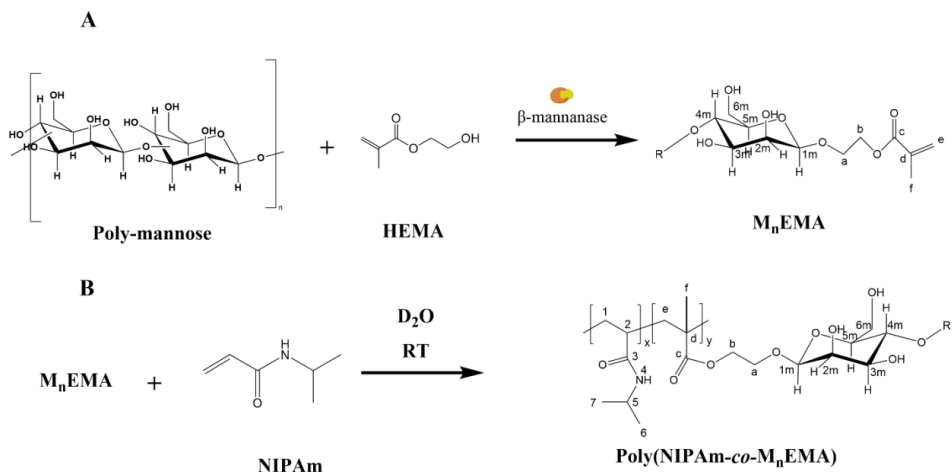
Scheme 1. Synthesis of poly(NIPAm-*co*-MₙEMA)s: (A) Enzymatic synthesis of β-mannosyl acrylates (MₙEMAs). (B) Radical co-polymerization of NIPAm and MₙEMAs in D₂O. M₁EMA: R=H and M₂EMA R=β-4,1-mannose.

Two samples (P2M1 and P2M2) were nominally prepared with the same mass ratio of monomers (NIPAm:MₙEMA) in order to compare the effect of the length of the sugar moieties given the same weight content in the synthesized copolymer. Samples P1M1 and P2M1, on the one hand, and samples P1M2-P3M2, on the other hand, were prepared with the same glycomonomer (M₁EMA or M₂EMA, respectively) in different molar concentrations in order to investigate the effect of the comonomer ratio on the thermoresponsive behavior.

Poly(N-isopropylacrylamide-co-2-[β-mannosyloxy] ethyl methacrylate) [P1M1-P2M1]

^{1}H NMR (D₂O, 500 MHz) chemical shift scale from residual HDO (δ 4.77) δ in ppm: 4.72* (s, H1m, C **H**), 4.54-3.53 (m, br, Hb, C **H**₂; Ha, C **H**₂; H2m, C **H**; H5, N-C **H** (CH₃)₂; [H6m, H3m, H4m], C **H**), 3.32-3.42 (m, br, H5m), 1.29–2.35 (m, br, H1, C **H**₂ in main chain; He, C **H**₂; H2, C **H** in main chain), 0.8 –1.29 (m, br, Hf, C **H**₃; H6+H7, N-CH (C **H**₃)₂).

*Assigned in spectra at 45 ºC, HDO (δ 4.60).

^{13}C NMR (D₂0, 125 MHz) δC in ppm, chemical shift scale from the unified scale according to IUPAC[23]: 175.2 (C3), 99.9 (C1m), 76.3 (C5m), 73.0 (C3m), 70.5 (C2m), 66.7 (C4m), 64.4 (Cb), 61.0 (C6m), 41.7(C2), 34.7(C1), 21.22 (C6+C7)

Poly(N-isopropylacrylamide-co-2-[β-manno(bio)syloxy] ethyl methacrylate) [P1M2-P3M2]

^{1}H NMR (D₂O) chemical shift scale from residual HDO (δ 4.77) δ in ppm: 0.96–1.29 (m, H6+H7, N-C **H** (CH₃)₂), 1.29–1.90 (m, H1, C **H**₂ in main chain), 1.90–2.29 (m,H2, C **H** in main chain), 3.79–4.12 (m, H5, N-C **H** (CH₃)₂), 0.8 –1.2 (m, Hf, C **H**₃), 1.5 – 2.5 (m, He, C **H**₂), 4.74*

(s, H1m, C **H**), 4.72* (s, H1m', C **H**), 4.44- 4.01 (m, C **H** $_2$ +C **H**, Hb+H2m'+H2m), 4.01-3.61 (m, C **H** $_2$ + C **H**, Ha + H6m'+H6m+H4m+H4m'+H3m'), 3.61-3.53 (m, C **H** , H4m), 3.42 (m, C **H** , H5m+H5m').

*Assigned in spectra at 45 °C, HDO (δ 4.60)

^{13}C NMR (D$_2$0, 125 MHz) δC in ppm, chemical shift scale from the unified scale according to IUPAC[23]: 175.2 (C3), 100.1 (C1m'), 99.9 (C1m), 76.6 (C4), 76.3 (C5m'), 74.8 (C5m), 72.8 (C3m'), 71.5 (C3m), 70.4 (C2m'), 69.8 (C2m), 66.6 (C4m'), 64.3 (Cb), 60.9 (C6m), 60.5 (C6m'), 41.7 (C2), 34.7 (C1), 21.5 (C6+C7)

Poly(N-isopropylacrylamide) [PR1]

^{1}H NMR (D$_2$O) δ in ppm: 4.01-3.79 (s,br N-C **H** (CH$_3$)$_2$), 2.29-1.84 (m,br, C **H** in main chain), 1.84-1.30 (m, br, C **H** $_2$ in main chain), 1.30-0.92 (m, br, N-CH (C **H** $_3$)$_2$).

^{13}C NMR (D$_2$0, 125 MHz) δC in ppm, chemical shift scale from the unified scale according to IUPAC[23]: 175.4 (C3), 42.0 (C2), 34.7 (C1), 21.80 (C6, C7).

Nuclear Magnetic Resonance (NMR) spectroscopy

^{1}H and ^{13}C spectra of the glycomonomers before polymerization and of the glycopolymer solutions of poly(NIPAm-*co*-M$_n$EMA)s were recorded on a Bruker Avance III spectrometer (Bruker, Billerica, MA, USA) at 500.17 MHz for ^{1}H and at 125.77 MHz for ^{13}C. Quantification of monomers was performed as previously.[18] A second method for quantification was used to confirm the results from the first. This second method was done using the ERETIC2 quantification tool available in the NMR processing software Topspin (Bruker Biospin, 2018) as previously described.[24] The method can be used with an external standard. In our studies we used a stock of purified HEMA as external standard. Five solutions with concentrations of: 5, 11, 21, 32 and 54 mg/L were prepared from this stock. Full description of NMR data acquisition can be found in SI part B.

Study of the LCST transitions of poly(NIPAm-co-MnEMA)s by NMR spectroscopy

^{1}H NMR spectra were recorded as described in SI-B at a range of temperatures, first heating from 25 °C to 50-65 °C and then cooling from 50-65 °C to 25 °C. In general, all spectra of a single sample were taken sequentially in the same run. For each sample the samples were gradually heated to the selected temperature and equilibrated during 6 min if the change in temperature was smaller than 3 °C and 10-15 min if the change was above 3 °C.

To study the LCST transitions from the acquired spectra, the intensities of selected chemical shifts at different temperatures were scaled to the intensity at 25 °C and plotted against temperature. A 5-parameter sigmoidal model was then fitted to the data from where two parameters were derived, the onset of the LCST, T_{onset}, defined as the temperature at which the thermal transition starts (i.e. temperature at the maximum slope) and a parameter that we have named $LCST_{NMR}$, which was obtained by resolving the sigmoidal equation (Equation S1) for when the intensity was half of the initial intensity at 25 °C (I=0.5). This definition of LCST has been used for similar thermoresponsive polymers.[16] Details of the model fitting can be found in SI part C.

Polymerization kinetics

^{1}H NMR spectra were recorded during the polymerization of samples P2M1 and P3M2 to gain insights into the reaction kinetics. To this effect, ^{1}H spectra were acquired at different time intervals. This was possible because the polymerizations were conducted at room temperature and inside an NMR tube. Hence, the possible effect of interference due to sample convection at temperatures higher than room temperature were negligible. The reaction was followed for the first 9 h after initiation.

Dynamic light scattering (DLS)

The size of the particles as a function of temperature was followed with a Zetasizer Nano ZS (Malvern Instruments Ltd, Worshestershire, UK) at a set angle of 173° using the non-invasive backscatter technology. The instrument was equipped with a 4 mW He-Ne laser with a 632.8 nm wavelength and an Avalanche photodiode detection (APD) unit. The obtained correlation functions were analyzed using the cumulants method available in the Malvern software. The samples were diluted 10 times with D_2O (~1 mg/mL) and filtered through 0.45 μm pore size hydrophilic filter to remove dust and larger particles. The correlation functions were recorded at temperatures from 25 °C – 70 °C in 2 °C steps. The samples were equilibrated for 3 min at every temperature prior to the measurement.

In addition, dynamic and static light scattering (DLS and SLS) measurements were performed with sample P2M2 on an ALV/DLS/SLS-5022F, CGH-8F-based compact goniometer system (ALV-GmbH, Langen, Germany) with a 22 mW He-Ne-laser (632.8 nm) light source. The instrument was equipped with an automatic attenuator, controlled via software. A cuvette with the sample was placed in a cell housing filled with a refractive index matched liquid (cis-decahydronaphtalene). DLS measurements were performed at temperatures 25 – 45 °C with 2 °C step at 90° angle while SLS was measured at 25 and 45 °C and at the detector angles of 30° - 140°. From these measurements we derived hydrodynamic radius (R_h) and a radius of gyration (R_g) at 25 and 45 °C and calculated a shape parameter ρ= R_g/R_h. The treatment of the data from DLS and SLS is described in details in SI part D.

Small Angle X-ray Scattering (SAXS)

SAXS measurements were performed using the Ganesha SAXS Lab instrument (SAXS Lab, Denmark). The instrument was equipped with a GeniX 3D 30 W Cu x-ray tube (Xenocs) and a 2D 300 K Pilatus detector (Dectris). The measurements were acquired with a pin-hole collimated beam with the detector positioned asymmetrically to yield q-range of 0.012 – 0.67 Å^{-1} and 0.003 – 0.21 Å^{-1}. The sample-to-detector distance was 480 mm and 1540 mm, respectively.

The magnitude of the scattering vector is defined by $q = (4 \pi \sin\theta)/\lambda$, where the wavelength λ equals to 1.54 Å (Cu $K\alpha$ wavelength) and θ is half of the scattering angle. The temperature in the analysis chamber was controlled using a Julabo T Controller CF41 from Julabo Labortechnik GmbH (Germany). Samples were measured at the initial concentration (~10 mg/mL) and two temperatures, at 25 and 50 °C, with the equilibration time of 30 min before each measurement.

The obtained scattering curves were corrected for background scattering and data from different detector distances were combined to cover the desired q-range. The reduced data was evaluated with SasView[25] and fitted to the Unified Exponential/Power-law model developed by Beaucage that describes fractal-like behavior of polymers in solution and polymer micelle model.[26–28] The scattering intensity of fractal objects can be described with the fractal model, $I(q) \sim q^{-d}$ where the exponent d can be obtained by fitting this model to the scattering curve.[25] In order to fit such data, a corrected Beaucage model is often applied.[26–28] This model describes fractal polymer chains that consist of flexible cylinders and gives two radii of gyration (R_g).[28] The largest R_g is determined from the low-q or Guiner regime and represents the overall size of the particle whereas the second radius of gyration is obtained from the q region where the curve shows transition in the slope and describes the size of a subunit of the polymer chain (R_{sub}). The latter radius can be converted into persistence length (L_p) which is an indication of the chain stiffness and can be calculated as:[29,30]

$$L_p = (\sqrt{12R_g^2})/2 \hspace{3cm} \text{Equation 1.}$$

Cryogenic Transmission Electron Microscopy (cryo-TEM)

The polymerization solutions had high viscosity and were therefore diluted 10-fold before imaging with cryo-TEM (~1 mg/mL). For sample imaging, a 4 µL drop of the sample was placed on a lacey carbon coated formvar grid (Ted Pella Inc, Redding, CA, USA) and gently blotted with a filter paper to create a thin film. The grid was then prepared for imaging using an automatic plunge-freezer system (Leica Em GP, Leica Microsystems, Wetzlar, Germany) with the environmental chamber operated at 25 and 50 °C. The specimen was then vitrified by rapid plunging of the grid into liquid ethane (-183 °C). Thereafter, samples were stored in liquid nitrogen (-196 °C) and transferred into the microscope using a cryo transfer tomography holder (Fischione, Model 2550, E.A. Fischione Instruments, Inc., Corporate Circle Export, PA, USA). The grids were examined with a Jeol JEM-2200FS transmission electron microscope (JEOL, Tokyo, Japan) equipped with a field-emission electron source, a cryo-pole piece in the objective lens and an in-column energy filter (omega filter). Zero-loss images were recorded under low-dose conditions at an acceleration voltage of 200 kV on a bottom-mounted TemCam-F416 camera (TVIPS-Tietz Video and Image Processing Systems GmbH, Gauting, Germany) using SerialEM.

Size exclusion chromatography (SEC)

The polymers were analyzed by size exclusion chromatography (SEC). A sample volume of 20 µl (1 mg/ml) was injected on a TSKgel® G4000PW$_{XL}$ column (TOSOH Bioscience GmbH, Griescheim, Germany) connected to a chromatography system (Waters 600E System Controller, Waters, Milford, MA, USA), using RI (Waters 2414 Differential Refractometer) and UV detection (Waters 486 Tunable Absorbance Detector) at 234 nm. De-ionized water was used as eluent at a flow rate of 0.5 ml/min. The column was calibrated with dextran standards of 50, 150, 270 and 410 kDa (Fluka Chemie AG, Buchs, Swizerland).

3. Results and discussion

3.1 Synthesis of thermoresponsive glycopolymers [poly(NIPAm-*co*-M$_n$EMA)s]

The enzymatically synthesized M$_n$EMAs were used in conventional radical polymerizations with NIPAm to yield copolymers with the expected structure shown in Figure 1, as confirmed by ^{1}H and ^{13}C NMR spectra. A representative example is given in Figures S1 and S2 in the supplementary information for sample P3M2. We have previously fully resolved the ^{1}H NMR spectra of homopolymers based on M$_1$EMA and M$_2$EMA[18] and the spectrum of poly(NIPAm) is well known. [31,32]
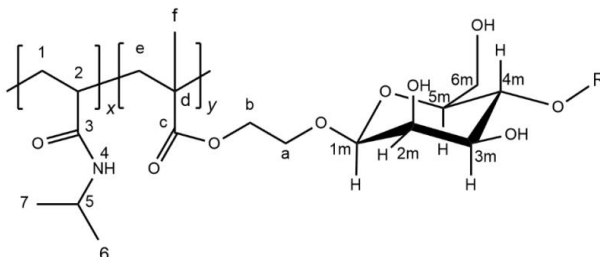

Figure 1. The expected molecular structure of the glycopolymers poly(NIPAm-co-MnEMA)s, indicating the structure of a β-mannosyl unit. M$_1$EMA: R=H and M$_2$EMA: R=β-4,1-mannose.

The polymerizations were monitored by measuring monomer conversions over time using NMR data. For all the poly(NIPAm-*co*-M$_n$EMA)s, the NMR data acquired during the reaction showed that the conversions given in Table 1 were reached after 2 – 3 h of reaction and there was no further increase after this time. Table 1 summarizes the synthesis results and all calculations were based on data extracted from NMR spectroscopy measurements

Table 1. Calculated yields, polymer compositions and thermoresponsive behavior of the glycopolymers [poly(NIPAm-*co*-M$_n$EMA)s].[a]

Polymer type	Sample Designation	Y_{feed} M_nEMA [mol/mol]	$Y_{polymer}$ M_nEMA [mol/mol]	Conversion NIPAm [mol%]	Conversion M_nEMA [mol%]	T_{onset}[b] [°C]	$LCST_{NMR}$[c] [°C]
Poly(NIPAm-co-M₁EMA)	P1M1	0.07	0.08	95	~100	34.1±0.1	40.1 (0.01)
	P2M1	0.18	0.18	92	~100	34.1±0.1	39 (0.02)
Poly(NIPAm-co-M₂EMA)	P1M2	0.02	0.03	83	~100	34.5±2.8	45.1 (0.01)
	P2M2	0.15	0.16	96	~100	35.4±0.3	40.1 (0.004)
	P3M2	0.18	0.18	97	~100	34.9±0.1	42.1 (0.02)
Poly(NIPAm)	PR1	-	-	100	-	34.7±0.01	34.7 (0.01)
Poly(NIPAm-co-EMA)	PR2	0.14	0.22	75	94	30.2±0.3	32.3 (0.03)
	PR2P					31.4±1.4	36.9 (0.02)

[a]All yields and compositions were calculated using NMR data. [b]Temperature at which the thermal transition starts, defined by parameter x_o in Equation S1. [c]As noted by NMR, it was defined as the temperature at which the intensity of the chemical shift studied is 50% of the intensity measured at 25 °C (i.e. $I_{LCST_{NMR}} = 0.5*I_{25}$, I=NMR intensity), and was obtained by resolving Equation S1 for y=0.5. Within parentheses we report the standard error of estimate (SSE) of the fitted model. A detailed explanation of how the parameters were derived can be found in SI part C.

The polymerizations showed conversions of NIPAm above 92 mol%, as determined from the ^{1}H NMR spectra. The conversion of the glycomonomer was estimated to ~100 mol%. Already in our previous work we demonstrated that these glycomonomers were readily polymerizable and able to reach full conversions in radical polymerizations.[18] Furthermore, the ^{13}C spectra showed no signal at 127.01 ppm that would correspond to the acrylate double bond in M_2EMA (Scheme 1, C-e).[18] Only peaks unequivocally assigned to unconverted NIPAm monomer at 130.14 and 126.72 ppm were found in that region. In addition, the signal at 17.4 ppm that originated from the $-CH_3$ of M_nEMA disappeared upon polymerization which we have previously reported (see SI figure S2).[18] Sample P1M2 had a lower molar monomer concentration compared to the rest of the samples. Nevertheless, relatively high conversions were also achieved in this polymerization, even without the addition of the accelerator as described in Table S1. Sample PR2 reached a conversion of 75 mol% for NIPAm. It has previously been shown that HEMA polymerizes faster than NIPAm in similar systems.[33] Size exclusion chromatography (SEC) showed very weak broad signals and all the samples eluted at the exclusion volume (Figure S6). This indicated the presence of aggregates in solution. We have previously described the same outcome for homopolymers synthesized from the same glycomonomers.[18] Furyk and coworkers have demonstrated that the polydispersity and M_w had little effect on LCST of finely mass fractionated samples of poly(NIPAm) as long as the polymer M_w was above 50 KDa and only slight deviations were noted with lower molecular weight samples.[34]

3.2 Thermoresponsive transitions of poly(NIPAm-*co*-M$_n$EMA)s by NMR spectroscopy

It is known that ^{1}H NMR spectroscopy of thermoresponsive polymers in D_2O solutions provides insights into the thermoresponsive behavior on the molecular level[6,35,36] In general, sharper signals are expected below the LCST and broader, or missing, signals after or close to the LCST because liquid state NMR spectroscopy is only expected to show signals related to sufficiently soluble/mobile polymers.[37] It has to be pointed out that we measured the LCST transitions in D_2O. Thus, the values may be different from those measured in H_2O. Previous studies have shown that the LCST of poly(NIPAm) in D_2O is higher than in H_2O by approximately 1 K.[38]

Figure 2A shows the initial screening of the acquired ^{1}H NMR spectra at 25, 35 and 50 °C for PR1 [poly(NIPAm)] as well as for the glycopolymer P2M2.
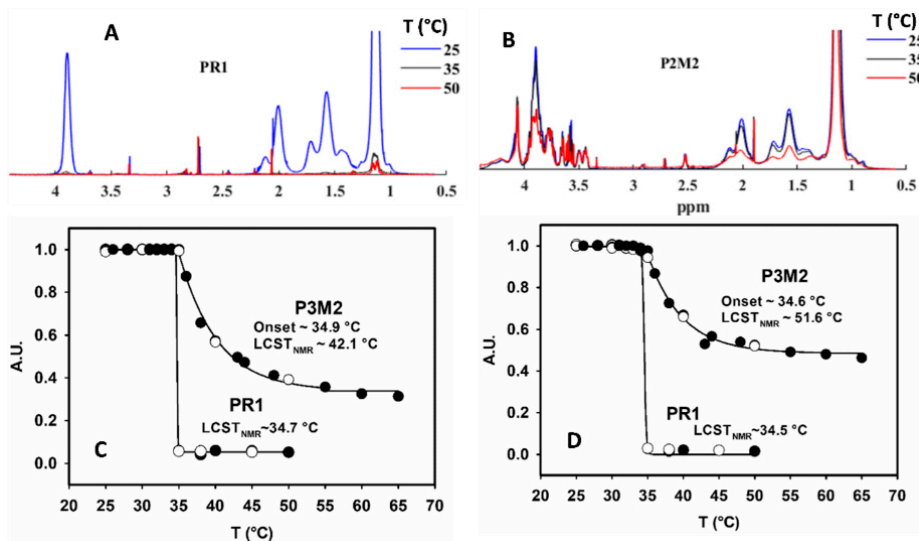
Figure 2. ^{1}H NMR (D$_2$O, 500 MHz) spectra taken at 25, 35 and 50 °C for (A) PR1 and (B) P2M2. The decrease of signal intensity occurred gradually for P2M2 compared to PR1. Determination of T_{onset} and $LCST_{NMR}$ for P3M2 compared to PR1: (C) from the chemical shift at 1.29–1.90 (H1, C **H** $_2$) and (D) from the chemical shift at 3.79–4.12 (H5, N-C **H** (CH$_3$)$_2$). Open circles correspond to a cooling cycle and filled circles to a heating cycle.

As expected, Figure 2A shows that at 35 °C, the intensity of all signals from PR1 [poly(NIPAm)] were practically zero (signal undetectable) due to the "coil-to-globule" transition that poly(NIPAm) underwent at its LCST.[36,39] In comparison, the glycopolymers, here illustrated by sample P2M2 in Figure 2B, showed that at 35 °C the intensity of the signals related to the poly(NIPAm) segments remained largely unchanged compared to the spectrum at 25 °C. Even at 50 °C only partial loss of intensity was shown. This was expected because the poly(NIPAm) segments underwent a thermal random coil to globule transition upon heating, while the sugar segments remained solubilized. We have observed that the homopolymer of M$_2$EMA does not undergo a thermal transition upon heating (data not shown). In other words, the sugar segments may have hampered the aggregation and precipitation of the polymer. This behavior was modeled as previously described (see SI section C) to derive the parameters T_{onset} and a $LCST_{NMR}$ reported in Table 1. Figure 2B and 2C shows the fitted model to the data for PR1 and P2M2 for two different chemical shifts.

Table 1 shows that the onset of the thermal transitions (T_{onset}) was similar for all synthesized polymers and occurred at the LCST for poly(NIPAm) ~ 35 °C. In poly(NIPAm), PR1, $T_{onset}=LCST_{NMR}$ as expected, since the thermal transition from coil-to-globule was sharp. In

comparison, the glycopolymers showed $LCST_{NMR}$ above the T_{onset} due to a gradual thermal transition as previously described. In terms of the effect of the degree of substitution of sugar units and their length in the LCST transitions, we observed that the glycopolymers of M$_2$EMA had statistically significantly higher $LCST_{NMR}$ values compared to the ones based on M$_1$EMA (See Figure S3B in SI). In general, we observed that the higher the molar content of the M$_n$EMAs, the lower the estimated $LCST_{NMR}$. Additionally, the reference copolymer based on HEMA showed a significantly lower onset of thermal transition compared to the rest of the samples (30.8 ± 0.8 ºC). This difference was significant regardless of the purity of the reference sample (PR2 or PR2P). The effect of copolymerization with HEMA was small in the thermal transitions of poly(NIPAm) compared to the effect induced by the glycomonomers. Figure 2C and 2D also show that the spectra taken during the heating cycle (filled circles) and during the cooling cycle (empty circles) were very close (negligible hysteresis). This verified the reliability of the method used to estimate the polymer segment mobility from the spectra, and to demonstrate that the changes were reversible.

We want to point out that there was a difference in the estimation of $LCST_{NMR}$ calculated from the chemical shifts corresponding to protons in in the main chain of the poly(NIPAm) segments (H1 and H2 in Figure 1) compared to the estimation derived from the chemical shift of the protons in the side chain (H5, H6, H7 in Figure 1). In general, the loss of intensity from the main chain protons due to temperature increase, occurs at a faster rate than for the side chain protons. This was indicative of a difference of mobility of the poly(NIPAm) segments of the polymer backbone compared to the side chains. This difference in mobility has been systematically studied by Futscher and coworkers.[40] They studied the molecular changes in poly(NIPAm) and in its monomer (NIPAm) in solution across the LCST transition and determined that the hydrogen bonding with the amide groups in the side chains is different to the hydration of the hydrophobic main chain hydrocarbons.[40] However, in the present study the signals used for the side chain calculations, illustrated in Figure 2D for proton H5, overlapped with signals that correspond to the glycopolymer segments. Consequently, we reported the calculated T_{onset} and $LCST_{NMR}$ for the main chain, illustrated for H1 in Figure 2C.

3.3 Thermoresponsive transitions of poly(NIPAm-*co*-M$_n$EMA)s by DLS, SAXS and cryo-TEM

DLS, cryo-TEM and SAXS techniques were employed to obtain further knowledge on the structural changes associated with the thermal transitions observed with NMR spectroscopy. While NMR data provides information about the immediate vicinity of the atoms, DLS and SAXS reveal information on how this correlates with the polymer structural changes and aggregation and cryo-TEM provides imagery of the structures. Hence, these techniques provide complimentary information.

A comparison of the NMR data and the results from the DLS analysis is shown in Figure 3. Inserts A and C summarize the thermoresponsive behavior of poly(NIPAm-*co*-M$_1$EMA)s and of poly(NIPAm-*co*-M$_2$EMA)s, respectively, in terms of the intensity of the signal at 1.29–1.90 (H1,

C H$_2$) by NMR. Inserts B and D show the corresponding change in hydrodynamic radius (R_h) measured by DLS from 25 to 70 °C.
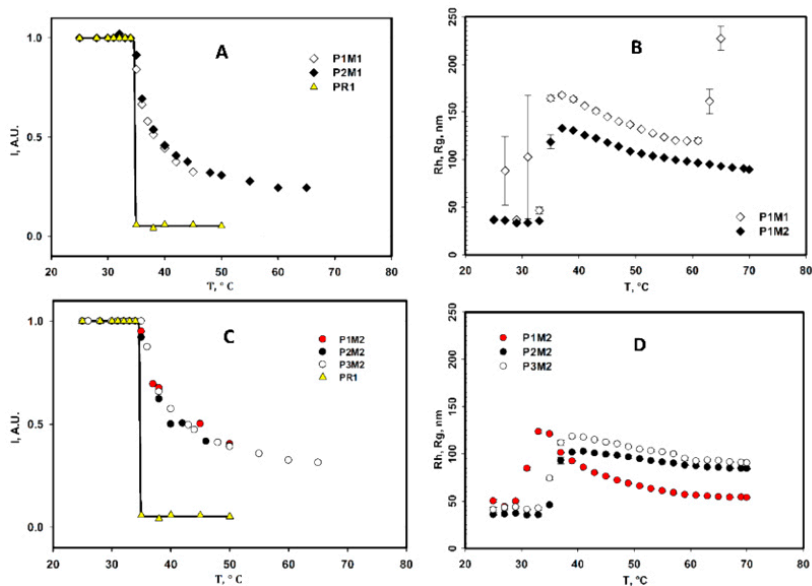

Figure 3. Thermal transitions of the glycopolymers studied by NMR spectroscopy (A and C) and by DLS (C and D).

Figure 3 shows that DLS and NMR spectroscopy data was temperature independent in the range 25 – 35 °C. In DLS the R_h reached a maximum size around ~37-39°C, followed by gradual shrinking up to 70 °C. Therefore, the results will be discussed in terms of these two temperature ranges in the following sections.

We would like to point out that while all samples showed the same trend at similar temperature ranges, sample P1M2 showed a shift towards lower temperatures in DLS (Figure 3D). P1M2 has a particular low sugar content (3 mol %). This sample, when compared to the rest, illustrated that a certain degree of substitution of sugar needs to be exceeded to induce an effect on the thermal transition of poly(NIPAm). That is, at this low degree of sugar substitution, the increase of R_h started earlier than for glycopolymers with at least 8 mol % sugar content (P1M1) and the shrinkage of the R_h after 35 °C was much more pronounced than for the rest of the samples. This was an indication that there were not enough sugar moieties to stabilize all of the poly(NIPAm) segments. Hence, thermal transition was only slightly hampered by the hydrophilic interaction of the few sugar units. These results suggested that, in our particular case, we needed that the sugar content had a value between 3 and 8 mol % to induce an effect on the LCST of poly(NIPAm).

Consequently, we had mostly focused on studying samples with content higher than 8 mol % with SAXS and cryo-TEM.

3.4 Characterization of poly(NIPAm-*co*-M$_n$EMA)s at 25 -35 °C

As previously explained, DLS and NMR spectroscopy data were temperature independent in the range 25 – 35 °C. In this range, the hydrodynamic radius (R_h) was between 35 – 62 nm. Additionally, cryo-TEM images of P1M1 and P2M2 at 25 °C (Figure 4A and 4C, respectively) showed already a large amount of small aggregates 20 – 40 nm in diameter and elongated structures of up to 80 nm. These dimensions suggested that the polymers aggregated already at 25 °C into pearl shaped objects that, in turn, could aggregate into elongated shapes. This aggregation occurred without any external trigger and was likely driven by attractive interaction between the sugar moieties since poly(NIPAm) segments would not undergo any conformational change below ~35 °C, as shown in Table 1. Furthermore, it is known that poly(NIPAm) exists in an expanded conformation in water below the LCST.[41] This type of self-aggregation of synthetic glycopolymers is highly desirable as it does not rely solely on hydrophobic interactions for applications such as drug delivery and nano reactors.[42] We found the same type and size of aggregates in all samples at 25 °C regardless of the type, size or length of the sugar substituents. Self-assembly similar to what we have seen in our glycopolymers has been described in double-hydrophilic block glycopolymers (DHBGs) of poly(2-hydroxyethyl methacrylate)-*b*-poly(2-(β-glucosyloxy) ethyl methacrylate) [PHEMA-*co*-PGEMA] in milli-Q water.[4] These glucose based block copolymers showed R_h of 4.25 and 19.8 nm as a function of the length of the PHEMA block according to DLS at room temperature.[4] The authors proposed that the glycopolymers self-assemble into micellar structures. In the present case we have calculated the shape parameter $\rho=R_g/R_h$ from DLS data at 25 °C for one of our glycopolymers P2M2 (See SI Table S2). In comparison, a solid sphere gives ρ~0.775.[43] For P2M2 at 25 °C, ρ=1.22 that corresponds to an elongated shape which correlated with the aggregates formed at 25 °C into elongated structures.
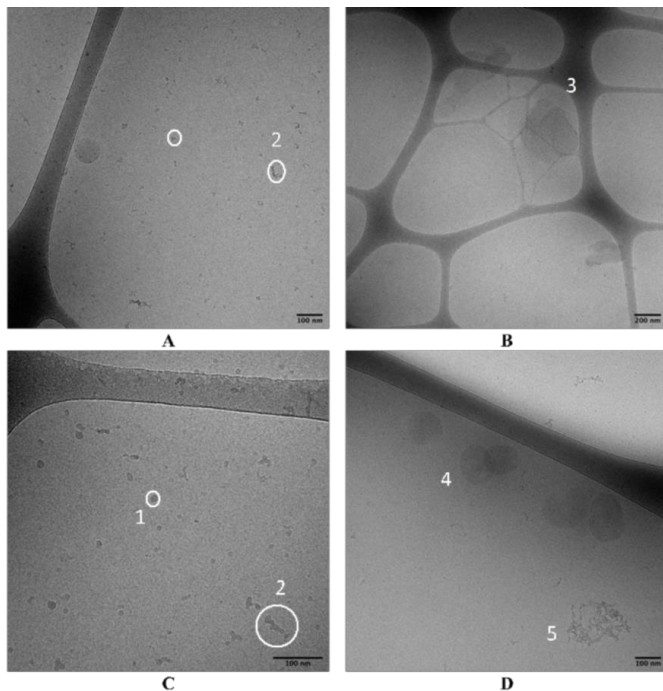
Figure 4. Cryo-TEM images prior to blotting at 10-fold dilution (~ 1 mg/mL) of P1M1 incubated at 25 °C (A) and at 50 °C (B), and of P2M2 incubated at 25 °C (C) and at 50 °C (D). Structures observed: 1) pearl shaped aggregates, 2) elongated structures; 3) disc-shaped structures that overlap; 4) globular structures and; 5) fractal aggregates.

Further characterization was done with SAXS. At 25 °C, the SAXS data showed that all of the samples exhibited similar scattering behavior in solution. Figure 5A and B show a gradual change in the power-law decay through the extended q-range in the scattering curves at 25 °C. Such a scattering behavior is consistent with a self-similarity in the morphology of the different polymers in solution and suggested a fractal-like behavior. All of the curves at 25 °C shown in Figure 5 were fitted to the Beaucage model[27,28] and the obtained results are summarized in Table 3.

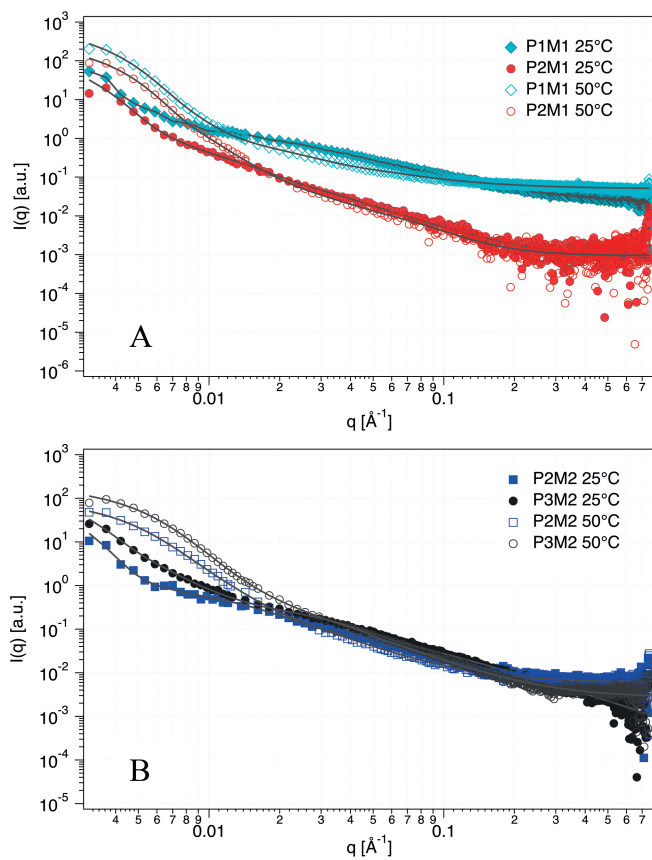**Figure 5.** (A) SAXS curves of P1M1 (light blue rhombus) and P2M1 (red circles) (10 mg/mL) at 25 °C (filled symbols) and 50 °C (empty symbols). Solid lines are fits to the corrected Beaucage model. (B) SAXS curves of the P2M2 (dark blue square) and P3M2 (black circles) (10 mg/mL) at 25 °C (filled symbols) and 50 °C (empty symbols). Solid lines are fits to the corrected Beaucage model and polymer micelle model.

Table 2. Parameters obtained from the fitting poly-(NIPAm-co-MnEMA) SAXS data at 25°C to the corrected Beaucage model for a fractal object.[a]

Sample designation[b]	Parameters (fractal object)				
	R_g [nm]	d	R_{sub} [nm]	L_p [nm]	d_{sub}
P1M1 (8 mol%)	89	3.70	14	24	1.52
P2M1 (16 mol%)	75	4.40	14	24	2.00
P2M2 (16 mol%)	85	3.3	12	21	1.54
P3M2 (18 mol%)	80	3.2	5	8	1.50

[a]Detailed description of the reported parameters can be found in materials and methods. [b]Within parentheses is the molar content of the sugar substituent for each copolymer (M1 or M2).

Table 3 shows that the radius of gyration (R_g) of the glycopolymers at 25 °C was within a range of 75 – 89 nm. This correlates to the cryo-TEM images with the elongated shapes seen formed from the smaller pearl-shaped structures. The R_g at 25 °C decreased with increasing content of sugar monomers included in the structure regardless of the number of mannose units. This effect was more clearly seen from the SAXS data of the di-substituted glycopolymers, in which the magnitude of R_g decreased with the level of substitution and so did the size of the subunit (Table 2, R_{sub}), even if the difference in sugar content between the two di-substituted glycopolymers was narrower (16 vs 18 mol%) compared to the mono-substituted (8 vs 16 mol%). The persistence length (L_p) that characterizes the chain stiffness remained constant for the mono-substituted glycopolymers (~24 nm) and decreased significantly for the di-substituted ones (21 vs 8 nm).

It can be argued that for a larger density of bulky side groups the chain flexibility would decrease, as it has been previously observed with softwood hemicellulose and galactose side groups.[24] However, in the case of hemicellulose the backbone is significantly more water soluble, while for the poly(NIPAm) the backbone is significantly less soluble. When temperature increases and there is a small change in solvent quality, hemicellulose would remain in solution, while poly(NIPAm) would precipitate. In our glycopolymers, the introduction of the sugar groups conferred even more solubility to the polymer back bone, but at the same time the sugar moieties tended to show an attractive interaction, which was likely to be a combination of e.g. hydrophobic interaction, specific orientation and hydrogen bonding. The sugars interacted attractively with each other and led to a closer contact between the chain backbones as a "zip lock", thus forming aggregates even at 25 °C without precipitation.

Therefore, we concluded that the synthesized glycopolymers can aggregate below the LCST of poly(NIPAm) thanks to the effect induced by the attraction of the sugar moieties. This behavior could be advantageous in applications where self-assembly is required.

3.4 Temperature dependent conformational changes of poly(NIPAm-*co*-M$_n$EMA)s (T>35 °C)

We studied the glycopolymers before the LCST of the poly(NIPAm) (estimated at ~35 °C), concluding that there was some form of aggregation that was driven by attractive interaction, likely due to a combination of e.g. hydrophobic interaction and specific orientation, between the sugar moieties and therefore temperature independent. After 35 °C, however, we expected to see structural changes driven by the segments of poly(NIPAm).

After the temperature rose beyond 35 °C, DLS showed a rapid increase of R_h, followed up by a steady decrease of R_h up to 70 °C for all samples except P1M1 for which this decrease was up to 63 °C (this will be discussed in detail later). The initial increase in R_h was in the order of 2-4 times the average R_h at 25 °C reaching a semi-plateau in 102 – 168 nm at about ~37-39 °C, reported as R_{hmax} in Table 2. This behavior was modeled with a linear regression for which we saw that this increase in R_h was faster in poly(NIPAm-*co*-M$_1$EMA)s compared to poly(NIPAm-*co*-M$_2$EMA)s. The initial increase of R_h was due to unfavorable poly(NIPAm)-water interactions that led to the collapse of the polymer chains, and eventually to aggregation due to hydrophobic interaction among the collapsed chains.[44] At the same time the sugar-sugar interactions were still present and would interfere with the hydrophobic interactions, thus causing a gradual thermal transition as oppose to a sharp transition as previously described.

As the temperature increased beyond ~39 °C, we observed a gradual decrease of R_h in DLS (Figure 2) over a wide range of temperatures, the minimum size reached is reported as R_{hmin} in Table 2. This decrease of R_h was first linear and then proceeded at a slower rate (second degree polynomial fit). This gradual decrease in R_h suggested that the polymer coils would shrink in size with increasing temperature. A similar decrease of R_g after an increase has also been seen in double-hydrophilic thermoresponsive block glycopolymers (DHTBG) of poly(di(ethylene glycol)methyl ether methacrylate) and a galactose functionalized poly(6-O-vinyladipoyl-D-galactose).[16] It was suggested that this shrinking behavior was most likely related to the increase in hydrophobicity of the hydrophobic segments leading to a shrinkage of the structures present.[16] Accordingly, at 50 °C cryo-TEM images showed that the small aggregates seen at 25 °C appear to have rearranged into large irregular structures. These structures resembled disk-like aggregates for samples with M$_1$EMA and globular aggregates for samples with M$_2$EMA (Figure 4). These aggregates were sometimes attached together to form fractal aggregates. In particular, we calculated the shape parameter $\rho=R_g/R_h$ of 0.85 with DLS at 45 °C for P2M2 (See SI Table S2) which suggested a spherical shape somewhat hollow (R_g/R_h~1 is indication of a hollow sphere)[16] which correlates with the globular aggregates seen in cryo-TEM. Additionally, along the globular/disc shapes we saw other type of fractal aggregates apparently made up of the elongated aggregates seen at 25 °C (Figure 4). The formation of aggregates was due to unfavorable poly(NIPAm)-water interactions that led to the collapse of the polymer chains. However, further aggregation and eventual precipitation was hampered due to the presence of the sugar moieties that rendered the polymer slightly more hydrophilic. This behavior can be likened to coacervate forming polymers.[44] These polymers cannot cause enough dehydration of their chains above the

LCST, but instead they form micrometer-scale dispersions and cannot undergo a drastic conformational change. It has been reported that this type of polymers is better suited for biological applications because their gentle thermoresponsive behavior is less disruptive in biological or biomimetic systems.[44] When poly(NIPAm) aggregates and precipitates, it is due to a gain in entropy because of the dehydration of the hydrophobic moieties of the polymer, which, in turn, compensates for the loss of entropy arising from the collapse of the polymer chains into globules.[44] By introducing sugar moieties as pendant groups, it is likely that the gain of entropy decreased and the chains could not undergo full dehydration.

Table 3. Summary of characteristic R_hs measured by DLS of poly(NIPAm-*co*-M$_n$EMA)s solutions.[a]

Sample designation[b]	Parameter			
	R_h @ 25 °C, nm	$R_h$max[c], nm	R_h @ 50 °C, nm	R_h min[d], nm
P1M1 (8 mol%)	36 ± 0.9	168 ± 1.8	137 ± 0.8	119 ± 0.9
P2M1 (18 mol%)	37 ± 0.9	133 ± 0.9	107 ± 0.8	90 ± 0.4
P1M2 (3 mol%)	50 ± 1.4	123 ± 1.9	69 ± 0.4	54 ± 0.1
P2M2 (16 mol%)	36 ± 0.2	102 ± 0.5	95 ± 1.1	84 ± 0.7
P3M2 (18 mol%)	41 ± 2.7	118 ± 0.8	106 ± 0.6	90 ± 0.1

[a]All R_hs at each temperature correspond to the average of 3 measurements. [b]Values within parentheses correspond to the molar content of the sugar substituent (M1 or M2). [c]Measured as the maximum R_h in the DLS curve. [d]Measured as the minimum R_h reached in the DLS curve after 35 °C.

We also studied the glycopolymers by SAXS at 50 °C, as a representative temperature in the temperature range in which the R_h was gradually decreasing and the results were summarized in Table 4. In general, we saw that at 50 °C, the size of the polymer particles (R_g) decreases by about 26 - 36% (one sugar) and by 45 – 54 % (two sugars) depending on the degree of sugar substitution compared to their size at 25 °C. This decrease was also seen in the size of the subunit (R_{sub}) indicating that the whole structure was collapsing, which correlated with the shrinking behavior seen in DLS.

Table 4. Parameters obtained from the fitting poly-(NIPAm-*co*-M$_n$EMA) SAXS data at 50 °C to the corrected Beaucage model.[a]

Sample designation[b]	Parameters									
	Fractal model					Micelle model				
	R$_g$ [nm]	d	R$_{sub}$ [nm]	L$_p$ [nm]	d$_{sub}$	R$_g$ core [nm]	R$_g$ corona [nm]	N$_{head}$	V$_{head}$ [nm^3]	V$_{tail}$ [nm^3]
P1M1 (8 mol%)	57	4.7	8	14	1.6	-	-	-	-	-
P2M1 (16 mol%)	55	3.90	5	9	2.90	-	-	-	-	-
P2M2 (16 mol%)	47	4.65	8	15	2.27	16	28	30	22	322
P3M2 (18 mol%)	37	3.42	3	5	2.15	14	22	41	7	100

[a]Detailed description of the reported parameters can be found in materials and methods. All values are averages from three measurements. [b]Values within parentheses correspond to the molar content of the sugar substituent (M1 or M2).

Figure 5 shows that the SAXS data of the glycopolymers recorded at 50 °C, exhibited a similar trend to the data recorded at 25 °C but with a more pronounced increase in the intensity with q at the transition from an intermediate- to a low-q region. The large exponent at low-q can be described as Porod behavior ($\sim q^{-4}$) indicating that polymers collapsed into compact objects with sharp interfaces.[45] This type of increase in the power-law behavior with temperature has been previously reported in literature for temperature-responsive triblock copolymers that contain poly(NIPAm) blocks.[26,27] These compact objects corresponded to those described on the basis of the cryo-TEM results as disc-shaped structures (see Figure 4B) for mono-mannose substituted glycopolymers and globular shape structures with sharp edges for the di-substituted ones (Figure 4D). As previously described, we also saw in cryo-TEM irregular fractal aggregates that coexist along the globular/discs aggregates. SAXS data showed that the scattering was dominated by the former as indicated by the $d_{sub} \sim 2$ at the intermediate q-range characteristic to dense mass fractals.[28] Hence, the data was fitted using the same model (fractal) used for the data at 25 °C (Table 4). However, it was also possible to fit the SAXS data at 50 °C for the di-mannose substituted glycopolymers (P2M2 and P3M2) to a polymer micelle core shell model, i.e., a spherical particle with a dense core consisting of polymer heads and a corona consisting of Gaussian polymer tails.[46] This model is often employed to describe block copolymer micelles.[47] Here we made an assumption that the globular structures seen in cryo-TEM were micelles with a core made of poly(NIPAm) with scattering length density (SLD) of 0.1×10^{-6} Å^{-2} and the corona consisted of mannan with the SLD of 0.145×10^{-6} Å^{-2}. According to the fit shown in Table 4, the glycopolymers with two mannose units formed micelle-type particles with an overall radius of 44 and 36 nm for P2M2 and P3M2, respectively (Table 4). Particles with a higher substitution degree of di-mannose (18 mol%) had a slightly smaller core but a corona with a larger radius than the less substituted ones (16 mol%). This suggested that a smaller amount of collapsed chains was surrounded by a

larger amount of sugar units "protecting" the core. Here the water could interact with the sugar units preventing further aggregation and consequent precipitation.

3.5 Aggregation and precipitation of P1M1

As we previously described, DLS, NMR and SAXS data showed that the structures formed upon heating beyond the LCST of poly(NIPAm) did not reach equilibrium but continued to shrink up to 70 °C. However, it is expected that the structures would eventually aggregate and collapse, given that the LCST behavior is entropy driven. This assumption was validated using sample P1M1, for which DLS showed that at 63 °C there was a sharp increase of R_h which indicated further aggregation and eventually the copolymer precipitated. This was also observed by NMR spectroscopy. At temperatures beyond 60 °C it was not possible to record any spectra because there were no phases with sufficient mobility. Thus, the shimming of the sample failed. It is expected that all the other samples would eventually also aggregate and precipitate at temperatures above 70 °C. Sample P1M1 was based on M_1EMA and had a lower average of mannose units per chain compared to the other glycopolymers. A higher sugar content and long sugar units prevented the aggregation of collapsed chains up to 70 °C. These observations were in agreement with that seen in other poly(NIPAm) based glycopolymers with α-linked mannose units, synthesized by Paul and coworkers.[17] They observed that glycopolymers functionalized with high mannose content (34 and 97 mol%) did not show temperature responsive behavior up to 40 °C compared to sugar contents under 7 mol%.[17] The thermal responsiveness would be affected by the sequence of the sugar units within the polymer backbone. The degree of dehydration will depend on the sugar unit distribution and their hydrophilicity would govern the solubility of the polymer even above LCST of poly(NIPAm).

Scheme 2 shows a graphical representation of the proposed structures formed as the temperature increases in the solutions of poly(NIPAm-co-M_nEMA)s.
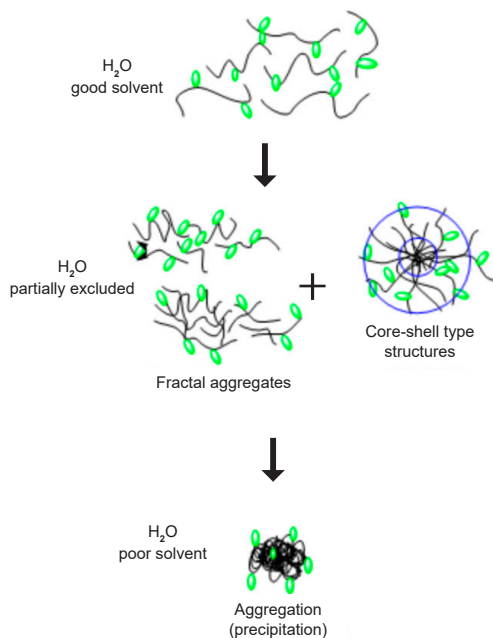
Scheme 2. Graphical representation of aggregation sequences of thermoresponsive poly(NIPAm-*co*-M$_n$EMA) in water. Top to bottom: 25 to 35 °C; 35 – 63 °C for P1M1 and 35 -70 °C for all the other samples; 63 °C for P1M1 and above 70 °C for all the other samples.

3.6 Conformational changes as a function of the concentration

We believe that the type of structures formed as temperature increases were concentration dependent. For example, we had imaged by cryo-TEM one sample of di-mannose substituted copolymer (P2M2) at the initial concentration and at 10-fold dilution (~10 mg/L vs ~1 mg/L) at 25 and 50 °C, respectively. At both temperatures, we observed the same type of structures as previously described. However, a larger amount of elongated particles and even fractal aggregates were seen at the higher concentration at 25 °C compared to the diluted sample (Figure S4). Similarly, at 50 °C, the effect of concentration was much more pronounced than at 25 °C. While both the diluted and the concentrated samples contain globular aggregates and fractal aggregates of similar dimensions, the former were found in higher numbers under dilute conditions, whereas the latter dominated under concentrated conditions (Figure S5). The polymers assembled randomly into mostly fractal-like structures at a high concentration, as expected for a strongly attractive interaction. Consistently, in a more dilute sample more time was given for the polymer to aggregate in a more controlled and organized manner giving less extended aggregates.

4. Conclusions

We have synthesized biobased thermoresponsive glycopolymers from glycomonomers prepared by enzymatic catalyzed synthesis, and the well-known thermoresponsive polymer poly(NIPAm). The polymerizations had high conversions reached after 2-3 h. We then systematically characterized their solution properties and their conformational changes upon heating employing ^{1}H NMR, DLS, SAXS and cryo-TEM. We saw that the glycopolymers aggregated at room temperature due to the attractive interaction of the sugar moieties, which results from hydrophobic interactions, specific orientation and hydrogen bonding. This behavior could be advantageous in applications where self-assembly is required. We then showed that the glycopolymers had a LCST-type phase transition as well as aggregation properties beyond the LCST of poly(NIPAm).

We saw that upon increasing temperature beyond the LCST of ply(NIPAm), the glycopolymers were able to rearrange into sharp edged structures with varying shapes (fractal, discs and globular). The size and shape of these structures varied in function of the size and degree of substitution of the mannose pendant moieties offering handles for the variation of the structures to target specific applications. To the best of our knowledge there is little research into the thermal transitions of thermoresponsive glycopolymers with a random distribution of sugar moieties along the polymer backbone, in particular glycopolymers featuring β-linked mannose units. We expect that the findings of this work will form the basis for the synthesis of a library of glycopolymers with diverse structures/function using alternative comonomers and/or other polymerization techniques.

5. Supporting Information.

Expanded description of polymerization method, acquisition and processing of NMR data spectroscopy, procedure to calculate parameters T_{onset} and $LCST_{NMR}$ reported in Table 1, additional DLS data, ^{1}H and ^{13}C NMR spectra, additional graphs for Table 1, and as well as additional cryo-TEM images and inserts of the SEC chromatograms.

6. Author Contributions

The manuscript was written through contributions of all authors. All authors have given approval to the final version of the manuscript.

7. Funding Sources

8. Acknowledgments

University, for providing experimental resources. In particular, we thank Anna Carnerup for performing the measurements in challenging conditions.

9. Abbreviations

Cryo-TEM, cryogenic transmission electron microscopy; DLS, dynamic light scattering; HEMA, 2-hydroxy ethyl methacrylate; LCST, lower critical solution temperature; M_nEMAs, 2-(β-manno[oligos]yloxy) ethyl methacrylates); M_1EMA, 2-(β-mannosyloxy) ethyl methacrylate); M_2EMA, 2-(β-manno[bio]syloxy) ethyl methacrylate); NMR, nuclear magnetic spectroscopy; poly(NIPAm-*co*-M_nEMA)s, poly(N-isopropyl acrylamide)-*co*-(2-[β-manno[oligo]syloxy] ethyl methacrylate)s; poly(NIPAm), poly(N-isopropylacrylamide); SEC, size exclusion chromatography; SAXS, small angle X-ray scattering

10. References

(1)   Pramudya, I.; Chung, H. Recent Progress of Glycopolymer Synthesis for Biomedical Applications. *Biomater. Sci.* **2019**, *7* (12), 4848–4872.

(2)   Adharis, A.; Vesper, D.; Koning, N.; Loos, K. Synthesis of (Meth)Acrylamide-Based Glycomonomers Using Renewable Resources and Their Polymerization in Aqueous Systems. *Green Chem.* **2018**, *20* (2), 476–484.

(3)   Lee, Y. C.; Lee, R. T. Carbohydrate-Protein Interactions: Basis of Glycobiology. *Acc. Chem. Res.* **1995**, *28* (8), 321–327.

(4)   Adharis, A.; Ketelaar, T.; Komarudin, A. G.; Loos, K. Synthesis and Self-Assembly of Double-Hydrophilic and Amphiphilic Block Glycopolymers. *Biomacromolecules* **2019**, *20* (3), 1325–1333.

(5)   Miura, Y. Design and Synthesis of Well-Defined Glycopolymers for the Control of Biological Functionalities. *Polym. J.* **2012**, *44* (7), 679–689.

(6)   Zhang, Q.; Weber, C.; Schubert, U. S.; Hoogenboom, R. Thermoresponsive Polymers with Lower Critical Solution Temperature: From Fundamental Aspects and Measuring Techniques to Recommended Turbidimetry Conditions. *Mater. Horizons* **2017**, *4* (2), 109–116.

(7)   Cortez-Lemus, N. A.; Licea-Claverie, A. Poly(N-Vinylcaprolactam), a Comprehensive Review on a Thermoresponsive Polymer Becoming Popular. *Prog. Polym. Sci.* **2016**, *53*, 1–51.

(8)   Yang, B.; Duhamel, J. Extraction of Oil from Oil Sands Using Thermoresponsive Polymeric Surfactants. *ACS Appl. Mater. Interfaces* **2015**, *7* (10), 5879–5889.

(9)   Andrei, M.; Turturica, G.; Stanescu, P. O.; Teodorescu, M. Thermosensitive Injectable Hydrogels from Poly(N-Isopropylacrylamide)–Dextran Aqueous Solutions: Thermogelation and Drug Release Properties. *Soft Mater.* **2016**, *14* (3), 162–169.

(10)   Bhattarai, N.; Ramay, H. R.; Gunn, J.; Matsen, F. A.; Zhang, M. PEG-Grafted Chitosan as an Injectable Thermosensitive Hydrogel for Sustained Protein Release. *J. Control. Release* **2005**, *103* (3), 609–624.

(11)   von der Ehe, C.; Kretschmer, F.; Weber, C.; Crotty, S.; Stumpf, S.; Hoeppener, S.;
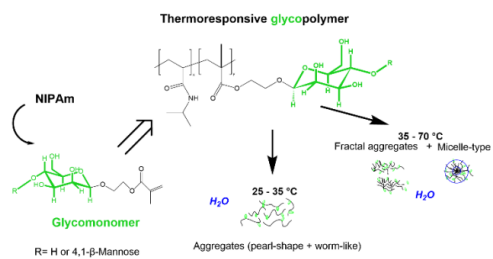
Gottschaldt, M.; Schubert, U. S. RAFT Copolymerization of Thioglycosidic Glycomonomers with N IPAm and Subsequent Immobilization onto Gold Nanoparticles. In *Controlled Radical Polymerization: Materials*; ACS Symposium Series; American Chemical Society, 2015; Vol. 1188, pp 221–256.

(12) Nagase, K.; Yamato, M.; Kanazawa, H.; Okano, T. Poly(N-Isopropylacrylamide)-Based Thermoresponsive Surfaces Provide New Types of Biomedical Applications. *Biomaterials* **2018**, *153*, 27–48.

(13) Quynh, T. M.; Yoneyama, M.; Maki, Y.; Nagasawa, N.; Dobashi, T. Thermosensitive Micelles Composed of Poly(Lactide)-*g*-Poly(NIPAM-*Co*-HEMA) Graft Copolymers. *Key Eng. Mater.* **2010**, *459*, 51–56.

(14) Luo, Y.; Liu, L.; Wang, X.; Shi, H.; Lv, W.; Li, J. Sugar-Installed Thermoresponsive Micellar Aggregates Self-Assembled from "Coil-Comb-Coil" Triblock Glycopolymers: Preparation and Recognition with Concanavalin A. *Soft Matter* **2012**, *8* (5), 1634–1642.

(15) Zhang, Q.; Wilson, P.; Anastasaki, A.; McHale, R.; Haddleton, D. M. Synthesis and Aggregation of Double Hydrophilic Diblock Glycopolymers via Aqueous SET-LRP. *ACS Macro Lett.* **2014**, *3* (5), 491–495.

(16) Quan, J.; Shen, F.-W.; Cai, H.; Zhang, Y.-N.; Wu, H. Galactose-Functionalized Double-Hydrophilic Block Glycopolymers and Their Thermoresponsive Self-Assembly Dynamics. *Langmuir* **2018**, *34* (36), 10721–10731.

(17) Paul, T. J.; Strzelczyk, A. K.; Feldhof, M. I.; Schmidt, S. Temperature-Switchable Glycopolymers and Their Conformation-Dependent Binding to Receptor Targets. *Biomacromolecules* **2020**, *21* (7), 2913–2921.

(18) Rosengren, A.; Butler, S. J.; Arcos-Hernandez, M.; Bergquist, K.-E. E.; Jannasch, P.; Stålbrand, H. Enzymatic Synthesis and Polymerisation of β-Mannosyl Acrylates Produced from Renewable Hemicellulosic Glycans. *Green Chem.* **2019**, *21* (8), 2104–2118.

(19) Kloosterman, W. M. J.; Jovanovic, D.; Brouwer, S. G. M.; Loos, K. Amylase Catalyzed Synthesis of Glycosyl Acrylates and Their Polymerization. *Green Chem.* **2014**, *16* (1), 203–210.

(20) Gridley, J. J.; Osborn, H. M. I. Recent Advances in the Construction of β-D-Mannose and β-D-Mannosamine Linkages. *J. Chem. Soc. Perkin Trans. 1* **2000**, *1* (10), 1471–1491.

(21) Hägglund, P.; Eriksson, T.; Collén, A.; Nerinckx, W.; Claeyssens, M.; Stålbrand, H. A Cellulose-Binding Module of the Trichoderma Reesei β-Mannanase Man5A Increases the Mannan-Hydrolysis of Complex Substrates. *J. Biotechnol.* **2003**, *101* (1), 37–48.

(22) Shen, Z.; Terao, K.; Maki, Y.; Dobashi, T.; Ma, G.; Yamamoto, T. Synthesis and Phase Behavior of Aqueous Poly(N-Isopropylacrylamide-Co-Acrylamide), Poly(N-Isopropylacrylamide-Co-N,N-Dimethylacrylamide) and Poly(N-Isopropylacrylamide-Co-2-Hydroxyethyl Methacrylate). *Colloid Polym. Sci.* **2006**, *284* (9), 1001–1007.

(23) Harris, R. K.; Becker, E. D.; De Menezes, S. M. C.; Granger, P.; Hoffman, R. E.; Zilm, K. W. Further Conventions for NMR Shielding and Chemical Shifts (IUPAC Recommendations 2008). *Magn. Reson. Chem.* **2008**, *46* (6), 582–598.

(24) Naidjonoka, P.; Hernandez, M. A.; Pálsson, G. K.; Heinrich, F.; Stålbrand, H.; Nylander, T. On the Interaction of Softwood Hemicellulose with Cellulose Surfaces in Relation to Molecular Structure and Physicochemical Properties of Hemicellulose. *Soft Matter* **2020**, *16* (30), 7063–7076.

(25) Hammouda, B. Analysis of the Beaucage Model. *J. Appl. Crystallogr.* **2010**, *43* (6), 1474–1478.

(26) Cook, M. T.; Filippov, S. K.; Khutoryanskiy, V. V. Synthesis and Solution Properties of a Temperature-Responsive PNIPAM–b-PDMS–b-PNIPAM Triblock Copolymer. *Colloid Polym. Sci.* **2017**, *295* (8), 1351–1358.

(27) Papagiannopoulos, A.; Zhao, J.; Zhang, G.; Pispas, S.; Radulescu, A. Thermoresponsive Aggregation of PS–PNIPAM–PS Triblock Copolymer: A Combined Study of Light Scattering and Small Angle Neutron Scattering. *Eur. Polym. J.* **2014**, *56* (1), 59–68.

(28) Beaucage, G. Small-Angle Scattering from Polymeric Mass Fractals of Arbitrary Mass-Fractal Dimension. *J. Appl. Crystallogr.* **1996**, *29* (2), 134–146.

(29) Hernandez-Cerdan, P.; Mansel, B. W.; Leis, A.; Lundin, L.; Williams, M. A. K. Structural Analysis of Polysaccharide Networks by Transmission Electron Microscopy: Comparison with Small-Angle X-Ray Scattering. *Biomacromolecules* **2018**, *19* (3), 989–995.

(30) Mansel, B. W.; Chu, C.-Y.; Leis, A.; Hemar, Y.; Chen, H.-L.; Lundin, L.; Williams, M. A. K. Zooming in: Structural Investigations of Rheologically Characterized Hydrogen-Bonded Low-Methoxyl Pectin Networks. *Biomacromolecules* **2015**, *16* (10), 3209–3216.

(31) Andersson, M.; Maunu, S. L. Structural Studies of Poly(N-Isopropylacrylamide) Microgels: Effect of SDS Surfactant Concentration in the Microgel Synthesis. *J. Polym. Sci. Part B Polym. Phys.* **2006**, *44* (23), 3305–3314.

(32) Tanaka, T.; Okamoto, M. Reversible Temperature-Responsive and Lectin-Recognizing Glycosylated Block Copolymers Synthesized by RAFT Polymerization. *Polym. J.* **2018**, *50* (7), 523–531.

(33) Gan, T.; Zhang, Y.; Guan, Y. In Situ Gelation of P(NIPAM-HEMA) Microgel Dispersion and Its Applications as Injectable 3D Cell Scaffold. *Biomacromolecules* **2009**, *10* (6), 1410–1415.

(34) Furyk, S.; Zhang, Y.; Ortiz-Acosta, D.; Cremer, P. S.; Bergbreiter, D. E. Effects of End Group Polarity and Molecular Weight on the Lower Critical Solution Temperature of Poly(N-Isopropylacrylamide). *J. Polym. Sci. Part A Polym. Chem.* **2006**, *44* (4), 1492–1501.

(35) Larsson, A.; Kuckling, D.; Schönhoff, M. 1H NMR of Thermoreversible Polymers in Solution and at Interfaces: The Influence of Charged Groups on the Phase Transition. *Colloids Surfaces A* **2001**, *190*, 185–192.

(36) Guo, H.; Brûlet, A.; Rajamohanan, P. R.; Marcellan, A.; Sanson, N.; Hourdet, D. Influence of Topology of LCST-Based Graft Copolymers on Responsive Assembling in Aqueous Media. *Polymer (Guildf).* **2015**, *60*, 164–175.

(37) Wang, N.; Ru, G.; Wang, L.; Feng, J. [1] H MAS NMR Studies of the Phase Separation of Poly(*N* -Isopropylacrylamide) Gel in Binary Solvents. *Langmuir* **2009**, *25* (10), 5898–

5902.

(38)   Halperin, A.; Kröger, M.; Winnik, F. M. Poly(*N* -Isopropylacrylamide) Phase Diagrams: Fifty Years of Research. *Angew. Chemie Int. Ed.* **2015**, *54* (51), 15342–15367.

(39)   Otake, K.; Inomata, H.; Konno, M.; Saito, S. Thermal Analysis of the Volume Phase Transition with N-Isopropylacrylamide Gels. *Macromolecules* **1990**, *23* (1), 283–289.

(40)   Futscher, M. H.; Philipp, M.; Müller-Buschbaum, P.; Schulte, A. The Role of Backbone Hydration of Poly(N-Isopropyl Acrylamide) Across the Volume Phase Transition Compared to Its Monomer. *Sci. Rep.* **2017**, *7* (1), 17012.

(41)   Ono, Y.; Shikata, T. Contrary Hydration Behavior of N -Isopropylacrylamide to Its Polymer, P(NIPAm), with a Lower Critical Solution Temperature. *J. Phys. Chem. B* **2007**, *111* (7), 1511–1513.

(42)   Oh, T.; Hoshino, Y.; Miura, Y. Aggregation of a Double Hydrophilic Block Glycopolymer: The Effect of Block Polymer Ratio. *J. Mater. Chem. B* **2020**. https://doi.org/10.1039/D0TB02093A

(43)   Zhang, G.; Wu, C. Reentrant Coil-to-Globule-to-Coil Transition of a Single Linear Homopolymer Chain in a Water Methanol Mixture. *Phys. Rev. Lett.* **2001**, *86* (5), 822–825.

(44)   Maeda, T.; Miki, T.; Yamamoto, K.; Aoyagi, T. Coil-Globule Transition and/or Coacervation of Temperature and PH Dual-Responsive Carboxylated Poly(N-Isopropylacrylamide). *Polym. J.* **2009**, *41* (3), 181–188.

(45)   Porod, G. X-Ray Low Angle Scattering of Dense Colloid Systems. *Kolloid-Zeitschrift* **1952**, *125* (51), 108–122.

(46)   Pedersen, J. S. Form Factors of Block Copolymer Micelles with Spherical, Ellipsoidal and Cylindrical Cores. *J. Appl. Crystallogr.* **2000**, *33* (3), 637–640.

(47)   Schillén, K.; Galantini, L.; Du, G.; Del Giudice, A.; Alfredsson, V.; Carnerup, A. M.; Pavel, N. V.; Masci, G.; Nyström, B. Block Copolymers as Bile Salt Sequestrants: Intriguing Structures Formed in a Mixture of an Oppositely Charged Amphiphilic Block Copolymer and Bile Salt. *Phys. Chem. Chem. Phys.* **2019**, *21* (23), 12518–12529.

For Table of Contents Only

Thermoresponsive glycopolymer

NIPAm

Glycomonomer

R= H or 4,1-β-Mannose

25 - 35 °C

H₂O

Aggregates (pearl-shape + worm-like)

35 - 70 °C
Fractal aggregates + Micelle-type

H₂O

Thermoresponsive Glycopolymers Based on Enzymatically Synthesized β-Mannosyl Acrylates and N-Isopropylacrylamide

Monica Arcos-Hernandez[a]*, Polina Naidjonoka[b‡], Samuel J. Butler[c‡], Tommy Nylander[b], Henrik Stålbrand[c]*, Patric Jannasch[a]*

[a]Centre for Analysis and Synthesis, Department of Chemistry, Lund University, PO Box 124, S-221 00 Lund, Sweden

[b]Physical Chemistry, Department of Chemistry, Lund University, PO Box 124, S-221 00 Lund, Lund, Sweden.

[c]Department of Biochemistry and Structural Biology, Department of Chemistry, Lund University, PO Box 124, S-221 00 Lund, Sweden.

A. Detailed synthesis of poly(N-isopropyl acrylamide)-*co*-(2-[β-manno[oligo]syloxy] ethyl methacrylate)s [Poly(NIPAm-*co*-M_nEMA)s]

A total of eight different polymers were prepared in solution. Two glycopolymers (P1M1-P2M1) based on M_1EMA and three (P1M2-P3M2) with M_2EMA were prepared. Additionally, three reference samples were prepared, a homopolymer of NIPAm (PR1) and a copolymer of NIPAm and HEMA (PR2). Details of the experimental design of the polymerizations can be found in Table S1.

Copolymers of M_nEMAs and NIPAm and the homopolymer of NIPAm were synthesized via conventional radical polymerization in D_2O at room temperature in an NMR tube as previously reported.[1] A system of initiator potassium persulfate (KPS) and accelerator N,N,N',N'-tetramethylethylenediamine (TEMED) were used. The polymerizations solutions were designed with a monomer concentration of 250 mmol/L and monomer:initiator:accelerator ([M]:[I]:[A]) ratios of 100:0.4:0.6 unless otherwise stated (Table S1).

The reference sample based on HEMA (PR2) was prepared in ethanol with 2,2'-azobis(isobutyronitrile) (AIBN) as initiator at 60 °C in a similar way previously described.[2]

Table S1. Synthesis data of the thermoresponsive glycopolymers and reference polymers based on NIPAm.

Sample type	Designation	y_{feed} M_nEMA [mol/mol]	[M] [mmol/L]	[M]:[I]:[A]	M_nEMA /NIPAm[a] [mg/mg]
Poly(NIPAm-*co*-M_1EMA)	P1M1	0.10	250	100:0.4:0.6	0.28 (0.21)
	P2M1	0.15	250	100:0.4:0.6	0.45 (0.55)
Poly(NIPAm-*co*-M_2EMA[b]	P1M2	0.02	120[3]	100:0.3:-	0.10 (0.10)
	P2M2	0.10	250	100:0.4:0.6	0.45
	P3M2	0.15	250	100:0.4:0.6	0.71 (0.86)
Poly(NIPAm)	PR1	-	250	100:0.4:0.6	-
Poly(NIPAm-*co*-HEMA)	PR2/PR2P[4]	0.15	250	100:0.4:0.6	0.20

I= initiator, KPS. A=accelerator, TEMED, M=monomer. PR1-PR2 are reference materials;[1]In parentheses the actual measured mass ratios using NMR,[2]No accelerator was added in this synthesis. [3][M] is lower than the other syntheses.[4]PR2 and PR2P are obtained from the same polymerization except PR2 is a crude sample and PR2P is from the same PR2 solution but purified. [5]Calculated as HEMA/NIPAm.

250 mL of the enzymatic synthesis mixture was used for purification and isolation of the individual monomers, M_nEMAs, as previously described.[1] After purification the M_nEMA monomer solutions contained 70-85% acetonitrile. The total mass available in the solutions was of 18.7 mg and 29.5 mg of M_1EMA and of M_2EMA respectively.

For polymerizations, a determined volume of monomer solutions was subjected to acetonitrile evaporation in a rotary evaporator. A gradual exchange of water for D_2O to the desired monomer concentration followed. This was done through careful evaporation of fractions of water at a

controlled temperature of 37 °C in the rotary evaporator, adding D_2O in multiple steps. The temperature was kept always under 37 °C (enzymatic reaction temperature) to prevent possible spontaneous polymerization of the monomers. Once the desired volume was achieved, the monomer solution was transferred to an NMR tube with septum via a glass microscale syringe equipped with a long needle. NIPAm, initiator (KPS) and accelerator (TEMED) solutions in D_2O were prepared and degassed separately before addition to the NMR tube containing the M_nEMA solution. The NMR tube was sealed and the polymerization progressed at room temperature.

This microscale polymerization preparation is challenging mainly because the glycomonomers have shown to precipitate from solution during concentration. These leads to losses of the glycomonomers along the process, thus limiting the net amount of glycomonomers for polymerizations. Optimization of recovery and purification methods in large scale are subject of ongoing work. Nevertheless, we purified enough glycomonomers to prepare several samples at a microscale.

Utmost care was taken on to maintain all parameters close to the nominal values of the experimental design (Table S1). The concentration of reactants was estimated before polymerization via NMR when possible (average prediction error of 2% measured in 5 external standards described below).

All samples were kept in solution in the NMR tubes after synthesis without further processing before characterization. Only part of the reference polymer solution P2R was used to obtain a purified polymer due to low monomer conversions (See Table 2). The purified sample P2R is labeled as P2RP. To obtain sample P2RP, some of sample P2R was precipitated twice in 10 times volume of diethyl ether, filtered and rinsed. The recovered white powder was vacuum dried to constant weight. The sample was then suspended in 600 uL of D_2O for characterization. Even though this sample is a reference sample and does not contain glycomonomer, we have used it as a model compound to reveal if the presence of unreacted monomer had any effect on the thermo-responsive behavior.

It is worth noting that in sample P1M2, the monomer molar concentration in the reaction is lower than the rest of the synthesis. Given the low amounts available of monomers, this reaction was the first polymerization performed and was designed to minimize the amount of monomer used. The monomer molar concentration in the reaction was 54 mmol/L to begin with, no polymerization occurred at first at this concentration so we increased the molar concentration of monomer to 120 mmol/L by evaporating some of the water in a rotary evaporator (Table S1). Fresh initiator solution was added and the polymerization then progressed at room temperature.

B. Nuclear Magnetic Resonance (NMR) spectroscopy detailed method

To acquire ^{1}H NMR spectra for each sample the spin-lattice (T1) was determined from a series of spectra using the standard inversion recovery sequence varying the delay time from 0.001 to 5 s. A relaxation delay of 5 x T1 (for a 90 ° pulse) and an acquisition time of 3 x T2 were used for the acquisition of the spectra. The 90 ° pulse was calibrated using the *pulsecal* program from Topspin. The number of scans and the parameter D1 was adjusted for each sample. All spectra for determination of low critical solution temperature (LCST) transitions were shimmed in solvent suppression mode with digitization mode set to *baseopt*. Spectra calibration, base line correction and phase correction were done using Topspin. In-house generated Matlab scripts as well as the freely available Matlab application RBNMR[3] were used for spectra analysis.

C. Determination of parameters T_{onset} and $LCST_{NMR}$ from ^{1}H NMR spectroscopy data

To determine the LCST transitions from the acquired spectra, the intensities of selected chemical shifts at different temperatures were calibrated to the intensity at 25 °C and plotted against temperature. The intensity is calibrated to the value of the intensity of the reference spectrum. All intensities in the series of experiments are then scaled with the same factor. This allows to immediately compare the spectra within the series of experiments.

A 5-parameter sigmoidal curve (equation S1) was then fitted using Sigmaplot® V.12.0. The fit provides with 5 parameters (a-e). From this fitting two parameters were derived, the T_{onset} of the LCST (determined as the temperature of greatest slope, x_0 in Equation S1) and a parameter that we have named $LCST_{NMR}$, which was obtained by resolving the temperature (x) for when the y=0.5 (the intensity is half of the initial intensity y=1):

$$y = y_0 + \frac{a}{\left[1 + e^{-\left(\frac{x - x_0}{b}\right)}\right]^c} \qquad \text{Equation S1}$$

D. DLS and SLS for P2M2 to determine shape factor

DLS and SLS data was measured to derive the shape factor $\rho = R_g/R_h$ reported in table S2 for sample P2M2 at 25 and 45 °C. The obtained scattering intensity $I(q)$ was brought to an absolute scale using: [T. Zemb and P. Lindner, Neutron, X-Rays and Light. Scattering Methods Applied to Soft Condensed Matter, NORTH HOLLAND, 2002.]

$$I(q) = \frac{\Delta I(q)}{I_{ref}(q)} \left(\frac{n}{n_{ref}}\right)^2 RR_{ref} \qquad \text{Equation S2}$$

where $\Delta I(q)$ is the background scattering, n is the refractive index of the solution, and $I_{ref}(q)$, n_{ref} and RR_{ref} are the scattered intensity, refractive index, and Rayleigh ratio, of the reference (toluene), respectively; q is the magnitude of the scattering vector:

$$q = \frac{4\pi n}{\lambda_0} sin\left(\frac{\theta}{2}\right) \qquad \text{Equation S3}$$

where λ_0, n and θ are the laser wavelength, refractive index of the solution and scattering angle, respectively. The radius of gyration R_G was calculated using Zimm plot. The derived Rg and Rh were used to calculate shape factor.

Table S2. DLS of P2M2 to determine shape factor.

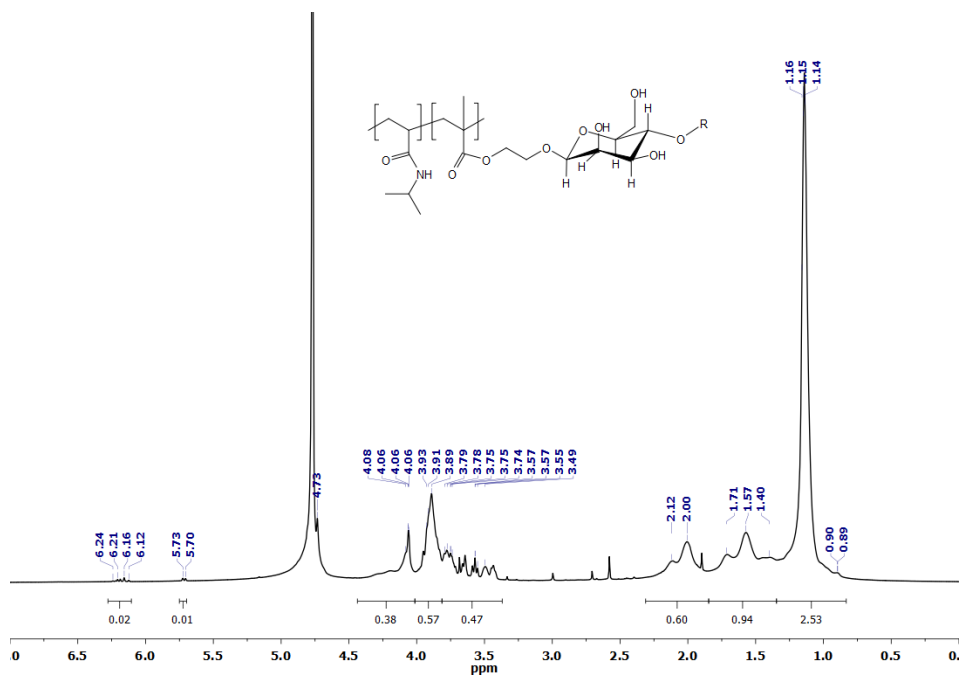| Temperature [°C]	R_g [nm]	R_h [nm]	$\rho = R_g/R_h$
25	49.1	40.11	1.22
45	50	58.63	0.85

E. ¹H and ¹³C NMR spectra for sample P3M2.

Figure S1. ¹H NMR (D₂O, 500 MHz) spectra of poly(N-isopropylacrylamide-co-2-[β-manno(bio)syloxy] ethyl methacrylate) P3M2 taken at 25 °C.
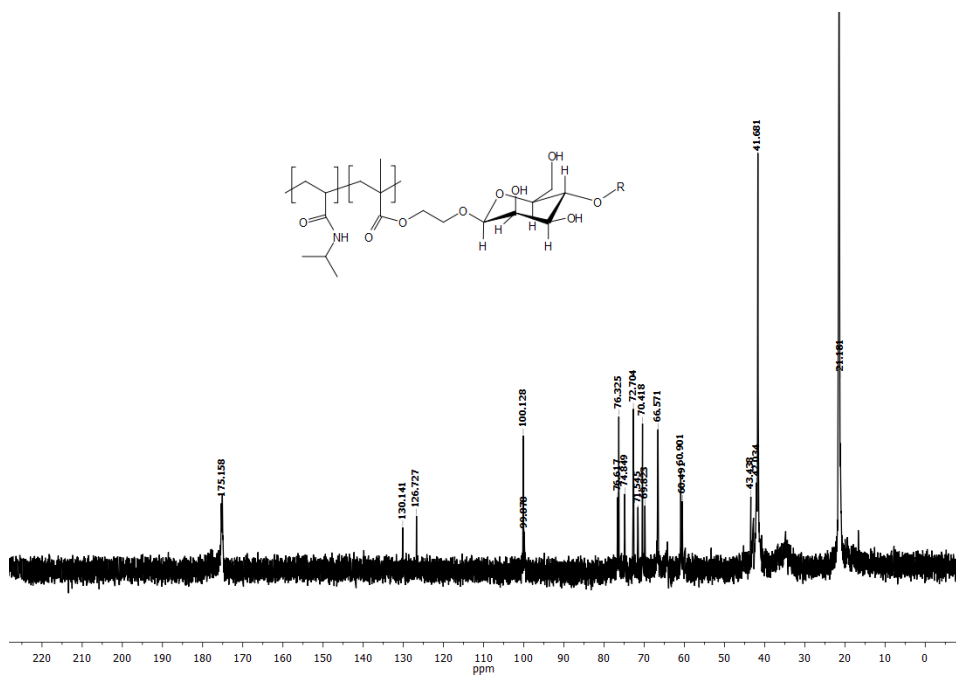
Figure S2. ^{13}C NMR (D20, 125 MHz) spectra of poly(N-isopropylacrylamide-co-2-[β-manno(bio)syloxy] ethyl methacrylate) P3M2 taken at 25 °C.

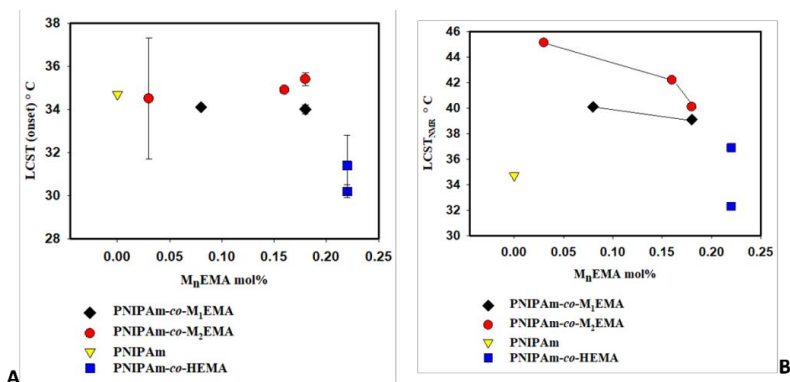## F. Analysis of LCST and LCST$_{NMR}$ by ^{1}H NMR spectroscopy

Figure S3. Estimated T_{onset} of the transition (A) and $LCST_{NMR}$ (B) of the glycopolymers and the reference materials by NMR analysis. Error bars correspond to the SSE of the curve fitting for the respective parameter.
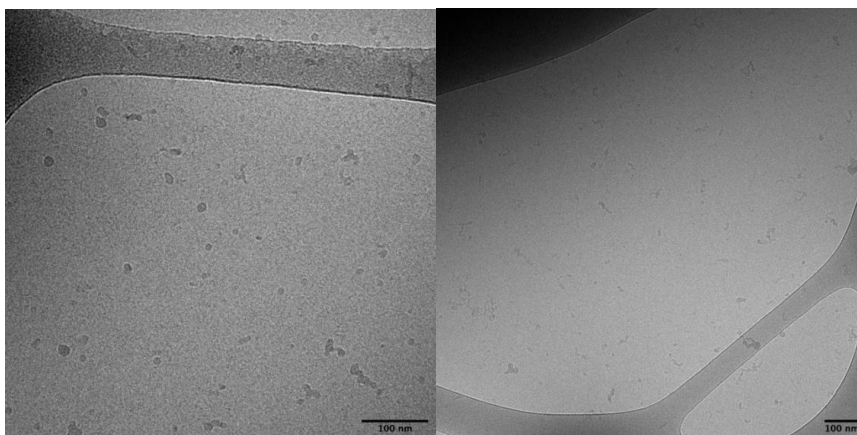
G. cryo-TEM concentration dependence in P2M2

Figure S4. Cryo-TEM images of P2M2 incubated at 25°C prior to blotting at 10-fold dilution ~1 mg/mL (left) and at the initial concentration ~10 mg/mL (right).
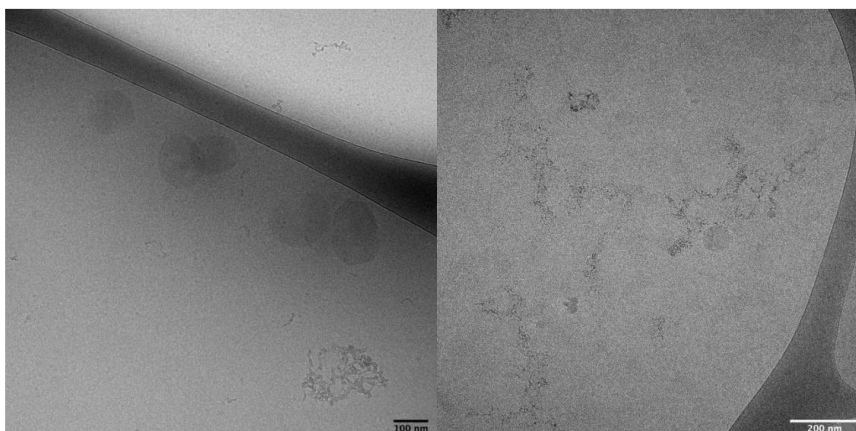
Figure S5. Cryo-TEM images of P2M2 incubated at 50°C prior to blotting at 10-fold dilution 1 mg/mL (left) and at the initial concentration ~10 mg/ml (right).

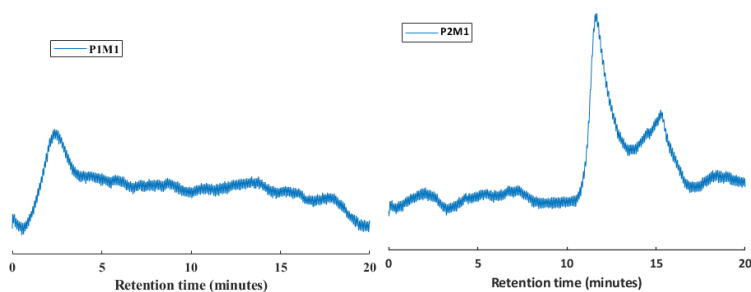## H. SEC chromatograms in water mobile phase

Figure S6. Inserts from the size exclusion chromatograms for samples P1M1 and P2M2.

(1)   Rosengren, A.; Butler, S. J.; Arcos-Hernandez, M.; Bergquist, K.-E. E.; Jannasch, P.; Stålbrand, H. Enzymatic Synthesis and Polymerisation of β-Mannosyl Acrylates Produced from Renewable Hemicellulosic Glycans. *Green Chem.* **2019**, *21* (8), 2104–2118.

(2)   Shen, Z.; Terao, K.; Maki, Y.; Dobashi, T.; Ma, G.; Yamamoto, T. Synthesis and Phase Behavior of Aqueous Poly(N-Isopropylacrylamide-Co-Acrylamide), Poly(N-Isopropylacrylamide-Co-N,N-Dimethylacrylamide) and Poly(N-Isopropylacrylamide-Co-2-Hydroxyethyl Methacrylate). *Colloid Polym. Sci.* **2006**, *284* (9), 1001–1007.

(3)   Nyberg, N. RBNMR. MATLAB Central File Exchange 2020.

Paper v

β-**Mannanase-catalyzed synthesis of alkyl mannooligosides**

J. Morrill, A. Månberger, A. Rosengren, **P. Naidjonoka**, P. von Freiesleben, K. B. R. M. Krogh, K. E. Bergquist, T. Nylander, E. N. Karlsson, P. Aldercreutz, H. Stålbrand

CrossMark

β-Mannanase-catalyzed synthesis of alkyl mannooligosides

Johan Morrill[1] · Anna Månberger[2] · Anna Rosengren[1] · Polina Naidjonoka[3] · Pernille von Freiesleben[5] ·
Kristian B. R. M. Krogh[5] · Karl-Erik Bergquist[4] · Tommy Nylander[3] · Eva Nordberg Karlsson[2] · Patrick Adlercreutz[2] ·
Henrik Stålbrand[1]

Abstract

β-Mannanases catalyze the conversion and modification of β-mannans and may, in addition to hydrolysis, also be capable of transglycosylation which can result in enzymatic synthesis of novel glycoconjugates. Using alcohols as glycosyl acceptors (alcoholysis), β-mannanases can potentially be used to synthesize alkyl glycosides, biodegradable surfactants, from renewable β-mannans. In this paper, we investigate the synthesis of alkyl mannooligosides using glycoside hydrolase family 5 β-mannanases from the fungi *Trichoderma reesei* (*Tr*Man5A and *Tr*Man5A-R171K) and *Aspergillus nidulans* (*An*Man5C). To evaluate β-mannanase alcoholysis capacity, a novel mass spectrometry-based method was developed that allows for relative comparison of the formation of alcoholysis products using different enzymes or reaction conditions. Differences in alcoholysis capacity and potential secondary hydrolysis of alkyl mannooligosides were observed when comparing alcoholysis catalyzed by the three β-mannanases using methanol or 1-hexanol as acceptor. Among the three β-mannanases studied, *Tr*Man5A was the most efficient in producing hexyl mannooligosides with 1-hexanol as acceptor. Hexyl mannooligosides were synthesized using *Tr*Man5A and purified using high-performance liquid chromatography. The data suggests a high selectivity of *Tr*Man5A for 1-hexanol as acceptor over water. The synthesized hexyl mannooligosides were structurally characterized using nuclear magnetic resonance, with results in agreement with their predicted β-conformation. The surfactant properties of the synthesized hexyl mannooligosides were evaluated using tensiometry, showing that they have similar micelle-forming properties as commercially available hexyl glucosides. The present paper demonstrates the possibility of using β-mannanases for alkyl glycoside synthesis and increases the potential utilization of renewable β-mannans.

Keywords β-Mannanase · Transglycosylation · Alcoholysis · Alkyl glycoside · Surfactant

✉ Henrik Stålbrand
  henrik.stalbrand@biochemistry.lu.se

[1] Department of Biochemistry and Structural Biology, Lund University, PO Box 124, S-221 00 Lund, Sweden

[2] Department of Biotechnology, Lund University, PO Box 124, S-221 00 Lund, Sweden

[3] Department of Physical Chemistry, Lund University, PO Box 124, S-221 00 Lund, Sweden

[4] Centre for Analysis and Synthesis, Department of Chemistry, Lund University, PO Box 124, S-221 00 Lund, Sweden

[5] Novozymes A/S, Krogshøjvej 36, 2880 Bagsværd, Denmark

Introduction

Plant biomass has the potential to substitute fossil resources in numerous sectors. In this development, considerable interest is devoted to biotechnology for the sustainable production of biofuels and biochemicals (Cherubini 2010). Alkyl glycosides are non-toxic and biodegradable non-ionic surfactants suitable for many applications including detergents, cleaners, and personal care products (von Rybinski and Hill 1998). They consist of a hydrophobic alkyl chain linked by a glycosidic bond to a hydrophilic glycoside.

Glycoside hydrolases (GHs) can be used to synthesize alkyl glycosides from carbohydrates and alcohols under relatively mild reaction conditions (Ochs et al. 2011; van Rantwijk et al. 1999). Enzymatic synthesis of alkyl glycosides has several advantages over chemical synthesis in that it enables production of anomerically pure molecules, without the use of several protection and deprotection steps for

Springer

chemoselectivity (van Rantwijk et al. 1999; von Rybinski and Hill 1998; Wang and Huang 2009). GH-catalyzed synthesis can be done either via thermodynamically controlled reversed hydrolysis or kinetically controlled transglycosylation (van Rantwijk et al. 1999).

In the Carbohydrate-Active Enzymes (CAZy) database (http://www.cazy.org) (Lombard et al. 2014), GHs are classified into families based on sequence similarity, and some GH families have further been divided into subfamilies, e.g., GH family 5 (GH5) (Aspeborg et al. 2012). Families are classified into clans, where clan A is the largest (Davies and Sinnott 2008; Henrissat and Bairoch 1996). The active sites of endo-acting GHs, e.g., GH5 β-mannanases, contain several subsites where the monosaccharide moieties of the substrate bind. The subsites are labeled from $-n$ to $+n$, where n is a positive integer, with $-n$ situated towards the non-reducing end and $+n$ towards the reducing end of the substrate (Fig. 1). Glycosidic bond cleavage occurs between monosaccharide moieties bound at the adjacent -1 and $+1$ subsites (Davies et al. 1997).

The GHs applicable for transglycosylation utilize a two-step catalytic mechanism which retains the configuration of the anomeric carbon (Sinnott 1990). The GH5 subfamily 7 (GH5_7) β-mannanases belonging to clan A studied in the present paper utilize this mechanism (Gilbert et al. 2008). The first step of the retaining mechanism is a nucleophilic attack on the anomeric carbon, which releases the leaving group and forms a covalent glycosyl-enzyme intermediate (Davies and Henrissat 1995; Zechel and Withers 2000). In the second step, a glycosyl acceptor, water in hydrolysis and another nucleophile in transglycosylation, performs a nucleophilic attack on the covalent intermediate which breaks the covalent bond, forming a new product (Fig. 1). Several GH5 β-mannanases have been shown to use saccharides as transglycosylation acceptors (Arcand et al. 1993; Coulombel et al. 1981; Couturier et al. 2013; Dias et al. 2004; Dilokpimol et al. 2011; Hakamada et al. 2014; Harjunpää et al. 1999; Hrmova et al. 2006; Larsson et al. 2006; Mizutani et al. 2012;

Morrill et al. 2015; Puchart et al. 2004; Rosengren et al. 2012; Rosengren et al. 2014; Schröder et al. 2006; Wang et al. 2014). Alcohols acting as acceptors in combination with glycosyl donor substrates can generate alkyl glycosides (Adlercreutz 2017; Rosengren et al. 2014). In the presence of both water and alcohol, these acceptors compete to attack the covalent intermediate. Secondary hydrolysis of products may also occur (Fig. 1), and the synthesis and breakdown of several products are possible before equilibrium is reached (Sinnott 1990; van Rantwijk et al. 1999).

To date, alkyl glycoside synthesis with GHs has been carried out with, e.g., β-glucosidases (Lundemo et al. 2013; Papanikolaou 2001; Turner et al. 2007), β-mannosidases (Itoh and Kamiyama 1995), α-amylases (Damián-Almazo et al. 2008; Larsson et al. 2005; Moreno et al. 2010), xylanases (Jiang et al. 2004; Matsumura et al. 1996; Matsumura et al. 1997; Matsumura et al. 1999; Ochs et al. 2011), and β-glucanases (Akiba et al. 1999). However, little is known about alkyl glycoside synthesis catalyzed by endo-acting GHs attacking β-mannans which are among the most abundant polysaccharides in nature, e.g., constituting the major part of softwood hemicellulose (Ebringerová 2006; Lundqvist et al. 2003; Scheller and Ulvskov 2010). We have previously observed transglycosylation with β-mannanases using methanol and 1-butanol as acceptors (Rosengren et al. 2012; Rosengren et al. 2014). β-Mannanases have several potential and existing applications to increase the use of this interesting natural resource (Moreira and Filho 2008; Yamabhai et al. 2016). In the present paper, we address a novel approach—the application of β-mannanases in synthesis of alkyl glycosides using renewable β-mannan as donor substrate. Successful use of β-mannanases for enzymatic synthesis is especially interesting since the β-mannosidic bond is arguably the most difficult glycosidic bond to synthesize by chemical means (Gridley and Osborn 2000). Frequently, activated (e.g., nitrophenyl) sugars are used as donor substrates in transglycosylation reactions with *exo*-acting GHs as catalysts (Teze et al. 2015; Teze et al. 2014). Our approach in the current paper, however, is different. We are studying the use of a natural, renewable
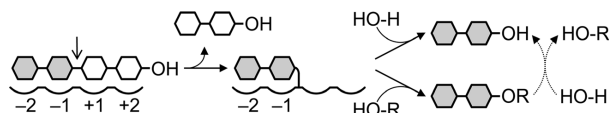

Fig. 1 Simplified scheme illustrating the retaining double-displacement mechanism used by the β-mannanases in this study. To the left, mannotetraose (M_4) is shown bound in subsites -2 to $+2$ with the reducing end bound in subsite $+2$. β-Mannanases may bind M_4 in multiple binding modes, e.g., from subsites -3 to $+1$ (Rosengren et al. 2012), resulting in other products. The enzyme performs a nucleophilic attack instead the glycosidic bond between subsites -1 and $+1$, indicated by the arrow, and releases the mannobiose unit in subsites $+1$ and $+2$

(white) while the mannobiose unit in subsites -1 and -2 (gray) forms a covalent intermediate with the enzyme. The covalent intermediate (in the center) can then be attacked by water (HO–H), leading to hydrolysis, or an alcohol (HO–R), leading to alcoholysis and the production of a glycosyl conjugate (alkyl mannobioside) shown to the right. The dashed arrows show possible secondary hydrolysis of the glycosyl conjugate

(non-activated) donor substrate (β-mannan) and endoglycosidases (β-mannanases) as catalysts, allowing the synthesis of alkyl glycosides with longer sugar heads. Furthermore, in the present study, we expand the length of the acceptor alcohol used compared to previous studies (Rosengren et al. 2014) of β-mannanases.

With the aim to reveal the applicability of β-mannanases in alkyl mannooligoside synthesis, three fungal GH5 β-mannanases were selected based on previously observed alcoholysis capabilities with methanol and butanol as well as different product profiles due to different modes of mannotetraose (M_4) attack: from *Trichoderma reesei*, *Tr*Man5A (Sabini et al. 2000) and its engineered subsite + 2 variant *Tr*Man5A-R171K (Rosengren et al. 2012), and from *Aspergillus nidulans*, *An*Man5C (Dilokpimol et al. 2011; Rosengren et al. 2014).

In this paper, we further study these three β-mannanases for the synthesis of alkyl mannooligosides using a longer-chain alcohol, i.e., hexanol, as acceptor (resulting in hexyl mannooligosides). A further novelty is the use of a natural β-mannan donor substrate. Mass spectrometry was used as a novel screening method to estimate the initial degree of alcoholysis products (DA) early in reactions where a significant amount of donor substrate remains. DA reflects the fraction of total products that are alkyl mannooligosides. One β-mannanase (*Tr*Man5A) was selected for further optimization on the basis of highest DA values and stable product during prolonged incubations. Using pre-hydrolyzed β-mannan as donor substrate, a sufficiently large reaction was set up to allow product characterization. The synthesized hexyl mannooligosides were separated and quantified using reversed-phase liquid chromatography, their structures were characterized, and their basic surfactant properties were determined.

Materials and methods

Cloning, expression, and purification

*Tr*Man5A was produced in the host *T. reesei* as described earlier (Hägglund et al. 2003) and was lyophilized. An aliquot of the obtained powder was solubilized in 50 mM sodium acetate buffer (pH 5.3). To remove saccharides present in the enzyme powder, the solution was concentrated by centrifugation in a spin column with 10 kDa cutoff followed by dilution in the buffer and this procedure was repeated several times.

For production of *Tr*Man5A-R171K, *Pichia pastoris* X-33 cells transformed with the constructed plasmid encoding *Tr*Man5A-R171K as described previously (Rosengren et al. 2012) were cultured and expressed as described in the EasySelect™ *Pichia* expression kit manual (Invitrogen, Lidingö, Sweden). The cells were streaked on an agar plate

containing yeast extract peptone dextrose (YPD) medium with 100 μg/mL Zeocin™ and incubated at 30 °C for 3 days. One colony was transferred to a 250-mL baffled Erlenmeyer flask containing 50 mL buffered glycerol-complex medium (BMGY) and incubated at 30 °C and 250 rpm to an OD_{600} of 2.0. The culture was then centrifuged for 30 min, the supernatant was discarded, and the pellet was dissolved in 400 mL buffered methanol-complex medium (BMMY) to an OD_{600} of 1.0 in two 2-L baffled Erlenmeyer flasks for expression. The expression culture was incubated at 30 °C and 250 rpm with methanol added every 24 h to a final concentration of 0.5%. Culture enzyme activity was monitored with the β-mannanase activity assay described below. After 6 days of expression, the supernatants were harvested by centrifugation and the cell pellets were discarded. The supernatant was concentrated and changed to 10 mM Tris-HCl buffer (pH 7.8) using spin columns with 10 kDa cutoff. Anion exchange chromatography was performed on a BioLogic DuoFlow FPLC® System (Bio-Rad, Hercules, CA, USA) with a 6-mL Resource Q anion exchange column (Amersham Pharmacia Biotech, Uppsala, Sweden). The flow rate was 1 mL/min, and 40 fractions of 5 mL each were collected over a sodium chloride gradient of 0–0.5 M. The purest fractions, evaluated with sodium dodecyl sulfate-polyacrylamide gel electrophoresis (SDS-PAGE) (Rosengren et al. 2012), were pooled and changed to 50 mM sodium acetate buffer (pH 5.3) using a spin column with 10 kDa cutoff.

For production of *An*Man5C, *P. pastoris* X-33 cells containing the gene encoding the enzyme were obtained from the Fungal Genetics Stock Center (FGSC), School of Biological Science, University of Missouri (Kansas City, MO, USA), with accession number 10106 (AN6427.2). The gene was previously cloned from complementary DNA of *A. nidulans* by others (Bauer et al. 2006). The cells were cultured and expressed, and the supernatant was harvested in the same way as described for *Tr*Man5A-R171K above. *An*Man5C was purified as described previously (Rosengren et al. 2014). The supernatant was concentrated by centrifugation in a spin column with 10 kDa cutoff. His-tag purification was performed with a 1-mL Ni-NTA Superflow cartridge according to the manufacturer's recommendations (Qiagen, Hilden, Germany). Fractions with pure protein, verified by SDS-PAGE, were pooled and changed to 50 mM sodium acetate buffer (pH 5.5), by centrifugation using a 10-kDa cutoff spin column.

Protein concentrations were determined using a NanoDrop® ND-1000 spectrophotometer (Saveen Werner, Malmö, Sweden) by measuring absorbance at 280 nm as described previously for *Tr*Man5A and *Tr*Man5A-R171K (Rosengren et al. 2012) as well as for *An*Man5C (Rosengren et al. 2014).

As assay buffers, 50 mM sodium acetate buffer (pH 5.3) for *Tr*Man5A and *Tr*Man5A-R171K and 50 mM sodium acetate buffer (pH 5.5) for *An*Man5C were used if not otherwise stated.

The 1-hexanol was dried with a 3 Å molecular sieve (Sigma-Aldrich, St. Louis, MO, USA) for at least 24 h before use.

β-Mannanase activity assay

β-Mannanase activity was assayed with 0.5% (w/v) locust bean galactomannan (LBG) (Sigma-Aldrich) in buffer using a scaled-down version of the 3,5-dinitrosalicylic acid (DNS) method described previously (Stålbrand et al. 1993). Six microliters of adequately diluted enzyme was mixed with 54 μl of 0.5% (w/v) LBG in a 96-well plate and incubated for 10 min at 37 °C in a PTC-200 thermocycler (Bio-Rad). One hundred twenty microliters DNS was added to the mixture to stop the reaction. The mixture was heated at 95 °C for 5 min and subsequently cooled in the thermocycler before the absorbance was measured at 540 nm in a SpectraCount™ plate reader (Packard, Meriden, CT, USA). The concentration of reducing ends was calculated from a standard curve of mannose.

β-Mannanase stability in alcohol

The stability of the three β-mannanases was tested in 25, 50, and 75% (v/v) methanol; in 5 and 25% (v/v) 1-hexanol; and without any alcohol. The three enzymes were each diluted with assay buffer and alcohol at the abovementioned concentrations prior to incubation. The stability test was performed at room temperature and at 37 °C. After 0, 2, 6, and 24 h of incubation, samples were taken and residual β-mannanase activity was assayed in each sample as described above.

Alcoholysis with M_4 and methanol

Alcoholysis with methanol was performed by incubating 2 μM of each enzyme with 5 mM mannotetraose (M_4) and 25% (v/v) methanol in 20 mM buffer at 37 °C for 4 h (Rosengren et al. 2012). Samples were taken every hour and analyzed with matrix-assisted laser desorption/ionization time-of-flight mass spectrometry (MALDI-TOF MS) as described previously (Hekmat et al. 2010; Rosengren et al. 2012). 0.5 μL of each reaction mixture was applied and quickly dried by heating on a stainless steel target plate. Then, 0.5 μL matrix (10 mg/mL 2,5-dihydroxybenzoic acid (DHB) in water) was applied over the sample and quickly dried by heating. A 4700 Proteomics Analyzer (Applied Biosystems, Foster City, CA, USA) in positive reflector mode was used with a laser intensity of 5000. Fifty subspectra with 20 shots on each were accumulated from a sample to generate a spectrum. Data Explorer version 4.5 (Applied Biosystems) was used for data analysis.

Alcoholysis with M_4 and 1-hexanol

Alcoholysis with 1-hexanol was performed in the same way as described with methanol, except that 25% (v/v) 1-hexanol was used instead of methanol, and prior to the sampling of the reaction mixture, the tube was shaken to mix the two phases. Reactions with TrMan5A were also performed with varying enzyme concentrations (0.2, 2, and 4 μM) and M_4 concentrations (5, 25, and 50 mM). Duplicate incubations were analyzed with MALDI-TOF MS as described above, except that the samples were diluted 10-fold in Milli-Q water before being applied on the target plate due to the presence of hexanol. In addition, reactions with 5, 25, and 50 mM M_4 were analyzed with high-performance anion exchange chromatography with pulsed amperometric detection (HPAEC-PAD) in order to analyze the rate of M_4 degradation in these reactions, using an ICS-5000 system and a CarboPac PA200 column (Thermo Fisher Scientific, Waltham, MA, USA).

Calculation of degree of alcoholysis products

In alcoholysis reactions with both alcohol and water present together with a donor saccharide, both hydrolysis products (oligosaccharides) and alkyl glycosides are likely formed. The product formation (here analyzed with MALDI-TOF MS) can be described by the DA, reflecting the fraction of total products that are alkyl mannooligosides. To make an initial estimation of the DA for a given reaction, the peak areas of alkyl mannooligosides and mannooligosaccharides that have accumulated from the start of a reaction to the sampling time were obtained from the same MALDI-TOF MS spectrum. Since different compounds are expected to have different response factors in MALDI-TOF MS (Duncan et al. 2008), the DA determined in this way does not reflect the absolute concentration relation of products. However, DA analysis can still serve as a straightforward initial method to compare different enzymes and/or reaction conditions. In this case, to estimate DA in reactions with M_4 as donor substrate, the MALDI-TOF MS peak areas of the alcoholysis products (alkyl mannooligosides) and oligosaccharide products were determined. Hexyl mannoside and mannose (M_1) were excluded in the present study due to being minor reaction products (very low MALDI-TOF MS response), and M_4 was excluded due to being the reaction donor substrate. DA was then calculated from MALDI-TOF MS peak areas according to Eq. (1).

$$DA = \frac{\text{Total area of alkyl mannooligosides}}{\text{Total area of oligosaccharide products and alkyl mannooligosides}}$$

(1)

The initial DA values after 1 h of incubation were calculated for reactions with 2 μM TrMan5A, TrMan5A-R171K, or

AnMan5C with 5 mM M_4 and 25% (v/v) methanol or 1-hexanol, as well as during the course of further reactions with 1-hexanol.

Separation and quantification of hexyl mannooligosides

To separate and quantify the synthesized hexyl mannooligosides, the reaction was performed as described above with 25% (v/v) 1-hexanol, 0.2 μM TrMan5A, and 25 mM M_4 for up to 8 h. Samples were taken every 2 h, and the reaction was stopped by heating the samples at 95 °C for 5 min. The samples were then diluted fourfold with water and acetonitrile (ACN) to 20% (v/v) ACN. The diluted samples were analyzed on an UltiMate 3000 high-performance liquid chromatography (HPLC) system (Thermo Fisher Scientific) using an Acclaim RSLC 120 C_{18} column with a Corona charged aerosol detector (CAD). Five microliters of each sample was injected and separated with a 0.5 mL/min mobile phase composed of 85% of 0.1% (v/v) acetic acid in water and 15% ACN over 20 min at a column temperature of 40 °C. Concentrations of hexyl mannooligosides were estimated using a standard curve of hexyl-β-D-maltoside (Sigma-Aldrich). Fractions were collected at chromatogram peaks during HPLC separation and analyzed with MALDI-TOF MS in order to determine peak identities.

Calculation of alcoholysis/hydrolysis ratio

In order to more accurately and mechanistically describe the competition between alcohol and water in the reaction mixture with TrMan5A, the alcoholysis/hydrolysis ratio (r_A/r_H) was calculated as described in the literature (van Rantwijk et al. 1999). In kinetically controlled transglycosylation reactions with alcohol as the main (non-water) acceptor, r_A/r_H describes the prevalence of the covalent intermediate being attacked by alcohol as opposed to water. Due to hexyl mannobioside (hexyl-M_2) being the dominant alkyl mannooligoside produced by TrMan5A, r_A/r_H was calculated according to Eq. (2) based on HPLC and HPAEC-PAD quantifications of hexyl-M_2 and mannobiose (M_2), respectively. Hydrolysis of M_4 generates two M_2 molecules, while alcoholysis generates M_2 and hexyl-M_2 in equimolar amounts (Fig. 1). Thus, the denominator is calculated by subtracting [alkyl-M_2] from [M_2] and dividing the obtained value by 2.

$$\frac{r_A}{r_H} = \frac{[\text{alkyl} - M_2]}{([M_2] - [\text{alkyl} - M_2])/2} \tag{2}$$

From the initial r_A/r_H, the theoretical yield (η) was extrapolated according to Eq. (3) (van Rantwijk et al. 1999) and

compared with experimental yield to assess secondary hydrolysis of alcoholysis products.

$$\eta = \frac{r_A/r_H}{1 + r_A/r_H} \tag{3}$$

The selectivity factor (S_c) indicating the enzyme's selectivity for the alcohol (Adlercreutz 2017; Hansson and Adlercreutz 2001) was also calculated from the initial r_A/r_H according to Eq. (4). In the case of 1-hexanol, the concentrations of 1-hexanol (5.9 g/L, equal to 58 mM) and water (55 M) in the water phase of the reaction mixture were used to calculate S_c.

$$S_c = \frac{r_A}{r_H} \times \frac{[\text{water}]}{[\text{alcohol}]} \tag{4}$$

Preparative synthesis and purification of hexyl mannooligosides

To prepare sufficient amounts of hexyl mannooligosides for characterization, the alcoholysis reaction was scaled up. Mannooligosaccharides were prepared by hydrolysis of 4 g ivory nut mannan (INM) (Megazyme, Bray, Ireland) for 4 h by 0.25 μM of the GH26 β-mannanase from $Podospora$ $anserina$, PaMan26A (Couturier et al. 2013; von Freiesleben et al. 2016), in 400 mL of 20 mM ammonium acetate buffer (pH 5.3) at 40 °C in a 2-L baffled Erlenmeyer flask with shaking at 150 rpm. The oligosaccharide composition of the resulting hydrolysate was determined with HPAEC-PAD, and the hydrolysate was lyophilized. Hydrolysate with 25 mM of M_4 was then used as donor substrate in a 35-mL reaction with 25% (v/v) 1-hexanol and 0.2 μM TrMan5A in 20 mM sodium acetate buffer (pH 5.3). The reaction was performed for 8 h at 37 °C and then stopped by boiling for 5 min. Hexyl mannooligosides in the sample were quantified with HPLC as described above. The obtained hexyl mannooligosides were then purified with preparative HPLC using a Waters Symmetry C_{18} Prep column using a 1260 Infinity system (Agilent Technologies, Santa Clara, CA, USA), with a 10–45% gradient of ACN versus 0.1% formic acid in water over 9 min at room temperature, followed by a steeper gradient of 45–90% ACN over 2 min and, finally, a wash step with 90% ACN for 2 min. Fractions were collected during the entire separation and analyzed with MALDI-TOF MS to identify fractions containing hexyl mannooligosides. The identified fractions were then pooled, lyophilized, and redissolved in 25 μl Milli-Q water.

Structural characterization of hexyl mannooligosides

For structural analysis, an aliquot of the lyophilized hexyl mannooligoside mixture synthesized above was analyzed with MALDI-TOF MS as described above. Peaks

corresponding to hexyl mannooligosides were then fragmented with MALDI-TOF/TOF tandem MS. From each precursor mass, to generate a spectrum, 10 subspectra were collected in positive reflector mode with 125 shots per subspectrum at a laser intensity of 6000.

Further structural analysis was carried out with nuclear magnetic resonance (NMR) spectroscopy. Before analysis, the lyophilized sample of hexyl mannooligosides was dissolved in 500 μl of 99.8% D_2O, equilibrated at room temperature overnight, lyophilized, and redissolved and equilibrated overnight again in 500 μl of 99.8% D_2O. ^1H, ^{13}C, correlation spectroscopy (COSY), total correlation spectroscopy (TOCSY), heteronuclear multiple-bond correlation (HMBC), and heteronuclear single quantum coherence (HSQC) NMR spectra were recorded at 10 °C and a ^1H spectrum also at 25 °C, on an Bruker Avance III spectrometer (Bruker, Billerica, MA, USA) at 500.17 and 125.78 MHz for ^1H and ^{13}C, respectively. Chemical shifts were given in ppm relative to tetramethylsilane (TMS) as external standard. Additionally, ^1H NMR was used to quantify the hexyl-M_2 and hexyl mannotrioside (hexyl-M_3) in the sample by comparing it to reference samples of hexyl-β-D-maltoside. The same sample was also analyzed and quantified with HPLC, using hexyl-β-D-maltoside as standard.

Determination of critical micelle concentration

In order to evaluate the surfactant properties of the synthesized hexyl mannooligosides, surface tension was measured as a function of hexyl mannooligoside concentration using a PAT-1 Drop and Bubble Shape Tensiometer (SINTERFACE Technologies, Berlin, Germany). This technique is based on analyzing the shape of the drop or bubble as described in the literature (Berry et al. 2015; Javadi et al. 2013). The shape is determined by the surface tension that strives to make a spherical drop and gravity forces that elongate the drop, which can be described by the Young-Laplace equation (Berry et al. 2015). The profile of the pendant drop was captured by a charge-coupled device (CCD) camera. To record data on small sample volumes, a 100-μl syringe with a needle that has an external diameter of 1.0 mm was fitted to the instrument and the sample was ejected manually. A typical drop volume was 5 μl. Since the technique is non-destructive, the same solution was reused for the following measurements, starting with the highest concentration and diluting to obtain the necessary concentration for the next point in the curve. If needed, the sample was freeze-dried between measurements. Measurements were performed at 22 °C for 350 s each and at least twice for every concentration. For comparison, surface tension curves were obtained in the same way with hexyl-β-D-glucoside and hexyl-β-D-maltoside individually and in a mixture with a 0.53:1 mole ratio.

Results

β-Mannanase stability in the presence of alcohol

To see if TrMan5A, TrMan5A-R171K, and AnMan5C retained their β-mannanase activity in the presence of alcohols, enzyme stability was evaluated with several concentrations of methanol and 1-hexanol, with activity assayed at regular time intervals. The three enzymes retained 80–100% of initial activity over 24 h at 37 °C with 25% methanol or 5% 1-hexanol (Fig. S1). The enzymes were moderately stable with 25% 1-hexanol, retaining 75–90% of initial activity for at least 6 h. Higher methanol concentrations decreased stability further, with 75% methanol deactivating all three enzymes after 2 h.

Alcoholysis with M_4 and methanol

In order to screen the enzymes' capacity to catalyze alcoholysis, each enzyme was incubated with 5 mM M_4 and 25% (v/v) methanol at 37 °C for up to 4 h. Alcoholysis products (methyl mannooligosides) and oligosaccharide products were detected with MALDI-TOF MS. After 1 h, the dominating product for both TrMan5A and AnMan5C was M_2 followed by methyl mannobioside (methyl-M_2) (Fig. 2), with TrMan5A also producing some mannotriose (M_3) and methyl mannotrioside (methyl-M_3). The dominating products for TrMan5A-R171K are M_3 and methyl-M_3 followed by M_2 and methyl-M_2. This is consistent with the observed subsite binding mode preferences with M_4 for TrMan5A and TrMan5A-R171K (Rosengren et al. 2012). The R171K substitution in the + 2 subsite of TrMan5A was previously shown to reduce the frequency of binding modes involving the + 2 subsite (Rosengren et al. 2012).

To advance the evaluation of alcoholysis with methanol by the three enzymes, the initial DA in the above reactions with methanol and M_4 was calculated based on MALDI-TOF MS peak areas of alcoholysis products and oligosaccharide products according to Eq. (1) (Table 1). DA values reflect the fraction of total products that are alcoholysis products and allow comparison between enzymes as described in the "Materials and methods" section. The most effective enzymes to perform alcoholysis with M_4 and methanol were TrMan5A-R171K and AnMan5C with initial DA values after 1 h of 0.43 and 0.42, respectively, followed by TrMan5A with a DA of 0.33 (Table 1). In addition, minor amounts (< 2% of total product peak area) of saccharides with degree of polymerisatio (DP) 5–9 were detected in incubations with TrMan5A and AnMan5C, indicating transglycosylation with saccharides as acceptors, but not with TrMan5A-R171K, in line with previous studies (Dilokpimol et al. 2011; Rosengren et al. 2012). The reactions were further followed during 4 h with sampling every hour, showing differences in DA during
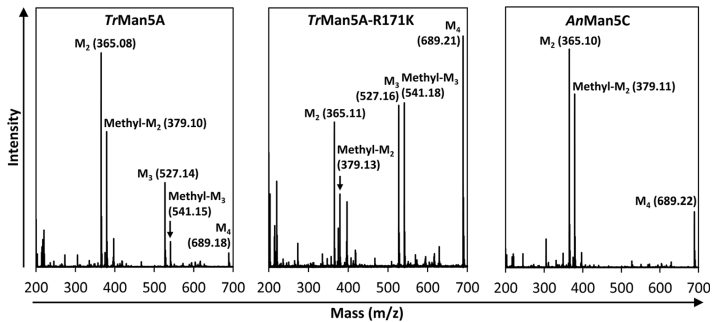
Fig. 2 MALDI-TOF-MS spectra of alcoholysis reaction with methanol after 1 h. Peaks correspond to experimentally determined monoisotopic masses of sodium adducts of present mannooligosaccharides and methyl mannooligosides. The theoretical monoisotopic sodium adduct masses of these compounds are as follows: M_1, 203.05; M_2, 365.11; M_3, 527.16; M_4, 689.21; methyl-M_1, 217.07; methyl-M_2, 379.12; and methyl-M_3, 541.17

the course of the reactions. Both TrMan5A and AnMan5C show a maximum DA at 1 h. However, the DA beyond 1 h was almost constant for TrMan5A and TrMan5A-R171K while it dropped distinctly (> 10-fold) for AnMan5C, possibly indicating secondary hydrolysis of the alcoholysis products.

Alcoholysis with M_4 and 1-hexanol

In order to screen and evaluate alcoholysis capacity with a longer-chain alcohol, 2 μM of each of the three enzymes was incubated with 5 mM M_4 and 25% (v/v) 1-hexanol for up to 4 h. Alcoholysis products (hexyl mannooligosides) and oligosaccharides were detected with MALDI-TOF MS, and DA was calculated in the same way as with methanol above according to Eq. (1). The dominating alcoholysis products were of the same mannooligoside DP as those obtained from alcoholysis with methanol, with TrMan5A producing mainly hexyl mannobioside (hexyl-M_2) and some hexyl mannotrioside (hexyl-M_3) (Fig. S2), TrMan5A-R171K mainly hexyl-M_3 and some hexyl-M_2, and AnMan5C exclusively hexyl-M_2. Oligosaccharides with DP 5–9 were again detected

Table 1 Degree of alcoholysis products (DA) (average of three MALDI-TOF MS spectra ± standard deviation) after 1 h of incubation with 5 mM M_4, 25% (v/v) methanol or 1-hexanol, and 2 μM of TrMan5A, TrMan5A-R171K, or AnMan5C

Enzyme	DA (methanol)	DA (1-hexanol)
TrMan5A	0.33 ± 0.04	0.026 ± 0.003
TrMan5A-R171K	0.43 ± 0.01	0.010 ± 0.001
AnMan5C	0.42 ± 0.01	0.004 ± 0.001

DA values were calculated from MALDI-TOF MS peak areas according to Eq. (1)

in minor amounts (< 2% of total product MALDI-TOF MS peak area) with TrMan5A and AnMan5C but not with TrMan5A-R171K. However, the DA values for all three enzymes were significantly lower than corresponding values for methyl mannooligosides produced by the same enzymes (Table 1). After 1 h of incubation, TrMan5A had the highest DA followed by TrMan5A-R171K and AnMan5C (Table 1). Again AnMan5C showed a drop in DA (> 10-fold) over 4 h of incubation, while TrMan5A and TrMan5A-R171K had almost stable DA values. On the basis of having the highest initial DA with 1-hexanol among the assayed enzymes, TrMan5A was chosen for further studies of alcoholysis with 1-hexanol.

Next, in order to optimize reaction conditions, the effect of varying TrMan5A concentrations on DA was studied, using 5 mM M_4 and 25% (v/v) 1-hexanol. Here, a lower enzyme concentration (0.2 μM) resulted in a higher DA compared to higher enzyme loads after 1 h (Fig. 3) where significant amounts of M_4 remained. The DA increased up to 1 h with 0.2 μM TrMan5A with a slight increase in DA over time during the course of the reaction, and the highest DA was observed after 4 h of incubation (Fig. 3). A slight decrease in DA was observed with the highest TrMan5A concentration (4 μM) with increased incubation time, which could potentially be a result of secondary hydrolysis (Fig. 3). TrMan5A at a concentration of 0.2 μM resulted in the highest DA after 1 h and a stable DA with increasing incubation time, and this TrMan5A concentration was therefore used in subsequent reactions.
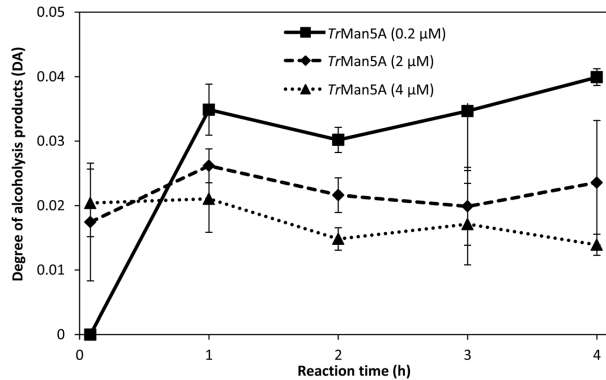
Further optimization of reaction conditions was performed by varying the concentration of the donor substrate, M_4. HPAEC-PAD quantification of the apparent rate of M_4 degradation was used in combination with DA values calculated from MALDI-TOF MS peak areas (Eq. (1)) in order to

🖄 Springer

203

Fig. 3 Degree of alcoholysis products (DA) over 0–4 h of incubations with 5 mM M_4, 25% (v/v) 1-hexanol, and 0.2, 2, or 4 μM TrMan5A. Error bars represent deviations between duplicate samples

estimate hexyl mannooligoside product yields with 5, 25, or 50 mM M_4. The use of 5 mM M_4 resulted in substrate depletion after 1 h, whereas the reaction continued with the higher concentrations. After 4 h of incubation, the reactions with 5 and 25 mM M_4 had similar DA values, but a higher rate of M_4 conversion was observed with 25 mM M_4 (Table 2). This suggests a higher hexyl mannooligoside yield with 25 mM M_4. The DA was lower with 50 mM M_4, possibly as a result of increased transglycosylation with saccharides as acceptors as indicated by higher MALDI-TOF MS detection of oligosaccharides with DP 5–9. After 4 h of incubation, saccharides with DP > 4 represented 1.4, 8.6, and 15% of total product peak area with 5, 25, and 50 mM M_4, respectively. Also, with 25 and 50 mM M_4, substantial amounts of M_4 remained after 4 h, indicating the possibility of higher hexyl mannooligoside production if the reaction would be prolonged. Therefore, an extended reaction time of 8 h with 25 mM M_4 was analyzed, and the reaction followed the same profile as the 4-h reaction, while the DA increased further as M_4 was fully consumed (Table 2). Based on these results, an M_4 concentration of 25 mM and a reaction time of up to 8 h were selected for

reaction scale-up as well as HPLC separation and quantification of hexyl mannooligosides (see the next section).

Purification and quantification of hexyl mannooligosides

Reversed-phase (C_{18}) HPLC with hexyl β-D-maltoside as standard was used to analyze reaction mixtures with 0.2 μM TrMan5A, 25 mM M_4, and 25% (v/v) 1-hexanol to more accurately separate and quantify hexyl mannooligosides produced by alcoholysis with TrMan5A. Analytical separation of hexyl-M_2 and hexyl-M_3 was obtained with HPLC as confirmed with MALDI-TOF MS peak mass identification (m/z values of 449.14 and 611.18 for hexyl-M_2 and hexyl-M_3, respectively) (Fig. 4). Retaining β-mannanases are unequivocally expected to yield transglycosylation products (in this case, hexyl mannooligosides) with the same β-anomeric configuration as the donor substrate (Harjunpää et al. 1995; Sinnott 1990). Thus, the expected β-configured structures of the synthesized hexyl-M_2 and hexyl-M_3 are shown in Fig. 5. When the M_4 was fully consumed after 8 h of incubation (DA

Table 2 Rates of mannotetraose (M_4) consumption and degree of alcoholysis products (DA) (average ± deviation between duplicate samples) at 1 and 4 h for alcoholysis reactions with 0.2 μM TrMan5A,

25% (v/v) 1-hexanol, and 5, 25, or 50 mM M_4. The lack of rate at 4 h with 5 mM M_4 is due to the M_4 being consumed after 1 h

| [M_4] (mM)	M_4 rate at 1 h (μM/min)	M_4 rate at 4 h (μM/min)	DA at 1 h	DA at 4 h	DA at 8 h
5	95 ± 4.7	–[a]	0.051 ± 0.016	0.043 ± 0.010	–[b]
25	123 ± 5.2	66 ± 10	0.022 ± 0.005	0.040 ± 0.002	0.059 ± 0.009
50	120 ± 84	60 ± 44	–[c]	0.021 ± 0.006	–[b]

Twenty-five millimolars of M_4 was selected for prolonged (8-h) reaction (rightmost column)

[a] M_4 consumed

[b] Reaction not carried out

[c] No hexyl mannosides detected

Fig. 4 Chromatogram showing separation of hexyl mannooligosides with reversed-phase HPLC using a C_{18} column. The two inserts show MALDI-TOF MS spectra with peak mass identifications corresponding to monoisotopic sodium adduct masses of hexyl-M_3 (theoretical mass 611.25) and hexyl-M_2 (theoretical mass 449.20)
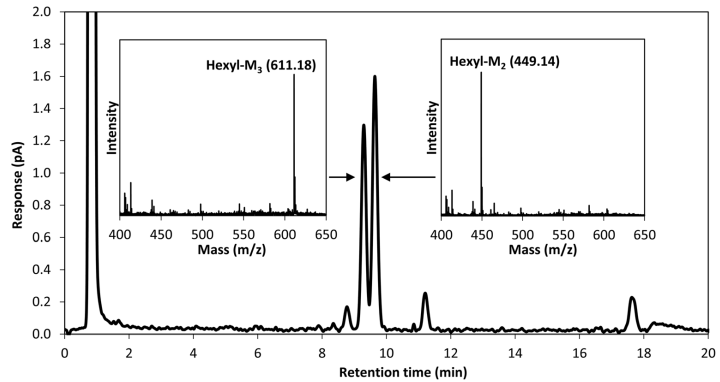
value 0.059, Table 2), the concentration of the dominant alcoholysis product (hexyl-M_2) was 0.48 mM, corresponding to a yield of 1.9% based on the initial M_4 concentration.

Based on the M_2 and hexyl-M_2 concentrations after 2 h of incubation (8.1 and 0.13 mM, respectively), the r_A/r_H was calculated according to Eq. (2), reflecting the competition between alcohol and water in attacking the covalent intermediate. Under these conditions (i.e., 0.2 μM *Tr*Man5A and 25 mM M_4), the r_A/r_H of *Tr*Man5A with 1-hexanol (25% (v/v)) was 0.033, corresponding to a theoretical alcoholysis product yield of 3.2% (Eq. (3)). Since the experimentally determined yield was 1.9%, the difference could possibly be the result of secondary hydrolysis (van Rantwijk et al. 1999). Although DA remained stable during prolonged incubations at lower M_4 concentrations (Fig. 3), it is possible that secondary hydrolysis might become more prominent at higher M_4 concentrations, assuming that hexyl mannooligosides would then be produced in higher amounts. With the assumption that the reaction occurs in the water phase (1-hexanol concentration 5.9 g/L or 58 mM), the enzyme's S_c for 1-hexanol was calculated (Eq. (4)). S_c describes the relative preference of an enzyme for an acceptor over water on an equimolar basis. In this case, S_c was calculated to be 31, indicating a strong preference of the *Tr*Man5A-catalyzed reaction for 1-hexanol over water at the reaction conditions used. This is higher than S_c values for 1-hexanol in the range of 0.5–9 which have been observed with some other GHs (Adlercreutz 2017; Hansson and Adlercreutz 2001; Lundemo et al. 2017), but slightly lower than the S_c of 58 for 1-hexanol observed with the *Thermotoga neapolitana* β-glucosidase Bgl3B (Turner et al. 2007).

Preparative synthesis and purification

In order to produce sufficient amounts of the identified hexyl mannooligosides for characterization, the reaction was scaled up. Here, a polymeric substrate, the linear INM polysaccharide, was used to obtain the donor saccharides. INM was pre-hydrolyzed into soluble mannooligosaccharides by *Pa*Man26A (Couturier et al. 2013), with M_4 being the main oligosaccharide produced as analyzed with HPAEC-PAD (Table S1). Using this as donor substrate for alcoholysis with 1-hexanol, *Tr*Man5A produced 0.16 mM hexyl-M_2 and 0.094 mM hexyl-M_3 in an 8-h reaction. Here, the yield of the major alcoholysis product, hexyl-M_2, was 0.6% based on initial M_4 concentration. With preparative reversed-phase (C_{18}) HPLC purification, a mixture consisting of 1.3 mg hexyl-M_2 and 1.1 mg hexyl-M_3 was obtained as a lyophilized powder.

Structural characterization of hexyl mannooligosides

After having synthesized and purified a mixture of hexyl-M_2 and hexyl-M_3, their structures were characterized. First, they were analyzed with MALDI-TOF MS, and peaks corresponding to the masses of hexyl-M_2 and hexyl-M_3 were fragmented with MALDI-TOF/TOF tandem MS. The observed fragmentation masses were consistent with those expected from the predicted structures (Fig. 5). Hexyl-M_2 fragmented into M_2 (−H_2O) and hexyl-M_1, while hexyl-M_3 also fragmented into M_3
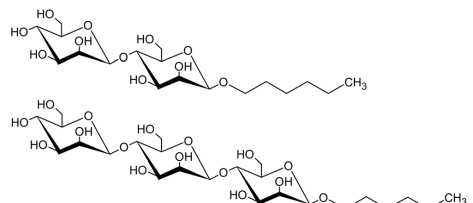

Fig. 5 The predicted structure of hexyl β-D-mannobioside (top) and hexyl β-D-mannotrioside (bottom)

(–H₂O) and hexyl-M$_2$ in addition to the above two fragments (Fig. S3).

To obtain more detailed structural information, the hexyl mannooligoside mixture was analyzed with NMR. In ^{1}H spectra collected at 10 °C, chemical shifts corresponding to anomeric protons (H-1) of three mannosyl units were observed at 4.67, 4.72, and 4.75 ppm and C-2 protons (H-2) at 4.0–4.2 ppm (Fig. 6). The chemical shifts at 4.72 and 4.75 ppm are in good agreement with H-1 shifts in terminal and internal β-mannosyl units reported for β-mannooligosaccharides previously (Harjunpää et al. 1995). Furthermore, with edited HSQC, the protons on the carbon of the hexyl –CH$_2$ group adjacent to an oxygen atom can also be identified (Fig. S4). The carbon on this –CH$_2$ group was observed to be coupled to the anomeric proton at 4.67 ppm in HMBC spectra, thus confirming bonding of the hexyl to that anomeric position (Fig. S4). No other chemical shift of anomeric protons showed such a correlation, and our conclusion is that both mannobiosides and mannotriosides in the sample have their anomeric proton chemical shift at 4.67 ppm.

Additionally, with ^{1}H NMR at 25 °C, a coupling constant between H-1 and H-2 ($J_{1,2}$) of 0.8 Hz was observed based on H-2 peak splitting on the hexyl-substituted mannosyl units (Fig. S5), which is consistent with previously reported $J_{1,2}$ values of ~ 1 Hz for β-mannosyl H-1s (Harjunpää et al. 1995; Lundqvist et al. 2002). We also observed a coupling constant between H-2 and H-3 ($J_{2,3}$) of 3.1 Hz (Fig. S5).

Since internal β-mannosyl units coupled to an adjacent mannosyl are only present in hexyl-M$_3$, whereas terminal β-mannosyl units exist in both hexyl-M$_2$ and hexyl-M$_3$, the peak integral ratio of internal H-1 at 4.75 ppm to that of terminal H-1 at 4.72 ppm gives the fraction of hexyl mannooligosides that are hexyl-M$_3$. In the ^{1}H NMR spectrum (Fig. 6), the ratio is 38:86. From this ratio, the amounts of hexyl-M$_2$ and hexyl-M$_3$ were determined to be 0.43 and 0.47 mg,

respectively, using hexyl CH$_2$ quantification based on reference samples of hexyl-β-D-maltoside. The same sample was also quantified with HPLC using hexyl-β-D-maltoside as standard, with the amounts of hexyl-M$_2$ and hexyl-M$_3$ determined to be 0.57 and 0.48 mg, respectively.

Determination of critical micelle concentration

To evaluate the surfactant properties of the purified hexyl mannooligosides, the critical micelle concentration (CMC) of the hexyl mannooligoside mixture was determined by means of surface tension measurements at different surfactant concentrations. The CMC was estimated from the breakpoint in the surface tension versus surfactant concentration curve (Dominguez et al. 1997). The hexyl mannooligoside surface tension curve indicates two breakpoints around 44 g/L (90 mM) and 72 g/L (147 mM) (Fig. 7), suggesting that the CMCs for the individual hexyl mannooligosides (hexyl-M$_2$ and hexyl-M$_3$) are in this region. For reference, surface tension measurements were also conducted with hexyl-β-D-glucoside and hexyl-β-D-maltoside individually and in mixtures with a molar ratio of 0.53:1. The results with two breakpoints at 26 g/L (82 mM) and 62 g/L (194 mM) in the surface tension curve of the reference mixture show the same trend as for the hexyl mannooligoside mixture (Fig. S6). The two breakpoints correspond to the CMCs of hexyl-β-D-glucoside (29 g/L or 110 mM) and hexyl-β-D-maltoside (59 g/L or 137 mM) determined separately (Fig. S6).

Discussion

The study and application of β-mannanases is of fundamental importance for the utilization and valorization of plant biomass due to the high amounts of β-mannan in prevalent

Fig. 6 ^{1}H NMR spectrum of the synthesized hexyl mannooligosides. Peaks corresponding to anomeric protons (H-1) and C-2 protons (H-2) as well as protons on the β, γ, δ, ε, and ζ carbons of the hexyl chain (H-β, H-(γ,δ,ε), and H-ζ) are indicated within brackets. Integral values for different peaks relative to the H-β peak are shown beneath the x-axis. The insert shows an enlargement of the region of the spectrum containing the three H-1 shifts as indicated with the dashed lines
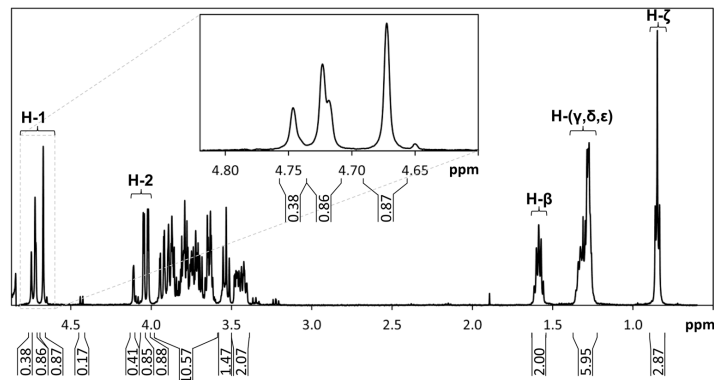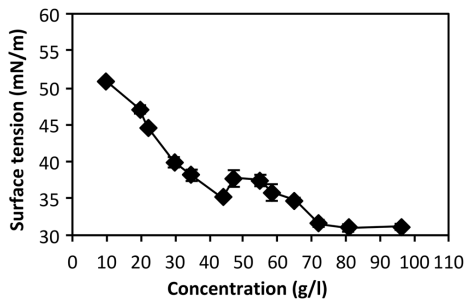
Fig. 7 Surface tension plot of the purified hexyl mannooligoside mixture as determined with drop shape tensiometry, showing two breakpoints around 44 g/L (90 mM) and 72 g/L (147 mM). All data points are averages of at least two measurements. Error bars indicate standard deviations

softwoods such as spruce (Lundqvist et al. 2002; Moreira and Filho 2008; Yamabhai et al. 2016). The present study describes the first reported instance of β-mannanase-catalyzed synthesis of alkyl mannosides with surfactant properties and opens up the possibility of using renewable β-mannans for enzymatic synthesis of surfactants. 1-Hexanol was used as acceptor, and polymeric β-mannan was used to prepare donor saccharides (mainly M_4). Previous studies have demonstrated the alcholytic capabilities of β-mannanases with shorter-chain primary alcohols such as methanol and 1-butanol (Rosengren et al. 2012; Rosengren et al. 2014). Transfer with 1-hexanol as acceptor has been demonstrated with other GHs such as β-mannosidases (Itoh and Kamiyama 1995), xylanases (Jiang et al. 2004), and β-glucosidases (Lundemo et al. 2013; Lundemo et al. 2014; Lundemo et al. 2017; Turner et al. 2007).

In the current study, relative MALDI-TOF MS peak areas of alcoholysis products and oligosaccharide products were used to estimate DA, reflecting the fraction of alcoholysis products formed in a reaction as explained in the "Materials and methods" section. MALDI-TOF MS is a good screening method for relative comparisons of enzymes and reaction conditions, although additional methods are needed for absolute quantification and the response cannot be expected to be the same for different types of molecules due to potential ion suppression in MALDI-TOF MS (Duncan et al. 2008). Often thin-layer chromatography is used to make an initial assessment of transglycosylation products (see, e.g., Jain et al. 2014). In the present paper, we show that MALDI-TOF MS analysis is an attractive alternative or a complementary screening method, which is at least as fast and gives additional information on the mass of products and thus more certain primary product identification.

In this study, the initial DA with 1-hexanol was significantly lower than with methanol for all three enzymes included in

the present study, indicating that 1-hexanol is more difficult to use as acceptor in alcoholysis compared to methanol. Several other studies have demonstrated decreasing yields of alkyl glycosides with increasing alkyl chain lengths, a contributing factor being the low water solubility of longer-chain alcohols (Ochs et al. 2011; Turner et al. 2007). The accessibility and properties of the positive subsite region are another factor that may influence transglycosylation reactions using acceptors with longer alkyl chains (Durand et al. 2016; Ochs et al. 2013).

Enzyme comparison revealed differences in alcoholysis capacity between the studied enzymes. With 1-hexanol, TrMan5A had the highest DA of the three β-mannanases (Table 1). Acceptor affinity in positive subsites is known to affect transglycosylation capacity (Rosengren et al. 2012; Rosengren et al. 2014; Tran et al. 2014). The R171K substitution in the + 2 subsite of TrMan5A has previously been shown to eliminate transglycosylation with saccharides as acceptors but not alcoholysis with methanol (Rosengren et al. 2012). Therefore, it might be expected that the competing reaction (with saccharides as acceptors) could be diminished. It is interesting to note that a lower DA using 1-hexanol as acceptor was observed with TrMan5A-R171K compared to TrMan5A (Table 1). However, further investigation would be needed to elucidate if R171 would have any role in the usage of 1-hexanol as acceptor. The + 1 subsite of AnMan5C contains a tryptophan, W283, that appears to facilitate transglycosylation with saccharides as acceptors (Dilokpimol et al. 2011), but here, a positive contribution to the usage of 1-hexanol as acceptor is unlikely since the DA was clearly lowest among the tested enzymes. Based on the comparably high DA for the wild-type TrMan5A (Table 1) and its stability during prolonged incubations (Fig. 3), this enzyme was selected for further studies of hexyl mannooligoside synthesis.

Varying reaction conditions can also affect alcoholysis product yields. In alcoholysis with 1-hexanol and TrMan5A, a lower enzyme concentration resulted in a moderate increase in DA (Fig. 3). Enzyme concentration has previously been shown to affect the observed ratio of hydrolysis products versus transglycosylation products, with a lower enzyme load favoring transglycosylation products (Guo et al. 2016; Manas et al. 2014), possibly due to increased secondary product hydrolysis at higher enzyme loads. The slight decrease in DA over time observed with the highest TrMan5A concentration used could possibly be the result of secondary hydrolysis of hexyl mannooligosides (Fig. 3). The concentration of the donor substrate (M_4 in this case) also affected alcoholysis, where a similar DA but a higher rate of M_4 conversion was observed with 25 mM M_4 compared to 5 mM (Table 2). Twenty-five millimolars of M_4 was therefore used in subsequent reactions. However, increasing the M_4 concentration too much appears to reduce alcoholysis, since a lower DA was observed with 50 mM M_4. Since oligosaccharides with

DP 5–9 were detected in the 50-mM reaction, this can possibly be due to transglycosylation with saccharides as acceptors competing with alcoholysis at higher M_4 concentrations, similar to the observed effect of transglycosylation on hydrolysis in, e.g., β-glucosidases (Bohlin et al. 2013). Higher substrate concentrations, in general, are expected to increase transglycosylation (Sinnott 1990) as exemplified with, e.g., a retaining GH5 β-mannosidase (Dias et al. 2004). The R171K substitution in the + 2 subsite of TrMan5A (Rosengren et al. 2012) may still be valuable at higher donor saccharide concentrations where oligosaccharide elongation would be more effective (Biely et al. 1981; Sinnott 1990), in line with products of DP 5–9 being detected with 50 mM M_4 for TrMan5A.

In the scaled-up reaction, a polymeric β-mannan (INM) was pre-hydrolyzed into mainly M_4 by PaMan26A (Couturier et al. 2013) and then used as donor substrate. Using polymeric substrates for enzymatic synthesis represents a step towards β-mannan utilization in biorefineries (Cherubini 2010). The lower yield of alcoholysis products observed with the pre-hydrolyzed INM compared to reactions with M_4 could be partially due to the presence of lower amounts of other oligosaccharides (M_2 and M_3) in the hydrolysate (Table S1), which might act as acceptors for transglycosylation and thereby possibly compete with alcoholysis as described above (Bohlin et al. 2013).

We successfully managed to purify (Fig. 4) and characterize the synthesized hexyl mannooligosides. The expected structures, hexyl β-mannobioside and hexyl β-mannotrioside (Fig. 5), are supported by the MALDI-TOF MS/MS (Fig. S3) and NMR data (Fig. 6, Fig. S4-S5). The surfactant properties of the purified hexyl mannooligosides were also determined by tensiometry. Two breakpoints in the surface tension versus concentration curve were observed (Fig. 7), which suggests that the solution is a mixture of two different types of surfactants with different surface activities, in line with the concluded chemical composition. This phenomenon has previously been observed for mixtures of alkyl polyglucosides with different alkyl chain lengths (Balzer and Luders 2000). Reference experiments with hexyl-β-D-glucoside and hexyl-β-D-maltoside, with the same alkyl chain length but different polar head groups, support this observation (Fig. S6). The existence of a minimum around the first breakpoint is consistent with the solubilization of the more hydrophobic (or surface-active) surfactant in the micelles when the total surfactant concentration increases (Lin et al. 1999).

In conclusion, β-mannanase-catalyzed synthesis of hexyl mannooligosides with surfactant properties has been demonstrated for the first time, using the Trichoderma reesei GH5 β-mannanase TrMan5A. Hexyl mannooligosides were synthesized from β-mannan and 1-hexanol and purified using preparative HPLC. Their surfactant properties were evaluated, showing similar CMC values compared to commercially available alternatives. Future studies could involve protein engineering which is a strategy with potential to increase

transglycosylation rate and/or yield (Lundemo et al. 2013; Lundemo et al. 2017). In some cases, subsite − 1 residues have been substituted, shown to be an applicable route when using activated (nitrophenyl) donor sugars and exo-glycosidases (Bissaro et al. 2014; Teze et al. 2015; Teze et al. 2014). When using natural non-activated donor sugars, as in the present study, another approach would potentially be needed. For β-mannanases (Dilokpimol et al. 2011; Rosengren et al. 2012) and other GHs (Armand et al. 2001; Feng et al. 2005), positive subsites have been shown to be important for acceptor interactions and thus influence transglycosylation capacity. Assuming that acceptor interaction is important also for longer-chain alcohols, the properties of these alcohols would imply that introduction of hydrophobic residues within positive subsites could be beneficial for efficient transglycosylation (Durand et al. 2016). Hydrophobic residues may also, in certain cases, reduce water accessibility and lower hydrolysis (Kuriki et al. 1996). Future work with β-mannanases and long-chain acceptors could involve identification of further positive subsite residues as targets for protein engineering.

Compliance with ethical standards

Ethical statement This article does not contain any studies with human participants or animals performed by any of the authors.

**Conflict of interest** The authors declare that they have no conflict of interest.

References

Adlercreutz P (2017) Comparison of lipases and glycoside hydrolases as catalysts in synthesis reactions. Appl Microbiol Biotechnol 101: 513–519

Akiba S, Yamamoto K, Kumagai H (1999) Transglycosylation activity of the endo-β-1,4-glucanase from Aspergillus niger IFO31125 and its application. J Biosci Bioeng 87(5):576–580

Arcand N, Kluepfel D, Paradis FW, Morosoli R, Shareck F (1993) β-Mannanase of Streptomyces lividans 66: cloning and DNA sequence

of the *manA* gene and characterization of the enzyme. Biochem J 290:857–863

Armand S, Andrews SR, Charnock SJ, Gilbert HJ (2001) Influence of the aglycone region of the substrate binding cleft of *Pseudomonas* xylanase 10A on catalysis. Biochemistry 40:7404–7409

Aspeborg H, Coutinho P, Wang Y, Brumer H, Henrissat B (2012) Evolution, substrate specificity and subfamily classification of glycoside hydrolase family 5 (GH5). BMC Evol Biol 12(1):186

Balzer D, Luders H (2000) Nonionic surfactants: alkyl polyglucosides. CRC

Bauer S, Vasu P, Persson S, Mort AJ, Somerville CR (2006) Development and application of a suite of polysaccharide-degrading enzymes for analyzing plant cell walls. Proc Natl Acad Sci U S A 103(30): 11417–11422

Berry JD, Neeson MJ, Dagastine RR, Chan DYC, Tabor RF (2015) Measurement of surface and interfacial tension using pendant drop tensiometry. J Colloid Interface Sci 454:226–237

Biely P, Vršanská M, Krátký Z (1981) Mechanisms of substrate digestion by endo-1,4-β-xylanase of *Cryptococcus albidus*. Lysozyme-type pattern of action. Eur J Biochem 119:565–571

Bissaro B, Saurel O, Arab-Jaziri F, Saulnier L, Milon A, Tenkanen M, Monsan P, O'Donohue M, Fauré R (2014) Mutation of a pH-modulating residue in a GH51 α-L-arabinofuranosidase leads to a severe reduction of the secondary hydrolysis of transfuranosylation products. Biochim Biophys Acta 1840:626–636

Bohlin C, Praestgaard E, Baumann MJ, Borch K, Praestgaard K, Monrad RN, Westh P (2013) A comparative study of hydrolysis and transglycosylation activities of fungal β-glucosidases. Appl Microbiol Biotechnol 97:159–169

Cherubini F (2010) The biorefinery concept: using biomass instead of oil for producing energy and chemicals. Energy Convers Manag 51(7): 1412–1421

Coulombel C, Clermont S, Foglietti MJ, Percheron F (1981) Transglycosylation reactions catalysed by two β-mannanases. Biochem J 195:333–335

Couturier M, Roussel A, Rosengren A, Leone P, Stålbrand H, Berrin JG (2013) Structural and biochemical analyses of glycoside hydrolase families 5 and 26 β-(1,4)-mannanases from *Podospora anserina* reveal differences upon manno-oligosaccharide catalysis. J Biol Chem 288(20):14624–14635

Damián-Almazo JY, Moreno A, López-Munguía A, Soberón X, González-Muñoz F, Saab-Rincón G (2008) Enhancement of the alcoholytic activity of α-amylase AmyA from *Thermotoga maritima* MSB8 (DSM 3109) by site-directed mutagenesis. Appl Environ Microbiol 74(16):5168–5177

Davies G, Henrissat B (1995) Structures and mechanisms of glycosyl hydrolases. Structure 3(9):853–859

Davies GJ, Sinnott ML (2008) Sorting the diverse: the sequence-based classifications of carbohydrate-active enzymes. Biochemist 30:26–32

Davies GJ, Wilson KS, Henrissat B (1997) Nomenclature for sugar-binding subsites in glycosyl hydrolases. Biochem J 321:557–559

Dias FMV, Vincent F, Pell G, Prates JAM, Centeno MSJ, Tailford LE, Ferreira LMA, Fontes CMGA, Davies GJ, Gilbert HJ (2004) Insights into the molecular determinants of substrate specificity in glycoside hydrolase family 5 revealed by the crystal structure and kinetics of *Cellvibrio mixtus* mannosidase 5A. J Biol Chem 279: 25517–25526

Dilokpimol A, Nakai H, Gotfredsen CH, Baumann MJ, Nakai N, Abou Hachem M, Svensson B (2011) Recombinant production and characterisation of two related GH5 endo-β-1,4-mannanases from *Aspergillus nidulans* FGSC A4 showing distinctly different transglycosylation capacity. Biochim Biophys Acta 1814(12): 1720–1729

Dominguez A, Fernandez A, Gonzalez N, Iglesias E, Montenegro L (1997) Determination of critical micelle concentration of some surfactants by three techniques. J Chem Educ 74:1227–1231

Duncan MW, Roder H, Hunsucker SW (2008) Quantitative matrix-assisted laser desorption/ionization mass spectrometry. Brief Funct Genomic Proteomic 7:355–370

Durand J, Biarnés X, Watterlot L, Bonzom C, Borsenberger V, Planas A, Bozonnet S, O'Donohue M, Fauré R (2016) A single point mutation alters the transglycosylation/hydrolysis partition, significantly enhancing the synthetic capability of an *endo*-glycoceramidase. ACS Catal 6:8264–8275

Ebringerová A (2006) Structural diversity and application potential of hemicelluloses. Macromol Symp 232:1–12

Feng HY, Drone J, Hoffmann L, Tran V, Tellier C, Rabiller C, Dion M (2005) Converting a β-glycosidase into a β-transglycosidase by directed evolution. J Biol Chem 280:37088–37097

Gilbert HJ, Stålbrand H, Brumer H (2008) How the walls come crumbling down: recent structural biochemistry of plant polysaccharide degradation. Curr Opin Plant Biol 11:338–348

Gridley JJ, Osborn HMI (2000) Recent advances in the construction of β-D-mannose and β-D-mannosamine linkages. J Chem Soc Perkin Trans 1:1471–1491

Guo D, Xu Y, Kang Y, Han S, Zheng S (2016) Synthesis of octyl-β-D-glucopyranoside catalyzed by Thai rosewood β-glucosidase-displaying *Pichia pastoris* in an aqueous/organic two-phase system. Enzym Microb Technol 85:90–97

Hägglund P, Eriksson T, Collén A, Nerinckx W, Claeyssens M, Stålbrand H (2003) A cellulose-binding module of the *Trichoderma reesei* β-mannanase Man5A increases the mannan-hydrolysis of complex substrates. J Biotechnol 101(1):37–48

Hakamada Y, Ohkubo Y, Ohashi S (2014) Purification and characterization of β-mannanase from *Reinekea* sp. KIT-YO10 with transglycosylation activity. Biosci Biotechnol Biochem 78:722–728

Hansson T, Adlercreutz P (2001) Enhanced transglucosylation/hydrolysis ratio of mutants of *Pyrococcus furiosus* β-glucosidase: effects of donor concentration, water content, and temperature on activity and selectivity in hexanol. Biotechnol Bioeng 75(6):656–665. https://doi.org/10.1002/bit.10043

Harjunpää V, Teleman A, Siika-Aho M, Drakenberg T (1995) Kinetic and stereochemical studies of manno-oligosaccharide hydrolysis catalysed by β-mannanases from *Trichoderma reesei*. Eur J Biochem 234(1):278–283

Harjunpää V, Helin J, Koivula A, Siika-aho M, Drakenberg T (1999) A comparative study of two retaining enzymes of *Trichoderma reesei*: transglycosylation of oligosaccharides catalysed by the cellobiohydrolase I, Cel7A, and the β-mannanase, Man5A. FEBS Lett 443(2):149–153

Hekmat O, Lo Leggio L, Rosengren A, Kamarauskaite J, Kolenova K, Stålbrand H (2010) Rational engineering of mannosyl binding in the distal glycone subsites of *Cellulomonas fimi* endo-β-1,4-mannanase: mannosyl binding promoted at subsite −2 and demoted at subsite −3. Biochemistry 49(23):4884–4896

Henrissat B, Bairoch A (1996) Updating the sequence-based classification of glycosyl hydrolases. Biochem J 316:695–696

Hrmova M, Burton RA, Biely P, Lahnstein J, Fincher GB (2006) Hydrolysis of (1,4)-β-D-mannans in barley (*Hordeum vulgare* L.) is mediated by the concerted action of (1,4)-β-D-mannan endohydrolase and β-D-mannosidase. Biochem J 1399:77–90

Itoh H, Kamiyama Y (1995) Synthesis of alkyl β-mannosides from mannobiose by *Aspergillus niger* β-mannosidase. J Ferment Bioeng 80(5):510–512

Jain I, Kumar V, Satyanarayana T (2014) Applicability of recombinant β-xylosidase from the extremely thermophilic bacterium *Geobacillus thermodenitrificans* in synthesizing alkylxylosides. Bioresour Technol 170:462–469

Javadi A, Mucic N, Karbaschi M, Won JY, Lotfi M, Dan A, Ulaganathan V, Gochev G, Makievski AV, Kovalchuk VI, Kovalchuk NM, Krägel J, Miller R (2013) Characterization methods for liquid interfacial layers. Eur Phys J Spec Top 222:7–29

Jiang Z, Zhu Y, Li L, Yu X, Kusakabe I, Kitaoka M, Hayashi K (2004) Transglycosylation reaction of xylanase B from the hyperthermophilic Thermotoga maritima with the ability of synthesis of tertiary alkyl β-D-xylobiosides and xylosides. J Biotechnol 114(1–2):125–134

Kuriki T, Kaneko H, Yanase M, Takata H, Shimada J, Handa S, Takada T, Umeyama H, Okada S (1996) Controlling substrate preference and transglycosylation activity of neopullulanase by manipulating steric constraint and hydrophobicity in active center. J Biol Chem 271(29):17321–17329

Larsson J, Svensson D, Adlercreutz P (2005) α-Amylase-catalysed synthesis of alkyl glycosides. J Mol Catal B Enzym 37(1–6):84–87

Larsson AM, Anderson L, Xu B, Muñoz IG, Usón I, Janson JC, Stålbrand H, Ståhlberg J (2006) Three-dimensional crystal structure and enzymic characterization of β-mannanase Man5A from blue mussel Mytilus edulis. J Mol Biol 357:1500–1510

Lin SY, Lin YY, Chen EM, Hsu CT, Kwan CC (1999) A study of the equilibrium surface tension and the critical micelle concentration of mixed surfactant solutions. Langmuir 15:4370–4376

Lombard V, Golaconda Ramulu H, Drula E, Coutinho PM, Henrissat B (2014) The carbohydrate-active enzymes database (CAZy) in 2013. Nucleic Acids Res 42:D490–D495

Lundemo P, Adlercreutz P, Karlsson EN (2013) Improved transferase/hydrolase ratio through rational design of a family 1 β-glucosidase from Thermotoga neapolitana. Appl Environ Microbiol 79(11):3400–3405

Lundemo P, Nordberg Karlsson E, Adlercreutz P (2014) Preparation of two glycoside hydrolases for use in micro-aqueous media. J Mol Catal B Enzym 108:1–6

Lundemo P, Nordberg Karlsson E, Adlercreutz P (2017) Eliminating hydrolytic activity without affecting the transglycosylation of a GH1 β-glucosidase. Appl Microbiol Biotechnol 101:1121–1131

Lundqvist J, Teleman A, Junel L, Zacchi G, Dahlman O, Tjerneld F, Stålbrand H (2002) Isolation and characterization of galactoglucomannan from spruce (Picea abies). Carbohydr Polym 48:29–39

Lundqvist J, Jacobs A, Palm M, Zacchi G, Dahlman O, Stålbrand H (2003) Characterization of galactoglucomannan extracted from spruce (Picea abies) by heat-fractionation at different conditions. Carbohydr Polym 51(2):203–211

Manas NHA, Pachelles S, Mahadi NM, Illias RM (2014) The characterisation of an alkali-stable maltogenic amylase from Bacillus lehensis G1 and improved malto-oligosaccharide production by hydrolysis suppression. PLoS One 9:e106481

Matsumura S, Kinta Y, Sakiyama K, Toshima K (1996) Enzymatic synthesis of alkyl xylobioside and xyloside from xylan and alcohol. Biotechnol Lett 18(11):1335–1340

Matsumura S, Sakiyama K, Toshima K (1997) One-pot synthesis of alkyl β-D-xylobioside from xylan and alcohol by acetone powder of Aureobasidium pullulans. Biotechnol Lett 19(12):1249–1253

Matsumura S, Sakiyama K, Toshima K (1999) Preparation of octyl β-D-xylobioside and xyloside by xylanase-catalyzed direct transglycosylation reaction of xylan and octanol. Biotechnol Lett 21(1):17–22

Mizutani K, Fernandes VO, Karita S, Luís AS, Sakka M, Kimura T, Jackson A, Zhang X, Fontes CM, Gilbert HJ, Sakka K (2012) Influence of a mannan binding family 32 carbohydrate binding module on the activity of the appended mannanase. Appl Environ Microbiol 78:4781–4787

Moreira LRS, Filho EXF (2008) An overview of mannan structure and mannan-degrading enzyme systems. Appl Microbiol Biotechnol 79(2):165–178

Moreno A, Damian-Almazo JY, Miranda A, Saab-Rincon G, Gonzalez F, Lopez-Munguia A (2010) Transglycosylation reactions of Thermotoga maritima α-amylase. Enzym Microb Technol 46(5):331–337

Morrill J, Kulcinskaja E, Sulewska AM, Lahtinen S, Stålbrand H, Svensson B, Abou Hachem M (2015) The GH5 1,4-β-mannanase from Bifidobacterium animalis subsp. lactis Bl-04 possesses a low-affinity mannan-binding module and highlights the diversity of mannanolytic enzymes. BMC Biochem 16:26

Ochs M, Muzard M, Plantier-Royon R, Estrine B, Remond C (2011) Enzymatic synthesis of alkyl β-D-xylosides and oligoxylosides from xylans and from hydrothermally pretreated wheat bran. Green Chem 13(9):2380–2388

Ochs M, Belloy N, Dauchez M, Muzard M, Plantier-Royon R, Rémond C (2013) Role of hydrophobic residues in the aglycone binding subsite of a GH39 β-xylosidase in alkyl xylosides synthesis. J Mol Catal B Enzym 96:21–26

Papanikolaou S (2001) Enzyme-catalyzed synthesis of alkyl-β-glucosides in a water–alcohol two-phase system. Bioresour Technol 77(2):157–161

Puchart V, Vrsanská M, Svoboda P, Pohl J, Ogel ZB, Biely P (2004) Purification and characterization of two forms of endo-β-1,4-mannanase from a thermotolerant fungus, Aspergillus fumigatus IMI 385708 (formerly Thermomyces lanuginosus IMI 158749). Biochim Biophys Acta 1674:239–250

Rosengren A, Hägglund P, Anderson L, Pavon-Orozco P, Peterson-Wulff R, Nerinckx W, Stålbrand H (2012) The role of subsite +2 of the Trichoderma reesei β-mannanase TrMan5A in hydrolysis and transglycosylation. Biocatal Biotransform 30(3):338–352

Rosengren A, Reddy SK, Sjöberg JS, Aurelius O, Logan D, Kolenová K, Stålbrand H (2014) An Aspergillus nidulans β-mannanase with high transglycosylation capacity revealed through comparative studies within glycosidase family 5. Appl Microbiol Biotechnol 98(24):10091–10104

Sabini E, Schubert H, Murshudov G, Wilson KS, Siika-Aho M, Penttila M (2000) The three-dimensional structure of a Trichoderma reesei β-mannanase from glycoside hydrolase family 5. Acta Crystallogr D Biol Crystallogr 56(1):3–13. https://doi.org/10.1107/S0907444999013943

Scheller HV, Ulvskov P (2010) Hemicelluloses. Annu Rev Plant Biol 61(1):263–289

Schröder R, Wegrzyn TF, Sharma NN, Atkinson RG (2006) LeMAN4 endo-β-mannanase from ripe tomato fruit can act as a mannan transglycosylase or hydrolase. Planta 224:1091–1102

Sinnott ML (1990) Catalytic mechanism of enzymic glycosyl transfer. Chem Rev 90(7):1171–1202

Stålbrand H, Siika-aho M, Tenkanen M, Viikari L (1993) Purification and characterization of two β-mannanases from Trichoderma reesei. J Biotechnol 29(3):229–242

Teze D, Hendrickx J, Czjzek M, Ropartz D, Sanejouand YH, Tran V, Tellier C, Dion M (2014) Semi-rational approach for converting a GH1 β-glycosidase into a β-transglycosidase. Protein Eng Des Sel 27:13–19

Teze D, Daligault F, Ferrières V, Sanejouand YH, Tellier C (2015) Semi-rational approach for converting a GH36 α-glycosidase into an α-transglycosidase. Glycobiology 25:420–427

Tran PL, Cha H-J, Lee J-S, Park S-H, Woo E-J, Park K-H (2014) Introducing transglycosylation activity in Bacillus licheniformis α-amylase by replacement of His235 with Glu. Biochem Biophys Res Commun 451(4):541–547

Turner P, Svensson D, Adlercreutz P, Karlsson E (2007) A novel variant of Thermotoga neapolitana β-glucosidase B is an efficient catalyst for the synthesis of alkyl glucosides by transglycosylation. J Biotechnol 130(1):67–74

van Rantwijk F, Woudenberg-van Oosterom M, Sheldon RA (1999) Glycosidase-catalysed synthesis of alkyl glycosides. J Mol Catal B Enzym 6(6):511–532

von Freiesleben P, Spodsberg N, Holberg Blicher T, Anderson L, Jørgensen H, Stålbrand H, Meyer AS, Krogh KBRM (2016) An *Aspergillus nidulans* GH26 endo-β-mannanase with a novel degradation pattern on highly substituted galactomannans. Enzym Microb Technol 83:68–77

von Rybinski W, Hill K (1998) Alkyl polyglycosides—properties and applications of a new class of surfactants. Angew Chem Int Ed Engl 37(10):1328–1345

Wang L-X, Huang W (2009) Enzymatic transglycosylation for glycoconjugate synthesis. Curr Opin Chem Biol 13(5–6):592–600

Wang Y, Vilaplana F, Brumer H, Aspeborg H (2014) Enzymatic characterization of a glycoside hydrolase family 5 subfamily 7 (GH5_7) mannanase from *Arabidopsis thaliana*. Planta 239:653–665

Yamabhai M, Sak-Ubol S, Srila W, Haltrich D (2016) Mannan biotechnology: from biofuels to health. Crit Rev Biotechnol 36:32–42

Zechel DL, Withers SG (2000) Glycosidase mechanisms: anatomy of a finely tuned catalyst. Acc Chem Res 33(1):11–18
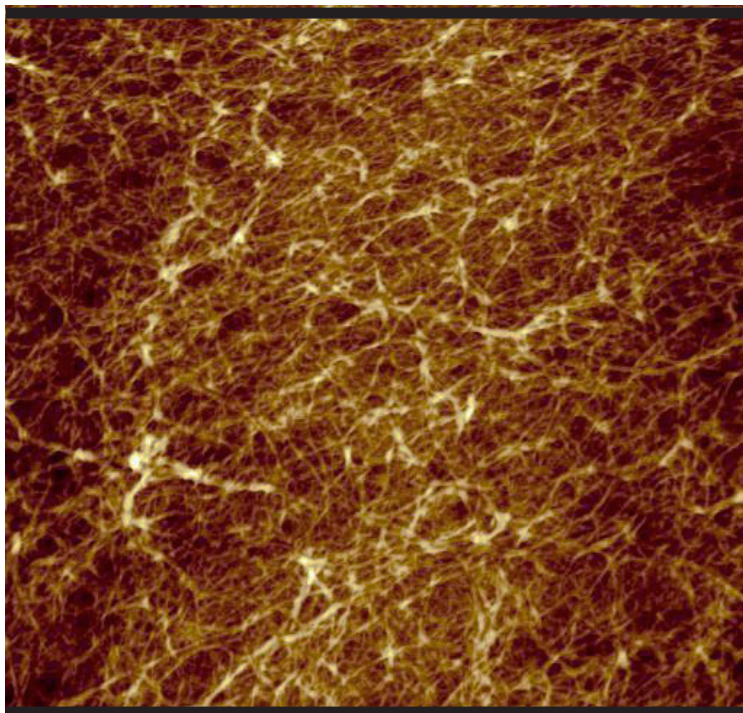
Topography image (5 x 5 μm) of cellulose microfibrils spin-coated on silica substrate.